UNIVERSITY OF NOTTINGHAM

PH.D. THESIS

Linear elastic fracture mechanics via the Material Point Method: A phase field approach

Ph.D candidate:

Emmanouil G. Kakouris

Supervisor:

Dr. Savvas P. Triantafyllou

Submitted in fulfilment of the requirements

for the degree of Doctor of Philosophy

in the

Centre for Structural Engineering and Informatics (CSEI)

Department of Civil Engineering

April 9, 2019

The University of Nottingham

UNITED KINGDOM · CHINA · MALAYSIA

This Ph.D. thesis was financially supported by the University of Nottingham.

Dedicated to...

UNIVERSITY OF NOTTINGHAM

Abstract

Faculty of Engineering

Department of Civil Engineering

Ph.D. thesis

Linear elastic fracture mechanics via the Material Point Method: A phase field approach

by Emmanouil G. Kakouris

Fracture is one of the main failure mechanisms of materials and structural components. During the past thirty years, various methods have been introduced to simulate crack initiation and growth. These include the introduction of Element Deletion Method and remeshing strategies within the standard Finite Element Method (FEM), cohesion based Finite Element strategies and the extended Finite Element Method. Very recently, a new method for crack propagation, namely the phase field method has been introduced; phase field models have been proven very robust in accurately predicting complex crack behaviour while at the same time avoiding standard re-meshing or enriching techniques.

To this point, phase field modelling has extensively been applied within a Finite Element framework while very little research and applications have been demonstrated with particle methods. However, treating the crack propagation problem using a grid based method is a challenging and computationally taxing task. The reliability and robustness of the Finite Element Method and in general mesh-based methods depends on the quality of the mesh itself. In this work, the phase field method is re-formulated and treated using an attractive Particle-In-Cell (PIC) scheme, namely the Material Point Method (MPM). In this approach, the coupled continuum/phase field governing equations are defined at a set of material points and interpolated at the nodal points of an Eulerian, i.e. non-deforming, mesh. The accuracy of the simulated crack path is thus decoupled from the quality of the underlying Finite Element mesh and relieved from corresponding mesh distortion errors.

This framework is then generalized for the case of anisotropic brittle fracture by introducing an anisotropic crack density functional. The anisotropic crack density functional gives rise to a family of phase field models, both second and fourth order, able to address brittle fracture simulation in anisotropic media. The proposed method is further extended into dynamic brittle fracture using both isotropic and anisotropic phase field models. Frictional contact problems involving phase field fracture are also examined and their post-fracture contact

response is investigated. On the proposed model, the local contact features are naturally handled using the Eulerian mesh and the damage evolution emerges without the need to numerically track discontinuities in the displacement field e.g. with jump and tip enrichment functions as well as complex crack paths can be obtained without any additional *ad hoc* rules. These advantages make the derived model a robust computational tool when arbitrary crack paths occur at impact-fracture problems.

Following, the proposed model is used to efficiently simulate crack paths induced from rocking response. The accuracy of the method is examined and verified based on existing analytical rocking response models; the method is then further extended into rocking system dynamics involving phase field fracture. Merits and drawbacks of the proposed formulation are examined using a set of benchmark tests. The influence of impact velocity, phase field and material point parameters on induced crack path is also examined. Validation based on experimental observations is also performed.

Contents

List of Figures

List of Tables

List of Abbreviations

ALE	**A**rbitrary **L**agrangian **E**ulerian
CDM	**C**ontinuum **D**amage **M**odels
CFL	**C**ourant - **F**riedrichs - **L**evy
CPDI	**C**onvected **P**article **D**omain **I**nterpolation
CPM	**C**racking **P**article **M**ethod
CSM	**C**ohesive **S**egments **M**ethod
CSMd	**C**oncentrated - **S**pring - **M**odel
CZM	**C**ohesive **Z**one **M**ethod
DEM	**D**iscrete **E**lement **M**ethod
DFM	**D**iscrete **F**racture **M**odels
EFGM	**E**lement **F**ree **G**alerkin **M**ethod
FEM	**F**inite **E**lement **M**ethod
GIMP	**G**eneralized **I**nterpolation **M**aterial **P**oint
IPM	**I**nverted **P**endulum **M**odel
LEFM	**L**inear **E**lastic **F**racture **M**echanics
LME	**L**ocal **M**aximum **E**ntropy
MERR	**M**aximum **E**nergy **R**elease **R**ate
MLS	**M**oving **L**east **S**quares
MPM	**M**aterial **P**oint **M**ethod
MSED	**M**inimum **S**train **E**nergy **D**ensity
MTS	**M**aximum **T**angential **S**tress
NURBS	**N**on - **U**niform **R**ational **B**-**S**plines
PD	**P**eri**d**ynamics
PF-FEM	**P**hase **F**ield **F**inite **E**lement **M**ethod

PF-MPM	**P**hase **F**ield **M**aterial **P**oint **M**ethod
PIC	**P**article **I**n **C**ell
PUM	**P**artition **U**nity **M**ethod
RKPM	**R**eproducing **K**ernel **P**article **M**ethod
SIF	**S**tress **I**ntensity **F**actor
SPH	**S**mooth **P**article **H**ydrodynamics
TLS	**T**hick **L**evel **S**et
VA	**V**ariational **A**pproach
WM	**W**inkler **M**odel
XFEM	e**X**tended **F**inite **E**lement **M**ethod

List of Symbols

$\mathbf{b}$	Body force vector
$\mathbf{B}$	Strain-displacement relation matrix
c	Phase field scalar value
d	Dimension of the problem ($d \in 1, 2, 3$)
$\mathbf{D}$	Constitutive matrix
E	Young's modulus
$\bar{\mathbf{f}}^{cont}$	Global contact force vector per unit surface
$\bar{\mathbf{f}}^{nor}$	Global normal contact force vector per unit surface
$\bar{\mathbf{f}}^{tan}$	Global tangential contact force vector per unit surface
F^c	Phase field "forcing" term
$\mathbf{F}^{cont}$	Global contact force vector
$\mathbf{F}^{ext}$	Global external force vector
$\mathbf{F}^{int}$	Global internal force vector
$\mathbf{F}^{irt}$	Global inertia force vector
$\mathbf{F}^{nor}$	Global normal contact force vector
$\mathbf{F}^{tan}$	Global tangential contact force vector
g	Degradation function
$\mathcal{G}_c$	Critical fracture energy density
h	Cell spacing
$\mathcal{H}$	History field
$\mathbf{I}$	Second-order identity tensor
j	Newton-Raphson iteration
k	Staggered iteration
k_f	Phase field model parameter

$\mathcal{K}$	Kinetic energy
$\mathbf{K}^c$	Global phase field matrix
$\mathbf{K}^u$	Global stiffness matrix
l_0	Length scale parameter
m	Increment
$\mathbf{M}^u$	Global mass matrix
$\mathbf{n}$	Outward unit normal vector
$\mathbf{n}^{cont}$	Outward unit normal vector at contact surface
N	Interpolation functions (basis functions)
$N_{\mathcal{D}}$	Total number of discrete fields
N_{iters}	Total number of iterations
N_n	Total number of grid nodes
N_p	Total number of material points
N_{staggs}	Total number of staggered iterations
N_{steps}	Total number of time steps (increments)
$\mathbf{p}$	Global momentum vector
$\mathbf{P}$	Eigen-vectors of strain tensor $\boldsymbol{\varepsilon}$
q_ξ	Polynomial order in ξ direction
R^c	Residual scalar value of phase field
$\mathbf{R}^u$	Global residual vector of displacement field
$\mathbf{R}_\theta$	Rotation matrix. Rotation by angle θ
$\mathbf{s}^{cont}$	Unit tangential vector at contact surface
S^c	Phase field driving force term
$\mathcal{S}^r$	Surface stiffness
t	Time
$\bar{\mathbf{t}}$	Traction/ pressure force vector
tol_c	Phase field residual tolerance
tol_u	Displacement field residual tolerance
$\mathbf{u}$	Global displacement vector
$\mathcal{W}^{ext}$	Work of external forces

$\mathcal{W}^{int}$	Work of internal forces
$\mathbf{x}$	Global position vector
$\mathcal{Z}_c$	Crack density functional
α	Penalty parameter
γ_{ijkl}	Tensor that corresponds to material anisotropy
Γ	Crack path
δ	Dirac function
$\boldsymbol{\varepsilon}$	Strain tensor
θ	Crack path orientation
λ	One of the Lamé constants (axial stretch)
$\boldsymbol{\Lambda}$	Eigen-values of strain tensor $\boldsymbol{\varepsilon}$
μ	One of the Lamé constants (shear modulus)
μ_f	Coulomb friction coefficient
ν	Poisson ratio
Ξ, H	Knot vectors
ρ	Mass density
$\boldsymbol{\sigma}$	Cauchy stress tensor
$\boldsymbol{\sigma}^+$	Positive part of Cauchy stress tensor (due to tension)
$\boldsymbol{\sigma}^-$	Negative part of Cauchy stress tensor (due to compression)
ϕ	Material orientation
ψ_{el}	Elastic strain energy density
ψ_{el}^+	Positive part of elastic strain energy density (due to tension)
ψ_{el}^-	Negative part of elastic strain energy density (due to compression)
ψ_{el_c}	Derivative of ψ_{el} with respect of c
Ψ_{el}	Total elastic strain energy
Ψ_f	Total fracture energy
Ψ_s	Total stored energy
Ω	Domain of a body

$\lvert(\cdot)\rvert$	Norm (absolute value) of the scalar $(\cdot)$
$\lVert(\cdot)\rVert$	Euclidean norm of tensors and vectors $(\cdot)$
$\operatorname{sign}(\cdot)$	The signum function: $\operatorname{sign}(\cdot) = (\cdot)/\lvert(\cdot)\rvert$
$\operatorname{Tr}(\cdot)$	Trace of $(\cdot)$
$\Delta(\cdot)$	Increment of $(\cdot)$
$\delta(\cdot)$	Iterative increment of $(\cdot)$
$\nabla(\cdot)$	Gradient of $(\cdot)$
$\partial(\cdot)$	Boundary of the domain $(\cdot)$
$\frac{\partial(\cdot)}{\partial\alpha}$	Derivative of $(\cdot)$ with respect to α
$\dot{(\cdot)}$	Time derivative of $(\cdot)$
$(\cdot)^T$	The transpose of $(\cdot)$
$(\cdot)^+$	Positive part of $(\cdot)$
$(\cdot)^-$	Negative part of $(\cdot)$
$(\cdot)_p$	Value of $(\cdot)$ at material point p
$(\cdot)_I$	Value of $(\cdot)$ at grid node I
$(\cdot)_{\mathcal{D}}$	Value of $(\cdot)$ at discrete field $\mathcal{D}$

Acknowledgements

I would like to express my deep gratitude to Associate Professor Savvas Triantafyllou, my research supervisor, for their patient guidance, enthusiastic encouragement and useful critiques of this research work.

I would also like to thank the thesis defence committee: Professors Adib A. Becker and Charles E. Augarde for the time they devoted and their constructive observations and comments.

The research described in this Ph.D. thesis has been financed by the University of Nottingham. A special thanks to the Faculty of Engineering, Nottingham University for providing me with this funding.

Thanks are also due to Assistant Professor Tao Liu, my second research supervisor, for the advices he supplied on numerous occasions. I wish also to express my gratitude to Associate Professor Manolis Chatzis from Oxford University for his guidance and support at the last Chapter of this thesis. Moreover, I would like to thank Professor Vlassis Koumousis from National Technical University of Athens, my Master's thesis advisor, for making me realize my passion for academic research and for equipping me with analytical and computational skills.

I would also like to thank all my colleagues at Nottingham University for their intellectual and motivational support and for making the department a pleasant working environment. Many thanks to the research group, namely Alex Kalamiotis, André de Araújo Vieira, Kostas Sfougaris, Zoi Tetta and Florentia Kariou for all the comments provided throughout the course of my Ph.D.

I would like to thank my companion, Maria, for her selfless support, continuous encouragement and personal sacrifices, throughout my life.

Finally, I am most thankful for the patience and support of my family.

Chapter 1

Introduction

1.1 Problem statement

Simulation of damage pertinent to crack initiation and crack growth is an intriguing and challenging aspect of computational mechanics. Damage modelling has received considerable attention during the past 30 years, as it is relevant to a number of natural and industrial processes, e.g., composite material behaviour (Wu et al., 2016), concrete fracture (Ferté et al., 2016), and ice mechanics (Konuk et al., 2009) amongst many. Within this setting, damage is being treated either within a continuum (or smeared) phenomenological framework (Murakami, 2012) or through discrete methods where the geometry of the crack is explicitly approximated, see, e.g. Sukumar et al. (2015). Thus, discrete methods can provide a better insight on the actual cracked configuration of a deformable body and form the basis for the study of related phenomena, e.g., corrosion (Duddu, 2014).

Initial efforts in discrete crack approaches include the Element Deletion Method (Song et al., 2008) and remeshing strategies (Azocar et al., 2010) whereas more sophisticated techniques involve the eXtended Finite Element method (XFEM) (Moës and Belytschko, 2002; Fries and Belytschko, 2006), cohesive element methods (Radovitzky et al., 2011; Snozzi and Molinari, 2013) and cohesive segments methods (Remmers et al., 2003). Cohesive element methods also based on the

notion of configurational force (Kaczmarczyk et al., 2014) are being used to address the crack initiation and propagation problem with the accuracy of the solution depending on the quality of the underlying Finite Element mesh.

In these methods, the evolution of complex crack paths, including merging cracks, needs to be tracked algorithmically. This means that there is the need to track the evolution of the discontinuities either with remeshing strategies so that the crack paths align with the element interfaces or with by enriching the displacement field approximation. Special discontinuous functions may also be required to predict branched cracks and resolve crack intersections (Daux et al., 2000). This increases the complexity of the underlying computational scheme and also the required computational resources especially in three-dimensional problems. Variational methods for fracture emerged in an effort to address such computational issues. Within this set of methods, Bourdin et al. (2008) used the mathematical framework of phase field theory (Fix, 1982) to provide a consistent theoretical framework of the analysis of crack propagation problems.

Phase field models represent cracks by means of an additional continuous field (termed the phase field) whose value depends on the state (cracked or uncracked) of the underlying geometrical domain (see, e.g. Borden et al. (2012)). The evolution of the additional field is defined on the basis of additional governing equations pertaining to the mathematics of phase field theory (Francfort and Marigo, 1998) linked however to a phenomenological framework such as Griffith's theory for brittle fracture (Griffith, 1921). The phase field evolution equations are weakly coupled to the standard governing equations (i.e., equilibrium, compatibility, and constitutive equations) of the continuum, effectively introducing a coupled-field problem. This is solved using any standard discretization procedure such as the Galerkin method (Bathe, 2007).

In this setting, the crack path emerges from the direct solution of the coupled-field framework. This renders phase field methods a promising computational tool to tackle fracture mechanics, at the cost however of introducing additional

unknowns, i.e. the phase field. Phase field modelling has been successfully applied within grid based methods, i.e. the FEM (see, e.g., previous studies (Miehe et al., 2010b; Verhoosel and Borst, 2013; Ambati et al., 2015a)) and its isogeometric variant (Borden et al., 2016) for the case of quasi-static fracture. Furthermore, phase field fracture modelling has been effectively applied to treat dynamic fracture propagation problems (Borden et al., 2012; Hofacker and Miehe, 2013; Schlüter et al., 2014).

However, treating crack propagation using a grid-based method introduces further challenges as robustness and accuracy directly depend on mesh quality and corresponding mesh distortion errors. Avoiding numerical errors due to mesh distortion is not a trivial task in grid-based Lagrangian methods (see, e.g. Kaczmarczyk et al. (2014) and Rangarajan et al. (2015)). Failure to bound such mesh-dependent errors may result in considerable loss of accuracy especially if large displacements and/or large deformations are taken into account.

Discrete Element Methods (Scholtès and Donzé, 2012), Smooth Particle Hydrodynamics (Batra and Zhang, 2007) and Peridynamics (Bobaru and Hu, 2012) can also efficiently deal with problems of fracture mechanics where large deformations take place. In the past, various meshless-based have been introduced in the field of fracture mechanics with particle refinement techniques, (Lee et al., 2003), enrichment strategies (Ventura et al., 2002; Amiri et al., 2014b) and cohesive theories (Klein et al., 2001; Soparat and Nanakorn, 2008; Zhang, 2010). Recently, phase field modelling has been introduced within the context of Local Maximum Entropy (LME) meshfree approximants to address the problem of fracture in thin shells (Amiri et al., 2014a). Although robust, especially when dealing with complex geometrical domains, purely meshless methods are computationally taxing, as a set of additional procedures is required to achieve convergence, i.e. higher-order integration schemes and neighbour searching (Nguyen et al., 2008).

To mitigate such issues, the Material Point Method (MPM) (Sulsky et al., 1994)

has been introduced as an extension of Particle-In-Cell (PIC) methods that efficiently treats history-dependent variables. In MPM, the continuum is represented by a set of (Lagrangian) material points that are moving within a fixed (Eulerian) computational grid where solution of the governing equations is performed. The constitutive equations are history dependent so material points are utilized to carry all the history dependent variables needed, such as plastic strains and strain-hardening, to track the complete deformation history process of a solid. Equally, the grid is used to evaluate the gradient and divergence terms of each material point.

Combining concepts pertinent to both the Eulerian and Lagrangian description of classical mechanics (Bathe, 2007), MPM has been proven advantageous in the analysis of large-scale, i.e. large-size three-dimensional problems involving material and geometric non-linearities, especially within the context of coupled-field problems, e.g. fluid-structure interaction (Li et al., 2014) and poro-mechanics (Jassim et al., 2013), also within a large deformation hydrodynamic setting (Abe et al., 2014; Bandara and Soga, 2015). The MPM has been found to offer significant computational advantages when compared to purely meshless methods since it does not require time-consuming neighbour searching.

With regards to fracture, the fact that material behaviour is monitored at material points that move within a fixed Eulerian grid implies that the transition from continuous to discontinuous displacement field can be modelled without the need for remeshing the computational grid and without the requirement to account for and mitigate mesh distortion due to crack propagation. Despite this, little research has been conducted to model the problem of damage modelling and in particular crack growth using the MPM.

In Schreyer et al. (2002) decohesion was treated by introducing a cohesive material constitutive framework at the material point level. Brittle fracture within

a MPM setting was examined for the first time in Nairn (2003) although considering only the case of pre-existing, i.e. explicit, crack geometries by allowing multiple velocity fields to be defined on the background grid. More recently, cohesive modelling approaches have been introduced in an effort to further generalize the applicability of the MPM for problems pertinent to arbitrary crack paths (Daphalapurkar et al., 2007; Bardenhagen et al., 2011; Yang et al., 2014; Sanchez et al., 2015). Continuum damage–based approaches have been introduced in Homel and Herbold (2017) and Nairn et al. (2017) also demonstrating the advantages of using domain decomposition methods to accelerate MPM.

1.2 Research Scope

Further to the current state of the art, this Ph.D. thesis introduces a Phase Field Material Point Method (PF-MPM) implementation to resolve quasi-static and dynamic brittle fracture in both isotropic and anisotropic materials. The resulting computational method is further extended in the dynamic regime and impact driven fracture problems are examined.

By introducing phase fields at the material point level rather than the nodal points of a fixed Lagrangian grid, the proposed method succeeds in monitoring crack initiation and growth in an efficient and robust manner.

Only the case of Linear Elastic Fracture Mechanics (LEFM) is examined in this work. Hence, plastic deformations induced either before or after crack initiation are neglected. Furthermore, the theory is formulated in the concept of small strain approximation which is a reasonable assumption for fracture in brittle materials. Finally, any strain rate dependence e.g. of the fracture toughness is beyond the scope of this work.

Resolving dynamic crack propagation, especially within an impact dynamics setting has to this point proven to be a challenging and arduous task. The MPM

provides a robust framework for the analysis of contact mechanics, especially within a large displacement setting.

The Phase field method has proven robust in tackling fracture propagation, especially in problems where fragmentation is involved. The overarching aim of this Ph.D. thesis was to derive and introduce a PF-MPM that can efficiently treat impact driven fracture. This is a direction not explored in the literature.

Numerical investigations demonstrate that compared to the standard phase field Finite Element implementation, the proposed method is highly advantageous in terms of accuracy. The dynamic impact fracture framework developed as a part of this Ph.D. renders the study of the rocking response of flexible structures feasible; this is not the case for standard Finite Element Methods.

1.3 Aims & Objectives

To achieve this, the following Research Objectives (ROs) are identified:

- **RO.1:** Introduce a phase field driven fracture framework in the MPM for quasi-static problems. Verification to be made against published results in the literature and validation based on experimental observations. The sensitivity of the resulting crack paths on the phase field and material point parameters is examined. The numerical robustness of the derived method is also examined.

- **RO.2:** Further extend this formulation to account for anisotropic brittle fracture. Derive the fully anisotropic phase field governing equations and quantify the effect of material anisotropy on the response of fracture media.

- **RO.3:** To implement the proposed PF-MPM into dynamic crack propagation problems. Considering the case of both isotropic and anisotropic materials that are subjected to dynamic loads. Extend the developed framework to solve frictional contact problems involving phase field fracture.

- **RO.4:** To study the appropriateness of the developed model to simulate rocking system dynamics. This will further serve as verification against existing models in the literature. Examination of crack paths induced by rocking response.

1.4 Methodology

To accomplish the aforementioned Research Objectives in Section 1.3, this research has been structured along seven work packages (WPs) (see also Fig. 1.1). All source codes described in this work, were developed from scratch. In the beginning of each WP, the Matlab programming language was utilized for the development of algorithms enabling rapid development and benchmarking.. However, the Matlab source codes were finally converted into Fortran source codes to accelerate the computing operations.

- **WP.1:** Development of the phase field damage models into an in-house code. Modification of the derived scheme to account for fracture only due to tension (the fracture due to compression is avoided). Derivation and implementation of the second order phase field model and testing it into isotropic materials. Extension to fourth order phase field models for increasing the convergence rates. Derivation of the coupled governing equations of the fourth order phase field model to simulate anisotropic brittle fracture.

- **WP.2:** Development of the standard MPM into an in-house code. Formulation of the method for quasi-static and dynamic problems. Both explicit and implicit time integration schemes are formulated in dynamic problems. Extension of standard linear basis (interpolation) functions to higher order B-Splines to overcome the grid crossing error, to increase the convergence rates and to regularize higher-order phase field models. Further development of the algorithm to simulate friction contact problems. Verification of the contact algorithm with analytical solutions.

  Coupling of phase field damage models with the MPM and implementation of a staggered solution procedure. Derivation of the proposed PF-MPM scheme.

- **WP.3:** Evaluation of the proposed scheme for the case of quasi-static brittle fracture problems. Investigation of key phase field (e.g. diffusion of damage around the crack path, material orientation) and MPM parameters (e.g. number of material points, cell spacing). Benchmark tests and verification of the derived scheme in both isotropic and anisotropic materials.

- **WP.4:** Extension of the proposed scheme into dynamic brittle fracture problems. Comparison of the results derived by the PF-MPM approach against the FEM.

- **WP.5:** Further development of the proposed scheme into frictional contact problems involving phase field fracture. Examination of key parameters i.e. loading velocity, fracture toughness and material orientation on the material response. Verification of the derived scheme with analytical solutions.

- **WP.6:** Development of the derived scheme to simulate the response of rocking systems and introduction of kinematical failure criteria. Stability

analysis examination of rocking bodies and verification based on existing models in the literature. Extension to deformable rocking bodies.

- **WP.7:** Implementation and evaluation of PF-MPM in simulating damage evolution in rocking systems.

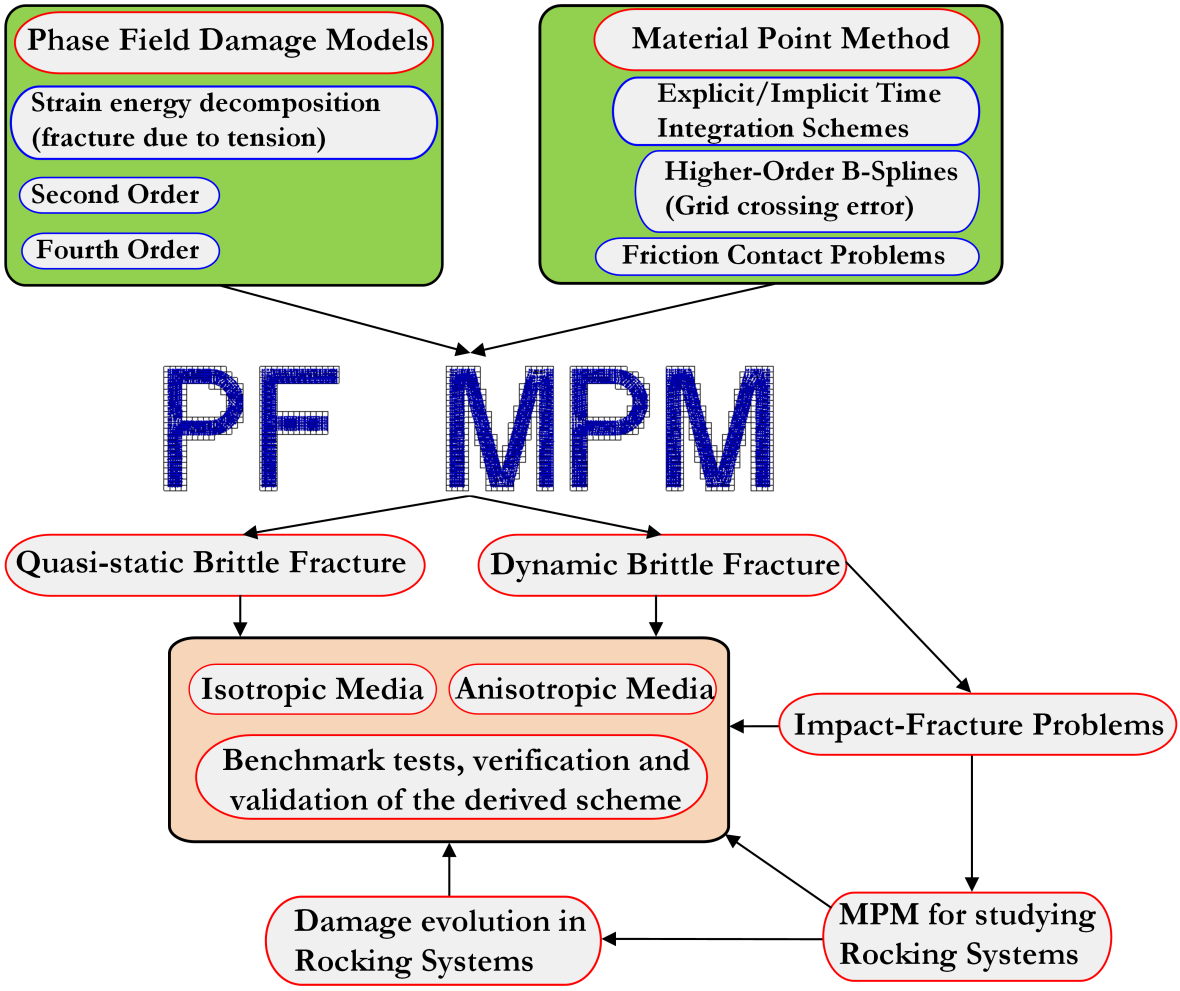

Figure 1.1: Methodology of the project.

1.5 Original contribution

As part of this work, the following contributions have been made:

- A MPM coupling with phase field models for brittle fracture is proposed for the first time in this work. The accuracy and the efficiency of the

method is demonstrated through a set of benchmark tests. The method is verified against the standard Finite Element implementation and validated using experimental results.

- The PF-MPM is further extended to account for brittle fracture in materials that possess anisotropic surface energy. The fully anisotropic phase field governing equations are derived herein, and an investigation of material anisotropy on the results is made. A set of benchmark problems is examined to verify the proposed formulation compared to the standard Phase Field Finite Element implementation.

- The PF-MPM is further extended to dynamic brittle fracture with isotropic and anisotropic surface energy. Impact-fracture problems are examined with the proposed method. The numerical procedure is implemented within a staggered solution approach and an explicit time integration scheme.

- The method is used to study fracture induced by rocking impact of deformable media further extending the current state of the art where only the case of a rigid body is examined.

- The derived scheme is utilized to simulate the damage (brittle fracture) induced by rocking systems with phase field models for the first time.

- MaPoMe is an open source code implementation of the derived scheme. Currently accessible via *MaPoMe* : http://www.nottingham.ac.uk/~ezzst1/downloads.html.

1.6 Publications

1.6.1 Publications in International Scientific Journals

This research has already contributed to two journal publications in peer-reviewed journal with one more currently under review.

[1] **Kakouris E.G.**, Triantafyllou S.P. (2018), "Phase-field material point method for dynamic brittle fracture with isotropic and anisotropic surface energy", *Computer Methods in Applied Mechanics and Engineering* (Submitted - under review).

[2] **Kakouris E.G.**, Triantafyllou S.P. (2018), "Material point method for crack propagation in anisotropic media: a phase-field approach", *Archive of Applied Mechanics, 88(1) pp. 287-316*.

[3] **Kakouris E.G.**, Triantafyllou S.P. (2017), "Phase-Field Material Point Method for Brittle Fracture", *International Journal for Numerical Methods in Engineering, 112(12), pp. 1750-1776*.

1.6.2 Proceedings of International Conferences

Furthermore, parts of this research have been presented in the following international conferences.

[1] Kakouris E.G., **Triantafyllou S.P.**, "Phase Field Material Point Method for Impact Induced Fracture", *13^{th} World Congress on Computational Mechanics, 22 - 27 July 2018, NY, US*.

[2] **Kakouris E.G.**, Chatzis M.N., Triantafyllou S.P., "A Material Point Method for Studying Rocking Systems", *16^{th} European Conference on Earthquake Engineering, 18 - 21 June 2018, Thessaloniki, Greece*.

[3] **Kakouris E.G.**, Triantafyllou S.P., "Dynamic brittle fracture via Material Point Method - A phase field implementation", *UKACM Conference on Computational Mechanics, 12 - 13 April 2017, Birmingham, UK.*

[4] **Kakouris E.G.**, Triantafyllou S.P., "Phase-Field Material Point Method for Anisotropic Brittle Fracture", *EMI International Conference, 25 - 27 October 2016, Metz, UK.*

[5] **Kakouris E.G.**, Triantafyllou S.P., "Material Point Method for Nonlinear Analysis of Hysteretic Processes", *12^{th} World Congress on Computational Mechanics, 24 - 29 July 2016, Seoul, Korea.*

[6] **Kakouris E.G.**, Triantafyllou S.P., "Phase-Field Material Point Method for Brittle Fracture", *11^{th} HSTAM International Congress on Mechanics, 27 - 30 May 2016, Athens, Greece.*

1.7 Thesis layout

The present work is organized as follows. In Chapter 2, a critical assessment of fracture propagation methods is presented. Next, the Material Point Method is discussed in Chapter 3. The Phase Field Material Point Method (PF-MPM) implementation for brittle fracture that constitutes the core contribution of this work is presented in Chapter 4. The extension of PF-MPM into anisotropic brittle fracture is described in Chapter 5 and a dynamic implementation of the method is examined in Chapter 6. Finally, an introduction of PF-MPM for studying rocking systems is described in Chapter 7 while the conclusion remarks and future work are presented in Chapter 8.

Chapter 2

Review of fracture propagation methods

2.1 Introduction

Computation often plays a crucial role for modelling and understanding the failure mechanism of materials. However, modelling the exact crack path, has been one of the most challenging tasks mainly due to the challenges imposed by the underlying physics and the computational complexity of the corresponding numerical models that increases the demand for resources. During the past thirty years, a wide variety of numerical methods have been introduced to accurately and efficiently model complex failure mechanisms considering minimal complexity and computational requirements.

Three main approaches exist in the literature to model fracture processes, namely:

- Continuum damage models
- Discrete fracture models
- Variational approaches

2.2 Crack initiation and propagation

There are three fracture modes that enable a crack to propagate under the action of external forces, namely mode I, II and III. In mode I (opening mode), the crack tip is driven by a tensile stress normal to the crack surface while mode II crack (sliding mode) emerges from a shear stress acting parallel to the plane of the crack and perpendicular to the crack front. Mode III crack (tearing mode) is driven by a shear stress acting out of the plane of the crack surface (Sun and Jin, 2012). The three fracture modes are shown in Fig. 2.1.

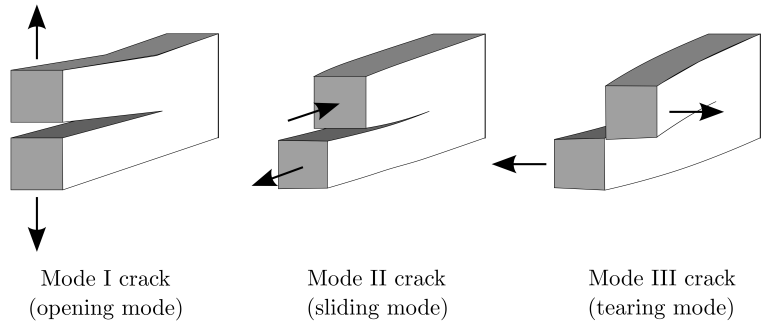

Figure 2.1: The three fracture modes.

In Linear Elastic Fracture Mechanics, there are three widely-used criteria to determine the initiation, propagation and direction of a crack path. These are the Maximum Tangential Stress (MTS) criterion (Erdogan and Sih, 1963), the Minimum Strain Energy Density (MSED) criterion (Sih, 1974) and the Maximum Energy Release Rate (MERR) criterion (Nuismer, 1975). The aforementioned crack growth criteria are briefly discussed in Sections 2.2.1, 2.2.2 and 2.2.3, respectively. A detailed discussion on this criteria can be found in Bouchard et al. (2003).

2.2.1 Maximum Tangential Stress (MTS) criterion

The stress field near the crack tip is shown in Fig. 2.2 where r and θ are the polar coordinates. According to MTS criterion (Erdogan and Sih, 1963), a crack

propagates in the direction for which the circumferential stress $\sigma_{\theta\theta}$ reaches a critical value along a small radius r at the crack tip. The circumferential stress $\sigma_{\theta\theta}$ is computed for mixed mode I/II crack propagation as

$$\sigma_{\theta\theta} = \frac{1}{\sqrt{2\pi r}} \cos\frac{\theta}{2}\left(K_I \cos^2\frac{\theta}{2} - \frac{3}{2}K_{II}\sin\theta\right) \tag{2.1}$$

where K_I and K_{II} are the Stress Intensity Factors (SIFs) (Sun and Jin, 2012) for the fracture modes I and II, respectively. The MTS can be expressed mathematically as

$$\begin{cases} \dfrac{\partial\sigma_{\theta\theta}}{\partial\theta} = 0, & \text{(2.2a)} \\ \dfrac{\partial^2\sigma_{\theta\theta}}{\partial\theta^2} < 0, & \text{(2.2b)} \end{cases}$$

Substituting Eq. (2.1) into (2.2a), the MTS leads to

$$\sigma_{\theta\theta} = K_I \sin(\theta) + K_{II}\left(3\cos(\theta) - 1\right) = 0 \tag{2.3}$$

while Eq. (2.2b) is used to determine the limitation of crack direction as

$$\theta < \arctan\left[\frac{K_I\sqrt{\frac{2}{\pi d_f}}}{3K_{II}\sqrt{\frac{2}{\pi d_f}}}\right] \tag{2.4}$$

where d_f is the fracture process zone length (see Matvienko (2012) for details). As it is highlighted by Bouchard et al. (2003), the limit angle that corresponds to pure shear is $\theta = 70.54^{\text{o}}$.

2.2.2 Minimum Strain Energy Density (MSED) criterion

The MSED was developed by Sih (1974) and considers that the crack emerges along the direction in which the strain energy density is the minimum. The

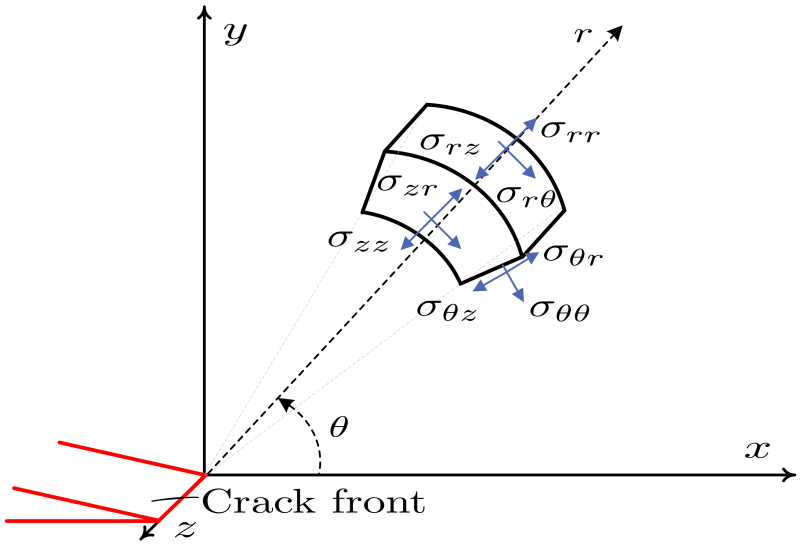

Figure 2.2: Stress fields near the crack tip.

MSED criterion can be expressed mathematically as

$$\begin{cases} \dfrac{\partial S_{el}}{\partial \theta} = 0, & \text{(2.5a)} \\ \dfrac{\partial^2 S_{el}}{\partial \theta^2} > 0, & \text{(2.5b)} \end{cases}$$

where $S_{el}(\theta)$ is the strain energy density factor defined as

$$S_{el}(\theta) = \frac{d\psi_{el}(\theta)}{d\Omega} r \tag{2.6}$$

where $\frac{d\psi_{el}}{d\Omega}$ is the strain energy density function per unit volume and $r \neq 0$ is the distance from the crack tip to point of crack initiation (see Fig. 2.2). The strain energy density factor $S_{el}(\theta)$ can be expressed for mixed-mode loading conditions as (Sih, 1974)

$$S_{el}(\theta) = \frac{1}{\pi r}\left(\alpha_{11}K_I^2 + 2\alpha_{12}K_I K_{II} + \alpha_{22}K_{II}^2\right) \tag{2.7}$$

where

$$\begin{cases} \alpha_{11} = \dfrac{1}{16\mu\pi}\left[(K_{el} - \cos(\theta))\,(1 + \cos(\theta))\right], & \text{(2.8a)} \\ \alpha_{22} = \dfrac{1}{16\mu\pi}\left[(K_{el} + 1)\,(1 - \cos(\theta)) + (1 + \cos(\theta))\,(3\cos(\theta) - 1)\right], & \text{(2.8b)} \\ \alpha_{12} = \dfrac{1}{16\mu\pi}\left[\sin(\theta)\,(2\cos(\theta) - K_{el} + 1)\right], & \text{(2.8c)} \end{cases}$$

and μ is the shear modulus of elasticity. The elastic parameter K_{el} is computed as

$$K_{el} = \begin{cases} 3 - 4\nu & \text{Plane strain} \\ \frac{3-\nu}{1+\nu} & \text{Plane stress} \end{cases} \tag{2.9}$$

where ν is the Poisson's ratio. A crack propagates when the minimum strain energy density factor reaches a critical value $S_{el,cr}$, i.e.

$$S_{el,min} = S_{el,cr} = \alpha_{11}K_I^2 + 2\alpha_{12}K_I K_{II} + \alpha_{22}K_{II}^2 \tag{2.10}$$

The MSED criterion is simple and it can be applied to various mixed fracture modes see e.g. (Lazzarin et al., 2008). An extension of the MSED criterion to three-dimensional problems can be found in Sih (1991).

2.2.3 Maximum Energy Release Rate (MERR) criterion

The energy balance of Griffith's theory states that the energy release per unit advancement of an existing crack has to be equal to the energy consumption for the creation of a new fracture surface. The MERR criterion (Nuismer, 1975) is an extension of Griffith's theory which states that a crack propagates in the direction along which the maximum potential energy is released.

This can be mathematically expressed as

$$\begin{cases} \dfrac{d\mathcal{G}}{d\theta} = 0, & \text{(2.11a)} \\ \dfrac{d^2\mathcal{G}}{d\theta^2} \leq 0, & \text{(2.11b)} \end{cases}$$

where $\mathcal{G}$ represents the strain energy release rate and is the energy required to create a unit of fracture surface. The strain energy release rate is defined as

$$\mathcal{G} = -\frac{\partial \Psi_s}{\partial \Gamma} \tag{2.12}$$

where Ψ_s is the total potential energy and Γ is the crack surface. Based on this criterion, a crack propagates when $\mathcal{G}$ reaches a critical value $\mathcal{G}_c$, i.e.

$$\mathcal{G} \geq \mathcal{G}_c \tag{2.13}$$

where $\mathcal{G}_c$ is the critical energy release rate and it is considered as a material parameter.

In pure fracture mode I, the strain energy release rate can be expressed in respect to SIF as

$$\mathcal{G} = \frac{K_I^2}{E'} \tag{2.14}$$

and the effective elastic modulus E' as

$$E' = \begin{cases} E & \text{Plane strain} \\ \frac{E}{1-\nu^2} & \text{Plane stress.} \end{cases} \tag{2.15}$$

In mixed mode planar problems, the strain energy release rate is defined as

$$\mathcal{G} = \frac{1}{E'} \left(K_I^2 + K_{II}^2 \right). \tag{2.16}$$

2.3 Continuum Damage Models

Continuum Damage Models (CDMs) account for the degradation/failure of materials through an internal damage variable which incorporates the micro and macro cracking effects of the material (Murakami, 2012). The mechanical

degradation of the materials is modelled through the following stress strain relation

$$\boldsymbol{\sigma}\left(\mathbf{u}, d_m\right) = (1 - d_m)\mathbf{D} : \boldsymbol{\varepsilon} \tag{2.17}$$

where $\mathbf{u}$ is the displacement field and d_m is a scalar damage parameter which varies from 0 to 1 for the undamaged and completely damaged material, respectively. Furthermore, $\mathbf{D}$ is the fourth-order elastic stiffness tensor and $\boldsymbol{\varepsilon}$ is the strain tensor. In CDMs, the scalar damage parameter d_m is a function of a state variable $\mathcal{J}$. That state variable depends on the strain tensor $\boldsymbol{\varepsilon}$, i.e. $d_m = d_m(\mathcal{J}\left(\boldsymbol{\varepsilon}\right))$. The CDMs are related to plasticity theories in a sense that the stress field evolves though internal variables (see e.g. Souza Neto et al. (2008)). According to the choice of state variable $\mathcal{J}$, the CDMs can be further classified into local, non-local and gradient-enhanced damage models.

2.3.1 Local damage models

In local damage models, the state variable $\mathcal{J}$ is the equivalent strain $\widetilde{\varepsilon}\left(\boldsymbol{\varepsilon}\right)$. In the past, various definitions have been proposed for the equivalent strain, see e.g. Simo and Ju (1987), Mazars (1986) and Vree et al. (1995). In Simo and Ju (1987), the equivalent strain $\widetilde{\varepsilon}\left(\boldsymbol{\varepsilon}\right)$ is defined as

$$\widetilde{\varepsilon} = \sqrt{2\psi_{el}\left(\boldsymbol{\varepsilon}\right)} \tag{2.18}$$

where ψ_{el} is the local elastic strain energy density. However, that definition does not distinguish between tensile and compressive strain components as a result it leads to unrealistic mechanical behaviour of quasi brittle fracture materials such as concrete, rock and ceramics.

To overcome that issue, Mazars (1986) proposed the following definition of $\widetilde{\varepsilon}$ as

$$\widetilde{\varepsilon} = \sqrt{\sum_{i=1}^{3}\left(\langle\varepsilon_i\rangle^{+}\right)^2} \tag{2.19}$$

where $\langle \boldsymbol{\varepsilon}_i \rangle^+, i = 1,2,3$ are the positive part of the principal strains. To this extent, Vree et al. (1995) introduced a third definition for the $\widetilde{\varepsilon}$ as

$$\widetilde{\varepsilon} = \frac{k_d - 1}{2k_d\,(1-2\nu)} I_1(\boldsymbol{\varepsilon}) + \frac{1}{2k_d}\left[\left(\frac{k_d-1}{1-2\nu} I_1(\boldsymbol{\varepsilon})\right)^2 + \frac{12k_d}{(1+\nu)^2} J_2(\boldsymbol{\varepsilon})\right]^{\frac{1}{2}} \tag{2.20}$$

In Eq. (2.20), ν is the Poisson's ratio, $I_1(\boldsymbol{\varepsilon})$ is the first invariant of the strain tensor and $J_2(\boldsymbol{\varepsilon})$ is the second invariant of the deviatoric strain tensor $\boldsymbol{\sigma}$. The model parameter k_d is defined as the ratio of the compressive uniaxial strength and the tensile uniaxial strength and it is introduced in Eq. (2.20) so that the compressive uniaxial stress $k_d\boldsymbol{\sigma}$ results the same effect as a uniaxial tensile stress. Further information about the aforementioned damage models can be found in Borst et al. (2012).

Local damage models are known to be highly mesh sensitive since the strain-softening is introduced locally, i.e. at a particular point, which may lead into locally ill-posed partial differential equation, i.e. loss of ellipticity in case of quasi-static analyses, and loss of hyperbolicity for dynamic calculations (Murakami and Liu, 1995). Loss of ellipticity occur when the condition

$$\det\left(\mathbf{n}_{sd} \cdot \mathbf{D} \cdot \mathbf{n}_{sd}\right) = 0 \tag{2.21}$$

is locally met where $\det$ is the determinant and $\mathbf{n}_{sd}$ is the normal vector to the discontinuity Γ as presented in Fig. 2.3. Ellipticity is necessary condition for the boundary value problems to ensure unique solution, otherwise an infinite number of possible solutions emerges (Borst et al., 2012). The localisation issues in local damage models can also be found in (Peerlings et al., 2002).

2.3.2 Non-local damage models

To overcome the previous discussed numerical issues, non-local damage models were introduced (Pijaudier-Cabot and Bazant, 1987). In non-local damage

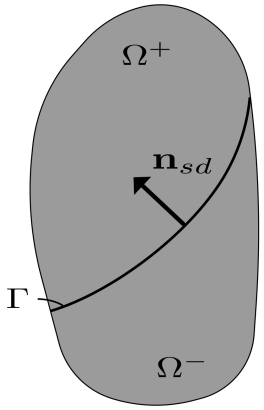

Figure 2.3: Decomposition of a solid body Ω into two continuous displacement fiels with an internal discontinuity Γ.

models, the state variable depends on a spatially averaged quantity, e.g. the non-local equivalent strain $\bar{\varepsilon}$. This quantity is weighted over an area around the point of interest. The weighting area is defined through a length scale parameter l_c which is the radius of that area and acts as a localization limiter to regularize the problem and avoid any loss of ellipticity locally. The introduction of a length scale parameter also allows to study size effects of materials (Le Bellego et al., 2003).

In non-local damage models, the equivalent strain $\bar{\varepsilon}$ is expressed as

$$\bar{\varepsilon}\left(\mathbf{x}\right) = \frac{1}{|\Omega_v|} \int_{\Omega_v} W(\xi) \widetilde{\varepsilon}(\mathbf{x}+\xi) d\xi \tag{2.22}$$

where $\mathbf{x}$ is the position vector, $\Omega_v \subset \Omega$ is an averaging volume, $\xi \in \Omega_v$, and W is a weight function. A commonly used weight function is the bell-shape Gaussian distribution which for the three-dimensional problem is evaluated as

$$W(\xi) = \frac{1}{2\pi^{3/2} l_c^3} \exp\left(\frac{-|\xi|)^2}{2l_c^2}\right). \tag{2.23}$$

Although the non-local damage models overcome the loss of ellipticity issue as well as they can be easily applied from the computational point of view, leads

to an increased band width for the tangential stiffness matrix and its symmetry can be lost (Borst et al., 2012; Pijaudier-Cabot and Huerta, 1991).

2.3.3 Gradient-enhanced damage models

In gradient-enhanced damage models, higher-order deformation gradients are introduced in the constitutive model, i.e. the state variable $\mathcal{J}$. Gradient-enhanced damage models can be directly derived from non-local theory (Peerlings et al., 1996). In particular, if a Taylor expansion is used for the equivalent strain $\widetilde{\varepsilon}$, i.e.

$$\begin{aligned}\widetilde{\varepsilon}(\mathbf{x}+\xi) = \widetilde{\varepsilon}(\mathbf{x}) + \frac{\partial\widetilde{\varepsilon}}{\partial x_1}\xi_1 + \frac{\partial\widetilde{\varepsilon}}{\partial x_2}\xi_2 + \frac{\partial\widetilde{\varepsilon}}{\partial x_3}\xi_3 + \\ \frac{1}{2!}\frac{\partial^2\widetilde{\varepsilon}}{\partial x_1\partial x_2}\xi_1\xi_2 + \frac{1}{2!}\frac{\partial^2\widetilde{\varepsilon}}{\partial x_2\partial x_3}\xi_2\xi_3 + \frac{1}{2!}\frac{\partial^2\widetilde{\varepsilon}}{\partial x_1\partial x_3}\xi_1\xi_3\end{aligned} \tag{2.24}$$

then the non-local equivalent strain of Eq. (2.22) can be written as

$$\bar{\varepsilon} = \widetilde{\varepsilon} + \bar{l}\Delta\widetilde{\varepsilon} \tag{2.25}$$

In Eqs. (2.24) and (2.25) any higher-order terms are neglected, $\bar{l}$ is a gradient parameter ($\bar{l} = 0.5l_c^2$) and Δ is the Laplace operator. However, Eq. (2.25) requires higher-order basis functions for its numerical approximation. To avoid this, Peerlings et al. (1996) proposed an alternative formulation so that Eq. (2.25) can be considered as an additional partial differential equation as

$$\bar{\varepsilon} - \bar{l}\Delta\bar{\varepsilon} = \widetilde{\varepsilon}. \tag{2.26}$$

The non-local equivalent strain $\bar{\varepsilon}$ is now an additional variable to be solved for the system of Eqs. (2.17) and (2.26) and it can be approximated by linear basis functions, i.e. C^0. Eq. (2.26) is further supplemented by the following natural boundary condition

$$\nabla\bar{\varepsilon}\cdot\mathbf{n}_{sd} = 0 \tag{2.27}$$

where $\mathbf{n}_{sd}$ is the outward unit vector normal to the crack path Γ.

An overview and a comparison of the material behaviour of both non-local and gradient-enhanced damage models can be in found in Peerlings et al. (2001). Furthermore, a comparison of gradient-enhanced damage and phase field damage models can be found in Borst and Verhoosel (2016) where it was found that their mathematical structure is almost identical. However, the derivation of these two models is different. The gradient-enhanced models are smeared approaches derived from an effort to eliminate the ill-posedness of differential equations by introducing the gradients of equivalent strain. In comparison, phase field models are a variational approach to fracture where a crack density functional is utilized to describe the discontinuities in the displacement field and it is regularised by introducing a length scale parameter. Further details of phase field interpretation can be found in Section 2.6.

2.4 Discrete fracture models (DFMs)

Within the continuum context, Discrete Fracture models (DFMs) consider cracks as geometric discontinuities. Hence, the cracks are considered to be discrete and they are modelled as strong discontinuities in the displacement field.

2.4.1 Remeshing and refinement strategies

In DFMs, cracks have been originally assumed to occur at the nodes of the Finite Element mesh. In this, a crack propagates when the nodal force, normal to the element boundaries, exceeds the maximum tensile force that the material can sustain. Thus, when this failure criterion is satisfied, new degrees of freedom are introduced at that node, creating a strong geometric discontinuity between the 'old' and the 'new' node.

Examples of remeshing strategies in the realm of LEFM can be found in Bittencourt et al. (1996), Bouchard et al. (2003) and Azocar et al. (2010) amongst many. Bittencourt et al. (1996) introduced a strategy for crack propagation modelling of arbitrary cracks in two-dimensional problems. In this, the Finite Element mesh is locally regenerated near the crack tip at each time step by using a robust remeshing algorithm. Mixed-mode SIFs are calculated to simulate the crack growth and their numerical results are compared against the experimentally obtained paths leading to good agreement.

Bouchard et al. (2003) also examined crack propagation with an automatic remeshing strategy and presented a comparison of different fracture criteria, i.e. MTS, MSED and MERR (see Section 2.2). Similarly, Azocar et al. (2010) considered automatic LEFM crack propagation method based on local Lepp–Delaunay mesh refinement. This technique allows for local mesh refinement near the crack tips with triangular meshes. The MTS criterion is also used to predict the crack path and their results are validated against the already published experimental results with excellent agreement.

In contrast, meshless methods, which are not equipped with a predefined computational mesh, do not require time consuming remeshing strategies. However, they may require particle refinement techniques close to crack tip to accurately represent the stress field. Examples of adaptive refinement procedures can be found in Lee et al. (2003) within the element-free Galerkin method but more details are also presented in Chapter 3.

2.4.2 Cohesive Zone Method (CZM)

Alternative DFMs based on cohesive theories have been utilized to overcome stress singularities in LEFM and to consider the nonlinear separation phenomena (Anderson, 1995). Barenblatt (1962) originally introduced the CZM to model fracture in brittle materials. Later, Dugdale (1960) extended the CZM to study

yielding and plastic zone around the crack tips and Hillerborg et al. (1976) proposed a linear decohesion relation between the fracture energy and the tensile strength of concrete.

In cohesive fracture theory, the material is not considered perfectly brittle as in Griffith's theory. Rather, there is a small zone in front of the crack that can exhibit some ductility. The fracture energy is gradually released at the crack tip based on crack opening and equals the critical fracture energy at full crack opening. If the cohesive zone is sufficiently small, the ductility zone becomes unimportant and the theory of LEFM can be applied.

The fracture energy function depends on the jump of the displacement field u_r across the discontinuity Γ, i.e. $\mathcal{G} = \mathcal{G}(\mathbf{u})$. Hence, the cohesive tractions are obtained though the following relation

$$\mathbf{t} = \frac{\partial \mathcal{G}}{\partial \mathbf{u}_r} \tag{2.28}$$

In Fig. 2.4, the traction-opening relations are shown for linear decohesion where $\mathcal{G}_c$ is the critical fracture energy which corresponds to the fracture energy per unit fracture surface at full crack opening and the fracture strength t_u. A review of other proposed traction-separation relationships across fracture surfaces can be found in Park and Paulino (2011).

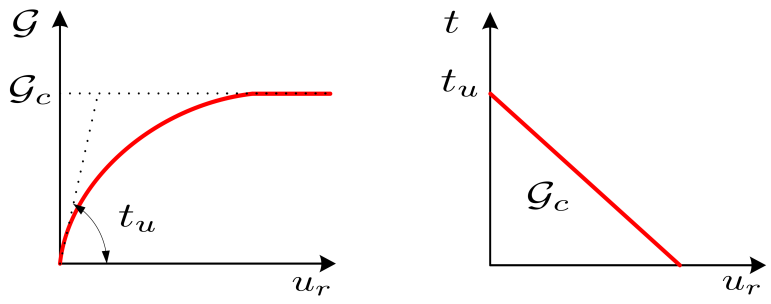

Figure 2.4: Cohesive Zone Method: Crack-opening relations.

In Finite Element-based methods, the Cohesive Zone Method (CZM) introduces cohesive elements at the Finite Element interfaces (see Fig. 2.5). These cohesive elements do not have any physical meaning. Rather, cohesive traction forces occur when the material interfaces are separated. The degradation along a discrete crack is a function of these traction forces. The traction forces are based on the relative displacements (crack opening) at the Finite Element interface. Crack paths can only evolve along the element interfaces, hence limiting the possible crack patterns that the method can account for or necessitating the use of a very fine mesh discretization. The cohesive elements can either be defined at the area of interest if the crack path is known *a priori*, e.g. from experimental observations, or at all element interfaces. In the second case, the computational costs are dramatically increased.

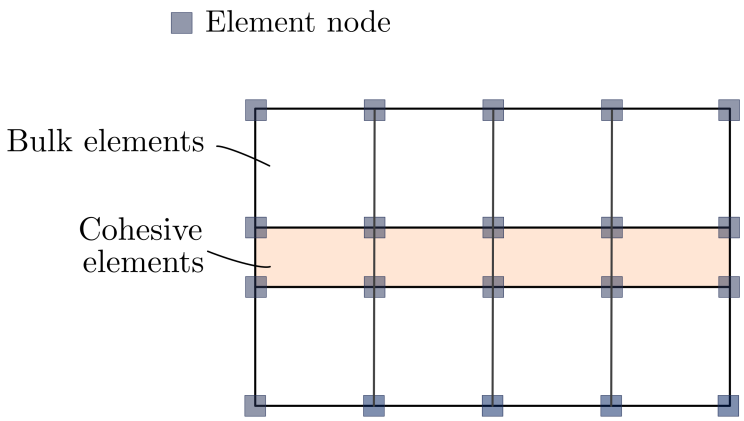

Figure 2.5: Cohesive Zone Method: Cohesive elements at the Finite Element interfaces.

Examples of the CZM with FEM can be found in Xu and Needleman (1994) for dynamic crack propagation problems where it was shown that crack branching emerged normally without any *ad hoc* branching criteria. Furthermore, Chen et al. (2009) introduced a Cohesive Zone Finite Element-based Method for modelling of hydraulic fracture. Apart from these, cohesive theories has also been applied to other mesh-based method e.g. the Boundary Element Method for the crack growth analysis in concrete Salen and Aliabadi (1995).

The main disadvantage of these procedures is that the crack paths always align with the structure mesh, making the resulting solution mesh dependent. A possible solution to overcome that issue is with remeshing techniques (Ingraffea and Saouma, 1985; Camacho and Ortiz, 1996). Another way to overcome this issue is with the Partition of Unity Methods (PUMs) introduced by Babuška and Melenk (1997) and described later in Section 2.4.3.

A third and natural way to overcome the sensitivity of the mesh is with particle methods. Cohesive theories with particle methods has been studies by Nguyen et al. (2015) with Smooth Particle Hydrodynamics, Klein et al. (2001) with Reproducing Kernel Particle Method and Soparat and Nanakorn (2008) with the Element-Free Galerkin Method. A description of the aforementioned particle method with their governing equations are presented later in Chapter 3. Cohesive fracture with MPM has also been studied and can be found in Schreyer et al. (2002) and Daphalapurkar et al. (2007).

The ability of cohesive theories to model the nonlinear separation phenomena in materials, attract many researchers to combine them with other numerical methods apart from CZM. For instance, a phase field model for cohesive fracture has been proposed by Verhoosel and Borst (2013) where the critical fracture energy is a function of the crack opening.

2.4.3 Partition of Unity Methods (PUMs)

In PUMs, a crack is treated as a strong discontinuity in the displacement field Babuška and Melenk (1997). This is implemented though local enrichment techniques in the displacement field. In particular, the enhanced displacement field can be interpolated, at point $\mathbf{x}$, as

$$\mathbf{u}\left(\mathbf{x}\right) = \sum_{\forall I} N_I\left(\mathbf{x}\right)\mathbf{u}_I \sum_{\forall I} \hat{N}_I\left(\mathbf{x}\right)\left(\mathbf{x}\right)\hat{\mathbf{u}}_I \tag{2.29}$$

where $N_I(\mathbf{x})$ are the interpolation functions, $\mathbf{u}_I$ is the standard displacement field (uncracked), $\hat{N}_I$ are the enriched basis functions and $\hat{\mathbf{u}}_I$ the additional degrees-of freedom due to the internal discontinuity.

In the past, various PU methods have been introduced in conjunction with mesh-based and meshfree methods. The most popular mesh-based PU method is the eXtended Finite Element Method (XFEM) introduced by Moës et al. (1999) and it is analysed in Section 2.4.3.1. Another novel PU enrichment was introduced by Simpson and Travelyan (2011) utilizing the Boundary Element Method to study problems in fracture mechanics.

PU meshless methods were introduced by Ventura et al. (2002) where the Element Free Galerkin Method is enriched in the framework of the XFEM. Furthermore, Amiri et al. (2014b) introduced an enriched meshless method based on LME approximation scheme for fracture. Very recently, Liang et al. (2017) proposed a MPM with enriched shape function for crack propagation problems.

2.4.3.1 eXtended Finite Element Method (XFEM)

The most popular PU method in fracture modelling is the eXtended Finite Element Method (XFEM) introduced by Moës et al. (1999). XFEM is an enrichment of the standard FEM with the PU to handle cracks as discontinuities in the displacement field and the evolution of the crack path can be treated without remeshing. This can be implemented by enriching a subset of nodes around the crack paths. In LEFM problems, there two types of enrichments to represent the discontinuities, namely the jump and tip enrichment. The enriched elements along an arbitrary crack path are also shown in Fig. 2.6.

The jump enrichment functions are practically modified Heaviside step functions which allows to represent the displacement jump along the crack path

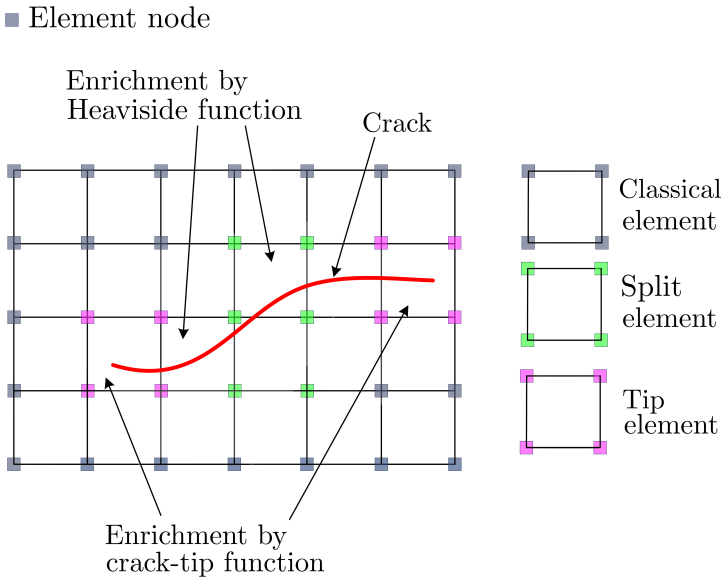

Figure 2.6: eXtended Finite Element Method.

and are defined as

$$H_{Jump} = \begin{cases} 1 & \text{above the crack} \\ -1 & \text{below the crack.} \end{cases} \tag{2.30}$$

The previous definition of the jump functions was introduced by Moës et al. (1999) and its objective is to locally enrich the support nodes along the crack to split the Finite Element in two parts. Other types of jump enrichment were introduced by Hansbo and Hansbo (2004) and higher order enrichment functions by Cheng and Fries (2012). Apart from these, appropriate discontinuous functions were also introduced by Daux et al. (2000) to deal with arbitrary branched and intersecting cracks.

The second type of enrichment, i.e. the tip enrichment consists of asymptotic functions which allows to represent the discontinuity at the two crack tips (see also Fig. 2.6). In Belytschko and Black (1999), the tip enrichment is defined as

$$F_j\left(r,\theta\right) = \left\{ \sqrt{r}\sin\left(\frac{\theta}{2}\right), \sqrt{r}\cos\left(\frac{\theta}{2}\right), \sqrt{r}\sin\left(\frac{\theta}{2}\right)\sin(\theta), \sqrt{r}\cos\left(\frac{\theta}{2}\right)\sin(\theta) \right\} \tag{2.31}$$

where r, θ are polar coordinates with reference point at the crack tip.

In XFEM, some of the nodes are locally enriched with the previous type of enrichment and some others are either not or partially enriched. In the last case, there is blending in the Finite Element and its shape functions do not form a partition of unity leading to numerical errors. These blending errors result in some loss of accuracy. Blending errors have been extensively examined by the research community and they can be minimized by e.g. enhanced strain formulations (Chessa et al., 2003) and the use of weight functions (Agathos et al., 2016) that provide a smooth blending within the split elements.

There is also problem pertinent to linear dependence between the enriched and non-enriched part of the approximation. In jump enrichment, that issue can be met for example when a crack merges or lies close to a node. In that case, the enriched and standard shape functions are almost identical leading to linear dependence problems. A solution to treat that issue is not to enrich nodes close to crack paths (Daux et al., 2000).

In XFEM, the displacement field approximation can be obtained, using the enrichment functions, as

$$\mathbf{u}\left(\mathbf{x}\right) = \sum_{I \in \mathcal{N}} N_I\left(\mathbf{x}\right) \mathbf{u}_I + \sum_{J \in \mathcal{N}^j} N_J\left(\mathbf{x}\right) H_{Jump}\left(\mathbf{x}\right) \hat{\mathbf{u}}_J + \sum_{T \in \mathcal{N}^t} \sum_{j} N_T\left(\mathbf{x}\right) F_j\left(\mathbf{x}\right) \tilde{\mathbf{u}}_{Tj} \tag{2.32}$$

where $\hat{\mathbf{u}}_J$, $\tilde{\mathbf{u}}_{Tj}$ are additional degrees of freedom due to the jump and tip enrichment, respectively. The $\mathcal{N}$ is the set of all Finite Element nodes while $\mathcal{N}^j$ and $\mathcal{N}^t$ are the set of jump and tip enrichment nodes (see also Fig. 2.6). Equation (2.32) introduced by (Moës et al., 1999) and it is considered as the standard XFEM without any blending or conditioning issues.

In XFEM, the cracks can be explicitly represented as a series of linear segments or triangles in two and three dimensional problems, respectively Duarte et al. (2001). An implicit approach to represent the crack surfaces is with the so called

level set method Stolarska et al. (2001). In this method, the crack surfaces are represented by using two level set functions, i.e. the normal and the tangent level set. The normal level set is defined as the signed distance from the crack surface while the tangent as the signed distance from a surface that is normal to the crack surface and intersects the crack surface at the crack tip/front. Then, the crack surface can be defined as the set of points for which the normal level set is equal to zero and the tangent level set assumes negative values.

To this point, it should be highlighted that the crack representation with level sets has not only been applied to mesh-based method but it is also a powerful technique to describe multiple crack surfaces in meshless methods. For example, an Element Free Galerkin method has been introduced by Zhuang et al. (2011) and Zhuang et al. (2012) in 2D and 3D problems, respectively where the crack surfaces are described and modelled using the level sets.

The XFEM has been studied extensively by the research community the last two decades and it has been successfully extended into three-dimensional problems (Duarte et al., 2001), multiple crack paths (Budyn et al., 2004) and dynamic crack propagation problems (Belytschko et al., 2003). However, more complicated phenomena, such as nucleation, branching and merging of cracks requires appropriate criteria to predict them (Daux et al., 2000), which might not always be available. Further details and an overview of the XFEM can be found in Fries and Belytschko (2010).

2.4.3.2 Cohesive Segments Method (CSM)

Another popular PUM and a reasonable extension of CZM is the CSM introduced by Remmers et al. (2003), using the XFEM approach solution procedure. As mentioned in Section 2.4.2, CZM uses cohesive interface elements aligned

with the Finite Element mesh, leading to mesh dependences when crack propagates. CSM overcomes this limitation by introducing arbitrary cohesive segments into the Finite Elements that act as discontinuities in the displacement field with the PUM.

The cracks are modelled as a set of overlapping cohesive segments where their support nodes are enriched with jump and tip enrichment functions similar to XFEM (see Section 2.4.3.1). A combination of overlapping crack cohesive segments results in a continuous crack as presented in Fig. 2.7.

Remmers et al. (2003) originally applied the CSM in quasi-static brittle fracture problems mainly focused on mode I separation problems. Later, Remmers et al. (2008) extended the CSM in simulating dynamic crack propagation problems where they demonstrated that the method can efficiently deal with multiple and branched cracks.

Following the concept of CSM, various PUM with cohesive theories have been successfully introduced with meshless methods. For instance, Barbieri and Meo (2011) introduced a meshless CSM for crack initiation and propagation in composites, utilizing the Reproducing Kernel Particle Method. Similarly, a meshfree method based on the local partition of unity for cohesive cracks was proposed by Rabczuk and Zi (2007), using the Element Free Galerkin Method.

2.5 Variational approaches (VAs)

VAs to fracture have been introduced to bridge the gap between the CDMs and DFMs where the fracture surfaces are described by an internal variable of the total stored energy functional (Bulinga, 1998; Bourdin et al., 2008). That internal variable can be obtained by minimizing of the stored energy where irreversibility constraints of the crack path and energy conservation hold.

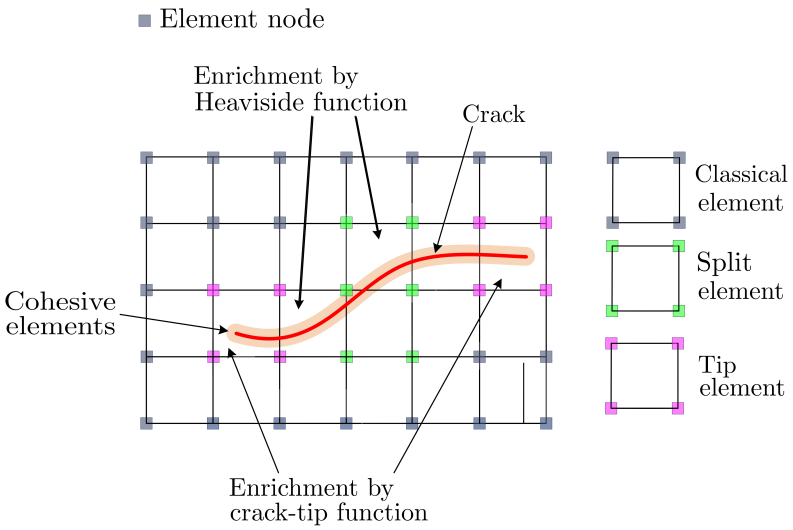

Figure 2.7: Cohesive Segments Method.

The numerical implementation of the variational approach to fracture requires the introduction of a length scale parameter to regularize the crack paths. The length scale parameter controls the diffusion of damage around the crack in a similar way as in non-local gradient-enhanced models, analysed in Section 2.3.3. However, as it has already mentioned in Section 2.3.3, the regularized crack paths converges to discrete cracks when the length scale parameter tends to zero.

The two most notable variational approaches to fracture are the Thick Level Set (TLS) (Moës et al., 2011) and Phase Field (PF) (Bourdin et al., 2008) models. A brief introduction to TLS is described in Section 2.5.1 and a detailed overview of PF models, that are proposed in this work, is presented in Section 2.6. A comparison of these two models for brittle fracture can be found in Cazes and Moës (2015).

2.5.1 Thick Level Set (TLS)

The TLS method was originally introduced by Moës et al. (2011) as a new method to model crack growth in solids by using level sets (Allaire et al., 2007)

to distinguish between the fully damaged and undamaged zones. This is implemented by utilizing a damage variable d_c in the computational domain that is explicitly dependent of the level set, i.e. $d_c(\phi_c)$. The level set ϕ_c is considered as a continuous auxiliary field in the domain of interest that tracks the crack growth.

In this, the crack front is considered as the zero level set (also called iso-zero) and its value away from the crack front are defined as the minimum distance between any point $\mathbf{x}$ and the zero level set. Mathematically this can be expressed as (Meer and Sluys, 2015)

$$\begin{cases} |\nabla \phi_c| = 1 & \text{on } \Omega \\ \phi_c = 0 & \text{on } \Gamma \end{cases} \tag{2.33}$$

where Γ is the crack front and Ω is the domain on which ϕ_c is defined (see also Fig. 2.8).

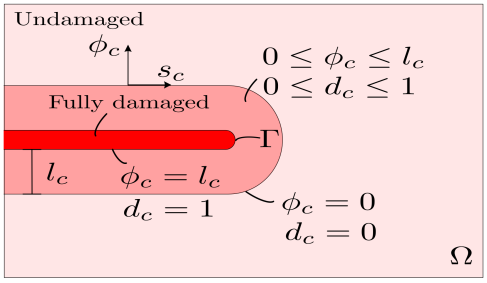

Figure 2.8: Thick Level Set method.

In TLS, the damage variable d_c is assumed to smoothly varies from one inside the crack to zero outside the crack as ϕ_c goes from l_c to 0, respectively. The diffusion of damage around the crack is controlled by the distance l_c. Hence,

the damage variable is evaluated as

$$d_c\left(\phi_c\right) = \begin{cases} 0 & \phi_c \leq 0 \\ f_c\left(\phi_c\right) & 0 \leq \phi_c \leq l_c \\ 1 & \phi_c > l_c \end{cases} \tag{2.34}$$

where $f_c(\phi_c)$ is a function that satisfies

$$f_c\left(0\right) = 0, \quad f_c\left(l_c\right) = 1, \quad f_c^{'} \geq 0 \in [0, l_c] \tag{2.35}$$

and it is considered as a material property. Bernard et al. (2012) suggested the following formulation for that function as

$$f_c\left(\phi_c\right) = \alpha_2 \arctan\left[\alpha_1 \left(\frac{\phi_c}{l_c} - \alpha_3\right)\right] \tag{2.36}$$

where

$$\begin{cases} \alpha_1 = 10 \\ \alpha_2 = \left[\arctan\left(\alpha_1(1-\alpha_3)\right) - \arctan\left(-\alpha_1\alpha_3\right)\right]^{-1} \\ \alpha_3 = 0.5 \\ \alpha_4 = -\alpha_2 \arctan(-\alpha_1\alpha_3). \end{cases} \tag{2.37}$$

Assuming $\psi_s\left(\boldsymbol{\varepsilon}, d_c\right)$ be the stored energy density of a solid body Ω, then the constitutive law and the configuration force, i.e. the the local driving forces for damage growth are defined as

$$\begin{cases} \boldsymbol{\sigma} = \dfrac{\partial \psi_s\left(\boldsymbol{\varepsilon}, d_c\right)}{\partial \boldsymbol{\varepsilon}}, & \text{Stress field} \quad (2.38a) \\ Y = \dfrac{\partial \psi_s\left(\boldsymbol{\varepsilon}, d_c\right)}{\partial d}, & \text{Configuration force .} \quad (2.38b) \end{cases}$$

Furthermore, the following local Kuhn-Tucker conditions are considered for damage growth

$$Y \leq Y_c, \quad \dot{d}_c \geq 0, \quad \left(Y - Y_c\right)\dot{d}_c = 0 \tag{2.39}$$

where Y_c is a threshold value that defines the critical local energy release and $\dot{d}_c$ is the time derivative of damage variable. the dissipated energy as the crack front moves of a distance $\delta\phi$ at a location s_c along the crack front can be expressed as

$$g_c\left(s_c\right) = \int_0^l d_c^{'}\left(\phi_c\right) Y\left(\phi_c, s_c\right)\left(1 - \frac{\phi_c}{\zeta_c(s_c)}\right) d\phi_c \tag{2.40}$$

where $d_c^{'}$ is the spatial derivatives of damage variable as $d_c^{'} = \partial d_c/\partial\phi_c$, ζ_c is the curvature of the zero level set and l is the size of damage zone $l \in [0, l_c]$. Further details about the theoretical and numerical aspects of TLS can be found in Moës et al. (2011) Bernard et al. (2012) and Meer and Sluys (2015).

The TLS has been successfully applied in quasi-static problems in Moës et al. (2011) and Bernard et al. (2012) where in the latter work a dissymetric behaviour was introduced to prevent unrealistic fracture in compressive areas. Furthermore, an extension of TLS in a dynamical context was proposed by Moreau et al. (2015) where the ability of the method to treat branched cracks is demonstrated. Finally, a 3D quasi-static crack implementation of TLS in quasi-brittle material can be found in Salzman et al. (2016)

2.6 Phase field damage models

2.6.1 Brittle fracture

The purpose of this work is to introduce a phase field approximation for brittle fracture within MPM. Thus, derivations presented herein pertain to Griffith's theory for brittle fracture (Griffith, 1921), although generalization to the case of ductile fracture can be also considered (see, e.g., Borden et al. (2016), Ambati et al. (2015b), and Miehe et al. (2016)). The phase field damage models utilize the MERR criterion to predict crack initiation and propagation in a solid (see Section 2.2.3).

An arbitrary deformable medium is shown in Fig. 2.9. The initial configuration ${}^{(0)}\mathcal{O} \subset R^d$ of the body at time $t = 0$ has a volume ${}^{(0)}\Omega$. The superscript d corresponds to the dimensionality of the problem, i.e., $d \in 1, 2, 3$. The boundary of the initial configuration is denoted as ${}^{(0)}\partial\Omega$. The medium is subjected to body forces $\mathbf{b} = \{b_1, b_2, b_3\}$ and tractions/ pressures $\bar{\mathbf{t}}$ applied on $\partial\Omega_{\bar{\mathbf{t}}} \subset \partial\Omega$. Furthermore, ${}^{(0)}\Gamma$ corresponds to an initial crack within the medium at time $t = 0$.

Under the action of the applied loads, the body undergoes a motion, that maps the initial configuration to the current configuration ${}^{(t)}\mathcal{O} \subset R^d$ at $t > 0$ with a volume ${}^{(t)}\Omega$. Furthermore, the initial crack ${}^{(0)}\Gamma$ evolves to the crack path ${}^{(t)}\Gamma$ at time t, where it must be that ${}^{(0)}\Gamma \subseteq {}^{(t)}\Gamma$.

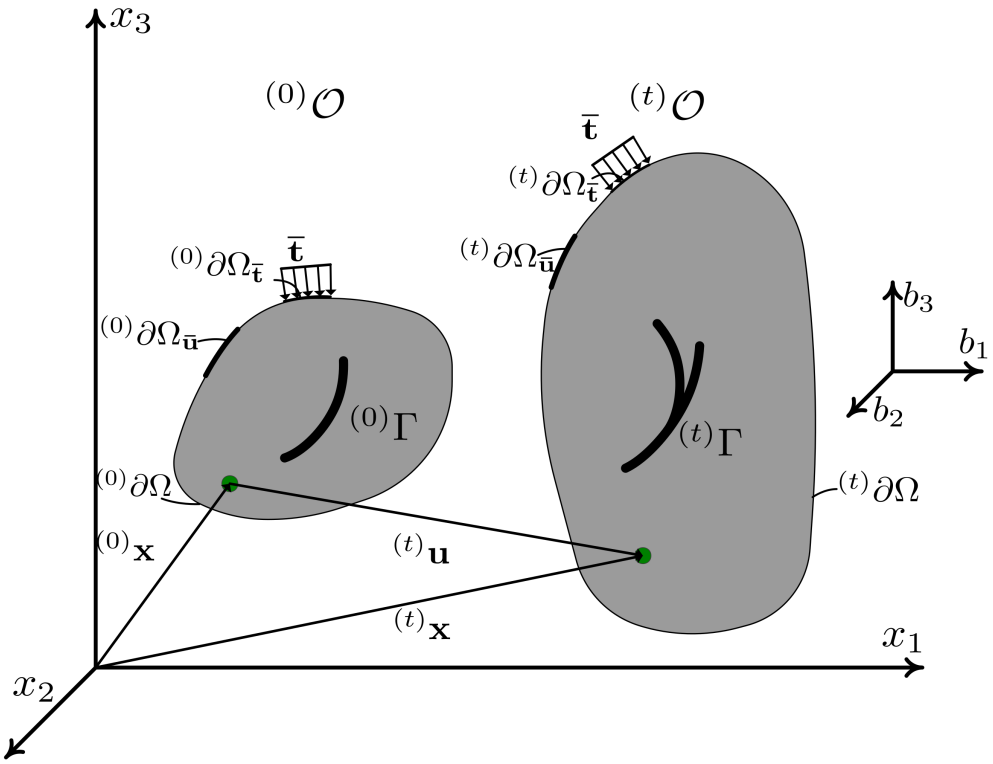

Figure 2.9: Deformation process: Solid body Ω with a crack path Γ.

According to Griffith's theory, the total stored energy Ψ_s of an elastic deformable body with an evolving crack along the path Γ is defined as [1]

$$\Psi_s = \Psi_{el} + \Psi_f = \int_{\Omega} \psi_{el}\left(\boldsymbol{\varepsilon}\right) d\Omega + \int_{\Gamma} \mathcal{G}_c d\Gamma \tag{2.41}$$

where Ψ_{el} is the elastic strain energy, Ψ_f is the fracture energy, $\psi_{el}\left(\boldsymbol{\varepsilon}\right)$ is the elastic energy density whereas $\boldsymbol{\varepsilon}$ is the symmetric strain tensor which under the small strain assumption is defined as

$$\boldsymbol{\varepsilon} = \frac{1}{2}\Big(\nabla \mathbf{u} + \nabla \mathbf{u}^T\Big) \tag{2.42}$$

where the (∇) is the gradient operator. The term $\mathcal{G}_c$ is the critical fracture energy density. The critical fracture energy density is a material parameter corresponding to the energy required to create a unit area of fracture surface (Sun and Jin, 2012).

The elastic energy density can be established in the following convenient form where the total stored energy is additively decomposed in parts of purely tensile and purely compressive origin, i.e.,

$$\psi_{el} = \psi_{el}^{+} + \psi_{el}^{-} \tag{2.43}$$

where ψ_{el}^{+} is the elastic energy density due to tension and ψ_{el}^{-} is the elastic energy density due to compression, respectively. There are various methodologies to address this energy split in the literature that are described later in Section 2.6.3.

Substituting equation (2.43) in relation (2.41), the expression for the brittle fracture stored energy assumes the following form

$$\Psi_s = \int_{\Omega} \psi_{el}^{+} d\Omega + \int_{\Omega} \psi_{el}^{-} d\Omega + \int_{\Gamma} \mathcal{G}_c d\Gamma. \tag{2.44}$$

[1] The subscript of time (t) is omitted from all variables for brevity.

Equation (2.44) effectively decomposes the total potential energy into purely tensile, compressive and fracture energy parts, thus constituting an efficient platform for the phase field derivations described in Section 2.6.2.

2.6.2 Phase field fracture

As evaluation of the fracture crack energy in equation (2.41) requires prior knowledge of the crack path Γ, computational fracture mechanics revert to crack tracking algorithms in order to identify the crack path during the solution procedure (Trädegard et al., 1998). To avoid such procedures, the phase field method approximates the path integral of the fracture energy with a volume integral defined over the entire domain of the deformable medium according to the following expression (Bourdin et al., 2008)

$$\int_{\Gamma} \mathcal{G}_c d\Gamma \approx \int_{\Omega} \mathcal{G}_c \mathcal{Z}_c d\Omega \tag{2.45}$$

where $\mathcal{Z}_c$ is a crack density functional. Several expressions are provided in the literature for the definition of $\mathcal{Z}_c$ involving the case of second-order (Bourdin et al., 2008; Miehe et al., 2010a) and fourth-order functionals. The latter have been found to allow for increased regularity in the exact solution of the phase field equation and hence, improves the convergence rates of the effective critical energy release rate and the strain energy (Borden et al., 2014).

In this Chapter, the isotropic second order definition for crack density functional $\mathcal{Z}_c$ of Eq. (2.46) (Bourdin et al., 2008) is adopted to facilitate verification of the proposed method as presented in Chapter 4. However, utilization of higher-order functionals is also demonstrated in Chapters 5 and 6.

$$\mathcal{Z}_c = \left[\frac{(c-1)^2}{4l_0} + l_0 |\nabla c|^2 \right]. \tag{2.46}$$

In equation (2.46), $c(\mathbf{x}, t) \in [0, 1]$ is a phase field defined over the domain Ω (see Fig. 2.10). By considering minimization of the functional with respect to c it can be shown that a value of $c = 1$ corresponds to uncracked regions of the domain Ω, i.e., regions away from the crack Γ. Similarly, values of $c = 0$ are retrieved on regions coinciding with the crack surface Γ. Involving the gradients of the phase field on the functional definition (2.46) introduces a smooth variation of the phase field from 0 to 1.

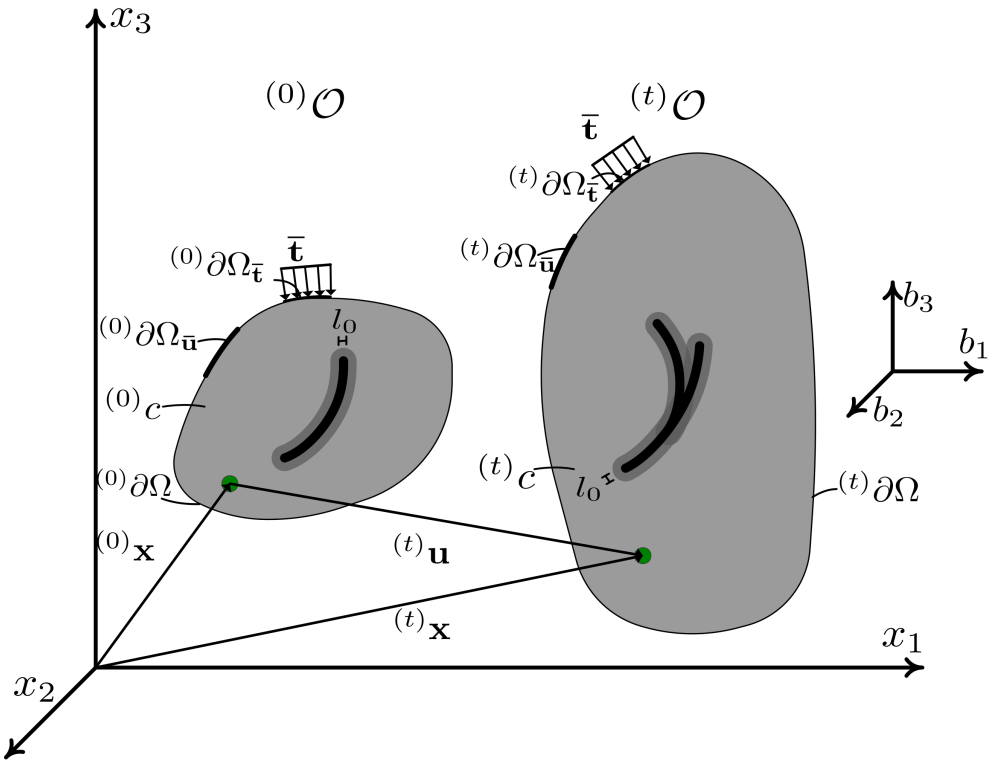

Figure 2.10: Deformation process: Phase field approximation of the crack path Γ.

The width of the region over which this smooth transition takes place is controlled by the length scale parameter $l_0 \in \mathbb{R}^+$ (see Fig. 2.10). The length scale parameter l_0 can be considered to correspond to a domain of degrading material parameters in the vicinity of the crack surface. From a purely mathematical standpoint, l_0 is a regularization parameter with values of $l_0 \to 0$ allowing for the phase field theory to practically converge to Griffith's theory. In practice, convergence is achieved by using a finite value for l_0. In view of relation (2.45),

the stored energy introduced in equation (2.41) assumes the following form

$$\Psi_s = \int_{\Omega} \psi_{el}^{+} d\Omega + \int_{\Omega} \psi_{el}^{-} d\Omega + \int_{\Omega} \mathcal{G}_c \mathcal{Z}_c d\Omega. \tag{2.47}$$

Having established through relation (2.45) that as a crack propagates within the domain Ω the value of the crack surface energy integral will be increasing, the corresponding decrease in the elastic energy due to the degradation of the material properties needs also to be considered in the vicinity of the crack Γ. This is achieved by introducing a degradation function $g(c)$ that is superimposed on the positive part of the elastic strain energy density. The degradation function should be continuously differentiable and monotonically decreasing with properties $g(0) = 0$, $g(1) = 1$ and $g'(0) = 0$ (Kuhn et al., 2015).

To facilitate verification of the proposed procedure, the degradation function introduced in Miehe et al. (2010a) is utilized herein, i.e.,

$$g = (1 - k_f)c^2 + k_f \tag{2.48}$$

where $0 \leq k_f \ll 1$ is a model parameter introduced in Ambrosio and Tortorelli (1990) to avoid ill-posedness. According to the arguments provided in Braides (1998) as well as the numerical investigations presented in Borden et al. (2012) this parameter can be considered redundant. Results derived from our set of numerical experiments also seem to agree with the aforementioned. Therefore in this work also $k_f = 0$. In view of the aforementioned, the expression for the stored energy finally assumes the following form

$$\Psi_s = \int_{\Omega} g\psi_{el}^{+} d\Omega + \int_{\Omega} \psi_{el}^{-} d\Omega + \int_{\Omega} \mathcal{G}_c Z_c d\Omega. \tag{2.49}$$

The elastic stress field on the medium is readily derived from the elastic strain energy density (Bathe, 2007) through the following relation

$$\boldsymbol{\sigma} = g\frac{\partial \psi_{el}^{+}}{\partial \boldsymbol{\varepsilon}} + \frac{\partial \psi_{el}^{-}}{\partial \boldsymbol{\varepsilon}} = g\boldsymbol{\sigma}^{+} + \boldsymbol{\sigma}^{-} \tag{2.50}$$

where $\boldsymbol{\sigma}^{+}$ and $\boldsymbol{\sigma}^{-}$ are the stress fields due to tension and compression, respectively. Finally, the damage elastic tangent constitutive matrix can be analytically derived as

$$\mathbf{D} = \frac{\partial \boldsymbol{\sigma}}{\partial \boldsymbol{\varepsilon}}. \tag{2.51}$$

2.6.2.1 Derivation of the coupled strong form

The coupled strong form of the brittle-fracture phase field formulation is established herein by employing the methodology introduced in Borden et al. (2014). The energy balance equation of the problem is defined in Eq. (2.52) as

$$\dot{\mathcal{K}}\left(\dot{\mathbf{u}}\right) + \dot{\mathcal{W}}^{int}\left(\dot{\mathbf{u}}, \dot{c}\right) - \dot{\mathcal{W}}^{ext}\left(\dot{\mathbf{u}}\right) = 0 \tag{2.52}$$

where $\dot{c} = dc/dt$ is the phase field time derivative and $\nabla\dot{c}$ corresponds to the rate of the phase field spatial derivative, i.e.,

$$\nabla\dot{c} = \frac{d}{dt}\left(\frac{\partial c}{\partial x_i}\right) \tag{2.53}$$

for $i = 1, ..., d$. The kinetic energy rate functional $\dot{\mathcal{K}}\left(\dot{\mathbf{u}}\right)$ is evaluated as

$$\dot{\mathcal{K}}\left(\dot{\mathbf{u}}\right) = \frac{d}{dt}\int_{\Omega}\frac{1}{2}\rho|\dot{\mathbf{u}}|^{2}d\Omega \tag{2.54}$$

and $\dot{\mathcal{W}}^{ext}\left(\dot{\mathbf{u}}\right)$ is the rate of external work functional expressed as

$$\dot{\mathcal{W}}^{ext}\left(\dot{\mathbf{u}}\right) = \int_{\partial\Omega_{\bar{\mathbf{t}}}}\left(\bar{\mathbf{t}}\cdot\dot{\mathbf{u}}\right)d\partial\Omega_{\bar{t}} + \int_{\Omega}\left(\mathbf{b}\cdot\dot{\mathbf{u}}\right)d\Omega. \tag{2.55}$$

Finally, the rate of internal work functional $\dot{\mathcal{W}}^{int}\left(\dot{\mathbf{u}}, \dot{c}\right)$ is evaluated as

$$\dot{\mathcal{W}}^{int}\left(\dot{\mathbf{u}}, \dot{c}\right) = \frac{d\Psi_s}{dt} = \frac{d}{dt}\int_{\Omega}\left(\psi_{el} + \mathcal{G}_c\mathcal{Z}_c\right)d\Omega. \tag{2.56}$$

Applying the divergence theorem and performing the necessary algebraic manipulation, the balance of energy equation (2.52) becomes

$$\begin{aligned}&\int_{\partial\Omega_{\bar{\mathbf{t}}}}\left(\left[\boldsymbol{\sigma}\mathbf{n} - \bar{\mathbf{t}}\right]\cdot\dot{\mathbf{u}}\right)\,d\partial\Omega + \int_{\Omega}\left(\left[\rho\ddot{\mathbf{u}} - \nabla\cdot\boldsymbol{\sigma} - \mathbf{b}\right]\cdot\dot{\mathbf{u}}\right)\,d\Omega + \\ &\int_{\partial\Omega}\left(\left[\mathcal{G}_c l_0 2\nabla c\right]\cdot\mathbf{n}\dot{c}\right)\,d\partial\Omega + \int_{\Omega}\left[\psi_{el_c} + \frac{\mathcal{G}_c\left(c-1\right)}{2l_0} - \mathcal{G}_c l_0 2\Delta c\right]\dot{c}\,d\Omega = 0\end{aligned} \tag{2.57}$$

where $\mathbf{n}$ is the outward unit normal vector of the boundary and $\psi_{el_c} = \partial\psi_{el}/\partial c = 2\left(1-k_f\right)c\psi_{el}^{+}$ is the derivative of elastic strain energy density with respect to the phase field c.

Since Eq. (2.57) must hold for arbitrary values of $\dot{\mathbf{u}}$ and $\dot{c}$, the resulting strong form is eventually derived as

$$\begin{cases}\nabla\cdot\boldsymbol{\sigma} + \mathbf{b} = \rho\ddot{\mathbf{u}}, & \text{on } \left[{}^{(0)}\Omega, {}^{(t)}\Omega\right] \\ \left(\frac{4l_0\left(1-k_f\right)\mathcal{H}}{\mathcal{G}_c} + 1\right)c - 4l_0^2\Delta c = 1, & \text{on } \left[{}^{(0)}\Omega, {}^{(t)}\Omega\right]\end{cases} \tag{2.58}$$

where $\mathcal{H}$ is the history field defined as the maximum ψ_{el}^{+} obtained in time space $[0, t]$. The history field $\mathcal{H}$ (see, e.g., Miehe et al. (2010a)) essentially enforces the necessary irreversibility condition pertinent to the crack propagation problem, i.e., ${}^{(t)}\Gamma \subseteq {}^{(t+\Delta t)}\Gamma$ and satisfies the following Kuhn-Tucker conditions for elastic loading and unloading, i.e.,

$$\psi_{el}^{+} - \mathcal{H} \leq 0 \quad \dot{\mathcal{H}} \geq 0 \quad \dot{\mathcal{H}}\left(\psi_{el}^{+} - \mathcal{H}\right) = 0. \tag{2.59}$$

The coupled field equations (2.58) are subject to the following set of boundary and initial conditions

$$\begin{cases} \boldsymbol{\sigma}\mathbf{n} = \bar{\mathbf{t}}, & \text{on } [{}^{(0)}\partial\Omega_{\bar{\mathbf{t}}}, {}^{(t)}\partial\Omega_{\bar{\mathbf{t}}}] \\ \mathbf{u} = \bar{\mathbf{u}}, & \text{on } [{}^{(0)}\partial\Omega_{\bar{\mathbf{u}}}, {}^{(t)}\partial\Omega_{\bar{\mathbf{u}}}] \\ \mathbf{u} = {}^{(0)}\mathbf{u}, & \text{on } {}^{(0)}\Omega \\ \dot{\mathbf{u}} = {}^{(0)}\dot{\mathbf{u}}, & \text{on } {}^{(0)}\Omega \\ \ddot{\mathbf{u}} = {}^{(0)}\ddot{\mathbf{u}}, & \text{on } {}^{(0)}\Omega \\ \nabla c \cdot \mathbf{n} = 0, & \text{on } [{}^{(0)}\partial\Omega, {}^{(t)}\partial\Omega] \\ c = {}^{(0)}c, & \text{on } {}^{(0)}\Omega \end{cases} \tag{2.60}$$

where $\bar{\mathbf{u}}$ is the prescribed displacement field on $\partial\Omega_{\bar{\mathbf{u}}}$ boundary, $\dot{\mathbf{u}}$ is the velocity field, $\ddot{\mathbf{u}}$ is the acceleration field and ρ is the mass density. Furthermore, ${}^{(0)}\mathbf{u}$, ${}^{(0)}\dot{\mathbf{u}}$, ${}^{(0)}\ddot{\mathbf{u}}$ and ${}^{(0)}c$ are the initial conditions for the displacement, velocity, acceleration and phase field, respectively.

2.6.3 Elastic energy density decomposition

The decomposition of the elastic strain energy density into a positive (due to tension) ψ_{el}^{+} and negative (due to compression) ψ_{el}^{-} (see Eq. (2.43)) is an integral aspect of phase field methodology employed to essentially couple the evolution of phase field c to the evolution of tensile stresses within the domain Ω. During the past few years, various methodologies have been introduced to address this energy split; a detailed review of the existing models can be retrieved in Ambati et al. (2015a).

The three most widely used elastic energy decompositions are:

- Isotropic (no strain decomposition)
- Anisotropic volumetric/ deviatoric split (Amor et al. (2009))

- Split based on a spectral decomposition of the elastic strain (Miehe et al. (2010b))

In the next Sections 2.6.3.1, 2.6.3.2 and 2.6.3.3 the aforementioned decompositions are described and discussed.

2.6.3.1 Isotropic (no strain decomposition)

The isotropic case, does not lead to a decomposition of the elastic energy density however it is described within this context to help clarify further developments. For an linear elastic isotropic medium, the elastic energy density is readily expressed as a function of the strain field $\boldsymbol{\varepsilon}$ according to equation (2.61) below

$$\psi_{el}{}^{iso} = \frac{1}{2}\lambda \left(\mathrm{Tr}\left[\boldsymbol{\varepsilon}\right]\right)^2 + \mu \mathrm{Tr}\left[\boldsymbol{\varepsilon}^2\right] \tag{2.61}$$

where λ and μ are the Lamé constants and the symbol Tr denotes the trace of $\boldsymbol{\varepsilon}$.

The isotropic model in Eq. (2.61) does not distinguish between fracture behaviour in tension and compression, i.e. in Eq. (2.43) the $\psi_{el}^{+} = \psi_{el}{}^{iso}$ and $\psi_{el}^{-} = 0$. Adopting isotropic model into phase field brittle fracture model leads to unrealistic crack patterns in compression (see e.g. Ambati et al. (2015a)). In order to prevent fracture under compression, two modified formulations of Eq. (2.61) were proposed from Amor et al. (2009) and Miehe et al. (2010b).

2.6.3.2 Anisotropic volumetric/ deviatoric split (Amor et al. (2009))

In Amor et al. (2009), the strain tensor $\boldsymbol{\varepsilon}$ is decomposed into a volumetric and a deviatoric part as

$$\boldsymbol{\varepsilon} = \boldsymbol{\varepsilon}^{vol} + \boldsymbol{\varepsilon}^{dev} \tag{2.62}$$

where the volumetric strain tensor is defined as

$$\boldsymbol{\varepsilon}^{vol} = \frac{1}{d}\,\mathrm{Tr}\left[\boldsymbol{\varepsilon}\right]\mathbf{I} \tag{2.63}$$

whereas the deviatoric as

$$\boldsymbol{\varepsilon}^{dev} = \boldsymbol{\varepsilon} - \frac{1}{d}\,\mathrm{Tr}\left[\boldsymbol{\varepsilon}\right]\mathbf{I} \tag{2.64}$$

In the above relations, the symbol Tr is the trace whereas $\mathbf{I}$ denotes the dxd identity matrix.

Similarly, the elastic energy density is decomposed into a volumetric and a deviatoric part as

$$\psi_{el} = \psi_{el}^{vol} + \psi_{el}^{dev}. \tag{2.65}$$

The volumetric part ψ_{el}^{vol} is computed as

$$\psi_{el}^{vol} = \frac{1}{2}K_d\,\mathrm{Tr}\left[\boldsymbol{\varepsilon}\right]^2 \tag{2.66}$$

where $K_d = \lambda + 2\mu/d$, while the deviatoric part from Eq. (2.67) below

$$\psi_{el}^{dev} = \mu\,\mathrm{Tr}\left[\left(\boldsymbol{\varepsilon}^{dev}\right)^2\right]. \tag{2.67}$$

In Eq. (2.66), the volumetric part ψ_{el}^{vol} can further be distinguished into (volumetric) expansive $\psi_{el}^{vol^+}$ and (volumetric) compressive $\psi_{el}^{vol^-}$ parts as

$$\psi_{el}^{vol^+} = \frac{1}{2}K_d\langle\mathrm{Tr}\left[\boldsymbol{\varepsilon}\right]\rangle^{+^2} \tag{2.68}$$

and

$$\psi_{el}^{vol^-} = \frac{1}{2}K_d\langle\mathrm{Tr}\left[\boldsymbol{\varepsilon}\right]\rangle^{-^2}, \tag{2.69}$$

respectively. The symbols $\langle.\rangle^+$ and $\langle.\rangle^-$ are defined as $\langle\mathcal{X}\rangle^+ = \left(\mathcal{X} + |\mathcal{X}|\right)/2$ and $\langle\mathcal{X}\rangle^- = \left(\mathcal{X} - |\mathcal{X}|\right)/2$, respectively.

Thus, the anisotropic Amor et al. (2009) decomposition, assumes that only the strain energy associated to (volumetric) expansion and shear contribute to the

positive part of strain energy, i.e.

$$\psi_{el}^{+} = \psi_{el}^{vol^{+}} + \psi_{el}^{dev}. \tag{2.70}$$

The (volumetric) compressive part of strain energy is assumed to contribute to the negative part of strain energy as

$$\psi_{el}^{-} = \psi_{el}^{vol^{-}}. \tag{2.71}$$

The stress field can be readily computed from Eq. (2.50) where $\boldsymbol{\sigma}^{+}$ is defined as

$$\boldsymbol{\sigma}^{+} = K_d \langle \mathrm{Tr}\left[\boldsymbol{\varepsilon}\right] \rangle^{+} + 2\mu \boldsymbol{\varepsilon}^{dev} \tag{2.72}$$

and $\boldsymbol{\sigma}^{-}$ as

$$\boldsymbol{\sigma}^{-} = K_d \langle \mathrm{Tr}\left[\boldsymbol{\varepsilon}\right] \rangle^{-}, \tag{2.73}$$

respectively.

2.6.3.3 Split based on a spectral decomposition of the elastic strain (Miehe et al. (2010b))

In Miehe et al. (2010b), a spectral decomposition is utilized for the strain tensor. Hence, the positive part (due to tension) of the strain tensor $\boldsymbol{\varepsilon}^{+}$ is defined through the following spectral decomposition

$$\boldsymbol{\varepsilon}^{+} = \mathbf{P} \boldsymbol{\Lambda}^{+} \mathbf{P}^{T} \tag{2.74}$$

where $\mathbf{P}$ is a matrix whose columns comprise the eigen vectors of the strain tensor $\boldsymbol{\varepsilon}$ and $\boldsymbol{\Lambda}^{+}$ is a diagonal matrix defined as

$$\boldsymbol{\Lambda}^{+} = \mathrm{diag}\left(\langle \lambda_1 \rangle^{+}, \langle \lambda_2 \rangle^{+}, \langle \lambda_3 \rangle^{+} \right) \tag{2.75}$$

where $\lambda_i, i = 1, \ldots, 3$ are the eigen values of the strain tensor. The negative part of the strain tensor in equation (2.78) is evaluated as

$$\boldsymbol{\varepsilon}^- = \boldsymbol{\varepsilon} - \boldsymbol{\varepsilon}^+. \tag{2.76}$$

Considering the previous spectral decomposition of the strain tensor, the elastic energy can be additively decomposed in parts of purely tensile and purely compressive origin, i.e.

$$\psi_{el}^+ = \frac{1}{2}\lambda\langle \mathrm{Tr}\,[\boldsymbol{\varepsilon}]\rangle^{+^2} + \mu\,\mathrm{Tr}\left[\left(\boldsymbol{\varepsilon}^+\right)^2\right] \tag{2.77}$$

and

$$\psi_{el}^- = \frac{1}{2}\lambda\langle \mathrm{Tr}\,[\boldsymbol{\varepsilon}]\rangle^{-^2} + \mu\,\mathrm{Tr}\left[\left(\boldsymbol{\varepsilon}^-\right)^2\right], \tag{2.78}$$

respectively.

Similarly, the positive and negative part of the stress field are defined as

$$\boldsymbol{\sigma}^+ = \lambda\langle \mathrm{Tr}\,[\boldsymbol{\varepsilon}]\rangle^+\mathbf{I} + 2\mu\boldsymbol{\varepsilon}^+ \tag{2.79}$$

and

$$\boldsymbol{\sigma}^- = \lambda\langle \mathrm{Tr}\,[\boldsymbol{\varepsilon}]\rangle^-\mathbf{I} + 2\mu\boldsymbol{\varepsilon}^-, \tag{2.80}$$

respectively

The objective of both anisotropic models, i.e. Amor et al. (2009) and Miehe et al. (2010b) is similar, that is to avoid fracture in compression and especially during crack closure. However, from Eq. (2.70) and the Amor et al. (2009) model, it is noticed that when all three principal strains are negative the $\psi_{el}^{vol^+} = 0$ but $\psi_{el}^{dev} \neq 0$. Hence, for that particular case the Amor et al. (2009) model will still cause unrealistic degradation of the material. In contrast, the Miehe et al. (2010b) decomposition model leads to a strongly non-linear stress-strain relation that is more computational taxing than the Amor et al. (2009) model.

In general, both anisotropic decomposition models produce similar numerical results (see e.g. Ambati et al. (2015a) for a detailed comparison of these two models). In this work, the model of Miehe et al. (2010b) is adopted to facilitate verification of the proposed method.

Chapter 3

Review of particle methods

3.1 Introduction

Treating crack propagation using a grid-based method introduces further challenges as robustness and accuracy directly depend on mesh quality and corresponding mesh distortion errors (Kaczmarczyk et al., 2014). Crack propagation problems involve moving material discontinuities and in some cases also involve large displacements and/or large deformations (see e.g. Raina and Miehe (2016) for crack propagation in soft biological tissues at finite deformations). Mesh distortion caused by large displacements/ deformations kinematics significantly reduces the validity of results, especially in the case of dynamic impact where the deformability of interfaces can significantly alter stress waves both in terms of amplitude as well as directionality.

Particle methods have gained popularity over the past few years. They were developed with the ultimate objective of minimizing the reliance on a mesh to accurately approximate the governing equations. Some major advantages of particle methods are:

- h-adaptivity can be easily incorporated by introducing additional cloud of particles in the areas of interest. In contrast, in mesh-based methods,

h-adaptivity and mesh refinement necessitate the reconstruction of the mesh, hence increasing online computational costs.

- Problems with large displacement and/or large deformations are treated in a more robust manner since a mesh is not required, hence mesh distortion is by definition avoided.

- Problems with moving material discontinuities e.g. crack propagation problems are handled with ease because there is no mesh alignment sensitivity.

Although particle methods overcome some critical numerical issues over the mesh-based methods, they have the following disadvantages:

- They utilize rational functions, i.e. polynomials, which require higher-order integration scheme to be accurately computed.

- They require neighbour searching at each time step

- A large number of particles is required so that the true macroscopic response depends on particle interaction.

- Taking the above three points into account, the particle methods are, in general, more time consuming than mesh-based methods.

- The imposition of essential boundary conditions is not straightforward as in mesh-based methods because their shape functions are approximants and not interpolants (they do not necessary satisfy the Kronecker delta property). The imposition of essential boundary conditions is not straightforward as in mesh-based methods because their shape functions are approximants and not interpolants (they do not necessary satisfy the Kronecker delta property). An approach to overcome that issue is with Local Maximum Entropy approximation (Arroyo and Ortiz, 2006) where

its shape functions have a weak Kronecker-delta property at the boundary. However, the computational cost in computing the Maximum Entropy shape functions is expensive as a result it has been coupled with other meshless methods, i.e. where imposition of boundary conditions is needed (Ullah et al., 2013).

3.2 Discontinuities

In fracture mechanics, cracks are represented as a discontinuity in the displacement field. In meshless methods, two methods exist for the mathematical description of discontinuities, namely the methods of extrinsic and intrinsic enrichment. In extrinsic approaches, the displacement field is enriched with additional terms as in the case of XFEM to account for discontinuity, i.e. crack. However, as it is also discussed in Chapter 2, this leads to additional unknowns in the final solution and hence to higher computational cost.

In contrast, intrinsic approaches do not require additional unknowns since the displacement field discontinuities are modeled by modifying the support domain of weight functions at particles on or close to the crack paths. There are generally two ways to implement that, namely the visibility (Belytschko et al., 1994) and the diffraction (Organ et al., 1996) schemes (see also Fig. 3.1). In the visibility scheme, the weight function support domain of a particle $\mathbf{x}_I$ is truncated by a line and hence discontinuities at the displacement field emerge. However, visibility approaches can lead to suspicious oscillations for the displacement field around the crack tip $\mathbf{x}_c$ since the shape functions are suddenly changed (Organ et al., 1996).

In comparison, the diffraction approach was introduced as an improvement to the visibility scheme where an additional small zone around the crack tip is

introduced to overcome the oscillations at the displacement field on it. However, the evaluation of the shape functions with the diffraction method is quite complex making it computationally expensive (Nguyen et al., 2008).

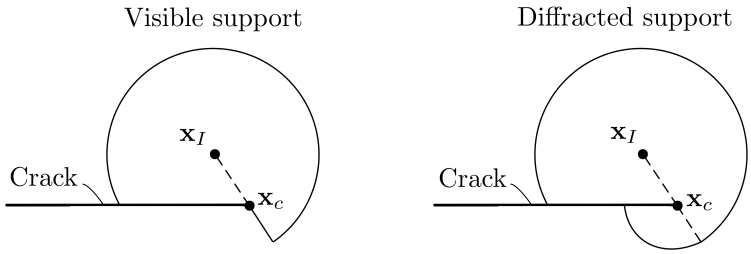

Figure 3.1: Visibility (left) and diffraction (right) schemes.

In the following Sections 3.3 to 3.8, the most commonly used particle methods are briefly described where their governing equations are presented to facilitate compassion with the MPM.

3.3 Smooth particle hydrodynamics (SPH)

The Smoothed Particle Hydrodynamics (SPH) is considered one of the oldest meshless methods. It was initially developed in 1977 by Lucy (1977) to study astrophysical problems. The SPH is being increasingly used on various applications with a lot of attention in fluid motion problems. In the SPH, the continuum is represented by a set of Lagrangian (see Section 3.9.2) particles which interact with each other within a range controlled by a smooth Kernel weight function (Liu, 2010).

In the SPH, the displacement field $\mathbf{u}_{\text{SPH}}(\mathbf{x})$ is approximated by

$$\mathbf{u}_{\text{SPH}}(\mathbf{x}) = \sum_{I \in \mathcal{S}} W(\mathbf{x} - \mathbf{x}_I)\, \mathbf{u}_I \Omega_I \tag{3.1}$$

where $W(\mathbf{x} - \mathbf{x}_I)$ is the smoothing kernel function, Ω_I is the volume of the domain surrounding the node I, and $\mathcal{S}$ is the set of nodes I for which $W(\mathbf{x} - \mathbf{x}_I) \neq$

0. The SPH approximation is also illustrated in Fig. 3.2 where $r_{IJ} = \|\mathbf{x}_I - \mathbf{x}_J\|/r_c$ is the distance of particle $\mathbf{x}_I$ to $\mathbf{x}_J$ and r_c is the smooth length scale parameter that controls the radius of the smoothing kernel (see Fig. Fig. 3.2).

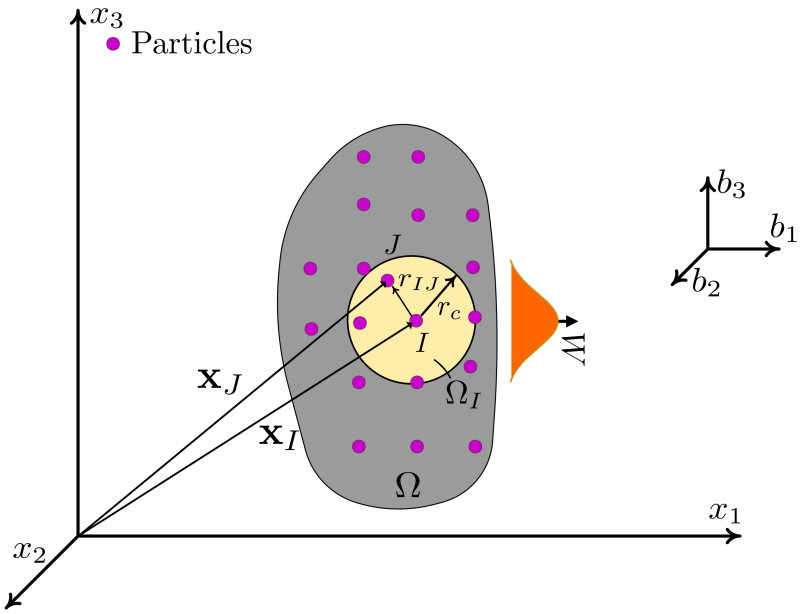

Figure 3.2: Smooth particle hydrodynamics approximation: Particle I interacts with J within cut-off region r_c.

A commonly used weight function, also called the Lucy kernel, is defined as

$$W(r_{IJ}, r_c) = W_{IJ} = a_{SPH} \begin{cases} (1+3r_{IJ})(1-r_{IJ})^3, & r_{IJ} \leq 1 \\ 0, & r_{IJ} > 1 \end{cases} \tag{3.2}$$

where $a_{SPH} = 5/\pi {r_c}^2$ for the two-dimensional problem.

The mass and momentum governing equations which are defined based on Eq. (3.3) below

$$\begin{cases} \frac{D\rho}{Dt} = -\rho \nabla \cdot \dot{\mathbf{u}}, & \text{mass conservation} \\ \frac{D\dot{\mathbf{u}}}{Dt} = \frac{1}{\rho} \nabla \cdot \boldsymbol{\sigma} + g, & \text{momentum conservation} \end{cases} \tag{3.3}$$

are discretized in the SPH as

$$\begin{cases} \frac{D\rho_I}{Dt} = \sum_{J\in\Omega_I} m_J \left(\dot{\mathbf{u}}_I - \dot{\mathbf{u}}_J\right) \nabla_I W_{IJ}, & \text{mass conservation} \\ \frac{D\dot{\mathbf{u}}_I}{Dt} = \sum_{J\in\Omega_I} m_J \left(\frac{\boldsymbol{\sigma}_I}{\rho_I^2} + \frac{\boldsymbol{\sigma}_J}{\rho_J^2} - \Pi_{IJ}\right) \nabla_I W_{IJ} + g, & \text{momentum conservation} \end{cases} \tag{3.4}$$

where $\dot{\mathbf{u}}$ is the velocity, $\boldsymbol{\sigma}$ is the stress tensor, g is the external body force per unit mass and D/Dt is material derivative following the motion. The mass density ρ is computed as

$$\rho_I = \sum_{J\in\Omega_I} M_J W_{IJ} \tag{3.5}$$

where M_J is the mass associated with node I. The term Π_{IJ} is applied in Eq. (3.4) to resolve the unphysical oscillation in the solution (Douillet-Grellier et al., 2016).

Further details can be found in an overview of the SPH in Liu (2010). With respect to fracture, the SPH has be studied by Douillet-Grellier et al. (2016) and Batra and Zhang (2007) amongst many. Douillet-Grellier et al. (2016) employed classical constitutive models with SPH simulations to examine mixed-mode fracture. Batra and Zhang (2007) utilized a modified smoothed particle hydrodynamics method to analyse elastodynamic crack problems where the discontinuity was treated by using the diffraction and visibility criteria.

3.4 Reproducing Kernel Particle Method (RKPM)

Reproducing Kernel Particle Method (RKPM) can be considered as an improvement/ correction of SPH though the enforcement of the reproducing conditions (Liu et al., 1995). In RKPM, the displacement field approximation is defined as

$$\mathbf{u}_{\text{RKPM}}(\mathbf{x}) = \sum_{I\in\mathcal{S}} \boldsymbol{\Phi}(\mathbf{x}, \mathbf{x}_I) W(\mathbf{x} - \mathbf{x}_I) \mathbf{u}_I \Omega_I \tag{3.6}$$

where $\mathbf{\Phi}(\mathbf{x}, \mathbf{x}_I) = \Phi_{IJ}$ is the correction function that enforces the reproducibility conditions and $\Phi_{IJ} W_{IJ}$ is the reproducing kernel shape function referenced to node I. The discretized equations, introduced in Eq. (3.4) are modified as

$$\begin{cases} \frac{D\rho_I}{Dt} = \sum_{J\in\Omega_I} m_J \left(\dot{\mathbf{u}}_I - \dot{\mathbf{u}}_J\right) \nabla_I \Phi_{IJ}, & \text{mass conservation} \\ \frac{D\dot{\mathbf{u}}_I}{Dt} = \sum_{J\in\Omega_I} m_J \left(\frac{\boldsymbol{\sigma}_I}{\rho_I^2} + \frac{\boldsymbol{\sigma}_J}{\rho_J^2} - \Pi_{IJ}\right) \nabla_I \Phi_{IJ} + g, & \text{momentum conservation} \end{cases} \tag{3.7}$$

Further details for the RKPM and the expression of the correction function can be found in Sherburn et al. (2015). Crack growth in the realm of RKPM has beed studied by Zhang (2010) utilizing a cohesive crack method and by Sherburn et al. (2015) for modelling the penetration and perforation of brittle geomaterials.

3.5 Moving least squares (MLS)

The Moving Least Squares (MLS) method was introduced by Shepard (1968) in 1968 for reconstructing continuous functions from a set of points and further extended by Lancaster and Salkauskas (1981) for surface generation problems. At present, the MLS shape functions are highly within the Element Free Galerkin (EFGM) (see Section 3.6.2.1).

In MLS, the displacement field is approximated by

$$u_{\text{MLS}}(x) = \mathbf{p}_{\text{MLS}}^T(x)\, \alpha_{\text{MLS}}(x) \tag{3.8}$$

where $\mathbf{p}(x)$ is a polynomial of order m (e.g. $m = 2$ linear and $m = 3$ quadratic basis) defined as

$$\mathbf{p}_{\text{MLS}}^T(x) = \begin{bmatrix} 1 & x & x^2 & \dots & x^m \end{bmatrix} \tag{3.9}$$

and $\alpha_{\text{MLS}}(x)$ are the unknown and non-constant coefficients (these depend on x)

$$\alpha_{\text{MLS}}^T(x) = \begin{bmatrix} \alpha_0(x) & \alpha_1(x) & \alpha_2(x), & \dots, & \alpha_m(x) \end{bmatrix}. \tag{3.10}$$

The MLS shape functions are determined by minimizing a weighted functional J_{MLS}

$$J_{\text{MLS}}(x) = \sum_{I \in \mathcal{S}} W(x - x_I) \left[\mathbf{p}_{\text{MLS}}^T(x_I)\, \alpha_{\text{MLS}}(x) - u_I \right]^2 \tag{3.11}$$

where $W(x - x_I)$ is the weight function for point x and u_I is the displacement field value at node I.

Eq. (3.11) leads to the following compact form

$$\mathbf{A}_{\text{MLS}}(x)\, \alpha(x) = \mathbf{B}_{\text{MLS}}(x)\, \mathbf{u}_{\text{MLS}}. \tag{3.12}$$

The matrices $\mathbf{A}_{\text{MLS}}(x)$ and $\mathbf{B}_{\text{MLS}}(x)$ are defined by

$$\mathbf{A}_{\text{MLS}}(x) = \sum_{I=1}^{n} W(x - x_I)\, \mathbf{p}_{\text{MLS}}(x_I)\, \mathbf{p}_{\text{MLS}}^T(x_I) \tag{3.13}$$

and

$$\mathbf{B}_{\text{MLS}}^T(x) = \left[W(x - x_1)\, \mathbf{p}_{\text{MLS}}(x_1), \quad ..., \quad W(x - x_n)\, \mathbf{p}_{\text{MLS}}(x_n) \right], \tag{3.14}$$

respectively where n is the number of point in the neighbourhood of x for which $W(x - x_I) \neq 0$. Solving Eq. (3.12) for $\alpha(x)$ and further substituting in Eq. (3.8), the MLS approximants are eventually defined as

$$u_{\text{MLS}}(x) = \sum_{I \in \mathcal{S}} \Phi_I(x)\, u_I = \mathbf{\Phi}^T \mathbf{u}_{\text{MLS}} \tag{3.15}$$

where

$$\mathbf{\Phi}^T = \mathbf{p}_{\text{MLS}}^T(x) \left[\mathbf{A}_{\text{MLS}}(x) \right]^{-1} \mathbf{B}_{\text{MLS}}(x) \tag{3.16}$$

and the shape function $\Phi_I(x)$ of node I

$$\Phi_I(x) = \mathbf{p}_{\text{MLS}}^T(x) \left[\mathbf{A}_{\text{MLS}}(x) \right]^{-1} W(x - x_I)\, \mathbf{p}_{\text{MLS}}^T(x_I). \tag{3.17}$$

The weight functions $W(x - x_I)$ should be positive and ensure a unique solution of the coefficient matrix $\alpha(x)$ Belytschko et al. (1994). Furthermore, the computation of Eq. (3.17) requires extra computational cost since the inversion of matrix $\mathbf{A}_{\text{MLS}}(x)$ should be evaluated. The inverted matrix $\mathbf{A}_{\text{MLS}}(x)$ may lead to singularities (Nguyen et al., 2008).

The MLS was studied in crack propagation problems by Most and Bucher (2003) where it was coupled with stochastic Finite Elements. They utilized a fictitious crack model for the crack growth where the micro cracks emerge from maximum principal tensile strain exceedance criteria and the macro cracks from a micro crack after a certain critical width is reached.

Arzani et al. (2017) also examined two-dimensional crack growth problems using the transparency method for the treatment of discontinuities. The transparency method provides a smooth description of the shape function around the crack tip by endowing the surface, or line, of discontinuity with a varying degree of transparency. The crack tip is considered completely transparent and vanishes away from it.

3.6 Weighted residual methods

A linear differential equation may be written in the following form

$$L(\mathbf{u}) = f \tag{3.18}$$

where $L(\mathbf{u})$ is a linear differential operator, $\mathbf{u}$ is the unknown variable and f is a forcing term. In weighted residual methods trial functions are utilized to obtain an approximate solution of $\mathbf{u}$ (Bathe, 2007). In this, it is assumed that the unknown function, herein the displacement field, and its corresponding test

functions are approximated by

$$\mathbf{u}_{\mathrm{WM}}(\mathbf{x}) = \sum_{I}^{n} \Phi_I(\mathbf{x})\,\mathbf{u}_I \tag{3.19}$$

and

$$\mathbf{w}(\mathbf{x}) = \sum_{I=1}^{n} \Psi_I(\mathbf{x})\,\mathbf{w}_I, \tag{3.20}$$

respectively, where δu_I are arbitrary coefficients, $\mathbf{u}_I$ are unknowns of the problem and n is the number of nodes/ particles. The $\Phi_I(\mathbf{x})$ and $\Psi_I(\mathbf{x})$ are the interpolation functions evaluated at node I of displacement field and trial solution, respectively.

Substituting the approximate solution Eq. (3.20) on the differential operator Eq. (3.18) leads to

$$R = f - L\left(\sum_{I=1}^{n} \Psi_I \mathbf{u}_I\right) \tag{3.21}$$

where R is the residual that should be sufficient small to yield good agreement with the exact solution. Collocation and Galerkin methods are the most widely used weighted residual methods and they are analysed in Sections 3.6.1 and 3.6.2.1, respectively.

3.6.1 Collocation method

In Collocation method, the continuum is represented by a set of points $\mathbf{x}_I$, $I = 1, ..., n$, where the interpolation functions of the trial solution (Eq. (3.20)) are chosen to be the Dirac delta distributions $\delta(\mathbf{x} - \mathbf{x}_I)$. A major advantage of the Collocation method is that it does not require integration and its shape functions are only computed at nodes, increasing its efficiency over Galerkin method. However, the Collocation method requires the evaluation of high-order derivatives and the resulting stiffness matrix is non-symmetric (Nguyen et al., 2008).

The strong form of the partial differential equations is discretized with the Collocation method and hence, it requires high-order basis functions (at least second order). This is also the main difference with Galerkin methods where a weak form is used. Thus, the first of Eqs. (2.58) is expressed as

$$\int_{\partial\Omega_{\bar{\mathbf{t}}}} \left([\boldsymbol{\sigma}\mathbf{n} - \bar{\mathbf{t}}] \cdot \mathbf{w}\right) d\partial\Omega + \int_{\Omega} \left([\rho\ddot{\mathbf{u}} - \nabla \cdot \boldsymbol{\sigma} - \mathbf{b}] \cdot \mathbf{w}\right) d\Omega \tag{3.22}$$

and the weighted residual form requires the following function spaces

$$S_u = \{\mathbf{u} \in C^1(\Omega) \mid \mathbf{u}(\partial\Omega_{\bar{\mathbf{u}}}) = \bar{\mathbf{u}}\}$$

$$V_u = \{\mathbf{w} \in L^1_{loc} \mid \mathbf{w}(\partial\Omega_{\bar{\mathbf{u}}}) = 0\}$$

where $C^1(\Omega)$ are continuous and differential functions and L^1_{loc} are locally integrable functions without any continuity requirement (Schillinger et al., 2015). The $\bar{\mathbf{t}}$ are the traction/ pressure forces and $\bar{\mathbf{u}}$ is the prescribed displacement applied on boundary $\Omega_{\bar{\mathbf{t}}}$ and $\Omega_{\bar{\mathbf{u}}}$, respectively.

Crack propagation with an Enriched Meshfree Collocation Method for elastic fracture problems was studied by (Yoon et al., 2006) where the discontinuity on the displacement field is modeled by using the visibility criterion. Recently, a Phase Field Isogeometric Collocation method was introduced by Schillinger et al. (2015) as an effort to alleviate the computational demands of phase field fracture by reducing the number of point evaluations.

3.6.2 Galerkin method

In Galerkin method, the differential equation is satisfied by converting it into an integral equation. The differential equation is multiplied by a test function and then averaged over the domain. The unknown variables u_I is then determined

by solving the n equations below

$$\int_{\Omega} \Psi_I R \, d\Omega = 0, \quad I = 1 \ldots, n \tag{3.23}$$

where Ω is the solution domain.

3.6.2.1 Element Free Galerkin Method (EFGM)

One of the oldest meshless Galerkin methods that utilizes a weak form of equilibrium equation (see first of Eqs. (2.58)) is the Element Free Galerkin Method (EFGM) Belytschko et al. (1994). In EFGM, the trial and test functions are constructed using the MLS interoperation schemes for the weak form. Hence, the shape functions are utilized to approximate the field variables, using their values at nodes/ particles of the solution domain.

In EFGM, the weak form of equilibrium equation is defined as

$$\begin{aligned} &\int_{\Omega} (\rho \ddot{\mathbf{u}} \cdot \mathbf{w}) \, d\Omega + \int_{\Omega} (\boldsymbol{\sigma} : \nabla \mathbf{w}) \, d\Omega = \int_{\partial\Omega_{\bar{\mathbf{t}}}} (\bar{\mathbf{t}} \cdot \mathbf{w}) \, d\partial\Omega_{\bar{\mathbf{t}}} + \int_{\Omega} (\mathbf{b} \cdot \mathbf{w}) \, d\Omega + \\ &\int_{\Omega} ((\mathbf{u} - \bar{\mathbf{u}}) \cdot q) \, d\Omega_{\bar{\mathbf{u}}} + \int_{\Omega} (\lambda \cdot q) \, d\Omega_{\bar{\mathbf{u}}} \end{aligned} \tag{3.24}$$

where $\mathbf{u}(\mathbf{x}) \in H^1$, Lagrange multipliers $\lambda \in H^0$, test functions $\mathbf{w} \in H^1$ and $q \in H^0$. The symbols H^1 and H^0 denote the Sobolev spaces of degree one and zero, respectively. It should be noticed that the trial functions do not satisfy the essential boundary conditions. Hence, Lagrange multipliers are imposed to invoke the essential boundary conditions.

To obtain a discrete solution of equation (3.24), the displacement field and the Lagrange multipliers together with their test functions are expressed as

$$\mathbf{u}_{\text{EFGM}}(x) = \sum_{I=1}^{n} \Phi_I(x) \, \mathbf{u}_I \tag{3.25}$$

$$\lambda_{\text{EFGM}}(\mathbf{x}) = \sum_{I=1}^{n} N_I(s)\,\lambda_I, \quad \mathbf{x} \in \Omega_{\bar{\mathbf{u}}} \tag{3.26}$$

$$\mathbf{w}_{\text{EFGM}}(x) = \sum_{I=1}^{n} \Phi_I(x)\,\mathbf{w}_I \tag{3.27}$$

and

$$q_{\text{EFGM}}(\mathbf{x}) = \sum_{I=1}^{n} N_I(s)\,\delta\lambda_I, \quad \mathbf{x} \in \Omega_{\bar{\mathbf{u}}} \tag{3.28}$$

where $N_I(s)$ is the Lagrange interpolants and s is the arc length along the boundary Belytschko et al. (1994). Substituting the approximation Eqs. (3.25) to (3.28), Eq. (3.24) is rewritten in the following matrix form as

$$\begin{bmatrix} \mathbf{K} & \mathbf{G} \\ \mathbf{G}^T & \mathbf{0} \end{bmatrix} \begin{bmatrix} \mathbf{u} \\ \lambda^T \end{bmatrix} = \begin{bmatrix} \mathbf{f} \\ \mathbf{q} \end{bmatrix} \tag{3.29}$$

where

$$[K^u] = \int_{\Omega} [B(\mathbf{x})]^T [D] [B(\mathbf{x})]\, d\Omega, \tag{3.30}$$

$$\mathbf{G}_{IK} = -\int_{\Omega_{\bar{\mathbf{u}}}} \Phi_I N_K\, d\Omega_{\bar{\mathbf{u}}}, \tag{3.31}$$

$$\mathbf{f}_I = \int_{\Omega_{\bar{\mathbf{t}}}} \Phi_I \bar{\mathbf{t}}\, d\Omega_{\bar{\mathbf{t}}} + \int_{\Omega} \Phi_I \mathbf{b}\, d\Omega \tag{3.32}$$

and

$$\mathbf{q}_K = -\int_{\Omega_{\bar{\mathbf{u}}}} N_K \bar{\mathbf{u}}\, d\Omega_{\bar{\mathbf{u}}}. \tag{3.33}$$

In (3.30), $[D]$ is the constitutive matrix in Voigt notation, defined as

$$[D] = \begin{bmatrix} D_{1111} & D_{1122} & D_{1112} \\ D_{2211} & D_{2222} & D_{2212} \\ D_{1211} & D_{1222} & D_{1212} \end{bmatrix}. \tag{3.34}$$

and $[B(\mathbf{x})]$ the strain-displacement matrix expressed as

$$[B(\mathbf{x})]_I = \begin{bmatrix} \Phi_{I,1}(\mathbf{x}) & 0 \\ 0 & \Phi_{I,2}(\mathbf{x}) \\ \Phi_{I,2}(\mathbf{x}) & \Phi_{I,1}(\mathbf{x}) \end{bmatrix} \tag{3.35}$$

Finally, the shape function matrix $[N(\mathbf{x})]$ in Eq. (3.33) is computed as

$$[N(\mathbf{x})]_K = \begin{bmatrix} N_K(\mathbf{x}) & 0 \\ 0 & N_K(\mathbf{x}) \end{bmatrix} \tag{3.36}$$

Crack propagation problems using the EFGM were examined by Ventura et al. (2002) in the concept of XFEM. Recently, Rabczuk et al. (2010) introduced a new method called Cracking Particle Method (CPM) without any enrichment by utilizing the EFGM. In this, the crack paths are modelled by a set of cracked segments that split the particles located on them into two particles lying on opposite sides of the crack. Although CPM offers great advantages in crack path modelling by adding or removing cracking particles on the domain, it requires particle refinement along the crack path for accurate results to be derived. Ai and Augarde (2018a) introduced an adaptivity scheme to overcome that issue as well as to improve the accuracy of the method in dealing with branched cracks. An extension of their proposed adaptive scheme in three-dimensional problems can be found in Ai and Augarde (2018b).

3.7 Peridynamics (PD)

Continuum mechanics approaches face numerical difficulties when internal discontinuities exist, i.e. crack paths, since the spatial derivatives of their governing equations are undefined along these regions. Peridynamics (PD) was recently introduced by Silling (2000) as a new continuum mechanics approach

permits internal discontinuities since it does not require the evaluation of spatial derivatives. Instead, the governing equations of the PD are integro-differential equations where the divergence of the stress term (see the first of Eqs. (2.58)) of the strong form is replaced by an integral function of a force on particle at $\mathbf{x}$ as

$$\rho\ddot{\mathbf{u}} = \int_{\Omega_{\mathbf{x}}} \mathbf{f}\left(\mathbf{u}(\hat{\mathbf{x}},t) - \mathbf{u}(\mathbf{x},t), \hat{\mathbf{x}} - \mathbf{x}\right)\, d\Omega_{\mathbf{x}} + \mathbf{b}(\mathbf{x},t). \tag{3.37}$$

The symbol is $\mathbf{f}$ the pairwise force function in the Peridynamics bond that connects particle $\hat{\mathbf{x}}$ to $\mathbf{x}$, $\mathbf{u}$ is the displacement field and $\mathbf{b}(\mathbf{x},t)$ is the body force. In PD, the integral of Eq. (3.37) is defined over a region $\Omega_{\mathbf{x}}$ that is called the 'horizon' of $\mathbf{x}$ (see also Fig. 3.3). For the case of a linear micro elastic potential, the pairwise force is defined as

$$\mathbf{f}(\eta,\xi) = \begin{cases} \frac{\xi+\eta}{\|\xi+\eta\|}\mathcal{A}(\xi)\frac{(\|\xi+\eta\|-\xi)}{\xi}, & \xi \leq \delta \\ 0 & \xi > \delta \end{cases} \tag{3.38}$$

In Eq. (3.38), $\xi = \hat{\mathbf{x}} - \mathbf{x}$ is the relative position of two particles $\hat{\mathbf{x}}$ and $\mathbf{x}$ while $\eta = \hat{\mathbf{u}} - \mathbf{u}$ their relative displacement. where $\mathcal{A}(\xi)$ is called micro-modulus and has the meaning of the bond elastic stiffness. A notable disadvantage of PD is that requires neighbour particle searching at each time step.

Applications of PD in fracture mechanics can be found in the literature e.g. in Ha and Bobaru (2010) for dynamic crack propagation crack branching problems and in Yolum et al. (2016) for ductile fracture of moderately thick plates.

3.8 Discrete element method (DEM)

Discrete methods has gain popularity and last few years in the realm of fracture mechanics since cracks can be naturally represented by breaking the particles' bond. DEM is widely-used discrete meshless method that solves the dynamic

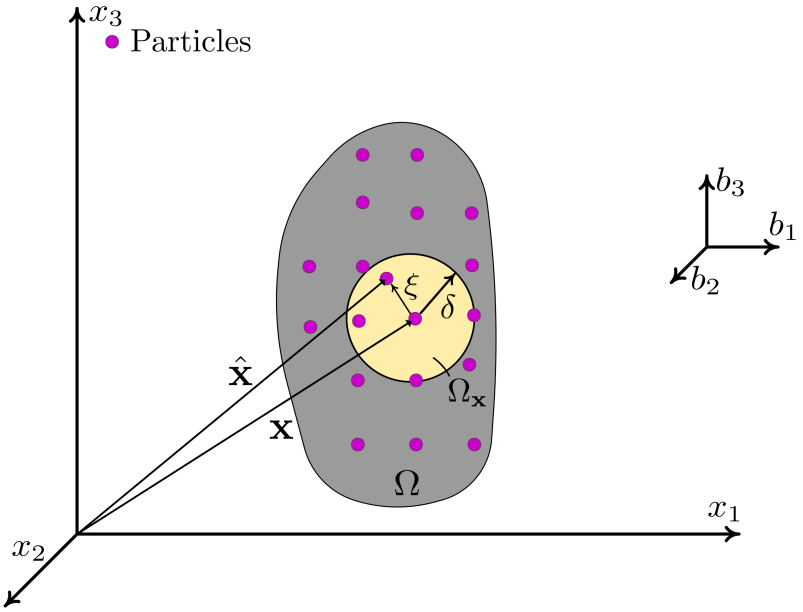

Figure 3.3: Peridynamics: Particle $\hat{\mathbf{x}}$ interacts with $\mathbf{x}$ within 'horizon' $\Omega_{\mathbf{x}}$

evolution of solid body by studying the movement and interaction of material's grains (Luding, 2008). DEM can be considered as an extension of the Molecular Dynamics (MD) simulation (Rapaport, 2004) where cluster of atoms are using for the particle interaction.

In DEM, the Newton's equations of motion for the translational and rotational degrees of freedom are expressed as

$$\begin{cases} m_I \ddot{\mathbf{u}}_I = \mathbf{f}_I + \mathbf{b}_I, \\ I_I \dot{\omega}_I = \mathbf{t}_I, \end{cases} \tag{3.39}$$

where $\mathbf{f}_I$ all of the forces acting on particle I from all the other particles and the boundaries and derive from a potential energy density.

The evaluation of acting force is usually limited to an area of influence around particle I, r_c as it is shown in Fig. 3.4. The mass of particle I is denoted as m_I, the acceleration as $\ddot{\mathbf{u}}_I$ and the body forces as $\mathbf{b}_I$. The I_I is the moment of inertia, ω_I the angular velocity and $\mathbf{t}_I$ the total torque of particle I. The total torque is

defined as

$$\mathbf{t}_I = \sum_{I=1}^{n} (\mathbf{l}_I \times \mathbf{f}_I + \mathbf{q}_I) \tag{3.40}$$

where n is the number of particles and $\mathbf{q}_I$ are the torques at contact due to rolling, torsion and friction. The branch vector $\mathbf{l}_I$ connects the centre of particle with the contact point.

In fracture mechanics problems, Scholtès and Donzé (2012) used DEM to model, and further validate with experimental observations, fracture initiation and propagation in soft and hard rocks. Furthermore, Tan et al. (2009) modeled fracture and damage in machining process of polycrystalline SiC with the DEM. Although, DEM is very efficient in crack propagation propagation problems, it is usually limited to small scales, e.g. micro, due to lack of computational power.

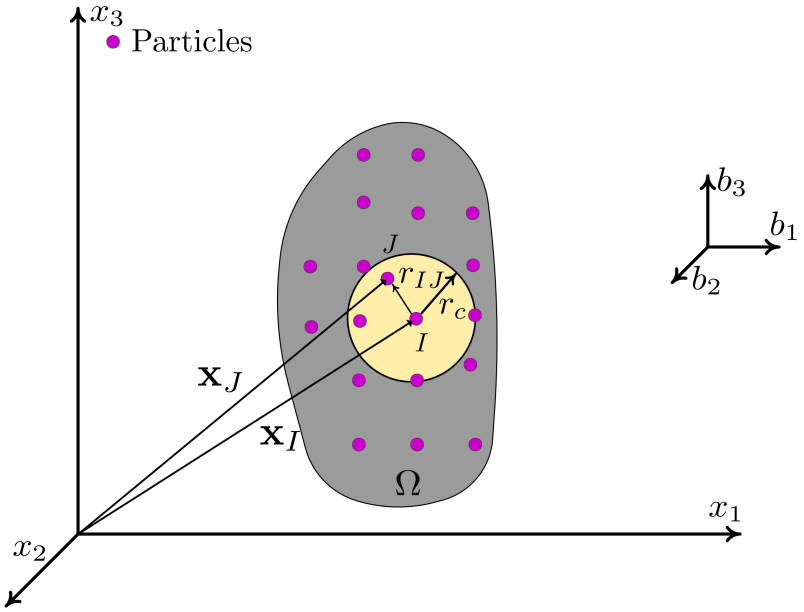

Figure 3.4: Discrete Element Method: Particle I interacts with J within cut-off region r_c.

3.9 The Material Point Method (MPM)

3.9.1 Introduction

The MPM is the latest variant of the so called Particle-In-Cell (PIC) methods for history - dependent problems. The PIC family of methods was introduced by Harlow (1964) in fluids. In Harlow (1964), the fluid is represented by Lagrangian mass points (particles) that are allowed to flow through a fixed computational grid. It is considered partially a Lagrangian method because particles store only information about their mass and position. In Harlow (1964), PIC was implemented to treat contact discontinuities and highly distorted fluid flow. However, when modelling convection problems, the method was found to suffer from energy dissipation when transferring the momentum from the grid to the particles and back. Brackbill and Ruppel (1986) overcame this problem by formulating a full particle method, called FLIP, in which each particle carries all the information including momentum and energy.

Later, Sulsky and Brackbill (1991) extended the FLIP method to handle fluid - structure elastic contact problems with materials governed by history independent constitutive equations applied at material points [1]. The FLIP method was modified by Sulsky et al. (1994) and Sulsky et al. (1995) to account for history dependent variables such as plastic strains and strain-hardening. Their approach gave rise to a MPM that can fully describe material non-linearities for solid mechanics.

3.9.2 Lagrangian - Eulerian formulation

Two formulations exist for the description of kinematics, i.e., (a) the Lagrangian and (b) the Eulerian description of a body motion (Bathe, 2007). In the Lagrangian approach the observer follows an individual point as it moves through

[1] The terms particle and material point will be used interchangeably throughout this work.

space and time. Conversely, in the Eulerian formulation the observer focuses on a specific location in the space through which the points move as time passes.

To better illustrate the differences between the two formulations, the case of an axially loaded bar is considered (see Fig. 3.5). Three points of the bar are marked at three time steps, namely t_1, t_2 and t_3. As illustrated in Fig. 3.5, positions x_1, x_2 and x_3 refer to the same point (c) but at different time instances t_1, t_2 and t_3, respectively (Lagrangian formulation). Conversely, different points are referred to the same position of the bar in Eulerian formulation. E.g. in position x_1, point (c) is located at time step t_1, point (b) at time step t_2 and point (a) at time step t_3.

In the Lagrangian approach, the coordinates of the body, i.e., the mesh, move with the material. This is particularly advantageous in solid mechanics for the application of boundary conditions since the boundary nodes remain on the boundary. Furthermore, treatment of history-dependent materials is straightforward because the same point is examined at different locations. However, severe deformation of the Lagrangian mesh may give rise to inaccurate results due to ill-conditioning of the corresponding Jacobian (see Section 3.9.3).

A fixed computational mesh is defined in the Eulerian approach. Thus, any numerical issues pertinent to element distortion are minimized. In contrast, the treatment of essential boundary conditions is not straightforward on a fixed mesh since the boundary nodes of the material vary with the time. Furthermore, history-dependent materials are are difficultly treated as different points are examined at each time step.

Therefore, novel numerical methods that are able to adopt merits of both approaches are vital nowadays to address very challenging engineering problems, e.g. crack propagation where severe mesh distortion errors and history-dependent materials are taken into account.

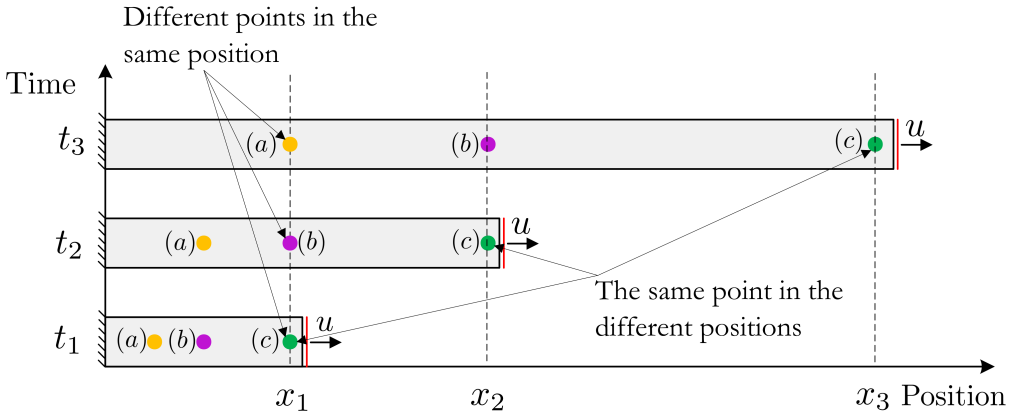

Figure 3.5: Eulerian and Lagrangian formulation.

3.9.3 The effect of element distortion

Finite Elements are in general most accurate in the prediction of displacement and stress field when they are undistorted. Fig. 3.6 illustrates the basic types of distortions (Bathe, 2007).

However, in practice, elements may have distortions to mesh complex geometries effectively. When the distortions are sufficiently small the solution error is bounded. However, in the case of large displacement kinematics, significant angular and curved edge distortions may arise as a result of the deformations. Thus, element distortions affect the accuracy of the non-linear response of the structure. In an analysis it is therefore necessary to monitor the changing shape of each element, and if element distortions adversely affect the response of the structure, a more suitable mesh may be required.

3.9.4 Material Point Method approximation

In the MPM, a deformable body is approximated with a set of material points $p = 1, 2, \ldots, N_p$, where $N_p \in \mathbb{Z}^+$ is the total number of material points (see Figs. 3.7 and 3.8). The material point discretization can be defined by any appropriate tessellation of Ω. Under the action of ${}^{(t)}\mathcal{O}$, the initial position vector ${}^{(0)}\mathbf{x}_p$ of a material point is mapped to the current position vector ${}^{(t)}\mathbf{x}_p$ at $t > 0$ (see Fig.

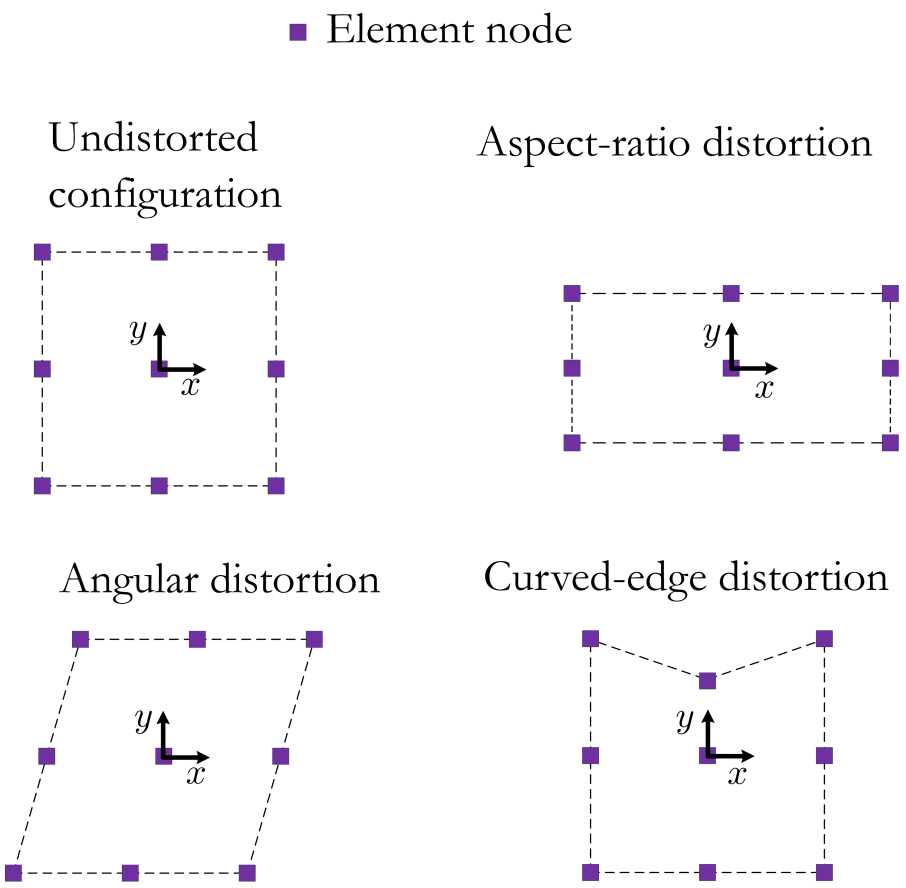

Figure 3.6: Classification of element distortions.

3.8). Consequently, the current position of a material point always depends on the initial position and time t. The displacement vector of the material point is defined as ${}^{(t)}\mathbf{u}_p = {}^{(t)}\mathbf{x}_p - {}^{(0)}\mathbf{x}_p$.

Through this discretization, the mass density distribution of the deformable body is readily defined as

$$\rho\left(\mathbf{x},t\right) = \sum_{p=1}^{N_p} \rho_p \Omega_p \delta\left(\mathbf{x} - {}^{(t)}\mathbf{x}_p\right) \tag{3.41}$$

where $\rho_p = M_p/\Omega_p$ is the mass density of the material point, M_p is the material point mass, Ω_p is the material point volume and δ is the Dirac function.

Similarly, the domain volume Ω is additively decomposed into the corresponding material point domain contributions according to the following expression

$$\Omega\left(\mathbf{x},t\right) = \sum_{p=1}^{N_p} \Omega_p \delta\left(\mathbf{x} - {}^{(t)}\mathbf{x}_p\right). \tag{3.42}$$

In this work, the tributary volumes Ω_p of each material point are defined according to the following methodology. An isoparametric discretization of the material domain is first performed using quadrilateral elements. Material points are then defined at the positions of the Gauss points of each individual element at their natural coordinate system. The corresponding volumes are then mapped back to the Cartesian system by means of the isoparametric transformation. Defining material points at the Gauss points of the corresponding finite element mesh has been chosen to facilitate comparison against standard Finite Element implementation.

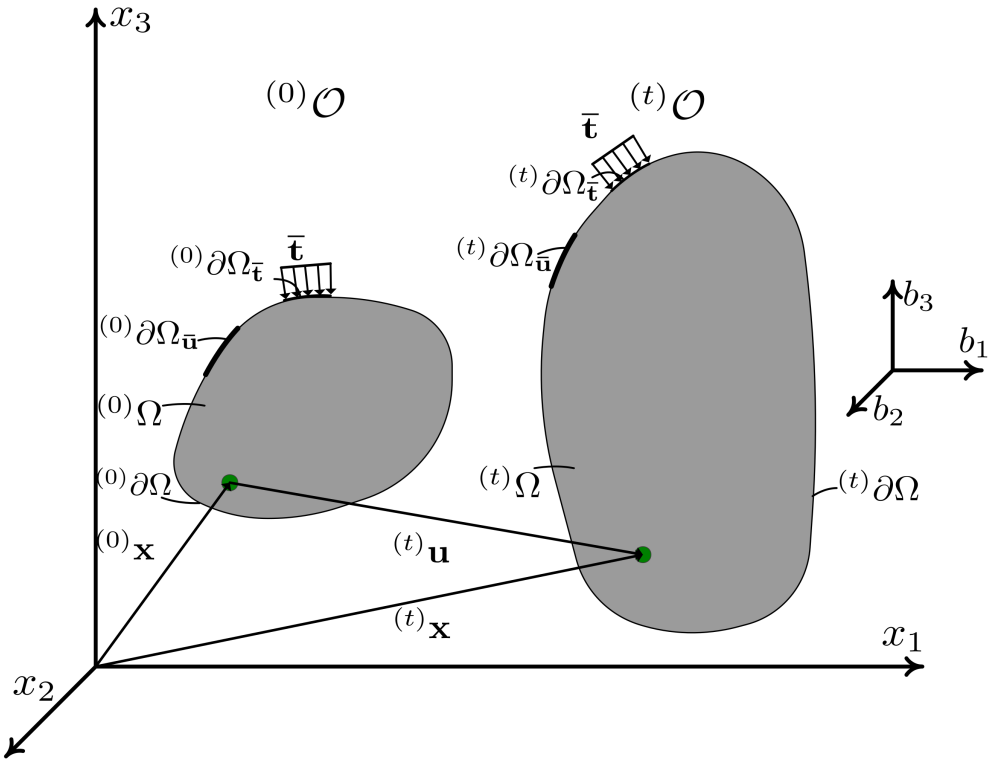

Figure 3.7: Deformation process: Continum solid body Ω.

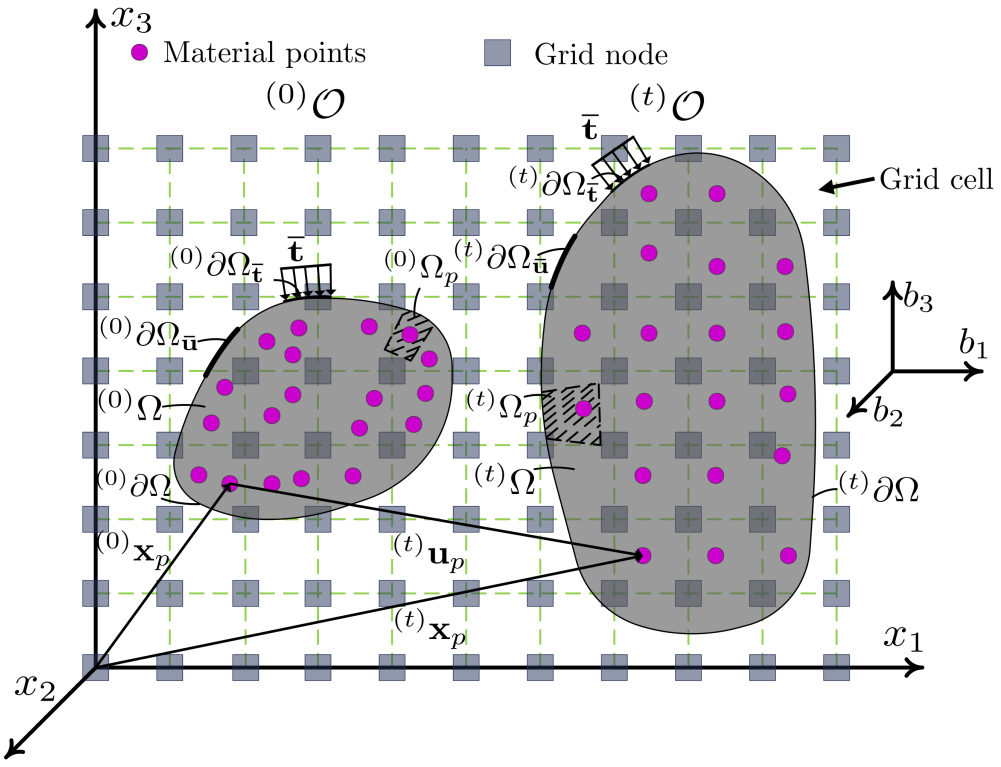

Figure 3.8: Deformation process: Material point method approximation.

3.9.4.1 Eulerian mesh

Integral to the computational scheme of MPM is the definition of a computational grid where the solution of the governing equations of motion is performed. This grid is termed the Eulerian mesh (or Eulerian grid). The Eulerian grid is a non-deforming mesh corresponding to the space that the material points move through (see Figs. 3.9 and 3.10). Referring to Figs. 3.9 and 3.10, the Eulerian Mesh is divided into active cells [2], i.e., cells where one or more material points exist at a certain time t and inactive cells where no material point exists. In this work, the Eulerian grid is constantly updated according to the topology of the material points, thus reducing the solution space at any time instant.

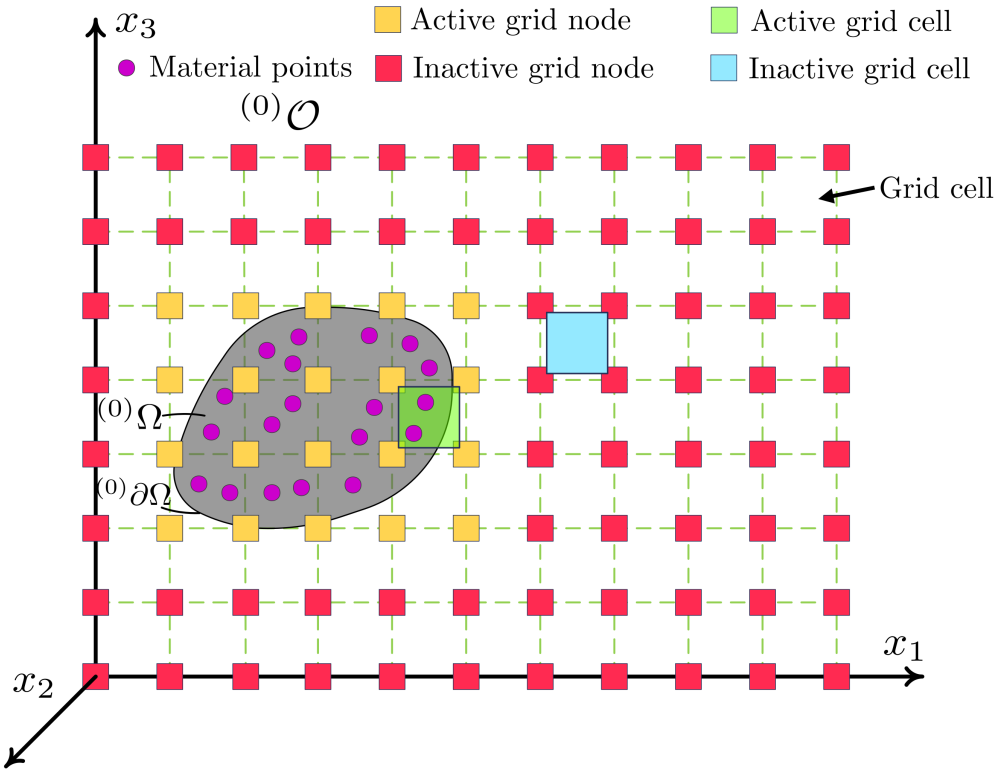

Figure 3.9: Active part detection of the Eulerian grid: Initial configuration.

[2] The terms cell and element will be used interchangeably throughout this work.

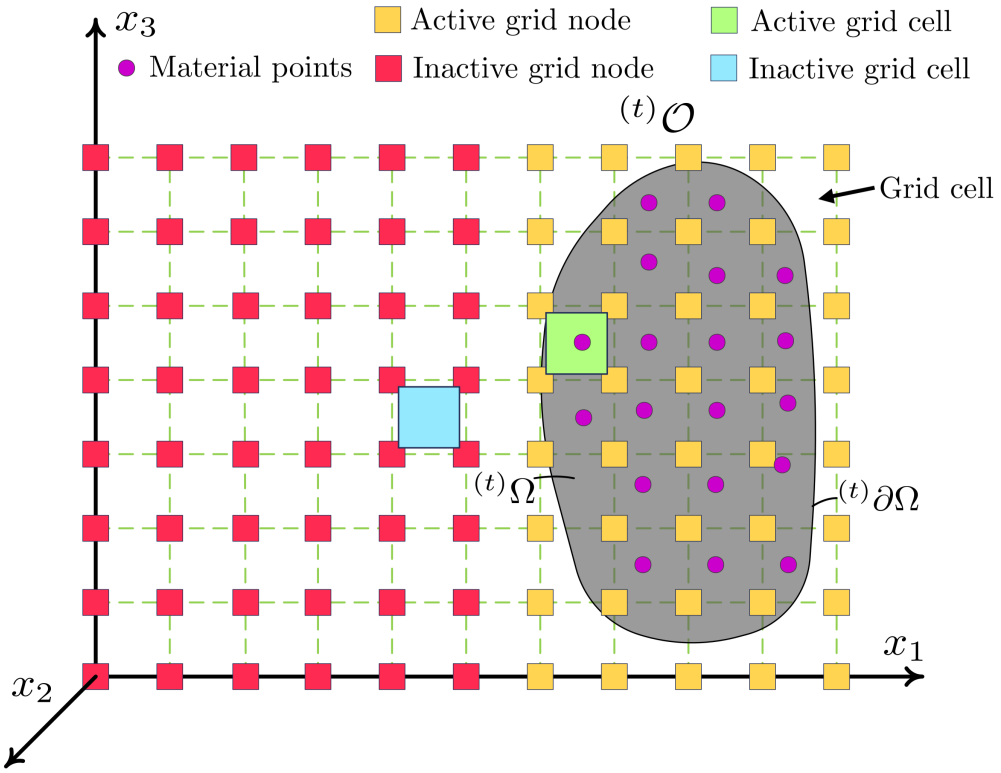

Figure 3.10: Active part detection of the Eulerian grid: Deformed configuration.

3.9.4.2 Equilibrium discrete equations

The discrete form of the MPM equilibrium equations is derived in a straightforward manner by means of the Galerkin approximation (Bathe, 2007). The weak form of the equilibrium equations introduced in the first of Eqs. (2.58) is expressed as

$$\int_{\Omega} (\rho \ddot{\mathbf{u}} \cdot \mathbf{w})\, d\Omega + \int_{\Omega} (\boldsymbol{\sigma} : \nabla \mathbf{w})\, d\Omega = \int_{\partial\Omega_{\bar{\mathbf{t}}}} (\bar{\mathbf{t}} \cdot \mathbf{w})\, d\partial\Omega_{\bar{\mathbf{t}}} + \int_{\Omega} (\mathbf{b} \cdot \mathbf{w})\, d\Omega \qquad (3.43)$$

where the following trial solution and weighting function spaces are defined

$$\mathcal{V} = \{\mathbf{u} \in \left(H^1(\Omega)\right)^d \mid \mathbf{u} = \bar{\mathbf{u}} \text{ on } \partial\Omega_{\bar{\mathbf{u}}}\}$$

and

$$\mathcal{U} = \{\mathbf{w} \in \left(H^1(\Omega)\right)^d \mid \mathbf{w} = 0 \text{ on } \partial\Omega_{\bar{\mathbf{u}}}\},$$

respectively. The weighting functions $\mathbf{w}$ satisfy the essential boundary conditions of the problem. Substituting Eqs. (3.41) and (3.42) into the weak form (3.43), the following relation is established

$$\sum_{p=1}^{N_p}(\rho_p\ddot{\mathbf{u}}_p\cdot\mathbf{w}_p)\Omega_p+\sum_{p=1}^{N_p}(\boldsymbol{\sigma}_p:\nabla\mathbf{w}_p)\Omega_p=\int_{\partial\Omega_{\bar{\mathbf{t}}}}(\bar{\mathbf{t}}\cdot\mathbf{w})\,d\partial\Omega_{\bar{\mathbf{t}}}+\sum_{p=1}^{N_p}(\mathbf{b}_p\cdot\mathbf{w}_p)\Omega_p \quad (3.44)$$

where $\mathbf{w}_p$, $\boldsymbol{\sigma}_p$ and $\mathbf{b}_p$ are the test function, stress field and body forces evaluated at material point $\mathbf{x}_p$. Relation (3.44) which essentially collocates the weak equilibrium of the continuum into the material points derived from the tessellation of the deformable body.

Considering the following Galerkin interpolation scheme for the test functions and their spatial derivatives

$$\mathbf{w}_p=\sum_{I=1}^{N_n}N_I(\mathbf{x}_p)\mathbf{w}_I \quad (3.45)$$

and

$$\nabla\mathbf{w}_p=\sum_{I=1}^{N_n}\nabla N_I(\mathbf{x}_p)\mathbf{w}_I, \quad (3.46)$$

respectively, where $N_n\in\mathbb{Z}^+$ is the number of grid nodes, $N_I(\mathbf{x}_p)$ are the interpolation functions evaluated at the material points and $\mathbf{w}_I$, $I=1,\ldots,N_n$ are the test function nodal values.

Both the interpolation functions and the test function nodal values are defined with respect to the underlying Eulerian mesh as described in Section 3.9.4.1. Thus, standard Finite Element interpolation functions can be utilized to interpolate material point defined quantities at the nodal points of the corresponding parent cell. In this work, B-spline interpolation functions are used as described later in Section 3.9.9.

Similar expressions are established for the displacement, velocity, and acceleration fields, i.e.,

$$\mathbf{u}_p = \sum_{I=1}^{N_n} N_I(\mathbf{x}_p)\mathbf{u}_I, \tag{3.47}$$

$$\dot{\mathbf{u}}_p = \sum_{I=1}^{N_n} N_I(\mathbf{x}_p)\dot{\mathbf{u}}_I, \tag{3.48}$$

and

$$\ddot{\mathbf{u}}_p = \sum_{I=1}^{N_n} N_I(\mathbf{x}_p)\ddot{\mathbf{u}}_I, \tag{3.49}$$

respectively, where $\mathbf{u}_I$, $\dot{\mathbf{u}}_I$, and $\ddot{\mathbf{u}}_I$ are the components of the nodal displacement, velocity and acceleration vectors, respectively, evaluated at node I.

Substituting (3.45) and (3.46) in relation (3.44) and performing the necessary algebraic manipulation, the following expression is derived

$$\sum_{I=1}^{N_n} \mathbf{w}_I \cdot \left[\mathbf{F}_I^{irt} + \mathbf{F}_I^{int} - \mathbf{F}_I^{ext}\right] = 0 \tag{3.50}$$

where

$$\mathbf{F}_I^{irt} = \sum_{p=1}^{N_p} (\rho_p \ddot{\mathbf{u}}_p \cdot N_I(\mathbf{x}_p))\Omega_p \tag{3.51}$$

$$F_{I,i}^{int} = \sum_{p=1}^{N_p} (\sigma_{p_{jk}} \cdot B_I^{ijk}(\mathbf{x}_p))\Omega_p \tag{3.52}$$

and

$$\mathbf{F}_I^{ext} = \int_{\partial\Omega_{\bar{\mathbf{t}}}} (\bar{\mathbf{t}} N_I(\mathbf{x}_p))\, d\partial\Omega_{\bar{\mathbf{t}}} + \sum_{p=1}^{N_p} \mathbf{b}_p N_I(\mathbf{x}_p)\Omega_p. \tag{3.53}$$

In relation (3.52), $\sigma_{p_{jk}}$ denotes the stress components $\boldsymbol{\sigma}_p = \{\sigma_{p_{jk}}\}$ whereas $\mathbf{B}_I(\mathbf{x}_p) = \{B_I^{ijk}(\mathbf{x}_p)\}$ is defined as

$$B_I^{ijk}(\mathbf{x}_p) = \frac{1}{2}\left(\frac{\partial N_I(\mathbf{x}_p)}{\partial x_j}\delta_{ik} + \frac{\partial N_I(\mathbf{x}_p)}{\partial x_k}\delta_{ij}\right) \tag{3.54}$$

where $i, j, k = 1 \ldots d$. As the test functions in equation (3.44) are chosen arbitrarily, equation (3.50) should hold for every set of nodal values $\mathbf{w}_I$. Thus, the

following equilibrium equation is finally established

$$\mathbf{R}^u_I(\mathbf{u}) = \mathbf{F}^{irt}_I + \mathbf{F}^{int}_I - \mathbf{F}^{ext}_I = 0, \quad I = 1\ldots, N_n \tag{3.55}$$

where $\mathbf{F}^{irt}_I$ is the vector of inertia forces, $\mathbf{F}^{int}_I$ is the vector of corresponding internal forces and $\mathbf{F}^{ext}_I$ corresponds for the equivalent vector of external forces evaluated at grid node I. The residual nodal values for the displacement field is denoted as $\mathbf{R}^u_I(\mathbf{u})$. Eq. (3.55) corresponds to nodal force equilibrium established at the nodes of the background mesh with the material point to background node mapping performed through relations (3.51), (3.52) and (3.53) for the inertia, internal and external forces, respectively.

Further considering the strain-displacement relation defined in equation (2.42), the strain components $\boldsymbol{\varepsilon}_p = \{\varepsilon_{p_{jk}}\}$ in each material point can be expressed as

$$\varepsilon_{p_{jk}} = \sum_{I=1}^{N_n} B^{ijk}_I(\mathbf{x}_p) u_{I,i}. \tag{3.56}$$

Substituting the corresponding strain-stress relation (constitutive model) and (3.56) into Eq. (3.52) and using Eq. (3.53) and (3.49), the following compact form is eventually derived

$$\mathbf{M}^u\ddot{\mathbf{u}} + \mathbf{K}^u\mathbf{u} = \mathbf{F}^{ext} \tag{3.57}$$

where $\mathbf{M}^u$ is the global lumped mass matrix of the structure whose M^u_I component is expressed as

$$M^u_I = \sum_{p=1}^{N_p} \Big(\rho_p N_I(\mathbf{x}_p)\Big)\Omega_p. \tag{3.58}$$

Similarly, $\mathbf{K}^u$ is the global stiffness matrix of the structure whose $K^u_{I,J,i,j}$ component is expressed as

$$K^u_{I,J,i,j} = \sum_{p=1}^{N_p} \left(\Big(D_{p_{lkmn}} B^{jmn}_J(\mathbf{x}_p)\Big) \cdot B^{ilk}_I(\mathbf{x}_p)\right)\Omega_p. \tag{3.59}$$

The term $D_{p_{lkmn}}$, accounts for the components of the constitutive matrix $\mathbf{D}_p$ evaluated at p^{th} material point, defined in equation (2.51).

To facilitate understanding of Eq. (3.59), the grid cell contributions can be written as the summation of the material points' stiffness contributions within each cell, i.e

$$[K^u_{\text{cell}}] = \sum_{p=1}^{n_p^{\text{cell}}} [k^u_p] \tag{3.60}$$

where n_p^{cell} is the number of material points located in the grid cell and $[k^u_p]$ is the nodal stiffness components of the p^{th} material point within the grid cell. The contribution of each material point within its parent cell is evaluated as

$$[k^u_p] = [B(\mathbf{x}_p)]^T [D_p] [B(\mathbf{x}_p)] \Omega_p. \tag{3.61}$$

For two-dimensional plane strain/stress problems, examined in this work ($d = 2$), the constitutive matrix can be rewritten in Voigt notation as

$$[D_p] = \begin{bmatrix} D_{1111} & D_{1122} & D_{1112} \\ D_{2211} & D_{2222} & D_{2212} \\ D_{1211} & D_{1222} & D_{1212} \end{bmatrix}. \tag{3.62}$$

and the strain-displacement matrix associated with grid node I as

$$[B(\mathbf{x}_p)]_I = \begin{bmatrix} N_{I,1}(\mathbf{x}_p) & 0 \\ 0 & N_{I,2}(\mathbf{x}_p) \\ N_{I,2}(\mathbf{x}_p) & N_{I,1}(\mathbf{x}_p) \end{bmatrix} \tag{3.63}$$

where $N_{I,1}(\mathbf{x}_p)$ and $N_{I,2}(\mathbf{x}_p)$ are the derivatives of shape functions with respect to x_1 and x_2, respectively. Finally, the global stiffness matrix (Eq. (3.59)) is calculated by assembling the individual contribution of each grid cell where any empty cells are ignored.

3.9.5 Computational cycle

The computational cycle of the MPM consists of five steps, i.e., (a) to (e), illustrated in Fig. 3.11. In the first step all the material point quantities, e.g. mass and momentum are projected onto the grid nodes. Then, the governing equations are solved at those grid nodes in an updated Lagrangian fashion. Next, the updated solution is mapped back from grid nodes to the material points by utilizing appropriate B-spline interpolation functions and all the material point quantities are updated. Finally, the Eulerian grid is reset before proceeding into next time step. The reset of the Eulerian grid is a crucial step within the MPM since any distortion error is avoided.

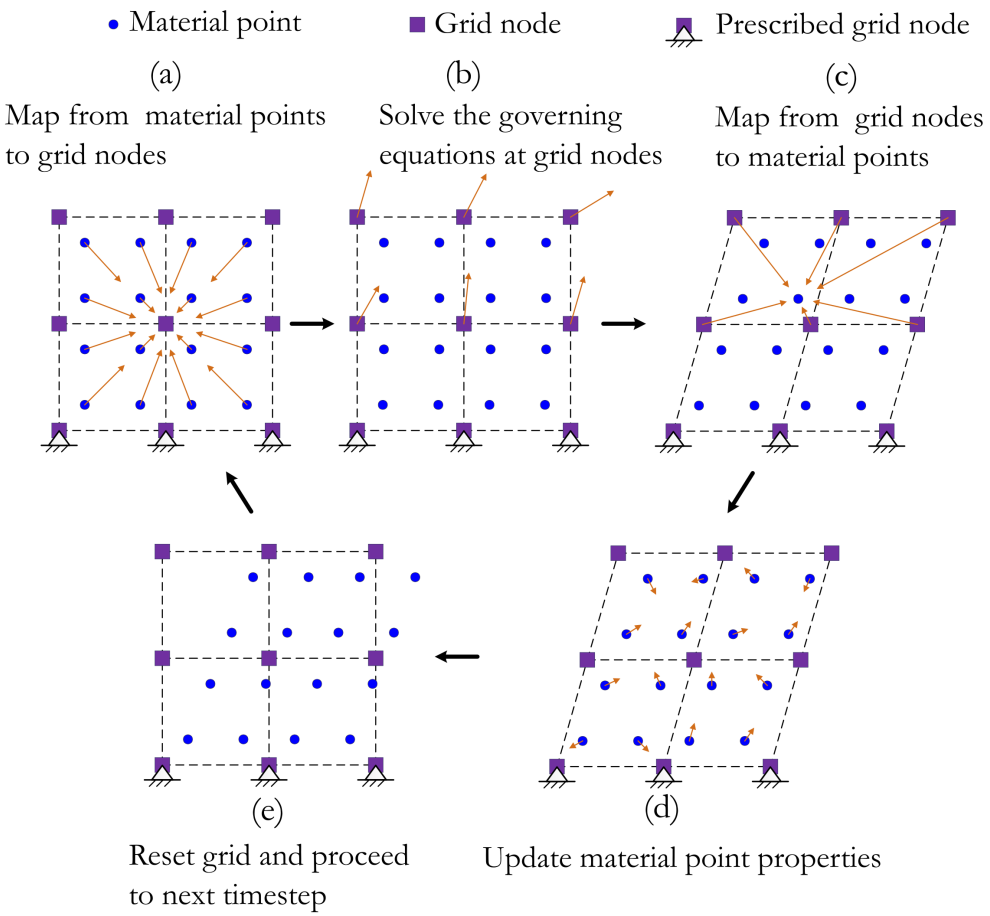

Figure 3.11: Material point method computational cycle.

3.9.6 Boundary conditions

To solve equation (3.57), a set of boundary conditions needs to be defined. Both natural and essential boundary conditions can be treated in the MPM.

As shown on Fig. 3.12, loads can be applied either on material points or directly on grid nodes. If a load is applied on a material point then the load is interpolated at the grid nodes of the parent cell. Thus, this equivalent nodal load is utilized to formulate the nodal vector of external forces.

Zero or non-zero kinematic boundary conditions can be applied at grid nodes in a similar manner to the traditional Lagrangian FEM (see Fig. 3.12). However, zero or non-zero kinematic boundary conditions can also be applied on material points. In this work, a penalty method is adopted to impose kinematic constraints on material points with the methodology described in Appendix A.

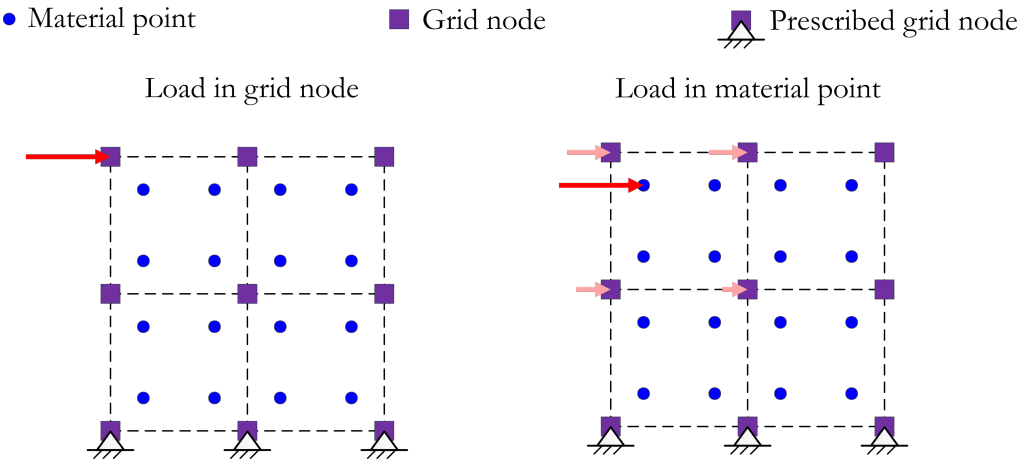

Figure 3.12: External load in grid node (left) and material point (right) (left).

3.9.7 Solution procedure

The MPM was initially implemented in an explicit time integration scheme to numerically solve equation (3.57) (Sulsky et al., 1995). In that implementation, a momentum formulation of the equations of motion was introduced within an Euler forward time integration scheme.

However, explicit integration algorithms are restricted by small time steps due to the Courant - Friedrichs-Levy (CFL) condition (Dokainish and Subbaraj, 1989). Therefore, during the past few years several implicit schemes were introduced to address that issue in MPM. The most noticeable implicit methods were introduced by Guilkey and Weiss (2003) and Sulsky and Kaul (2004). Guilkey and Weiss (2003) developed an implicit time integration algorithm based on a Newmark scheme. They explicitly formed the tangent stiffness matrix (see Eq. (3.59)) similar to the standard FEM (Bathe, 2007).

In Sulsky and Kaul (2004), an implicit solver was developed based on the matrix-free Newton-Krylov algorithm and Euler backward time integration scheme in an effort to reduce computational costs by avoiding the construction of the tangent stiffness matrix. That method is considered suitable when the stress-strain relation is described by complicated constitutive models as there is no requirement for evaluating either numerically or analytically the tangent constitutive matrix at the material level. Using an implicit solver larger time steps are allowed as compared to aforementioned explicit solvers.

Guilkey et al. (2006) formulated a quasi-static MPM to account for slow rate of loading. Their method is based on their previous work on implicit solution (Guilkey and Weiss, 2003), where the tangent stiffness matrix is explicitly formulated. Most recently, Sanchez et al. (2015) (based on Sulsky and Kaul (2004)) developed a quasi-static material point method based on matrix-free Krylov method and GMRES algorithm.

In this work, the computation of tangent stiffness matrix is adopted in quasi-static problems (see Sections 4 and 5) whereas an explicit time integration scheme is employed in dynamic problems (see Sections 6 and 7).

It is of interest to note that whereas in the FEM, integration points are located at optimal positions for Gauss integration, this is not the case for the MPM. In the latter, the number and the position of the material points in a computational

cell varies. This can be treated by increasing the number of material points, i.e. the integration point to enhance the accuracy of the MPM (Guilkey and Weiss, 2003).

3.9.8 Grid crossing error

MPM has been proven to be sensitive to the so-called cell crossing error manifested as an oscillation in the stress field when a material point moves from one background cell to another (Steffen et al., 2008; Gan et al., 2018). This has been treated in the literature by various methods, most notably by introducing the Generalized Interpolation Material Point Method (GIMPM) (Bardenhagen and Kober, 2004) or more recently with a Convected Particle Domain Interpolation technique (CPDI) (Sadeghirad et al., 2011; Sadeghirad et al., 2013).

In this work, higher order B-spline shape functions are used as background grid interpolation functions to treat this issue (Steffen et al. (2008) and Gan et al. (2018), see also Section 3.9.9). Besides their implementational efficiency, the extensive numerical investigations performed in this work demonstrate that the use of B-splines further improves the convergence rate of the coupled phase field formulation for crack propagation introduced (see Sections 5 and 6).

3.9.9 B-spline interpolation

B-Splines are defined through a non-decreasing sequence of real numbers (i.e. $\xi_I \leq \xi_{I+1}$), termed the knot vectors, and formally described as

$$\Xi = \{\xi_1, \xi_2, ..., \xi_{N_{n_\xi}+q_\xi+1}\} \tag{3.64}$$

where N_{n_ξ} and q_ξ are the number of basis functions and the polynomial order in the ξ direction, respectively. The I^{th} B-spline basis function of q_ξ-degree is

defined recursively as (Boor, 2001)

$$N_{I,q_\xi}(\xi) = \frac{\xi - \xi_I}{\xi_{I+q_\xi} - \xi_I} N_{I,q_\xi-1}(\xi) + \frac{\xi_{I+q_\xi+1} - \xi}{\xi_{I+q_\xi+1} - \xi_{I+1}} N_{I+1,q_\xi-1}(\xi) \tag{3.65}$$

where

$$N_{I,0}(\xi) = \begin{cases} 1 & \xi_I \leq \xi \leq \xi_{I+1} \\ 0 & \text{otherwise.} \end{cases} \tag{3.66}$$

Furthermore, the derivative of a B-Spline basis function is expressed as

$$N'_{I,q_\xi}(\xi) = \frac{q_\xi}{\xi_{i+q_\xi} - \xi_i} N_{I,q_\xi-1}(\xi) - \frac{q_\xi}{\xi_{i+q_\xi+1} - \xi_{i+1}} N_{I+1,q_\xi-1}(\xi). \tag{3.67}$$

Higher-order derivatives are evaluated recursively from relation (3.67). A B-Spline curve is evaluated as

$$\mathbf{C}(\xi) = \sum_{I=1}^{N_{n_\xi}} N_{I,q_\xi}(\xi)\mathbf{P}_I \tag{3.68}$$

where $\mathbf{P}_I \in \mathbb{R}_d, I = 1, 2, .., N_{n_\xi}$ are the coordinates of control points and d is the dimension of the problem.

Two-dimensional B-Splines basis functions and their derivatives can be evaluated by means of a tensor product as (Hughes et al., 2005)

$$N_{I,J,q_\xi,q_\eta}(\xi,\eta) = N_{I,q_\xi}(\xi) N_{J,q_\eta}(\eta) \tag{3.69}$$

and

$$N'_{I,J,q_\xi,q_\eta}(\xi,\eta) = N'_{I,q_\xi}(\xi) N'_{J,q_\eta}(\eta), \tag{3.70}$$

respectively. Three-dimensional B-Splines can also be defined in a similar manner.

The one-dimensional and two-dimensional quadratic basis functions ($q_\xi = q_\eta = 2$) together with their first derivatives are shown in Fig. 3.13, 3.14 and 3.15, 3.16, respectively, for knot vectors $\Xi = H = \{0, 0, 0, 0.25, 0.50, 0.75, 1, 1, 1\}$.

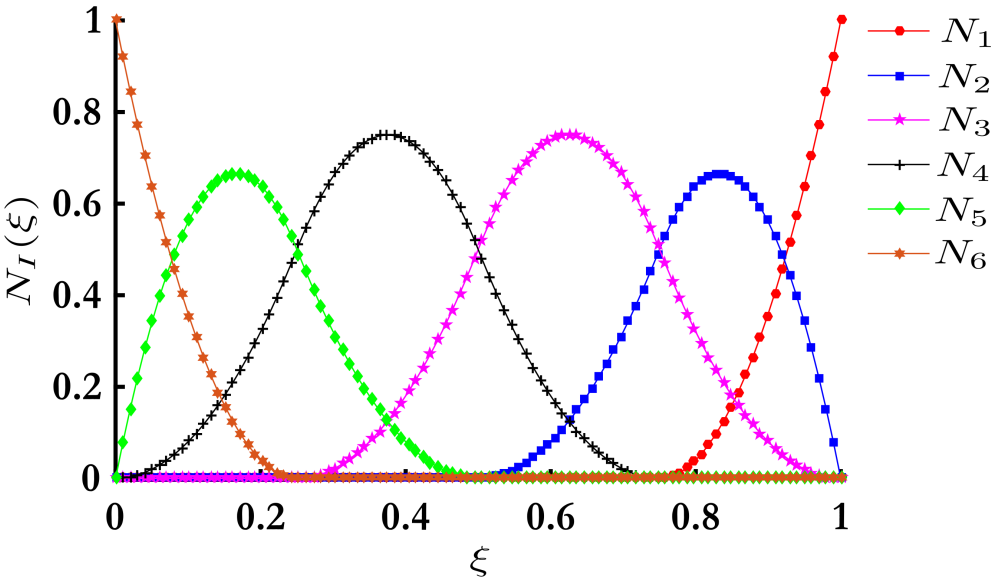

Figure 3.13: Higher-Order B-Splines (1D): Quadratic basis functions (C^1).

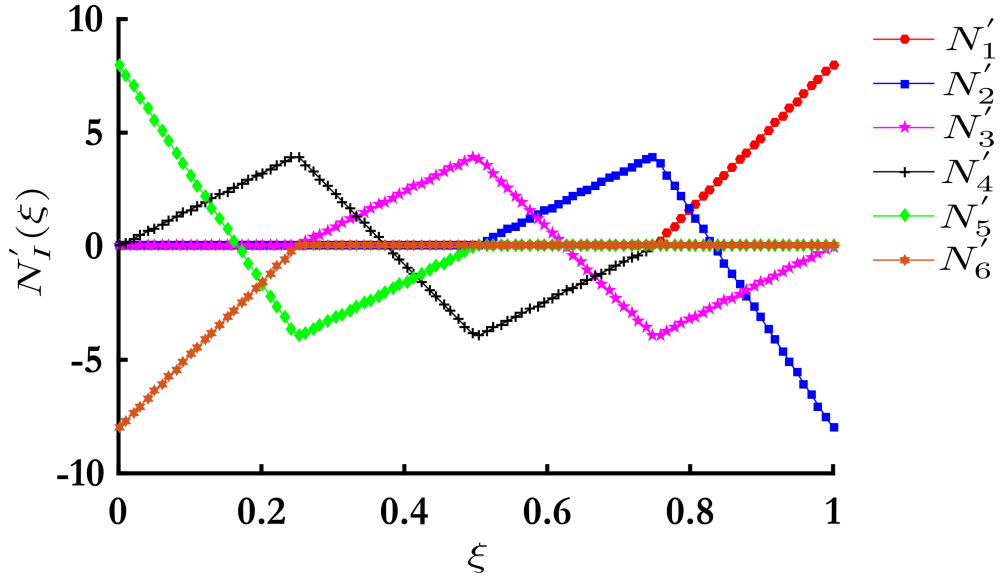

Figure 3.14: Higher-Order B-Splines (1D): First derivatives of quadratic basis functions (C^1).

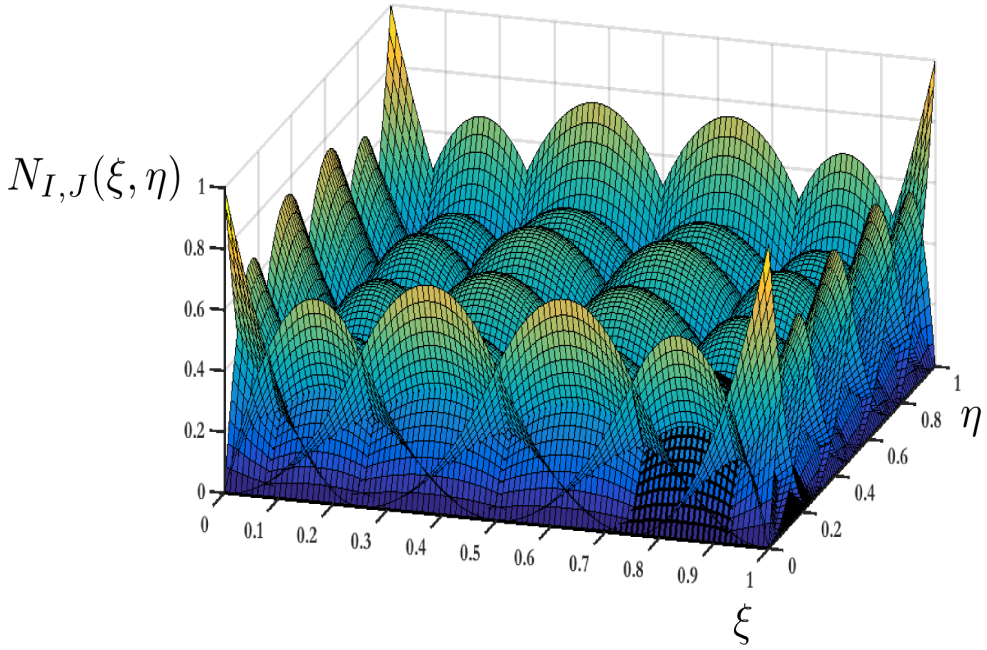

Figure 3.15: High-Order B-Splines (2D): Quadratic basis functions (C^1).

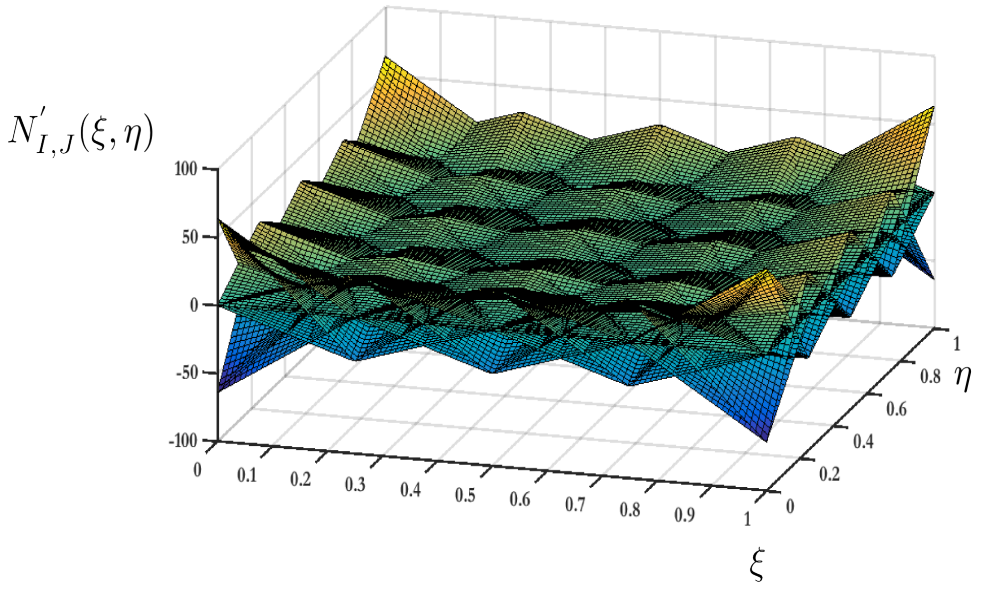

Figure 3.16: High-Order B-Splines (2D): First derivatives of quadratic basis functions (C^1).

B-spline functions are core to the development of isogeometric analysis where NURBS elements are utilized both to represent the exact geometry of a solid body and to define field variables e.g. displacement and phase field. In FEM, higher order B-spline functions are used to accurately represent complex geometries, e.g., curved surfaces with optimal convergence rate. In MPM, they are used to formulate the computational grid as they provide smooth derivatives that lead to more accurate strain and stress results. Further information can be sought in Hughes et al. (2005).

3.9.10 Advantages/Disadvantages of MPM

3.9.10.1 Advantages

The MPM makes use of the benefits of either Lagrangian or Eulerian descriptions, while avoiding the associated problems with each. Some advantages of the MPM are the following:

- Mesh distortion is eliminated. The Lagrangian particles (i.e. material points) are mapped onto a non-deforming Eulerian mesh (computational grid) where solution of the governing equations is performed. Avoiding numerical errors due to mesh distortion is not a trivial task in grid-based Lagrangian methods (see Kaczmarczyk et al. (2014)). Failure to bound such mesh-dependent errors may result in considerable loss of accuracy especially if large displacements and/or large deformations are taken into account (see Zhang et al. (2016), Charlton et al. (2017), and Sofianos and Koumousis (2018)).

- Grid based shape functions and neighbour searching. The grid is used to evaluate the gradient and divergence terms of each material point. Therefore, the their computation is as trivial as in the FEM method. Furthermore, the method does not require time-consuming neighbour searching if a structured background Eulerian grid is utilized. Therefore, MPM

can offer significant computational advantages when compared to purely meshless methods since they require extra computational time due to: (a) higher-order integration schemes to be accurately evaluated (complex shape functions) (b) neighbour searching (Nguyen et al., 2008).

- Contact problems can be solved in a consistent and robust manner. MPM can efficiently tackle contact problems without introducing extra computational complexity and cost to the overall procedure. The interaction of contact surfaces is implemented through materials points within a fixed computational mesh. Thus, there is no need for searching, refining or algorithmically tracking the contact areas. A benchmark example that demonstrates the merits of MPM in contact problems is shown in Fig. 3.18 for the case of two elastic rings. The geometry, boundary conditions and simulation parameters are shown in Fig. 3.17.

  The standard algorithm of MPM can naturally handle non-slip contact problems (Sulsky et al., 1994). However, extension into slip contact problems with MPM has also be introduced by many authors e.g. Bardenhagen et al. (2000), Huang et al. (2011), and Chen et al. (2017). In this work, a slip contact algorithm is adopted to address frictional contact problems involving brittle fracture as described in Sections 6 and 7.

- Coupling with other methods easily. Due to its particle in cell formulation, the method can be coupled with both mesh-based and particle-based methods. For example, MPM can be coupled with FEM to eliminate mesh distrortion at crucial regions, i.e., contact surfaces, see, e.g., (Lian et al., 2011).

  In addition, MPM can also be coupled with e.g. molecular dynamics simulation to accelerate the numerical procedure (Lu et al., 2006). Molecular Dynamics simulations are limited to nano scales due to their extremely

high computational demands. In contrast, the MPM which is a continuum approach method can be used from nano to macro scales. Hence, a potential coupling of continuum and atomistic approaches will assist the research community to examine and link the nano with macro material properties. The use of material points in the MPM provides a natural connection with the atoms in molecular dynamics. Material points are scaled down to the atomistic level so that they can be directly coupled with the atoms.

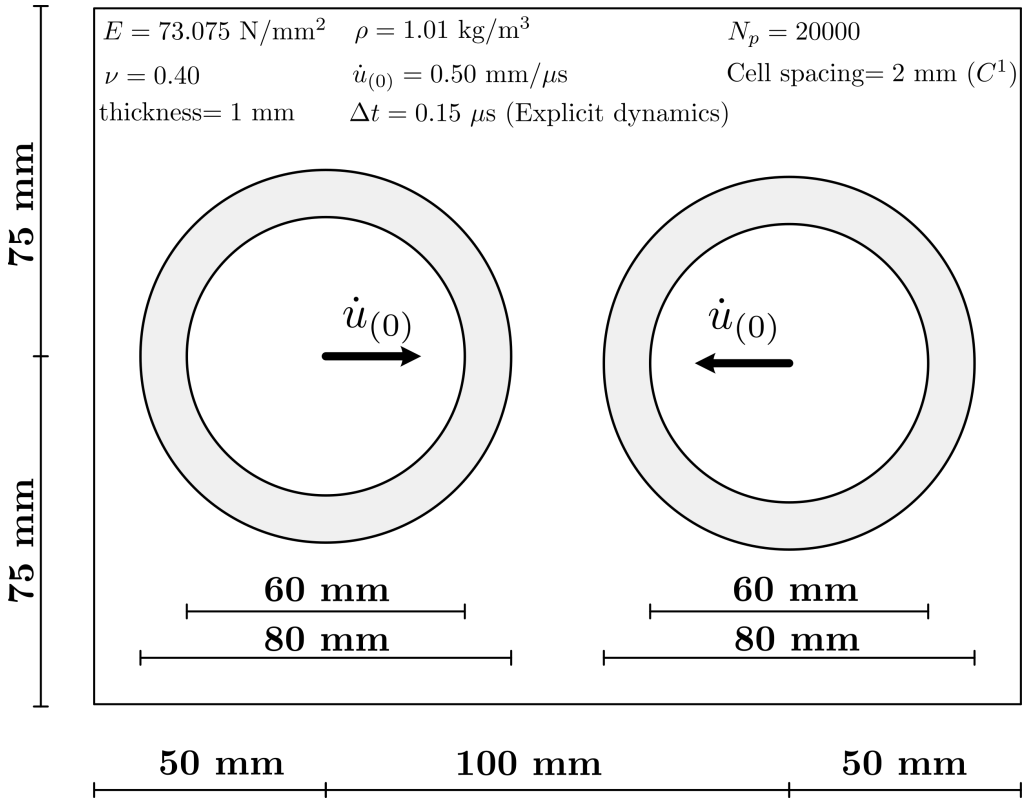

Figure 3.17: Impact of two elastic rings (MPM): Geometry and boundary conditions.

3.9.10.2 Disadvantages

The main disadvantages of MPM are summarized below:

- Mapping onto the Eulerian grid. The main disadvantage of MPM is the

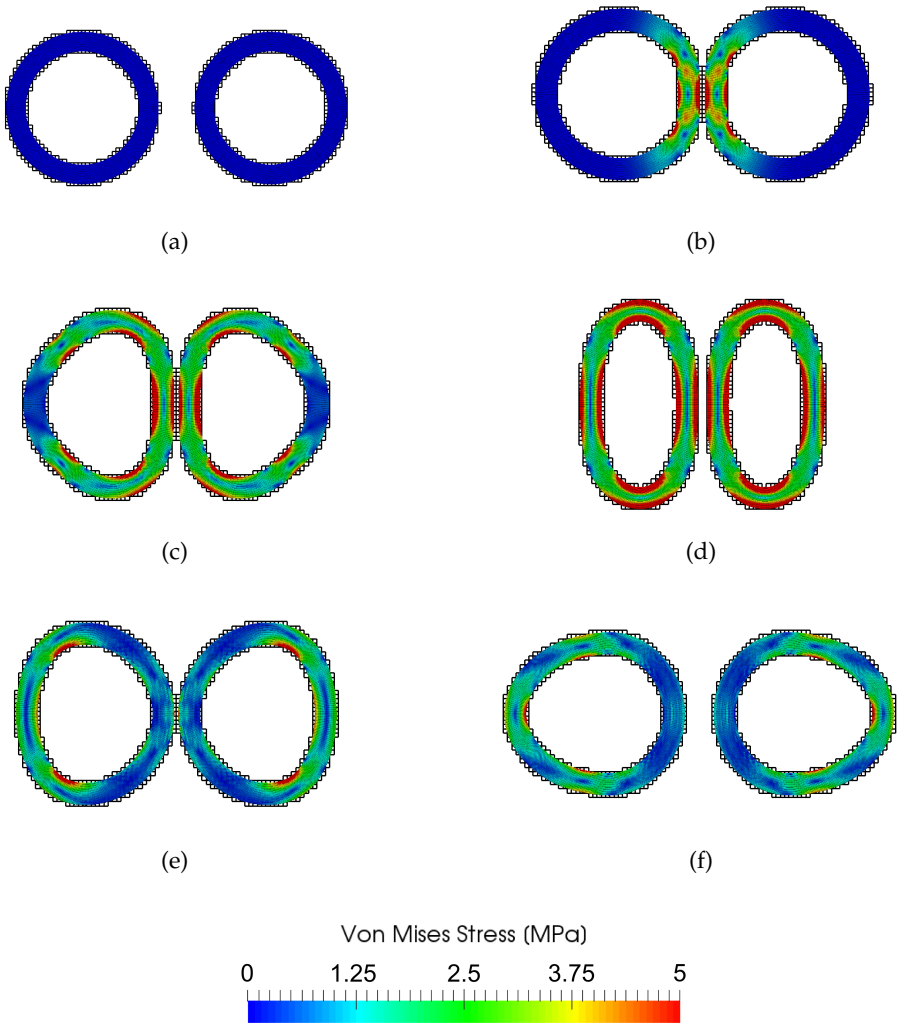

Figure 3.18: Impact of two elastic rings (MPM): Snapshots at time steps (a) $t = 0$ μs (b) $t = 4.5$ μs (c) $t = 7.5$ μs (d) $t = 14.25$ μs (e) $t = 24$ μs and (f) $t = 28.5$ μs.

extra computational cost due to mapping from material points to computational grid and vice versa. However, the computational cost can be eliminated using a parallel implementation of MPM.

- Grid crossing error (see Section 3.9.8).

- Particle density. The migration of material points from cell to cell results in solution procedure stability problems if inadequate particle density exists in a cell (Guilkey and Weiss, 2003; Coombs et al., 2018). Material points are not always located in optimal positions of their parent cell. Thus, an increased particle density should be used for more accurate solutions.

3.9.11 MPM vs FEM

In this Section a comparison between MPM and the standard FEM is presented to demonstrate the main similarities and differences of the two methods. The geometry, boundary conditions and material parameters of the cantilever beam are represented in Fig. 3.19(a). The cell spacing is chosen to be $h = 0.02$ m with C^0 linear basis functions whereas the initial cell density is 3x3 $= 9$ material points per cell. A constant displacement increment $\Delta u = 0.001$ m is applied on the free edge of the beam for 80 time increments. The load history is shown in Fig. 3.19(b).

The load displacement curve of the two methods is represented in 3.19(c) where the two methods illustrate excellent agreement. A comparison is also performed in MPM between the explicit computation of tangent stiffness matrix (see Eq. (3.59)) and the GMRES algorithm minimizing the residual vector of Eq. (3.55). The GMRES algorithm is implemented without preconditioning and zero initial guess at each time step. The two solutions are identical. Yet, the computational time is approximately less then 1 minute with the direct solver and approximately 20 minutes with the GMRES algorithm.

As already mentioned in Section 3.9.7, GMRES algorithm can effectively deal with extremely large problems and complex stress-strain relations because (a) it requires less storage requirements than direct solvers and (b) complicated constitutive matrices are never computed. However, the algorithm is computational taxing in comparison to direct solvers as illustrated in this benchmark problem. Hence, for the problems examined in this work, a direct solver is adopted to accelerate the numerical procedure.

The main differences between the FEM and the MPM are demonstrated in Fig. 3.20. Fig. 3.20(a), 3.20(c) and 3.20(e) correspond to the FEM results while 3.20(b), 3.20(d) and 3.20(f) are are referred to MPM simulation. In Fig. 3.20, it is obvious that the number of nodes, degree of freedom and elements are not constant in MPM as a result of the fixed Eulerian grid. However, the number of (Lagrangian) material points, that are used as integration points of their parent cell, are constant. This is in contrast to FEM where the number of nodes, degrees of freedom, elements and integration points remain constant throughout the analysis. The Eulerian grid is also constantly updated according to the material point footprints as described in Section 3.9.4.1 and Fig. 3.9 and 3.10.

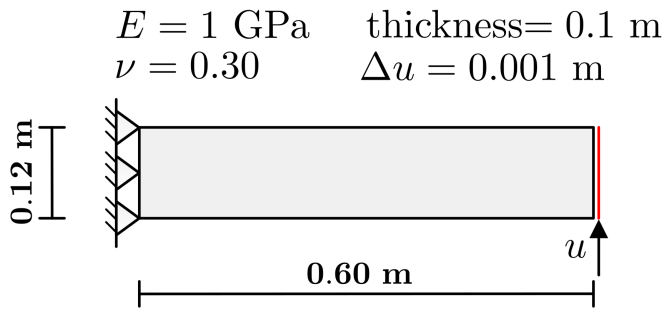

(a)

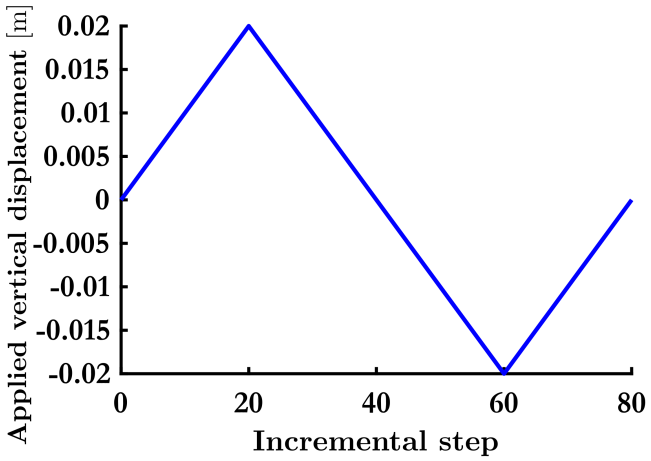

(b)

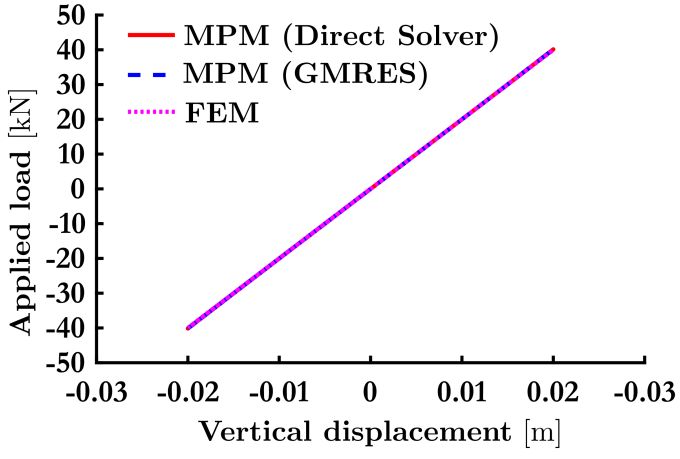

(c)

Figure 3.19: FEM vs MPM: (a) Geometry and boundary conditions (b) applied vertical displacement (c) Load-Displacement curve. Comparison between Finite Element Method and Material Point Method (Direct Solver and GMRES algorithm).

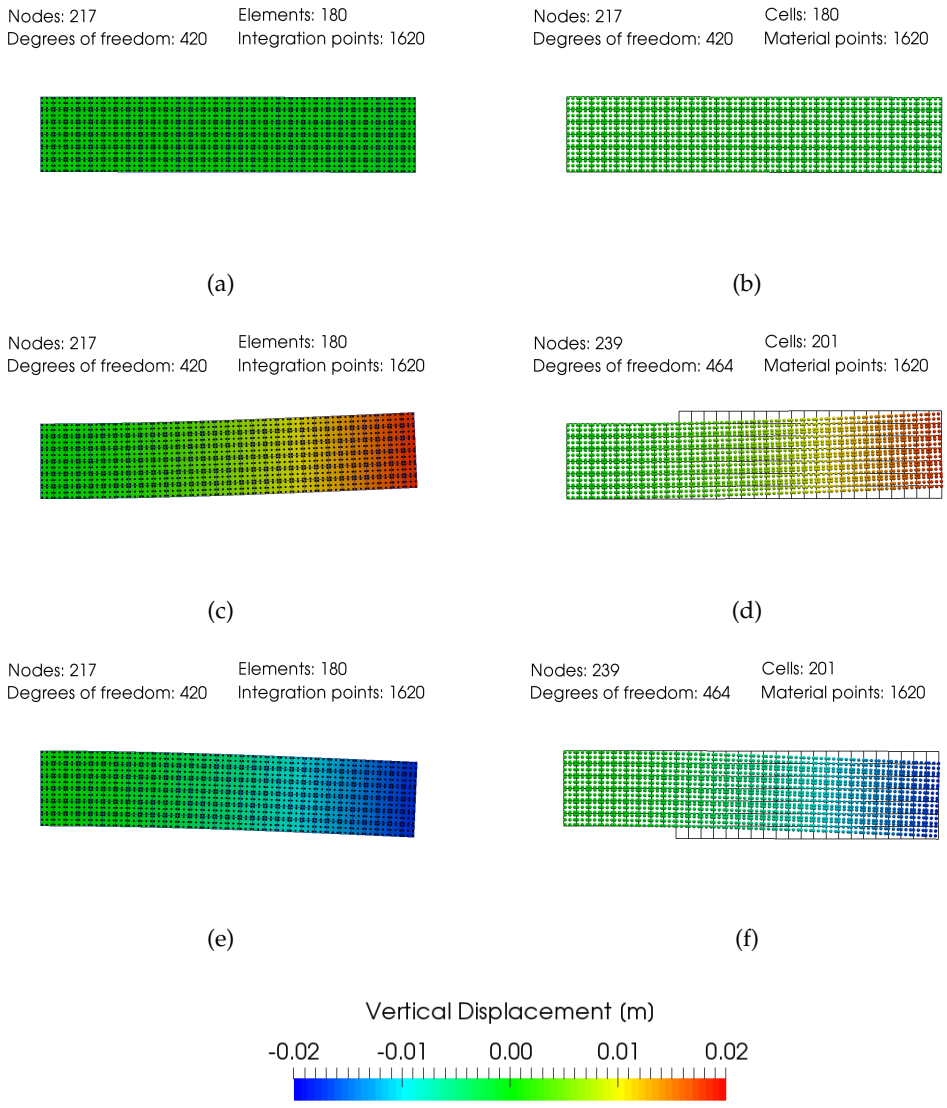

Figure 3.20: MPM vs FEM: FEM for (a) $u = 0$ m (c) $u = 0.02$ m and (e) $u = -0.02$ m. MPM for (b) $u = 0$ m (d) $u = 0.02$ m and (f) $u = -0.02$ m.

Chapter 4

Phase Field Material Point Method for brittle fracture

Part of this chapter is published in the International Journal for Numerical Method in Engineering (Kakouris and Triantafyllou, 2017).

4.1 Introduction

Employing a method where material behaviour is monitored at material points that move within a fixed Eulerian grid renders itself appealing for fracture propagation problems since in principle (a) the transition from continuous to discontinuous displacement field can be modelled without the need for remeshing the computational grid and (b) without special treatment of mesh distortion pertinent to an advancing crack. Despite this, little research has been conducted to model the problem of damage modelling and in particular crack growth using the MPM.

Nairn (2003), first, simulated simple types of fracture and cracking paths in the MPM developing a method called CRAMP (CRAcks with Material Points). This method introduces massless material points to transfer the information of the

crack path into grid nodes as well as multiple velocity fields at grid nodes near the crack to account for crack opening.

Variants of the MPM based on cohesive theories have also been introduced by Daphalapurkar et al. (2007) and Bardenhagen et al. (2011) where however crack propagation occurred in either a predefined weak plane or through dynamically adding cohesive zones to the fracture path.

A MPM with enriched shape functions has been recently introduced by Liang et al. (2017). Although this XFEM driven approach does not require the definition of multiple velocity fields, the background cell basis functions need to be enriched hence introducing additional assumptions pertinent to the type of tip enrichment utilized.

Continuum damage-based MPM approaches have been introduced by Nairn et al. (2017) and Homel and Herbold (2017). The former work is implemented in the realm of anisotropic damage mechanics whereas the latter demonstrates the merits of MPM in dynamic fracture and frictional contact problems.

The aforementioned approaches demonstrated the merits of MPM in simulating damage in terms of computational simplicity in particular when considering the case of large deformations and contact-fracture related problems. Further to the current state of the art, phase field modelling for brittle fracture is introduced in this Section within a MPM setting to address the general problem of quasi-static crack propagation in brittle materials using the MPM.

By introducing phase fields at the material point level rather than the nodal points of a fixed Lagrangian grid, the proposed method succeeds in monitoring crack initiation and growth in an efficient and robust manner. Numerical investigations demonstrate that compared to the standard Phase Field Finite Element implementation, the proposed method is advantageous in terms of accuracy. A staggered strategy is used for the solution of the governing coupled equations of the problem.

4.2 Discrete equations

PF-MPM approximation is based on the discretization of a deformable domain Ω with a set of material points move through a fixed Eulerian grid where the governing coupled phase field and equilibrium equation are solved. The PF-MPM approximation of a deformable body Ω with a crack path Γ is shown in Fig 4.1. According to this approximation, the governing equations of PF-MPM are introduced in Sections 4.2.1 and 4.2.2.

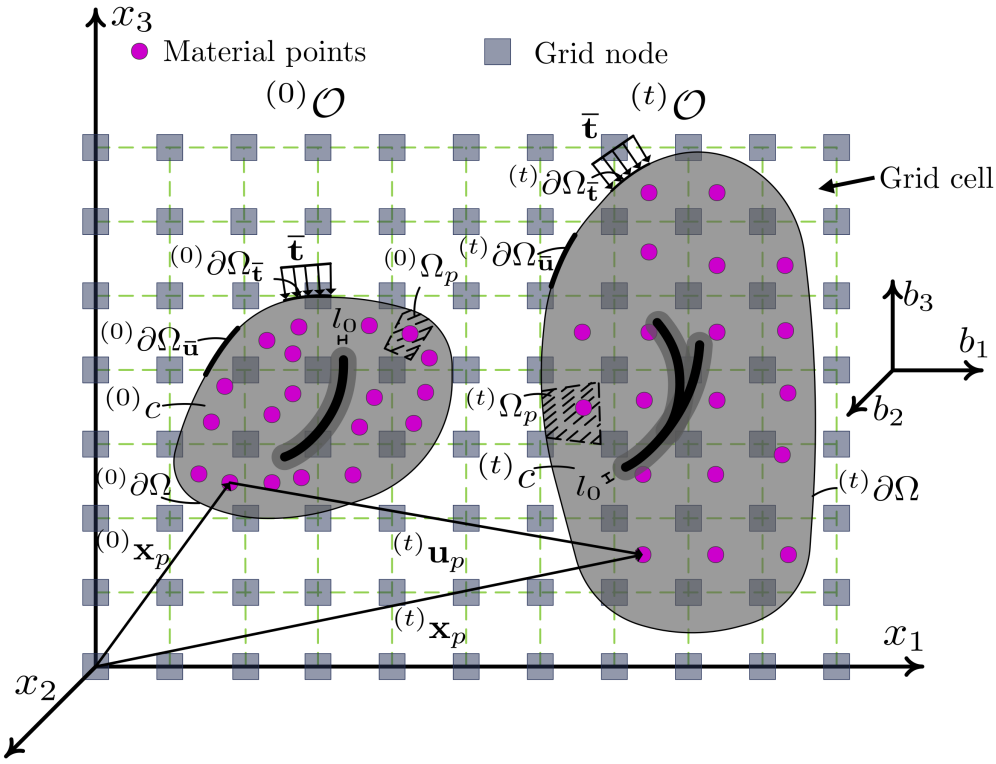

Figure 4.1: Deformation process: Phase Field Material Point Method approximation of the crack path Γ.

4.2.1 Equilibrium discrete equations

In this Chapter only quasi-static problems are considered. Therefore, the equilibrium discrete equations introduced in Section 3.9.4.2 reduce to relation (4.1) below

$$\mathbf{R}_I^u(\mathbf{u}) = \mathbf{F}_I^{int} - \mathbf{F}_I^{ext} = 0, \quad I = 1\ldots, N_n \tag{4.1}$$

or in compact form as

$$\mathbf{K}^u\mathbf{u} = \mathbf{F}^{ext} \tag{4.2}$$

where $\mathbf{K}^u$ is the global stiffness matrix of the structure whose $K^u_{I,J,i,j}$ component is expressed from relation (3.59). The constitutive matrix $\mathbf{D}_p$, evaluated at p^{th} material point, is readily evaluated from Eq. (2.51).

4.2.2 Phase field discrete equations

The weak form of the phase field governing equation assumes the following form

$$\int_\Omega \Big(\frac{4l_0(1-k_f)\mathcal{H}}{\mathcal{G}_c} + 1\Big) cq\, d\Omega + \int_\Omega 4l_0^2(\nabla c : \nabla q)\, d\Omega = \int_\Omega q\, d\Omega \tag{4.3}$$

where c is the phase field and q are the corresponding weighting functions for the phase field. The phase field c and the corresponding weighting functions q are defined with respect to the following spaces, i.e.,

$$\mathcal{Y} = \{c \in H^1(\Omega)\}$$

and

$$\mathcal{Q} = \{q \in H^1(\Omega)\}.$$

The continuous phase field and the corresponding weighting functions introduced in equation (4.3) are collocated at material points, resulting in the following discrete form (4.4)

$$\sum_{p=1}^{N_p} \mathcal{F}_p c_p q_p \Omega_p + \sum_{p=1}^{N_p} 4l_{0_p}^2(\nabla c_p : \nabla q_p)\Omega_p = \sum_{p=1}^{N_p} q_p \Omega_p \tag{4.4}$$

where c_p and q_p are values of the the phase field and weighting functions, respectively at the material point p. $\mathcal{F}_p$ is defined as

$$\mathcal{F}_p = \frac{4l_{0_p}(1-k_{f_p})\mathcal{H}_p}{\mathcal{G}_{c_p}} + 1 \tag{4.5}$$

where l_{0_p}, k_{f_p}, $\mathcal{H}_p$ and $\mathcal{G}_{c_p}$ are the length scale parameter, model parameter, history field and critical fracture energy density of material point $\mathbf{x}_p$, respectively.

Next, both c_p and q_p and interpolated at the nodal points of the background mesh. The value of the test function and its spatial derivatives at the p^{th} material point are expressed as

$$q_p = \sum_{I=1}^{N_n} N_I(\mathbf{x}_p) q_I \tag{4.6}$$

and

$$\nabla q_p = \sum_{I=1}^{N_n} \nabla N_I(\mathbf{x}_p) q_I, \tag{4.7}$$

respectively, where $N_I(\mathbf{x}_p)$ are the background mesh shape functions pertinent to the phase field interpolation and q_I are nodal values of the corresponding test functions.

The value of the phase field at the p^{th} material point is written as

$$c_p = \sum_{I=1}^{N_n} N_I(\mathbf{x}_p) c_I \tag{4.8}$$

where c_I are the phase field nodal values. Attention is drawn to the fact that the phase field is a scalar quantity. It follows from relation (4.8) that the gradients of the the phase field at the p^{th} material point are defined accordingly as

$$\nabla c_p = \sum_{I=1}^{N_n} \nabla N_I(\mathbf{x}_p) c_I. \tag{4.9}$$

Similar shape functions are considered for both the phase field and the corresponding weighting functions according to the Galerkin approximation (Bathe,

2007). In this work, the same family of interpolation functions is considered for both the displacement and the phase field (see also Miehe et al. (2010a)).

Substituting equations (4.6) and (4.7) in relation (4.4) and re-arranging terms, the following expression is derived

$$\sum_{I=1}^{N_n} q_I \cdot [S_I^c - F_I^c] = 0 \tag{4.10}$$

where in equation (4.10) above

$$S_I^c = \sum_{p=1}^{N_p} \mathcal{F}_p c_p N_I(\mathbf{x}_p)\Omega_p + \sum_{p=1}^{N_p} 4l_{0_p}^2(\nabla c_p \cdot \nabla N_I(\mathbf{x}_p))\Omega_p \tag{4.11}$$

and

$$F_I^c = \sum_{p=1}^{N_p} N_I(\mathbf{x}_p)\Omega_p, \tag{4.12}$$

respectively. Since the choice of the weighting functions is arbitrary, it must hold that

$$R_I^c(c) = S_I^c - F_I^c = 0, \quad I = 1\ldots, N_n \tag{4.13}$$

where $R_I^c(c)$ are the residual nodal values for the phase field. By substituting relations (4.11) and (4.12) into equation (4.13) results in

$$\sum_{p=1}^{N_p} \mathcal{F}_p c_p N_I(\mathbf{x}_p)\Omega_p + \sum_{p=1}^{N_p} 4l_{0_p}^2(\nabla c_p \cdot \nabla N_I(\mathbf{x}_p))\Omega_p = \sum_{p=1}^{N_p} N_I(\mathbf{x}_p)\Omega_p, \quad I = 1\ldots, N_n. \tag{4.14}$$

Further considering the phase field interpolation schemes defined in equations

(4.8) and (4.9), and substituting in equation (4.14), the following relation is established

$$\sum_{p=1}^{N_p} \mathcal{F}_p \left(\sum_{J=1}^{N_n} N_J(\mathbf{x}_p) c_J \right) N_I(\mathbf{x}_p) \Omega_p + \sum_{p=1}^{N_p} 4 l_{0_p}^2 \left(\left(\sum_{J=1}^{N_n} \nabla N_J(\mathbf{x}_p) c_J \right) \cdot \nabla N_I(\mathbf{x}_p) \right) \Omega_p = \sum_{p=1}^{N_p} N_I(\mathbf{x}_p) \Omega_p. \tag{4.15}$$

Re-arranging and collecting terms, equation (4.15) gives rise to the following convenient form

$$\mathbf{K}^c \mathbf{c} = \mathbf{F}^c \tag{4.16}$$

where $\mathbf{K}^c$ is an $(N_n \times N_n)$ coefficient matrix whose $K^c_{I,J}$ component is defined as

$$K^c_{I,J} = \sum_{p=1}^{N_p} \left(\mathcal{F}_p N_J(\mathbf{x}_p) N_I(\mathbf{x}_p) + 4 l_{0_p}^2 \Big(\nabla N_J(\mathbf{x}_p) \cdot \nabla N_I(\mathbf{x}_p) \Big) \right) \Omega_p \tag{4.17}$$

while $\mathbf{c}$ is the $(N_n \times 1)$ vector of unknown nodal phase fields and $\mathbf{F}^c$ is the $(N_n \times 1)$ vector whose F^c_I component is defined from relation (4.12).

The vector quantity $\mathbf{F}^c$ will be termed herein as the phase field "forcing" term. Similarly to the MPM displacement based equilibrium equations defined in Section 4.2.1, equation (4.16) is established and solved at the nodal points of the background mesh with the corresponding material point to background node mapping performed in equations (4.11) and (4.12).

4.3 Phase field MPM solution scheme

The coupled equilibrium and phase field evolution equations can be solved in a so called monolithic fashion, i.e., simultaneously within each incremental step. However, it has been demonstrated that a staggered solution approach (see also,

Simo and Miehe (1992) for the case of thermo-mechanical coupling) can be utilized where the phase field equations are solved independently and the resulting phase field prediction is then used to iteratively solve for the equilibrium equations (Miehe et al., 2010a). In this work, a staggered solution procedure has been implemented and the corresponding computational scheme is presented in Algorithm 1 (see page 104).

With regards to Algorithm 1, E_p, ν_p and g_p refer to the Young's modulus, Poisson's ratio and degradation function of the p^{th} material point. Pre-existing cracks can be modelled by defining an initial history field ($\mathcal{H}_{p_0}$) in all material points around the crack similar to Borden et al. (2012). Alternately, pre-existing cracks can also be introduced as discrete cracks in the geometry of the structure.

A displacement control incremental analysis procedure is implemented in this Section for the solution of the quasi-static brittle fracture problem, considering a set of N_{steps} incremental steps. In the beginning of each time step m, the active cells of the Eulerian grid are identified according to the material point positions and the inactive cells are discarded (Fig. 3.9 and 3.10). Next, the total number of grid nodes as well as grid degree of freedom are redefined according to total active grid nodes (N_n) and total active unconstrained grid degree of freedom (N_{dofs}). Furthermore, the basis functions $(\mathbf{N}(\mathbf{x}_p))$ as well as their derivatives $(\nabla\mathbf{N}(\mathbf{x}_p))$ at all material points need to be evaluated at each time step m. This is one of the main differences between FEM and MPM as in the former the number of nodes, degree of freedom, cells (N_{cells}) as well as basis functions and their derivatives remain constant during the analysis.

Following, the staggered iterative scheme $(k = 1, 2, \ldots, N_{staggs})$ initiates within the current incremental step. The phase field equations are solved for the current value of the history field $\mathcal{H}$ and the phase field nodal values c_I are derived. Using this phase field prediction, updated values for the degradation function at each material point g_p are derived and the displacement field equations are iteratively solved in the inner iterative loop $(j = 1, 2, \ldots, N_{iters})$. From this, the

incremental displacement field nodal values $\mathbf{\Delta u}_I$ are obtained.

The displacement field equations (4.1) are solved by incrementally applying the external forces $\mathbf{\Delta F}_I^{ext}$ to obtain the increments of the displacement field $\mathbf{\Delta u}$. and the following equations are solved using a Newton-Raphson method (inner iterations $j = 1, .., N_{iters}$).

$$\delta \mathbf{R}_I^u(\mathbf{\Delta u}) = \mathbf{\Delta F}_I^{int} - \mathbf{\Delta F}_I^{ext} = \mathbf{0}, \quad I = 1 \ldots, N_n \tag{4.18}$$

where the symbol $\mathbf{\Delta}$ denotes incremental quantities e.g. $\mathbf{\Delta X} = {}^{(m)}\mathbf{\Delta X} - {}^{(m-1)}\mathbf{\Delta X}$, whereas the symbol δ denotes iterative quantities e.g. $\delta \mathbf{X} = \mathbf{X}^{(j)} - \mathbf{X}^{(j-1)}$.

Convergence of the equilibrium equation iterative procedure is achieved when the Euclidean norm of the residual force vector introduced in equation (4.18) assumes a sufficiently small value, i.e., when $\|\delta \mathbf{R}^{u(j)}\| \leq tol_u$. Upon convergence, updated values for the history field $\mathcal{H}$ are evaluated and the residual of the phase field equation is established as the difference between the initial phase field forcing term estimate and the updated one. Outer, phase field iterations terminate when $\| {}^{(m)}\mathbf{R}^{c(k)} \leq tol_c \|$ where tol_c is a predefined tolerance. Although robust, the staggered until convergence scheme is prone to low convergence rates and practically bounds the maximum allowable incremental displacement step in a displacement controlled analysis. Very recently, a line-search assisted iterative scheme has been developed to treat such issues and further improve the convergence speed of the method (Gerasimov and De Lorenzis, 2016).

4.4 Numerical examples

In this Section the proposed method is compared against the Finite Element phase field implementation through a set of representative tests both in terms

Data: Define computational grid, material point properties (${}^{(0)}\mathbf{x}_p$, ${}^{(0)}\Omega_p$, E_p, ν_p, l_{0_p}, k_{f_p} , $\mathcal{G}_{c_p}$, ${}^{(0)}\mathcal{H}_p$, ${}^{(0)}\boldsymbol{\sigma}_p$, ${}^{(0)}\boldsymbol{\varepsilon}_p$)

for *each time step* $m = 1, 2, .., N_{steps}$ **do**

Reset the computational grid: Find active part of Eulerian Grid, N_n, N_{dofs}, N_{cells};

Compute: $\mathbf{N}({}^{(m)}\mathbf{x}_p)$, $\nabla\mathbf{N}({}^{(m)}\mathbf{x}_p)$ and $\mathbf{B}({}^{(m)}\mathbf{x}_p)$, for all material points (see Section 3.9.9 and Eq. (3.54)). ;

Define: $\delta\mathbf{R}^{u(1)} = \boldsymbol{\Delta}\mathbf{F}^{ext}$;

for *each staggered iteration* $k = 1, 2, .., N_{staggs}$ **do**

Compute: ${}^{(m)}\mathbf{F}^{c(k)}$ (see Eq. (4.12)). ;

Compute: $\mathbf{K}^c$ (see Eq. (4.17)). ;

Solve: $\mathbf{K}^c\,{}^{(m)}\mathbf{c}^{(k)} = {}^{(m)}\mathbf{F}^{c(k)}$;

Map phase field (${}^{(m)}\mathbf{c}^{(k)}$) from grid nodes to material points. Evaluate: ${}^{(m)}c_p^{(k)}$, ${}^{(m)}\nabla c_p^{(k)}$, ${}^{(m)}g_p^{(k)}$, for all material points (see Eq. (4.8), (4.9) and (2.48)). ;

Initialize $\boldsymbol{\Delta}\mathbf{u}^{(0)} = \mathbf{0}$;

for *each inner iteration* $j = 1, 2, .., N_{iters}$ **do**

Compute: $\mathbf{K}^u$ (see Eq. (3.59), for constitutive matrix see Eq. (2.51)) ;

Solve: $\mathbf{K}^u\delta\mathbf{u}^{(j)} = \delta\mathbf{R}^{u(j)}$, with displacement control. ;

Compute: $\boldsymbol{\Delta}\mathbf{u}^{(j)} = \boldsymbol{\Delta}\mathbf{u}^{(j-1)} + \delta\mathbf{u}^{(j)}$;

Compute: $\boldsymbol{\Delta}\boldsymbol{\varepsilon}_p^{(j)}$, for all material points (see Eq. (3.56)). ;

Compute: ${}^{(m)}\boldsymbol{\varepsilon}_p^{(j)} = {}^{(m-1)}\boldsymbol{\varepsilon}_p^{(j)} + \boldsymbol{\Delta}\boldsymbol{\varepsilon}_p^{(j)}$, for all material points. ;

Compute: ${}^{(m)}\boldsymbol{\sigma}_p^{(j)}$, for all material points (see Eq. (2.50)) ;

Compute: $\boldsymbol{\Delta}\mathbf{F}^{int(j)} = \{\boldsymbol{\Delta}\mathbf{F}_I^{int}\}$, $\boldsymbol{\Delta}\mathbf{F}_I^{int} = \sum_{p=1}^{N_p} {}^{(m)}\Omega_p^{(j)}\,{}^{(m)}\boldsymbol{\sigma}_p^{(j)} - {}^{(m-1)}\boldsymbol{\sigma}_p^{(j)} \cdot \mathbf{B}_I({}^{(m)}\mathbf{x}_p)$;

Compute Residual (Displacement-Field): $\delta\mathbf{R}^{u(j)} = \boldsymbol{\Delta}\mathbf{F}^{ext} - \boldsymbol{\Delta}\mathbf{F}^{int(j)}$;

Convergence Check (Displacement Field): If $\|\delta\mathbf{R}^{u(j)}\| \leq tol_u$ or $j \geq N_{iters}$ then "exit" from loop else $j = j + 1$ go to next inner iteration. ;

end

Compute: ${}^{(m)}\psi_{el_p}^{+}$, for all material points (see Eq. (2.77))

$$\rightarrow {}^{(m)}\mathcal{H}_p = \begin{cases} {}^{(m)}\psi_{el_p}^{+}, & \text{for } {}^{(m)}\psi_{el_p}^{+} > {}^{(m-1)}\mathcal{H}_p \\ {}^{(m-1)}\mathcal{H}_p, & \text{otherwise} \end{cases} ;$$

Compute Residual (Phase Field): ${}^{(m)}\mathbf{R}^{c(k)}$ (see Eq. (4.13)) according to ${}^{(m)}c_p^{(k)}$, ${}^{(m)}\nabla c_p^{(k)}$, ${}^{(m)}\mathcal{H}_p$;

Convergence Check (Phase Field): If $\|\,{}^{(m)}\mathbf{R}^{c(k)}\| \leq tol_c$ or $k \geq N_{staggs}$ then "exit" from loop else $k = k + 1$ go to next staggered iteration. ;

end

Compute: $\boldsymbol{\Delta}\mathbf{u}_p = \sum_{I=1}^{N_n} N_I({}^{(m)}\mathbf{x}_p)\boldsymbol{\Delta}\mathbf{u}_I^{(j)}$, for all material points. ;

Compute: ${}^{(m)}\mathbf{u}_p = {}^{(m-1)}\mathbf{u}_p + \boldsymbol{\Delta}\mathbf{u}_p$, for all material points. ;

Compute: ${}^{(m)}\mathbf{x}_p = {}^{(m-1)}\mathbf{x}_p + \boldsymbol{\Delta}\mathbf{u}_p$, for all material points. ;

end

Algorithm 1: Phase Field Material Point Method pseudo-code (Staggered Solution Algorithm).

of accuracy and computational efficiency. In all cases external loads are directly applied at material points. Kinematical constraints are imposed by means of the Penalty Method (Bathe, 2007). As these constraints are imposed on the material points rather than the background grid, the corresponding numerical implementation is presented in Appendix A. This is contrary to the Finite Element implementation where essential boundary conditions are imposed directly on the domain boundary. However, as shown from the actual verification results provided this does not affect the accuracy of the method. The density of material points utilized as necessitated by the fracture propagation problem ensures that material points are sufficiently close to the actual domain boundary where displacement variations can be considered negligible.

For the purpose of verification both the Phase Field Material Point Method (PF-MPM) and Phase Field Finite Element Method (PF-FEM) have been implemented in Fortran code. In all examples considered herein, the staggered until convergence solution strategy (Algorithm 1) was adopted. The phase field residual tolerance was set at $tol_c = 1.0e-6$. Simulation parameters, i.e., number of incremental steps, convergence tolerance and maximum number of iterations are similar for both schemes as defined in the corresponding Sections below. All tests were performed on a PC fitted with an Intel Xeon E5-1620 CPU and 32 GB of RAM.

4.4.1 Single edge-notched tension test

In this example a square plate under pure tension is examined and results are compared to the standard PF-FEM. The purpose of this example is to examine the accuracy of the proposed PF-MPM using as a reference the standard PF-FEM and published results in the literature. A discussion of the corresponding computational costs is also provided. The geometric configuration, boundary conditions and material parameters considered are presented in Fig. 4.2.

The square plate consists of 249000 material points. The Eulerian grid is formulated by 67600 (260 x 260) 4-node isoparametric quadrilateral elements with a uniform mesh size equal to $h = 0.004$ mm. Element size of the background mesh is defined such that $h < l_0$. The overall dimensions of the Eulerian grid are 1.04 mm x 1.04 mm ($x_{min} = y_{min} = -0.02$ mm , $x_{max} = y_{max} = 1.02$ mm). Material points are initially located at the Gauss point position of their corresponding parent cells and plane strain conditions are assumed.

For the PF-FEM case, the corresponding Finite Element mesh comprises 62250 4-node quadrilateral plane strain elements with bi-linear basis functions. Full integration is considered in each element with 4 Gauss points.

The material parameters considered are $E = 210$ kN/mm^2, $\nu = 0.30$, $l_0 = 0.0075$ mm and $\mathcal{G}_c = 0.0027$ kN/mm for the Young's modulus, Poisson's ratio ratio, length scale and fracture energy density, respectively. Zero displacement boundary conditions, i.e., $u_{p_x} = u_{p_y} = 0$, are imposed in all material points (nodes in the PF-FEM case) on the bottom edge of the specimen.

Both in the PF-MPM and PF-FEM implementations, a displacement control nonlinear static analysis scheme is utilized with a constant displacement increment $\Delta u = 10^{-6}$ mm. Displacement is monitored and controlled in the upper edge of the specimen where the vertical displacements of all material points (nodes in the PF-FEM cases) are kinematically constrained. The kinematic constraint penalty parameter (see Appendix A) was chosen to be $\alpha = 10000000$. The solution is implemented within a stagger solution algorithm with a single prediction step ($N_{staggs} = 1$) and $tol_u = 10^{-5}$.

The load paths derived from both PF-MPM and PF-FEM are presented in Fig. 4.3. The load paths are practically identical. Results obtained by both solution approaches also agree with the results provided in Miehe et al. (2010a). In particular, the critical vertical displacement and critical load obtained by PF-FEM are $u_{cr_{PF-FEM}} = 0.005626$ mm and $F_{cr_{PF-FEM}} = 0.7051$ kN, respectively.

The critical vertical displacement and critical load obtained by PF-MPM are $u_{cr_{PF-MPM}} = 0.005627$ mm and $F_{cr_{PF-MPM}} = 0.7052$ kN, respectively.

The results derived and the agreement between the two different approaches is justified by the fact that due to small displacements ($\approx 0.60\%$ of the total length of the plate), material points only marginally move from the Gauss points of the corresponding Finite Element mesh. The phase field distribution over the plate domain for both the FEM and MPM are presented in Fig. 4.4. The observed crack paths derived from both methods are identical.

Analysis time for PF-FEM was approximately 98 hrs whereas for PF-MPM 111 hrs. The increase in computational time due to the MPM implementation was of the order of 13% corresponding to the re-factorization of the stiffness matrix when material points move across background cells.

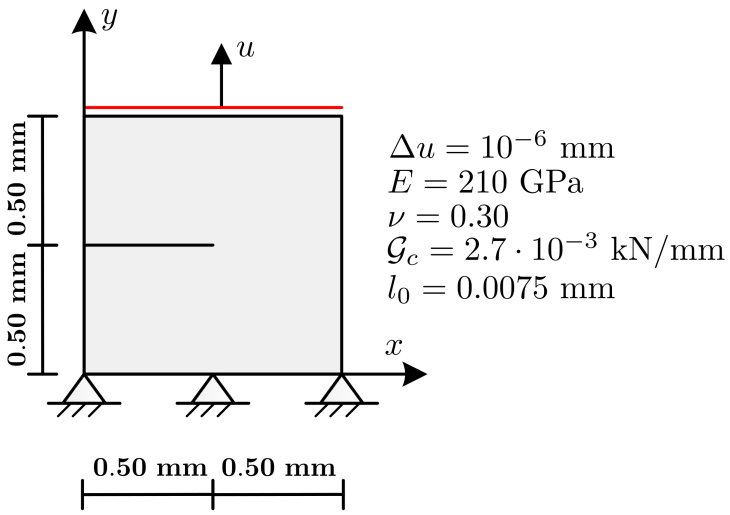

Figure 4.2: Tension test: Geometry and boundary conditions.

4.4.2 Single edge-notched shear test

In this case, the response of the square plate considered in Section 4.4.1 is investigated under pure shear conditions. The purpose of this example is to verify the PF-MPM against the PF-FEM in simulating mode II fracture (in-plane shear fracture). The same example has been previously examined in Miehe et al.

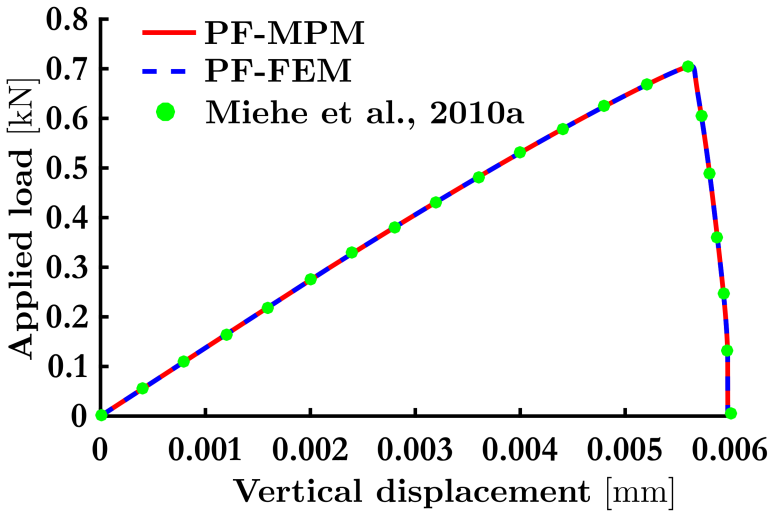

Figure 4.3: Tension test: Load-Displacement curve. Comparison between Material Point Method and Finite Element Method (FEM). Results obtained by Miehe et al. (2010a) are also presented.

(2010a) and Borden et al. (2012) considering a standard Finite Element scheme and its isogeometric formulation respectively.

The geometry, boundary conditions and material properties are shown in Fig. 4.5. The discretization of the Eulerian grid as well as the number of material points are the same as in the tension experiment of Section 4.4.1. Both in the PF-MPM and PF-FEM implementation the simulation is performed with a constant horizontal displacement increment $\Delta u = 10^{-5}$, mm monitored at the upper edge of the plate.

The load displacement curve is presented in Fig. 4.6. The results obtained by PF-MPM are compared to the results from PF-FEM. The latter have been derived considering a 40658 constant strain triangle Finite Element mesh and are in perfect agreement with the results reported in Miehe et al. (2010a). The critical horizontal displacement and critical load obtained by Finite Element Method are $u_{cr_{PF-FEM}} = 0.0087$ mm and $F_{cr_{PF-FEM}} = 0.5310$ kN, respectively; whereas the critical vertical displacement and critical load obtained by Material Point Method are $u_{cr_{PF-MPM}} = 0.0089$ mm and $F_{cr_{PF-MPM}} = 0.5416$ kN, respectively.

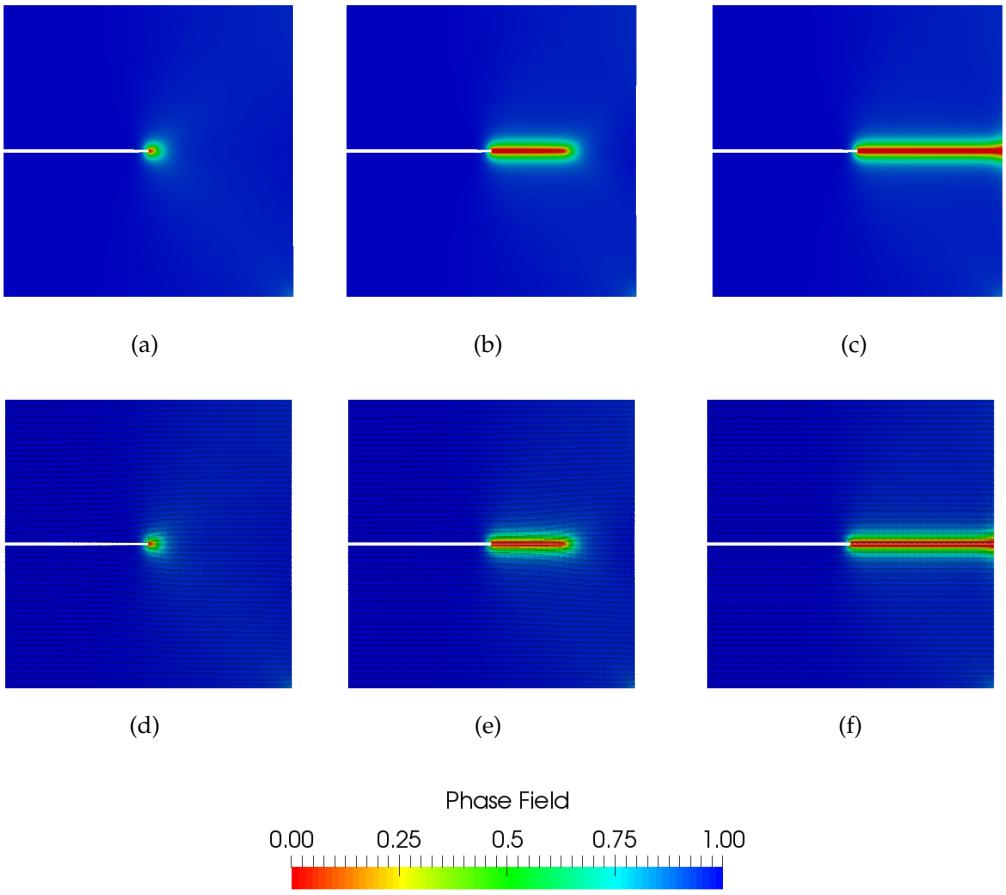

Figure 4.4: Phase Field in single-edge notched tension test with Finite Element Method for (a) $u = 0.0056$ mm, (b) $u = 0.0058$ mm and (c) $u = 0.0059$ mm, respectively. Phase Field in single-edge notched tension test with Material Point Method for (d) $u = 0.0056$ mm, (e) $u = 0.0058$ mm and (f) $u = 0.0059$ mm, respectively.

Fig. 4.7 illustrates the phase field of both FEM and MPM. The two methods illustrate good agreement in regards of the crack path with minor differences observed in the post-peak regime. These are attributed to the severe distortion of the triangular Finite Elements observed in the PF-FEM case which is however by definition avoided in the PF-MPM solution.

In particular, the distortion of the elements along the crack path is presented in Figs. 4.8(a)-(e). This is avoided in the MPM as shown in Fig. 4.8(b), 4.8(d) and 4.8(f) as the material points naturally follow the geometry of the crack. The evolution of the hydrostatic stress for the case of the Material Point implementation is shown in Fig. 4.9 for several time steps. Comparing Figs. 4.7(d)-(f) to Fig. 4.9 one is able to verify that the crack propagates only due to tension as a result of additive decomposition of the elastic energy introduced in equation (2.49). In Fig. 4.9, the positive values of the hydrostatic stress field highlight the areas under tension while the negative values the areas under compression. The computational times for PF-FEM and PF-MPM were approximately 23 hrs and 26 hrs, respectively resulting in an overhead of approximately 13%.

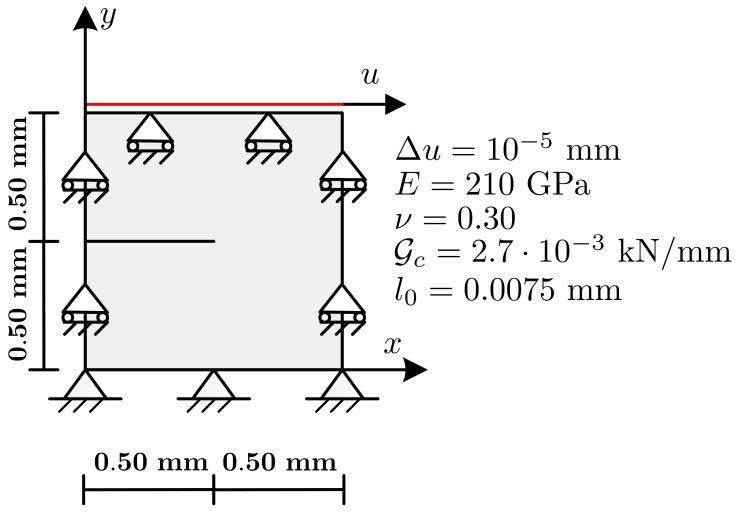

Figure 4.5: Shear test: Geometry and boundary conditions.

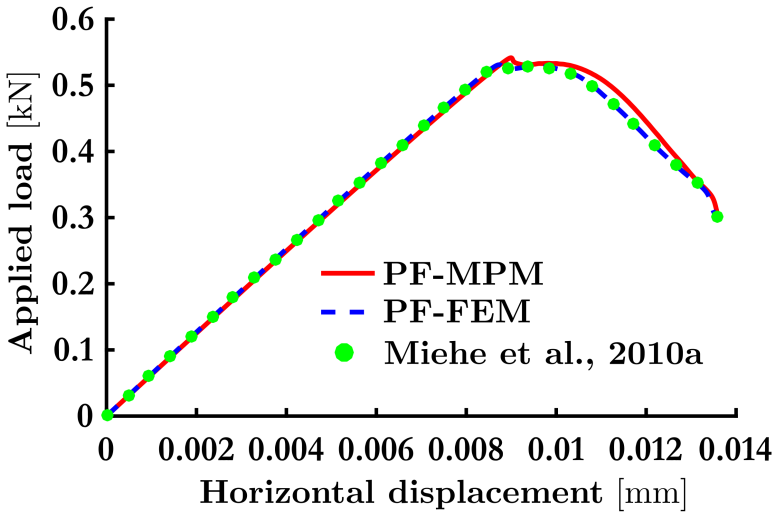

Figure 4.6: Shear test: Load-Displacement curve. Comparison between Material Point Method and Finite Element Method (FEM). Results obtained by Miehe et al. (2010a) are also presented.

4.4.3 L-Shaped panel test

In this example an L-Shaped concrete panel is examined under cyclic loading. In this example, a series of simulations is carried out to investigate the effect of the length scale parameter (l_0), cell spacing of the underlying Eulerian grid (h) and cell density on the accuracy of the PF-MPM scheme. Furthermore, the ability of the PF-MPM to model crack closure during uploading is demonstrated and validation against experimental observations is made. The efficiency of the PF-MPM to avoid any mesh distortion errors in crack propagation problems is illustrated where a comparison with the corresponding PF-FEM is made.

The geometry, boundary conditions and material properties are presented in Fig. 4.10. This example has also been considered in Ambati et al. (2015a) utilizing the phase field Finite Element scheme. In all simulations (both in the PF-MPM and PF-FEM implementation) a constant displacement increment $\Delta u = 10^{-3}$ mm is considered for 2000 time increments. The load history is shown in Fig. 4.11. The solution is implemented within a staggered solution algorithm for a single prediction step ($N_{staggs} = 1$) and $tol_u = 10^{-4}$. In all cases,

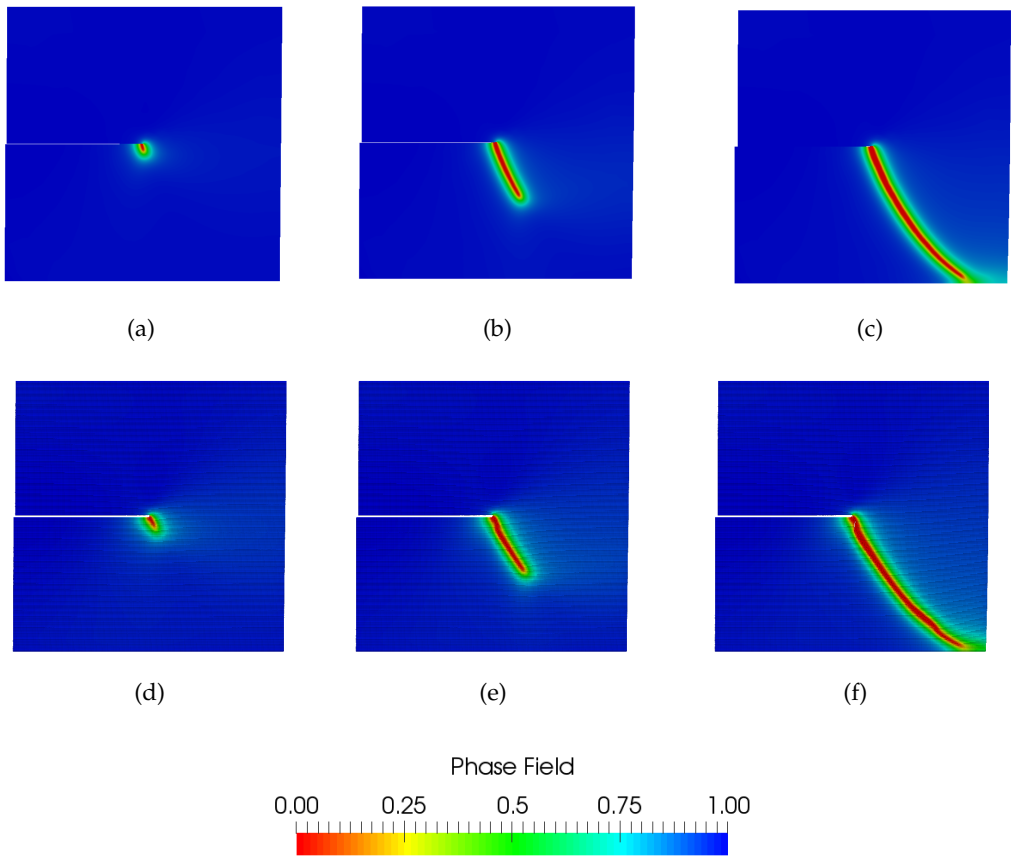

Figure 4.7: Phase Field in single-edge notched shear test with Finite Element Method for (a) $u = 0.009$ mm, (b) $u = 0.011$ mm and (c) $u = 0.0134$ mm, respectively. Phase Field in single-edge notched shear test with Material Point Method for (d) $u = 0.0092$ mm, (e) $u = 0.0117$ mm and (f) $u = 0.0136$ mm, respectively.

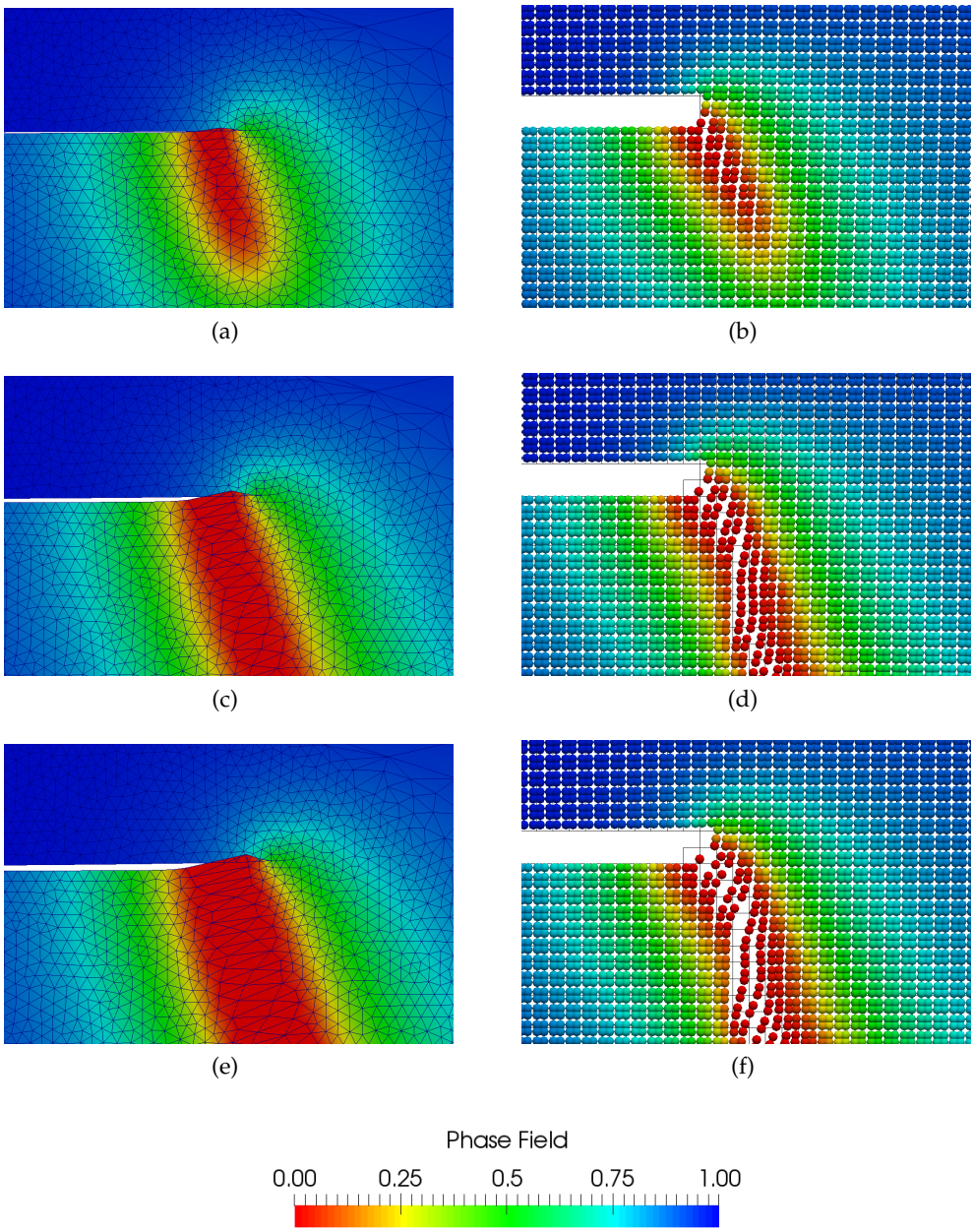

Figure 4.8: Distorted Elements in Finite Element Method (a) $u = 0.009$ mm, (c) $u = 0.011$ mm and (e) $u = 0.0134$ mm, respectively. No distortion in Material Point Method for (b) $u = 0.0092$ mm, (d) $u = 0.0117$ mm and (f) $u = 0.0136$ mm, respectively.

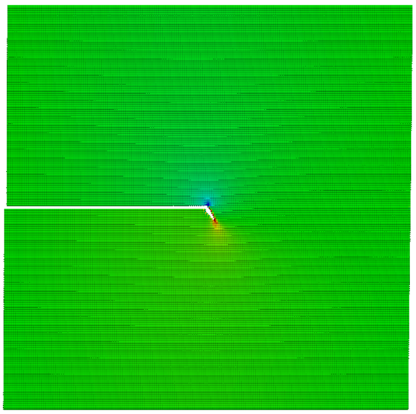

(a)

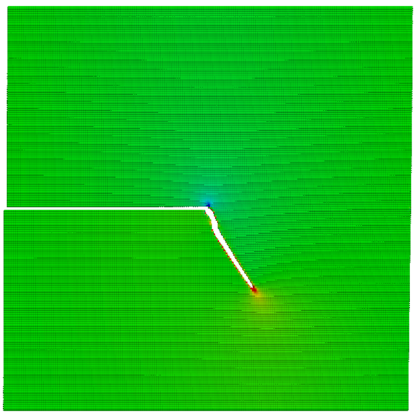

(b)

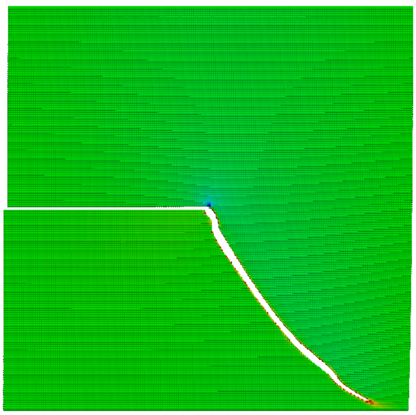

(c)

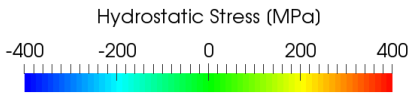

Figure 4.9: Hydrostatic Stress in single-edge notched shear test for (a) $u = 0.0092$ mm, (b) $u = 0.0177$ mm and (c) $u = 0.0136$ mm, respectively. Material Points with $c_p < 0.08$ have been removed.

the background grid is formulated using 4-node quadrilateral elements with bilinear basis functions. Plane stress conditions are assumed with a thickness $th = 100$ mm.

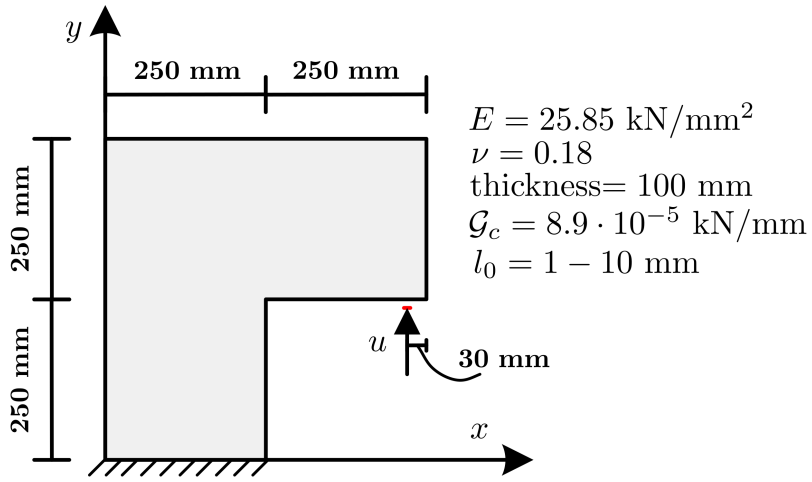

Figure 4.10: L-Shape panel test: Geometry and boundary conditions.

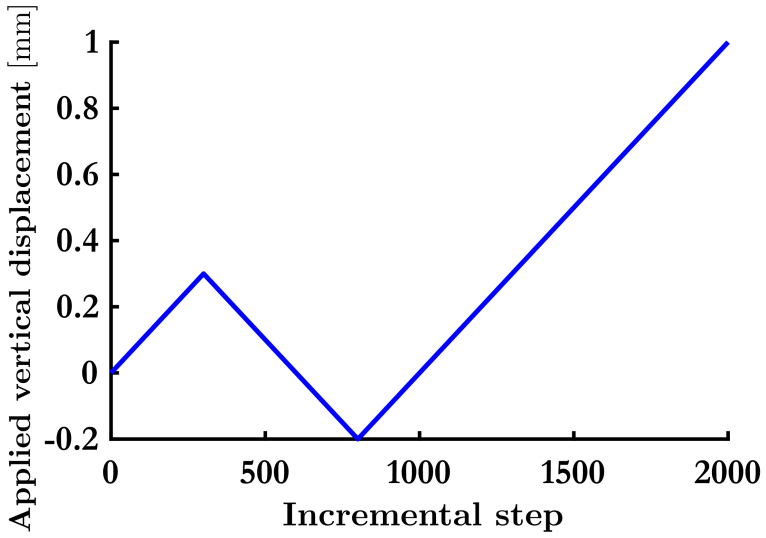

Figure 4.11: L-Shape panel test: Load History.

Initially, the PF-MPM implementation is compared to a PF-FEM solution considering a length scale parameter $l_0 = 2.5$ mm while the mesh size is $h = 2.5$ mm. Each background cell in the Material Point implementation is populated with 2x2 material points while full integration (4 Gauss points per element) is

considered for the FEM formulation . The corresponding load paths are shown in Fig. 4.12 where the two methods demonstrate very good agreement.

The relative error of the two methods is defined by Eq. (4.19) below

$$\text{Relative Error}[\%] = \frac{PF-MPM_{\text{solution}} - PF-FEM_{\text{solution}}}{PF-FEM_{\text{solution}}} \cdot 100 \qquad (4.19)$$

and it is presented in Fig. 4.13. The relative error significantly increases in the final stages of the loading scenario, i.e., on the softening regime of the member response. As in the case of the single edge-notched shear test examined in Section 4.4.2, this pertains to the different kinematics between the two solution procedures, with the PF-MPM implementation providing a more accurate representation of the actual crack path. The L^2 norm of the error is $\epsilon_{L^2} = \|\text{Relative Error}\| = 0.3\%$. The crack path obtained by the the proposed method demonstrate good agreement with the experimental crack observations as presented in Figs. 4.14(a) and 4.14(b), respectively. The analysis times for the PF-FEM was approximately 15 hrs whereas for PF-MPM it was 18 hrs resulting in an increase of 20%.

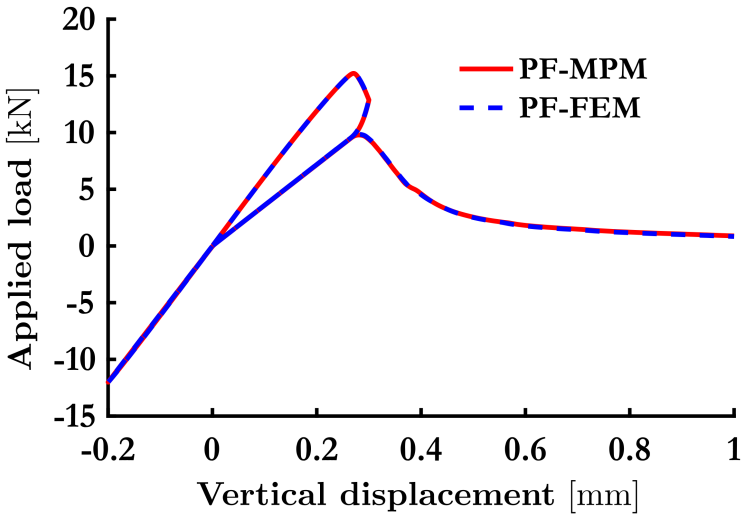

Figure 4.12: L-Shape panel test: PF-MPM vs PF-FEM implementation comparison. Load-displacement u paths. The cell density for the MPM method is 2x2, whereas in both cases $l_0 = 2.5$ mm and $h = 2.5$ mm.

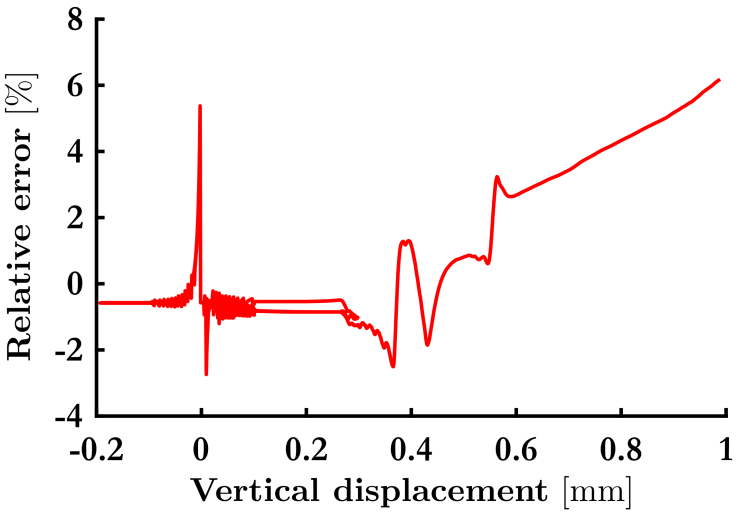

Figure 4.13: L-Shape panel test: PF-MPM vs PF-FEM implementation comparison. Relative Error vs applied vertical displacement u. The cell density for the MPM method is 2x2, whereas in both cases $l_0 = 2.5$ mm and $h = 2.5$ mm.

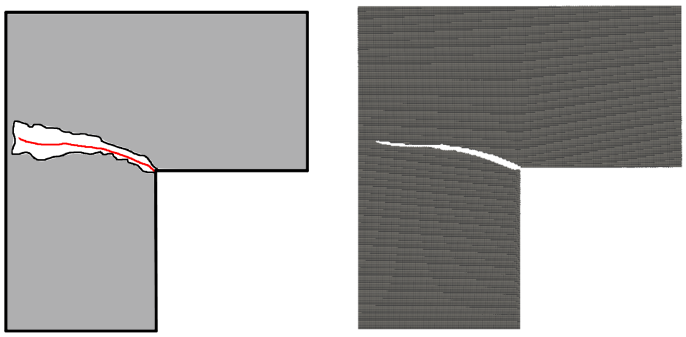

(a) (b)

Figure 4.14: Comparison of crack path between experimental (Winkler (2001), see also Ambati et al. (2015a)) (a) and simulation data (b). The red line represents the crack path obtained from simulation. Material Points with $c_p < 0.08$ have been removed.

Next, the sensitivity of the PF-MPM implementation to the cell density is investigated. Two cell densities are examined, namely 2x2 and 4x4. In the first case, each active cell contains approximately 2x2 = 4 Material Points whereas in the second approximately 4x4 = 16 Material Points are used to represent the deformable domain. The total number of material points utilized in each case is 30204 and 120404, respectively. The grid comprises 110 x 110 = 12100 cells with a cell spacing $h = 5$ mm for all runs. Four cases are considered for the length scale, namely $l_0 = \{10, 5, 2.5, 1\}$ mm.

The corresponding load paths are summarized in Figs. 4.15 and 4.16. Indicative results are presented in Table 4.1 where it can be seen that for the same length scale parameter, the influence of the cell density on the both the peak load and the corresponding critical displacement is marginal (less than 1%).

To further examine the robustness of the proposed scheme, the sensitivity of the analysis results on the cell spacing (h) is also investigated. Four cases are considered for the size h of the background grid, i.e., $h = 10$ mm, $h = 5$ mm, $h = 2.5$ mm and $h = 1$ mm whereas the cell density is kept constant at 2x2. The corresponding number of cells for cell spacing $h = 10$ mm, $h = 5$ mm, $h = 2.5$ mm and $h = 1$ mm are 55x55 = 3025, 110x110 = 12100, 220x220 = 48400 and 510x510 = 260100, respectively. The derived results are presented in Table 4.2 whereas the corresponding load paths are shown in Fig. 4.17 and 4.18

Opposite to the behaviour identified when varying the cell density, the cell spacing seems to have a stronger impact on the structural response. Differences in the measured peak load and corresponding displacement presented in Table 4.2 significantly increase with decreasing values of the length scale parameter l_0. This is expected as the smaller the value of the length scale parameter for a given cell size, the less the diffusion of damage around the crack path due to the phase field evolution, thus the more mesh-dependent the crack path is. When $h \leq l_0$, the results derived from both the different cell spacings converge; this is in accordance with the remarks presented in Miehe et al. (2010b) regarding the

effect of the the length scale to mesh size ratio on the accuracy of results.

The crack paths corresponding to the different length scale parameters are shown in Figs. 4.19(a)-(d) and 4.19(e)-(h) for cell spacing $h = 5$ mm and $h = 2.5$ mm, respectively. The experimentally observed crack path (Winkler (2001), see also Ambati et al. (2015a)), is shown in Fig. 4.14(a). The geometry of the crack path is only marginally affected when $h \leq l_0$. However, when $h > l_0$ (see. Figs. 4.19(c),(d) and (h)) the crack pattern diverges from the experimental observation.

In Fig. 4.20 the evolution of the phase field is shown for $l_0 = 2.5$ mm and $h = 2.5$ mm. Fig. 4.20(a) represents the degradation of structure when the critical load is observed. A degradation is also observed from time steps $u = 0.30$ mm to $u = 1$ mm in the region around of the load due to the cyclic load. In particularly, this region is on tension for load steps 300 until 800.

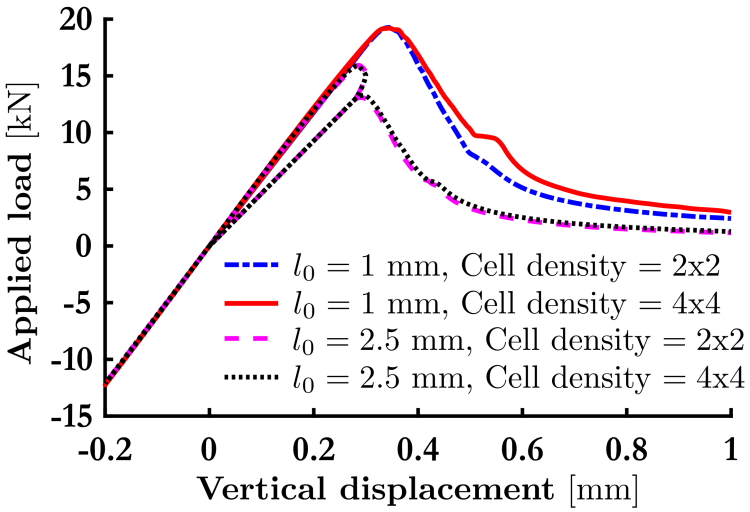

Figure 4.15: Influence of cell density for length scale parameter for $l_0 = 1$ mm and $l_0 = 2.5$ mm. The cell spacing is $h = 5$ mm.

4.4.3.1 Distortion error: PF-FEM vs PF-MPM

To assess the advantages of PF-MPM as compared to PF-FEM with regards to mesh distortion errors, the L-shaped panel benchmark is re-run considering

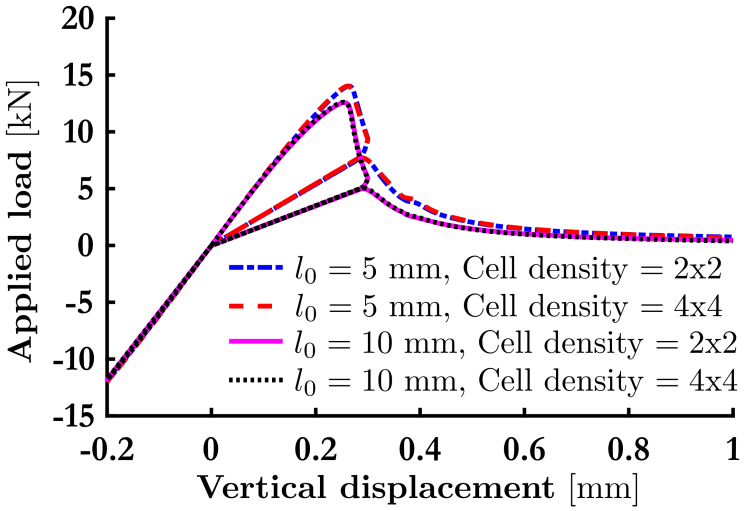

Figure 4.16: Influence of cell density for length scale parameter for $l_0 = 5$ mm and $l_0 = 10$ mm. The cell spacing is $h = 5$ mm.

Cell spacing 5 mm						
	Critical vertical displacement [mm]			Critical load [kN]		
l_0 [mm]	Cell Density		Diff	Cell Density		Diff
	2x2	4x4	[%]	2x2	4x4	[%]
10	0.255	0.254	0.392	12.5692	12.6099	0.323
5	0.264	0.262	0.757	14.0292	14.0343	0.036
2.5	0.286	0.284	0.699	15.9206	15.8939	0.167
1	0.345	0.345	0.000	19.2705	19.2039	0.345

Table 4.1: L-Shape panel test for different cell density

Cell density 2x2								
	Critical vertical displacement [mm]				Critical load [kN]			
l_0 [mm]	Cell spacing [mm]				Cell spacing [mm]			
	10	5	2.5	1	10	5	2.5	1
10	0.255	0.254	0.252	0.252	13.323	12.617	12.569	12.455
5	0.270	0.264	0.256	0.256	15.213	14.029	13.783	13.631
2.5	0.310	0.286	0.271	0.266	18.046	15.921	15.216	14.816
1	0.424	0.345	0.320	0.286	25.156	19.271	17.933	16.915

Table 4.2: L-Shape panel test for different cell spacing

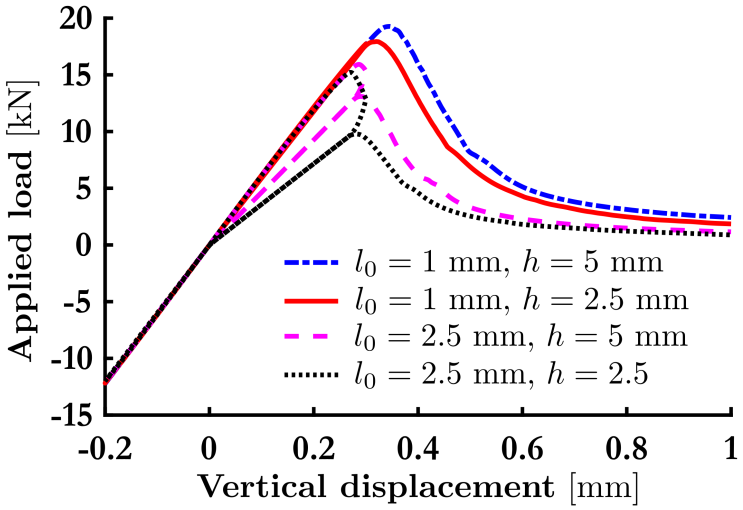

Figure 4.17: Influence of cell spacing h for length scale parameter for $l_0 = 1$ mm and $l_0 = 2.5$ mm. The cell density is 2x2.

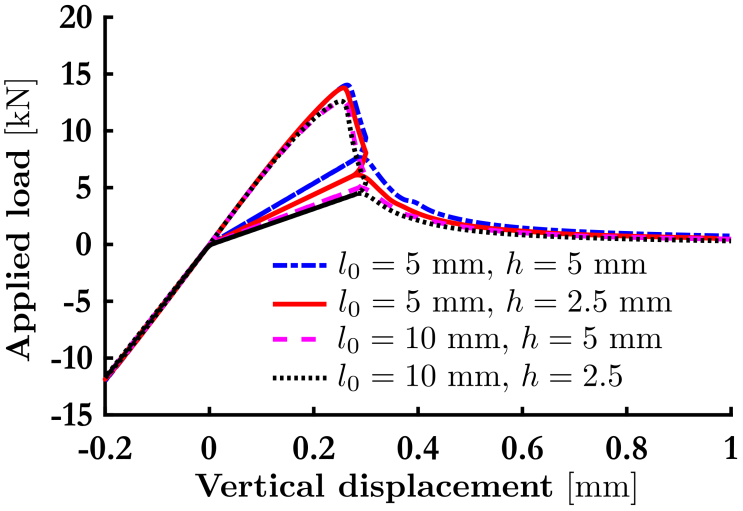

Figure 4.18: Influence of cell spacing h for length scale parameter for $l_0 = 5$ mm and $l_0 = 10$ mm. The cell density is 2x2.

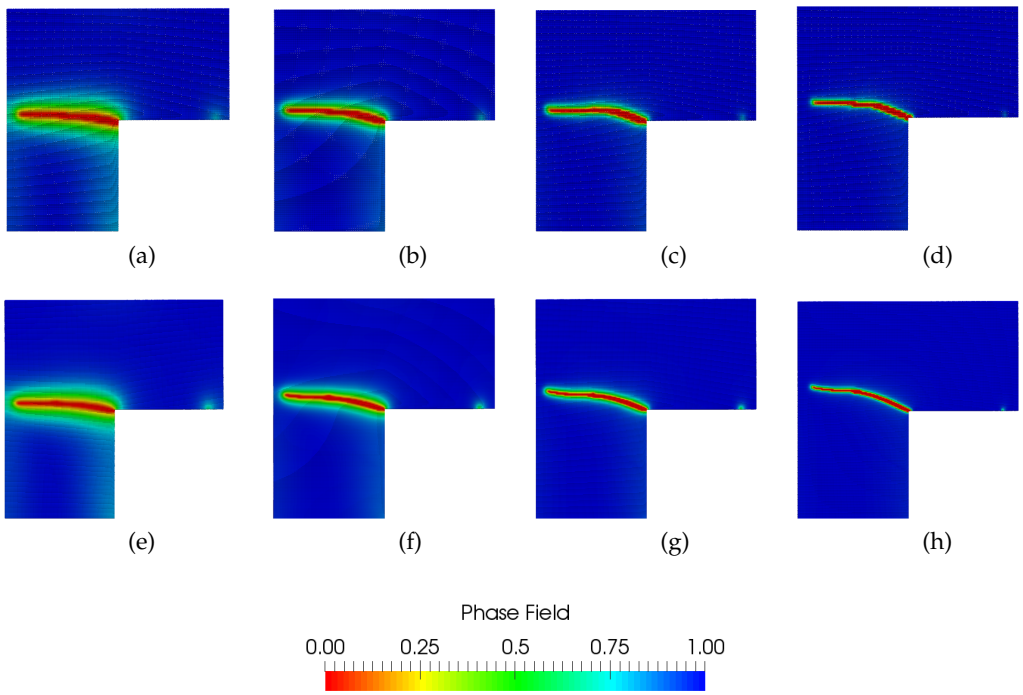

Figure 4.19: Phase Field in L Panel Test for cell spacing $h = 5$ mm ((a)-(d)) and $h = 2.5$ mm ((e)-(h)), respectively. Figs. (a) and (e) are for $l_0 = 10$ mm, (b) and (f) are for $l_0 = 5$ mm, (c) and (g) are for $l_0 = 2.5$ mm and (d) and (h) are for $l_0 = 1$ mm.

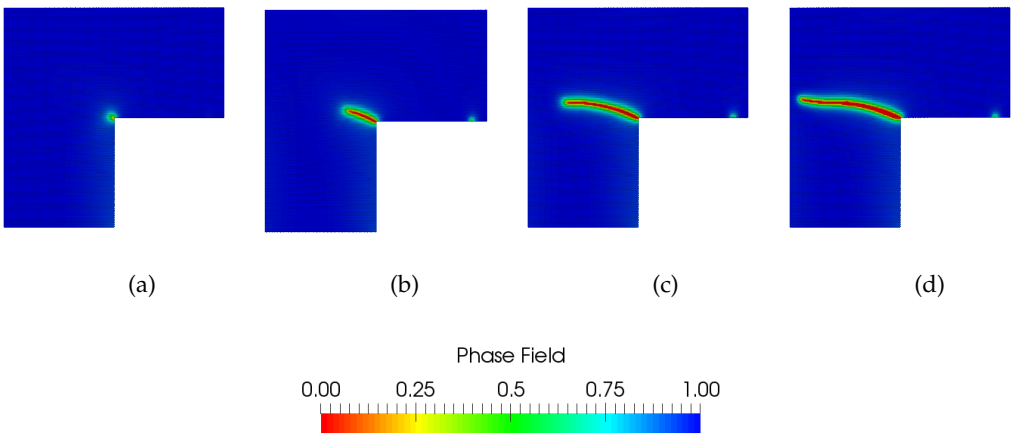

Figure 4.20: Phase Field in L-Panel test for $l_0 = 2.5$ mm and $h = 2.5$ mm. (a) $u = 0.27$ mm, (b) $u = 0.30$ mm, (c) $u = 0.45$ mm and (d) $u = 1.00$ mm.

a significantly larger critical fracture energy density $\mathcal{G}_c = 8.9 \cdot 10^{-1}$ kN/mm. All the other material parameters, boundary conditions and solution procedure parameters remain unchanged. The cell spacing is chosen to be $h = 10$ mm with cell density 3 x 3 while the length scale parameter is equal to $l_0 = 10$ mm. The same parameters and mesh size are also utilized for the PF-FEM simulation. A constant displacement increment $\Delta u = 10^{-1}$ mm is considered until complete failure.

The resulting load-displacement diagrams of both schemes are represented in Fig. 4.21. The critical vertical displacement and critical load obtained by the FEM are $u_{cr_{PF-FEM}} = 25.6$ mm and $F_{cr_{PF-FEM}} = 1324.12$ kN, respectively; whereas the critical vertical displacement and critical load obtained by the MPM are $u_{cr_{PF-MPM}} = 25.6$ mm and $F_{cr_{PF-MPM}} = 1316.16$ kN, respectively. The differences in critical values are less than 0.60%. However, after the critical load (crack initiation) the PF-FEM equilibrium path significantly diverges from the corresponding PF-MPM solution.

Both the evolution of phase field and the deformed configuration of the specimens are shown in Figs. 4.22 and 4.23 for the PF-FEM and PF-MPM, respectively. From Fig. 4.22, it is obvious that in PF-FEM the elements are highly distorted especially after the critical load (see Figs. 4.22(b) and 4.22(c)). PF-MPM is free of mesh-distortion errors thus allowing for a better representation of the actual crack path with the specimen being able to rotate until complete failure (see Fig. 4.23(d)). However, PF-FEM fails to converge for displacements $u > 278$ mm. Fig. 4.23 also represent the active cells in the corresponding time-steps.

4.4.4 Notched plate with hole

In the final example, a notched plate with hole is examined and compared to the experimental crack path obtained by Ambati et al. (2015a). In this examples, the influence of staggered solution algorithm in the accuracy of the solution is also

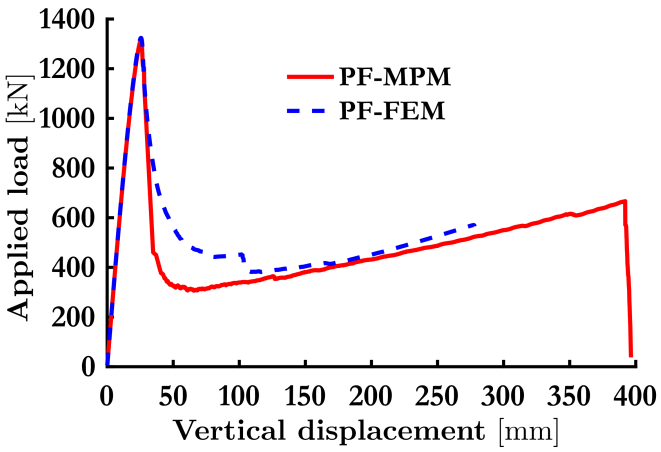

Figure 4.21: MPM vs FEM phase field implementation comparison for $h = 10$ mm, $l_0 = 10$ mm and $\mathcal{G}_c = 8.9 \cdot 10^{-1}$ kN/mm.

investigated. This involves both the number of the staggered iterations and the displacement increment required to achieve convergence.

The geometry and material parameters are presented in Fig. 4.24. The rectangular plate consists of 178236 material points. The Eulerian grid is formulated by 73080 (203 x 360) cells with cell spacing $h_x \approx 0.3497$ mm and $h_y = 0.35$ mm in x and y direction, respectively. The dimensions of the grid are 71 mm x 126 mm ($x_{min} = y_{min} = -3.00$ mm , $x_{max} = 68$ mm $y_{max} = 123$ mm). The cell spacing is chosen in order to be less or equal than the length scale parameter l_0. Four node cells with bilinear basis functions are used for the grid. The active cells at the beginning of the analysis are shown in Fig. 4.25. Plane stress conditions are assumed. Material points are randomly distributed in cells with the cell density varies from 1 to 4 material points per cell.

Zero displacement boundary conditions, i.e., $u_{p_x} = u_{p_y} = 0$, are imposed in all material points in the boundary of the lower pin. Next, the vertical displacements of all material points in the boundary of upper pin are kinematically constrained to have the same vertical displacement. The penalty parameter was chosen to be $a = 1000000$. Finally, the displacement is monitored and controlled in the boundary of upper pin.

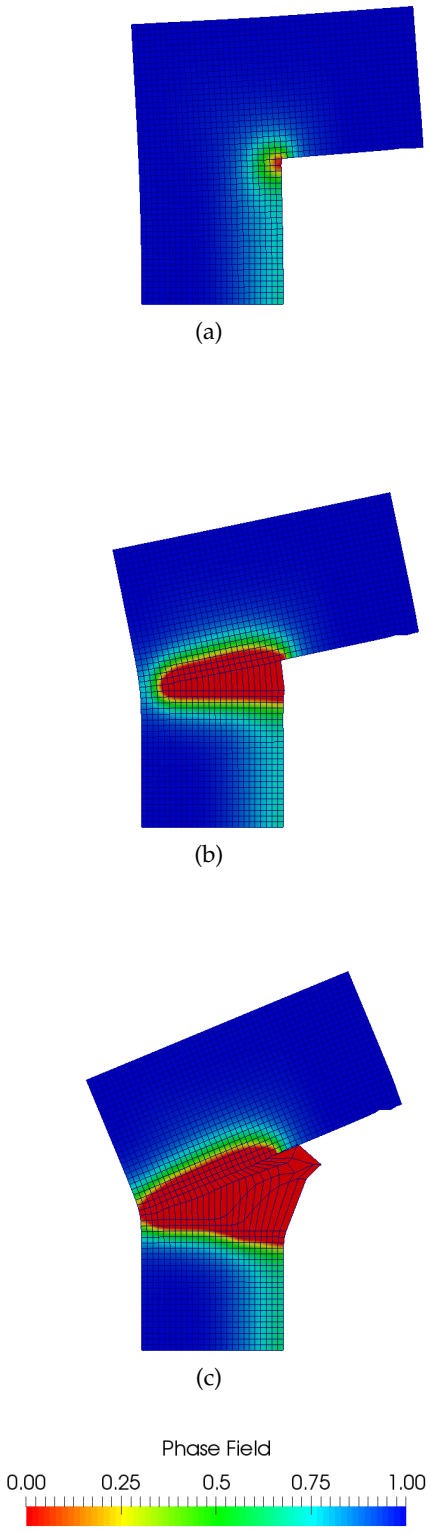

Figure 4.22: Phase Field Finite Element Method in L-Panel test for $h = 10$ mm, $l_0 = 10$ mm and $\mathcal{G}_c = 8.9 \cdot 10^{-1}$ kN/mm. (a) $u = 25.60$ mm, (b) $u = 90$ mm, (c) $u = 278$ mm.

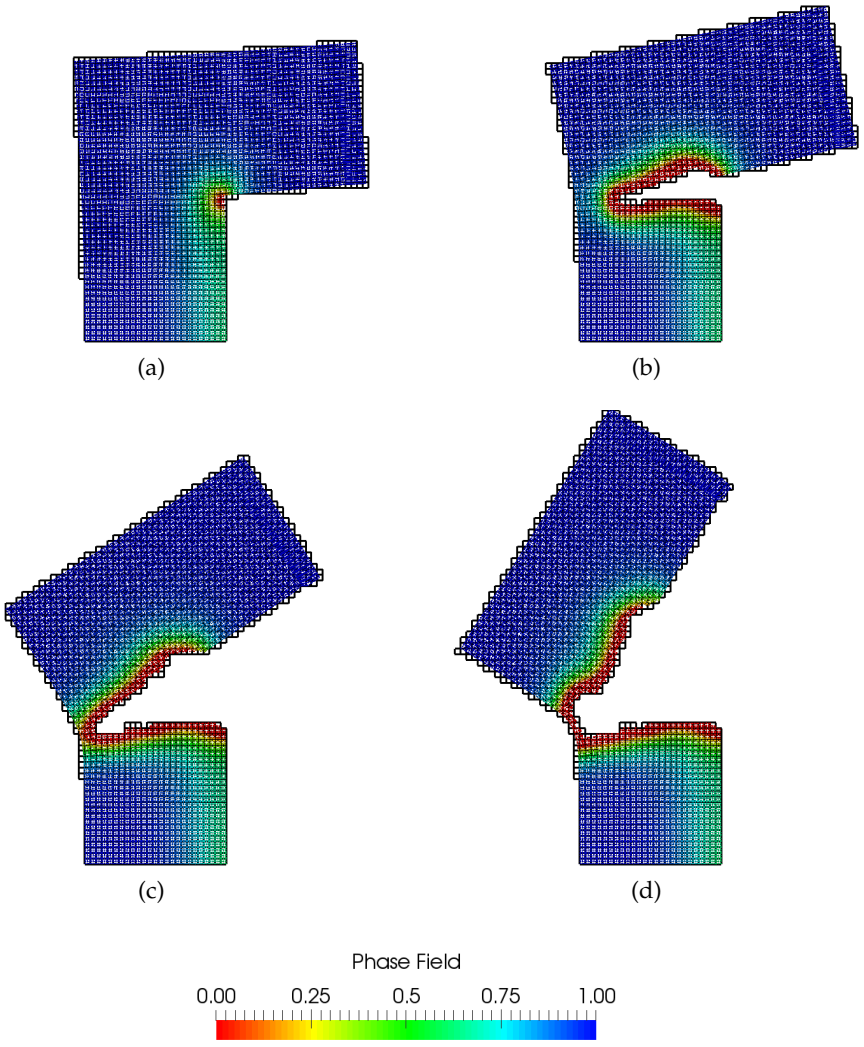

Figure 4.23: Phase Field Material Point Method in L-Panel test for $h = 10$ mm, $l_0 = 10$ mm and $\mathcal{G}_c = 8.9 \cdot 10^{-1}$ kN/mm. (a) $u = 25.60$ mm, (b) $u = 90$ mm, (c) $u = 278$ mm and (d) $u = 392$ mm.

To investigate the influence of staggered solution algorithm four cases are considered with constant displacement increment $\Delta u = 10^{-2}$, $\Delta u = 5 \cdot 10^{-3}$ mm, $\Delta u = 10^{-3}$ mm and $\Delta u = 5 \cdot 10^{-4}$ mm. Table 4.3 presents the influence of staggered iterations N_{staggs} and displacement increment Δu on critical load and its corresponding displacement. In all cases $tol_u = 10^{-5}$.

Increasing the number of staggered iterations, the fidelity of the solution is improved. After the third staggered iteration the algorithm is converging to a value and additional iterations marginally affect the results at the cost of increased number of evaluation. As shown in Table 4.3, i.e., $\Delta u = 10^{-3}$ mm and $\Delta u = 5 \cdot 10^{-4}$ mm, when the displacement increment Δu is sufficiently small then there is no need for additional staggered iterations.

Fig. 4.26 presents the influence of displacement increment Δu, for $N_{staggs} = 1$. For large values of displacement increment the results are overestimated. However, as long as the displacement increment is decreased the results are converging. Whereas, Fig. 4.27 represents the influence of staggered iterations on the results for $\Delta u = 5 \cdot 10^{-3}$ mm. The load-displacement curve is stabilized in third staggered iteration.

Fig. 4.28 represent the evolution of phase field in four time steps $u = 0.28$ mm, $u = 0.35$ mm, $u = 0.96$ mm and $u = 1.20$ mm, respectively. Whereas, Fig. 4.29 present the evolution of hydrostatic stress for the same time steps. Both Figs. 4.28 and 4.29 are referred to the solution obtained by staggered $N_{staggs} = 1$ iteration with constant displacement increment $\Delta u = 10^{-3}$ mm. the analysis time for this simulation was approximately 37hrs. The crack paths of both the proposed method and the experimental data from Ambati et al. (2015a) have good agreement and they are presented in Fig. 4.30.

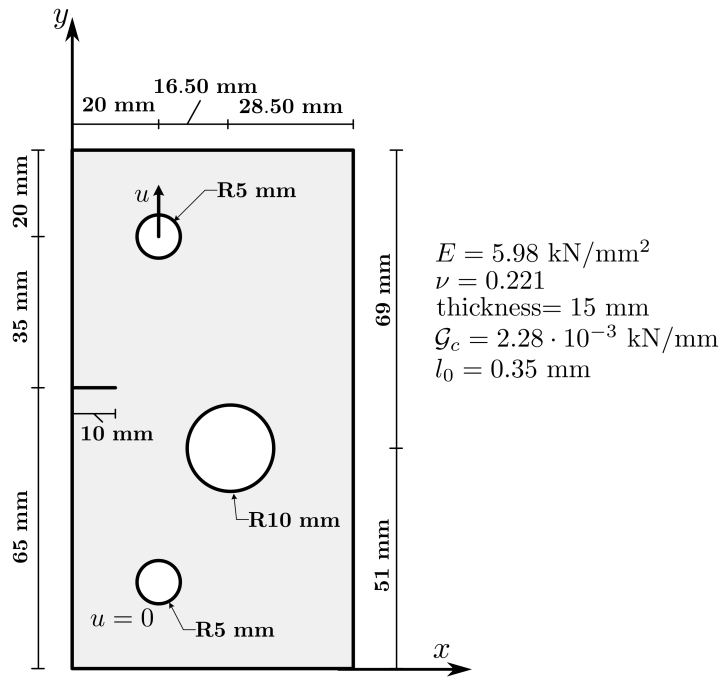

Figure 4.24: Notched Plate with Hole: Geometry and boundary conditions.

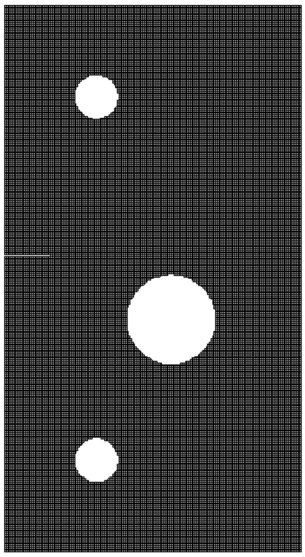

Figure 4.25: Notched Plate with Hole: Active cells in the beginning of the analysis.

	Critical vertical displacement [mm]			Critical load [kN]		
Δu [mm]	$N_{staggs} =$ 1	$N_{staggs} =$ 2	$N_{staggs} =$ 3	$N_{staggs} =$ 1	$N_{staggs} =$ 2	$N_{staggs} =$ 3
10^{-2}	0.400	0.350	0.330	10.233	9.421	9.103
$5 \cdot 10^{-3}$	0.355	0.325	0.315	9.501	9.006	8.823
10^{-3}	0.309	0.301	0.298	8.722	8.585	8.534
$5 \cdot 10^{-4}$	0.302	0.297	0.296	8.595	8.516	8.487

Table 4.3: Influence of Staggered Solution Algorithm

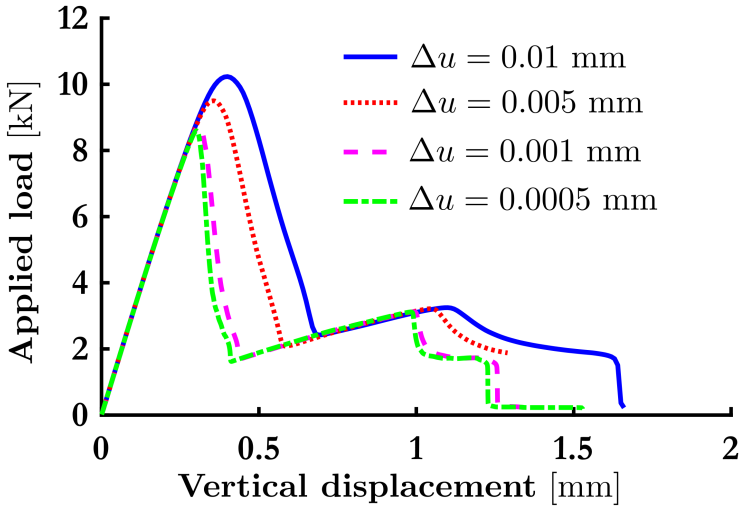

Figure 4.26: Load displacement response dependence on displacement increment size for 1 staggered iteration ($N_{staggs} = 1$).

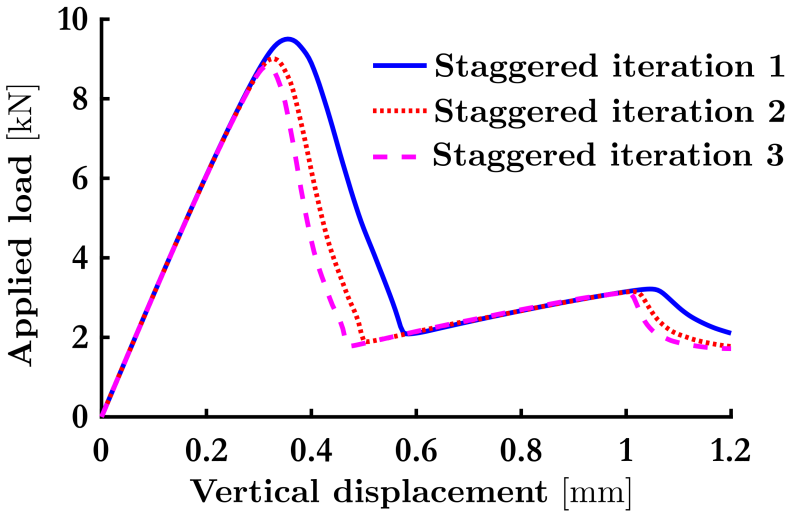

Figure 4.27: Load displacement response dependence on number of staggered iterations ($\Delta u = 5 \cdot 10^{-3}$ mm).

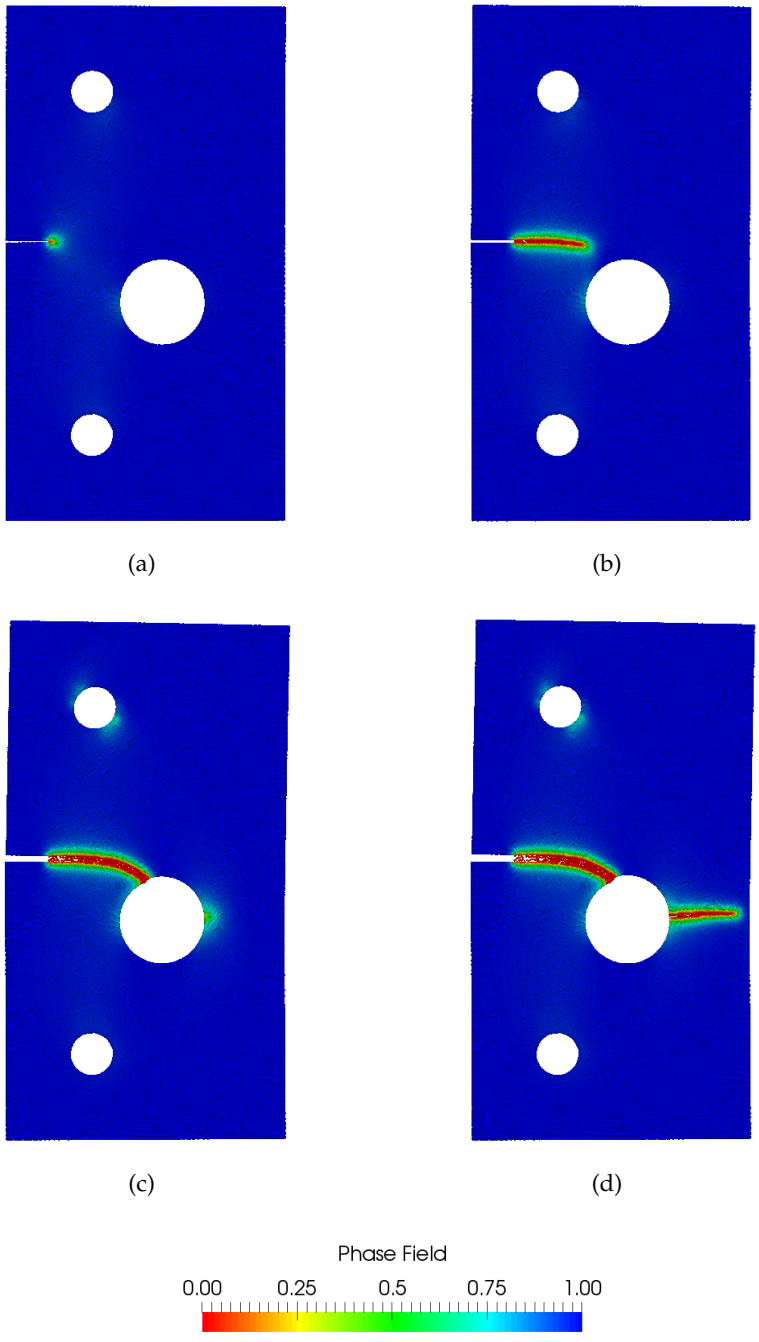

Figure 4.28: Phase Field in Notched Plate with Hole test for (a) $u = 0.28$ mm, (b) $u = 0.35$ mm, (c) $u = 0.96$ mm and (d) $u = 1.20$ mm, respectively. Displacement increment $\Delta u = 10^{-3}$ and staggered with 1 iteration.

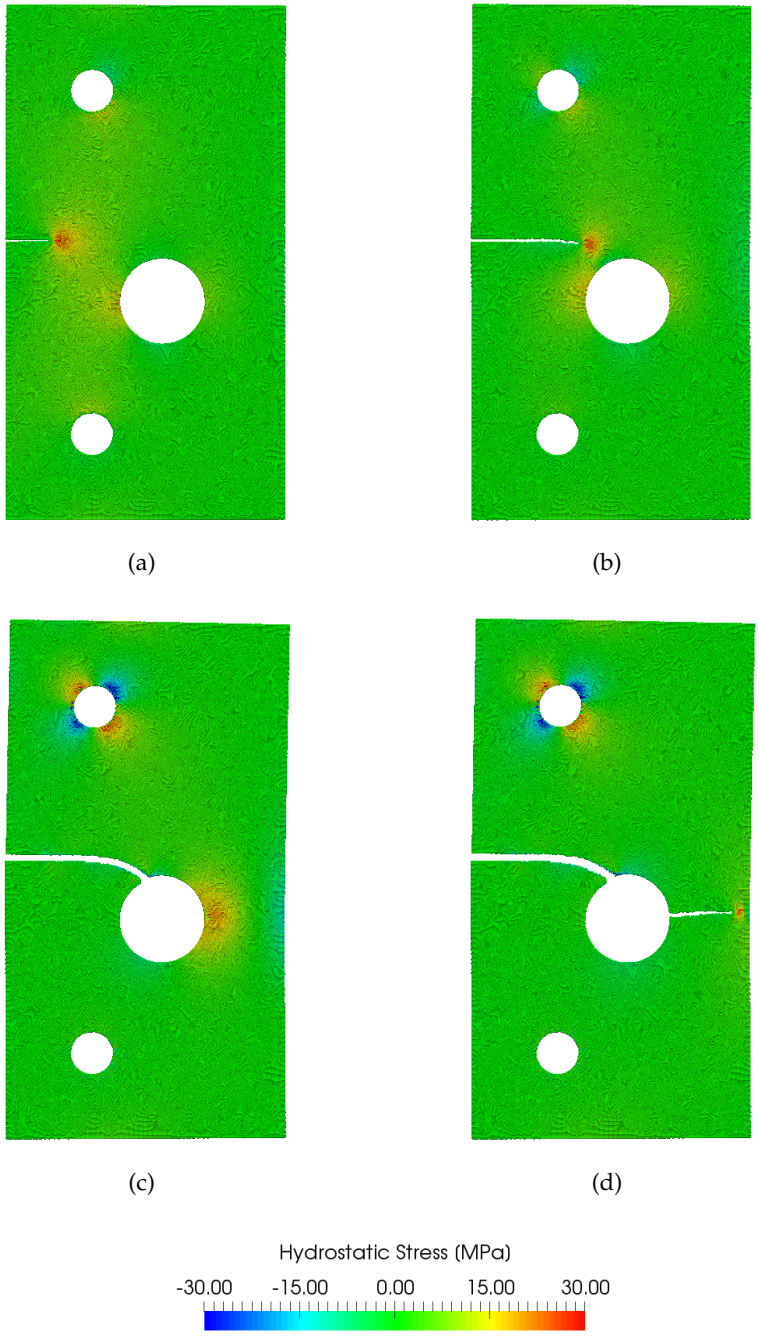

Figure 4.29: Hydrostatic stress in Notched Plate with Hole test for (a) $u = 0.28$ mm, (b) $u = 0.35$ mm, (c) $u = 0.96$ mm and (d) $u = 1.20$ mm, respectively. Displacement increment $\Delta u = 10^{-3}$ and staggered with 1 iteration. Material Points with $c_p < 0.08$ have been removed.

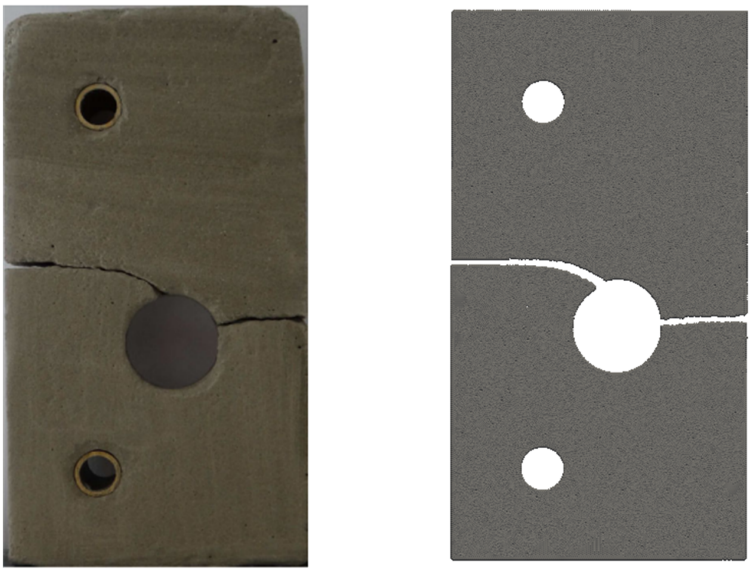

(a) (b)

Figure 4.30: Comparison of crack path between experimental Ambati et al. (2015a) (a) and simulation data (b). Material Points with $c_p < 0.08$ have been removed.

4.5 Conclusions

In this Section, a MPM for the simulation of crack propagation pertinent to brittle fracture is formulated. The crack geometry and underlying brittle fracture mechanics have been considered on the basis of a phase field formulation, appropriately adapted to be introduced within the MPM framework. Using this approach, the need for algorithmically tracking the crack path is alleviated thus reducing the underlying computational complexity. The deformable domain is approximated using a set of material points that are allowed to move within a fixed Eulerian mesh.

Fusing MPM with phase field modelling results in a coupled system of governing equations, namely the equilibrium and phase field evolution equations. Coupling is achieved through the definition of a history field that tracks the evolution of the tensile part of the elastic energy density. The latter is derived

on the basis of a spectral decomposition of the elastic strain tensor.

The resulting coupled field equations is numerically treated using a staggered solution scheme. In this, the phase field evolution equations are solved for constant displacement fields and a prediction for the phase field distribution is derived which is then used to iterate for the updated displacement field through the equilibrium equations.

A set of benchmark applications is presented to verify the proposed scheme whereas validation is also performed through experimental data available in the literature. From these, the accuracy of the method is established both in predicting the equilibrium paths as well as representing the actual geometry of the crack paths. The method succeeds in providing realistic crack path geometries as the background mesh is reused within each computational cycle, thus avoiding mesh distortion errors pertinent to the standard FEM. However, this comes at an increased computational cost for the MPM implementation considered in this Section, as re-factorization of the underlying stiffness matrix is required in each computational cycle. In the proposed scheme discontinuities are naturally created, since material points are naturally separated. This is not the case in the classical Phase Field Finite Element Method where Gauss points are always located in Gauss positions.

Chapter 5

Material Point Method for anisotropic brittle fracture

Part of this chapter is published in the Archive of Applied Mechanics (Kakouris and Triantafyllou, 2018a).

5.1 Introduction to anisotropic fracture

Anisotropy occurs naturally in several materials such as granitic rocks (Nasseri and Mohanty, 2008; Chandler et al., 2016), biological tissues (Holzapfel et al., 2000), single crystals (Ast et al., 2014) and composite sheets (Takei et al., 2013) due to inherent heterogeneities, inclusions and/or constituent distribution that in many cases are distributed in a random fashion. Industrial materials may also exhibit anisotropy due to their controlled or partially controlled manufacturing process as in the case of laminated composites. Anisotropy significantly affects crack formation. In cases of even weak anisotropy, stress concentrations pertinent to crack initiation and propagation will preferentially develop along the weak directions of the deformable medium. This intriguing mechanical response is being often highlighted in experiments (Takei et al., 2013).

Recently, phase field models have been extended to account for anisotropic fracture. In anisotropic fracture, the fracture energy is oriented-dependent. Thus, the propagation of cracks arise from the competition between the elastic energy release rate maximization and the fracture energy minimization. In phase field modelling, this is treated by introducing an anisotropic crack density functional. The anisotropic crack density functional modifies the fracture energy to be explicitly oriented-dependent. Recent works that demonstrate the merits of phase field models in anisotropic media are presented in Li et al. (2015), Teichtmeister et al. (2017), Gültekin et al. (2018) and Nguyen et al. (2017).

Fracture modelling with anisotropic fracture energy in MPM does not exist in the literature. In this chapter, the proposed PF-MPM (see chapter 4) is reformulated to incorporate a general anisotropic phase field description for crack propagation and its merits and bottlenecks are assessed as compared to a FEM implementation.

5.2 Phase field model for anisotropic fracture

5.2.1 Anisotropic phase field modelling

In the following, the case of an arbitrary deformable domain Ω is considered with external boundary $\partial\Omega$ and a crack path Γ as shown in Fig. 5.1(a). The deformable domain Ω is subjected to body forces $\mathbf{b} = \{b_1, b_2, b_3\}$. Furthermore, a set of traction/pressure loads $\bar{\mathbf{t}}$ is applied on the boundary $\partial\Omega_{\bar{\mathbf{t}}} \subseteq \partial\Omega$. Finally, a prescribed displacement field, denoted as $\bar{\mathbf{u}}$, is imposed on the boundary $\partial\Omega_{\bar{\mathbf{u}}} \subseteq \partial\Omega$.

As described in Section 2.6.1, the stored energy of the body Ω, Ψ_s can be expressed as

$$\Psi_s = \Psi_{el} + \Psi_f = \int_{\Omega} \psi_{el}\left(\boldsymbol{\varepsilon}\right) d\Omega + \int_{\Gamma} \mathcal{G}_c\left(\theta\right) d\Gamma. \tag{5.1}$$

The term $\mathcal{G}_c(\theta)$ corresponds to the critical fracture energy density released (surface energy density) over the crack path Γ. In the anisotropic case, this is considered to explicitly depend on the angle of orientation of the crack path θ (see Fig. 5.1(a)). Thus, the integral expression representing the fracture energy in Eq. (5.1) is defined on the assumption that both Γ and θ at the current configuration are known.

In phase field approximation, the path dependent fracture energy surface integral is transformed onto a volume integral defined over the entire domain Ω (Bourdin et al., 2008) - see also, Fig. 5.1(b). Hence, the phase field approximation gives rise to equation (5.2)

$$\Psi_f = \int_{\Gamma} \mathcal{G}_c(\theta)\, d\Gamma \approx \int_{\Omega} \bar{\mathcal{G}}_c \mathcal{Z}_{c,Anis} d\Omega \tag{5.2}$$

where the functional $\mathcal{Z}_{c,Anis} = \mathcal{Z}_{c,Anis}(c,\theta)$ and c is the phase field. Parameter $\bar{\mathcal{G}}_c$ in Eq. (5.2) corresponds to the energy required to create a unit area of fracture surface $\mathcal{A}_c(\theta)$. This is assumed to be constant for all directions with directionality of the fracture toughness being accounted for in the definition of the functional.

In view of Eq. (5.2), the definition of the anisotropic phase field functional must also satisfy the following condition

$$\mathcal{A}_c(\theta) = \int_{\Omega} \mathcal{Z}_{c,Anis} d\Omega$$

i.e., the first integral of the phase field functional should coincide with the fracture surface $\mathcal{A}_c = \mathcal{A}_c(\theta)$.

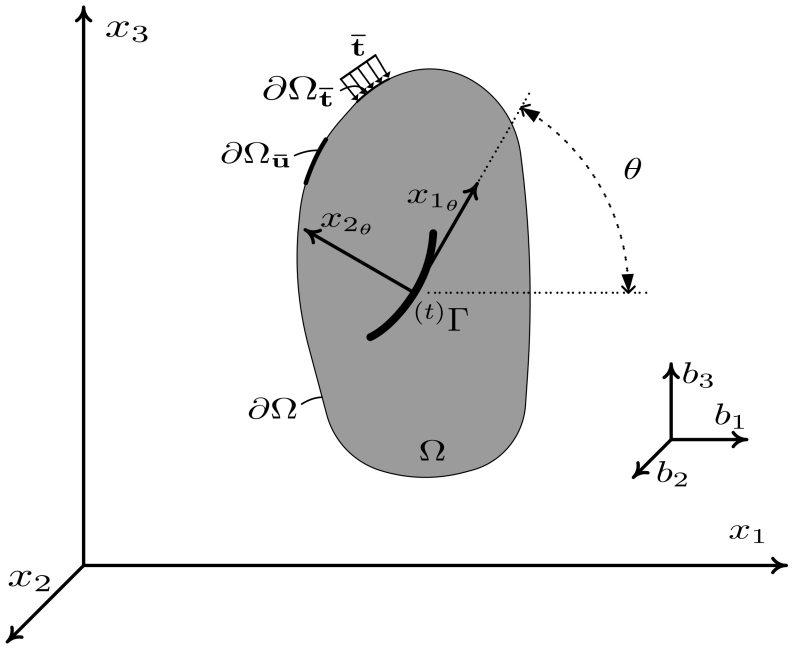

(a)

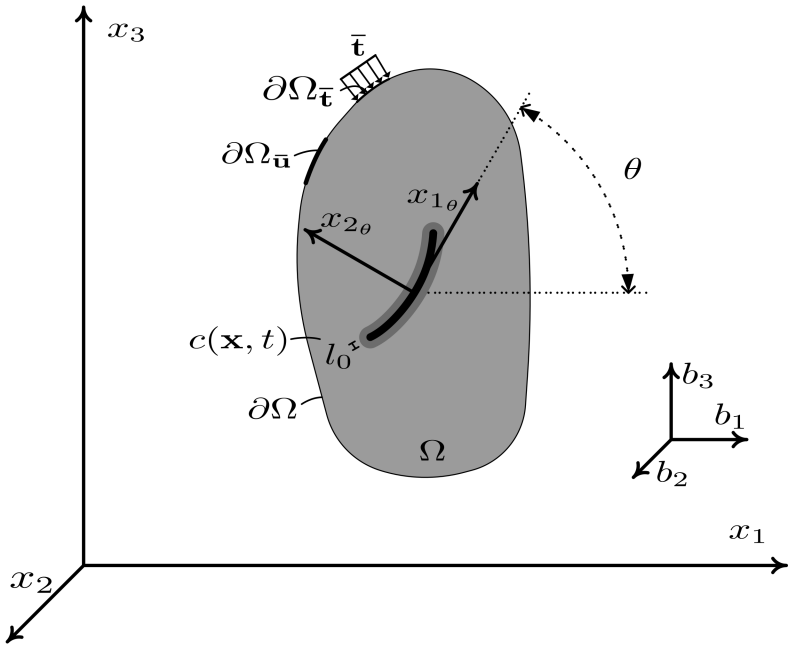

(b)

Figure 5.1: (a) Solid body Ω with a crack path Γ and (b) Phase field approximation of the crack path Γ.

5.2.2 Anisotropic crack density functional

To account for the general case of anisotropic material behaviour, $\mathcal{Z}_{c,Anis}$ is defined as the 4th order functional utilized in Li et al. (2015) according to Eq. (5.3)

$$\mathcal{Z}_{c,Anis} = \left[\frac{(c-1)^2}{4l_0} + l_0 |\nabla c|^2 + l_0^3 \sum_{ijkl} \gamma_{ijkl} \frac{\partial^2 c}{\partial x_i \partial x_j} \frac{\partial^2 c}{\partial x_k \partial x_l} \right] \tag{5.3}$$

where $c(\mathbf{x}, t) \in [0, 1]$ is the phase field defined over the domain Ω, $l_0 \in \mathbb{R}^+$ is the length scale parameter and γ_{ijkl}, $i, j, k, l = 1 \dots 3$ are the components of the 4^{th} order tensor corresponding to the anisotropic constitutive behaviour of the material.

The tensor $\boldsymbol{\gamma}$ is dimensionless and conveniently defined in the three dimensional space utilizing Voigt notation as

$$\boldsymbol{\gamma} = \begin{bmatrix} \gamma_{1111} & \gamma_{1122} & \gamma_{1133} & \gamma_{1112} & \gamma_{1123} & \gamma_{1113} \\ \gamma_{2211} & \gamma_{2222} & \gamma_{2233} & \gamma_{2212} & \gamma_{2223} & \gamma_{2213} \\ \gamma_{3311} & \gamma_{3322} & \gamma_{3333} & \gamma_{3312} & \gamma_{3323} & \gamma_{3313} \\ \gamma_{1211} & \gamma_{1222} & \gamma_{1233} & \gamma_{1212} & \gamma_{1223} & \gamma_{1213} \\ \gamma_{2311} & \gamma_{2322} & \gamma_{2333} & \gamma_{2312} & \gamma_{2323} & \gamma_{2313} \\ \gamma_{1311} & \gamma_{1322} & \gamma_{1333} & \gamma_{1312} & \gamma_{1323} & \gamma_{1313} \end{bmatrix} \tag{5.4}$$

In the two-dimensional case $\boldsymbol{\gamma}$ reduces to

$$\boldsymbol{\gamma} = \begin{bmatrix} \gamma_{1111} & \gamma_{1122} & \gamma_{1112} \\ \gamma_{2211} & \gamma_{2222} & \gamma_{2212} \\ \gamma_{1211} & \gamma_{1222} & \gamma_{1212} \end{bmatrix}. \tag{5.5}$$

The functional $\mathcal{Z}_{c,Anis}$ in Eq. (5.3) is defined in the global Cartesian system $\mathbf{x} = \{x_1, x_2, x_3\}$. The direction angle of the crack path θ can be explicitly introduced in the expression of $\mathcal{Z}_{c,Anis}$ through a coordinate transformation. In the 2D case, the Cartesian coordinate system $\mathbf{x} = \{x_1, x_2\}$ is transformed into $\mathbf{x}_\theta =$

$\{x_{1_\theta}, x_{2_\theta}\}$ where axis x_{1_θ} is defined along the crack path Γ and axis x_{2_θ} is normal to the crack interface (see Fig. 5.1). Hence, the transformation relation (5.6) holds

$$\mathbf{x}_\theta = \mathbf{R}_\theta \mathbf{x} \tag{5.6}$$

where θ is the counter-clockwise angle between x_1-axis and x_{1_θ}, and the transformation matrix $\mathbf{R}_\theta$ is defined as

$$\mathbf{R}_\theta = \begin{bmatrix} \cos(\theta) & -\sin(\theta) \\ \sin(\theta) & \cos(\theta) \end{bmatrix}. \tag{5.7}$$

Substituting Eq. (5.6) in Eq. (5.3) and further assuming that $\partial c\left(\mathbf{x}\left(\mathbf{x}_\theta\right)\right)/\partial \mathbf{x} \approx \partial c\left(\mathbf{x}\left(x_{2_\theta}\right)\right)/\partial \mathbf{x}$, the crack density functional $\mathcal{Z}_{c,Anis}$ is expressed as (see Appendix C for more details)

$$\begin{aligned} \mathcal{Z}_{c,Anis} = \left[\frac{(c-1)^2}{4l_0} + l_0 |\nabla c|^2 + l_0^3 \sum_{ijkl} \gamma_{ijkl} \frac{\partial^2 c}{\partial x_i \partial x_j} \frac{\partial^2 c}{\partial x_k \partial x_l} \right] \approx \\ \left[\frac{(c-1)^2}{4l_0} + l_0 \left(\frac{\partial c}{\partial x_{2_\theta}} \right)^2 + l_0^3 \gamma_\theta \left(\frac{\partial^2 c}{\partial x_{2_\theta}^2} \right)^2 \right] \end{aligned} \tag{5.8}$$

where

$$\begin{aligned} \gamma_\theta =& \gamma_{1111} \sin^4(\theta) + \gamma_{2222} \cos^4(\theta) + \gamma_{1212} \cos^2(\theta) \sin^2(\theta) \\ &+ \gamma_{1122} \cos^2(\theta) \sin^2(\theta) + \gamma_{2211} \cos^2(\theta) \sin^2(\theta) + \gamma_{1112} \cos(\theta) \sin^3(\theta) \\ &+ \gamma_{1211} \cos(\theta) \sin^3(\theta) + \gamma_{2212} \sin(\theta) \cos^3(\theta) + \gamma_{1222} \sin(\theta) \cos^3(\theta). \end{aligned} \tag{5.9}$$

Eq. (5.8) can be conveniently employed to highlight some interesting aspects of the adopted phase field formulation for the case of anisotropic fracture. Taking the Euler-Lagrange equation of Eq. (5.8), the state equation (5.10) is derived for

the phase field

$$\begin{aligned} c - 1 - 4l_0^2 \Delta c + 4l_0^4 \sum_{ijkl} \gamma_{ijkl} \frac{\partial^4 c}{\partial x_i \partial x_j \partial x_k \partial x_l} = 0 \Rightarrow \\ c - 1 - 4l_0^2 \left(\frac{\partial^2 c}{\partial x_{2_\theta}^2} \right) + 4l_0^4 \gamma_\theta \left(\frac{\partial^4 c}{\partial x_{2_\theta}^4} \right) = 0. \end{aligned} \tag{5.10}$$

Eq. (5.10) can be numerically solved subject to the following boundary conditions

$$\begin{aligned} & c\left(0\right) = 0 \\ & \frac{\partial c\left(0\right)}{\partial x_{2_\theta}} = 0 \\ & \frac{\partial c\left(\pm\infty\right)}{\partial x_{2_\theta}} \left(\approx \frac{\partial c\left(\pm x_{lb}\right)}{\partial x_{2_\theta}} \right) = 0 \\ & \frac{\partial^2 c\left(\pm\infty\right)}{\partial x_{2_\theta}^2} \left(\approx \frac{\partial^2 c\left(\pm x_{lb}\right)}{\partial x_{2_\theta}^2} \right) = 0 \end{aligned} \tag{5.11}$$

where x_{lb} is the distance from the crack Γ to the boundary; assuming a value $x_{lb} = 50 l_0$ yields a reasonable approximation. It is obvious from Eq. (5.9) that if $\gamma_{ijkl} = 0$ then $\gamma_\theta = 0$; hence the fourth order anisotropic phase field model introduced in Eqs. (5.10) reduces to the second order phase field model introduced in Eq. (2.46). For that case, the boundary conditions introduced in Eq. (5.11) reduce to

$$\begin{aligned} & c\left(0\right) = 0 \\ & \frac{\partial c\left(\pm\infty\right)}{\partial x_{2_\theta}} \left(\approx \frac{\partial c\left(\pm x_{lb}\right)}{\partial x_{2_\theta}} \right) = 0. \end{aligned} \tag{5.12}$$

A fourth order isotropic phase field model can be derived if $\gamma_\theta = \gamma_s$, where γ_s is a constant (i.e. independent of angle θ). For instance, if the fourth order tensor $\boldsymbol{\gamma}$ of Eq. (5.5) assumes the following form

$$\boldsymbol{\gamma} = \begin{bmatrix} \gamma_s & 0.50\gamma_s & 0 \\ 0.50\gamma_s & \gamma_s & 0 \\ 0 & 0 & \gamma_s \end{bmatrix} \tag{5.13}$$

then Eq. (5.9) becomes

$$\begin{aligned}\gamma_\theta =&\gamma_{1111}\sin^4(\theta)+\gamma_{2222}\cos^4(\theta)+\gamma_{1122}\cos^2(\theta)\sin^2(\theta)\\&+\gamma_{2211}\cos^2(\theta)\sin^2(\theta)+\gamma_{1212}\cos^2(\theta)\sin^2(\theta)\\=&\gamma_s\left(\sin^4(\theta)+\cos^4(\theta)+2\cos^2(\theta)\sin^2(\theta)\right)\\=&\gamma_s.\end{aligned} \tag{5.14}$$

5.2.3 Particular cases of the tensor γ_{ijkl}

A comparison between the second and fourth order phase field model is presented in Fig. 5.2. In Fig. 5.2, the length scale parameter is chosen to be $l_0 = 0.01$ m while $\gamma_\theta = 1.00$ is selected to derive a fourth order isotropic phase field model. Fourth order models offer a smooth representation of the phase field (Fig. 5.2(a)) as well as its first derivative (Fig. 5.2(b)). However, this is not the case for second order phase field models. Fourth order models also improve the accuracy and the convergence rate of the resulting numerical scheme as has been reported in Borden et al. (2014), Amiri et al. (2016), Hesch et al. (2016).

Some special cases are orthotropic and cubic symmetry of surface energy density $\mathcal{G}_c(\theta)$. For orthotropic symmetry the tensor $\boldsymbol{\gamma}$ is rewritten in 2D as

$$\boldsymbol{\gamma} = \begin{bmatrix} \gamma_{1111} & \gamma_{1122} & 0 \\ \gamma_{1122} & \gamma_{2222} & 0 \\ 0 & 0 & \gamma_{1212} \end{bmatrix} \tag{5.15}$$

whereas in cubic symmetry as

$$\boldsymbol{\gamma} = \begin{bmatrix} \gamma_{1111} & \gamma_{1122} & 0 \\ \gamma_{1122} & \gamma_{1111} & 0 \\ 0 & 0 & \gamma_{1212} \end{bmatrix} \tag{5.16}$$

in material principal axes. Figs. 5.3(a), 5.3(b), and 5.3(c) demonstrate the phase

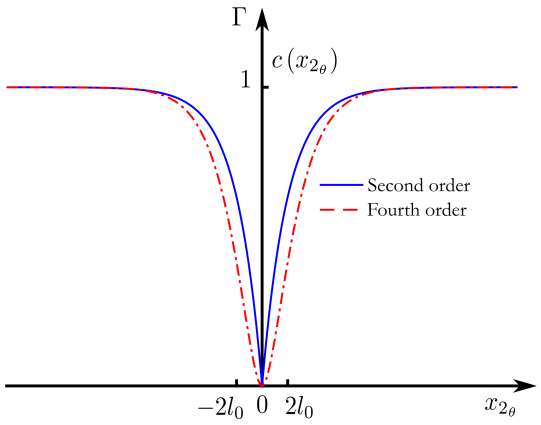

(a)

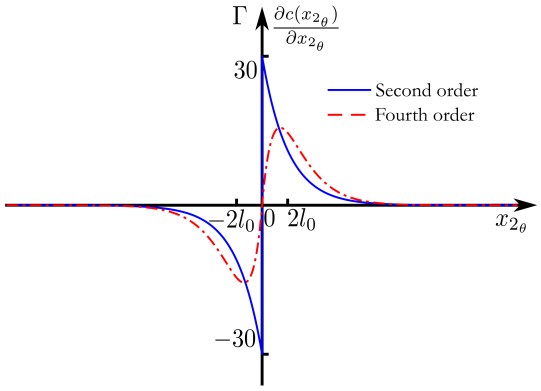

(b)

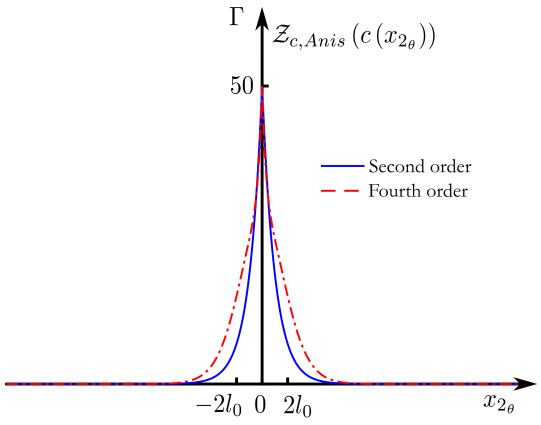

(c)

Figure 5.2: Second / Fourth order phase field model: (a) Phase field approximation $c\,(x_{2_\theta})$. (b) First derivative of phase field $\frac{\partial c(x_{2_\theta})}{\partial x_{2_\theta}}$ and (c) Crack density functional $\mathcal{Z}_{c,Anis}\,(c(x_{2_\theta}))$. Γ represents the position of the crack (see also Fig. 5.1).

field, its first derivative and crack density functional, respectively for several angles θ considering the case of orthotropic symmetry. In contrast, Figs. 5.3(a), 5.3(b) and 5.3(c) represent the same variables for cubic symmetry. In Figs. 5.3 and 5.4, the length scale parameter is chosen to be $l_0 = 0.01$ m. Furthermore, the anisotropic parameters are chosen to be $\gamma_{1111} = 20$, $\gamma_{2222} = 1$, $\gamma_{1122} = 0$ and $\gamma_{1212} = 74$ for orthotropic symmetry and $\gamma_{1111} = \gamma_{2222} = 1$, $\gamma_{1122} = 0$ and $\gamma_{1212} = 74$ for cubic symmetry. In Figs. 5.2, 5.3 and 5.4, Γ represents the position of the crack.

The surface energy density $\mathcal{G}_c(\theta)$ for each angle θ is numerically evaluated as

$$\mathcal{G}_c(\theta) = \int_{\Gamma} \mathcal{G}_c(\theta)\, d\Gamma \approx \int_{-\infty}^{+\infty} \bar{\mathcal{G}}_c \mathcal{Z}_{c,Anis} dx_{2_\theta} \approx \int_{-x_{lb}}^{+x_{lb}} \bar{\mathcal{G}}_c \mathcal{Z}_{c,Anis} dx_{2_\theta}. \tag{5.17}$$

Figs. 5.5(a) and 5.5(b) illustrate the surface energy densities $\mathcal{G}_c(\theta)$ and their reciprocals $1/\mathcal{G}_c(\theta)$, respectively in polar coordinates for isotropic symmetry with second and fourth order phase field model. The cases of cubic and orthotropic symmetry are also shown in Fig. 5.5. To derive these polar plots, the parameter $\bar{\mathcal{G}}_c$ is chosen to be $\bar{\mathcal{G}}_c = 0.70710$ kN/m for the fourth order isotropic, cubic and orthotropic symmetry whereas $\bar{\mathcal{G}}_c = 1$ kN/m for second order isotropic symmetry. The parameter $\bar{\mathcal{G}}_c$ is chosen so that all previously mentioned models have the same minimum value of surface energy density $\mathcal{G}_{c_{min}} = 1$ kN/m. Fig. 5.5 also represent the twofold and fourfold symmetry into orthotropic and cubic symmetry (Ting, 1996), respectively.

5.2.4 Influence of tensor γ_{ijkl} in surface energy density $\mathcal{G}_c(\theta)$

To further highlight the assumed anisotropic material behaviour with respect to fracture, the form of the surface energy density $\mathcal{G}_c(\theta)$ as a function of the fracture orientation θ is investigated in this Section for characteristic cases of anisotropy. Detailed derivations of the surface energy plots are provided in Appendix C.

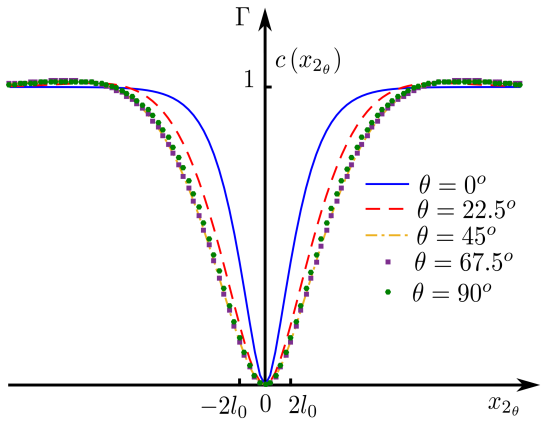

(a)

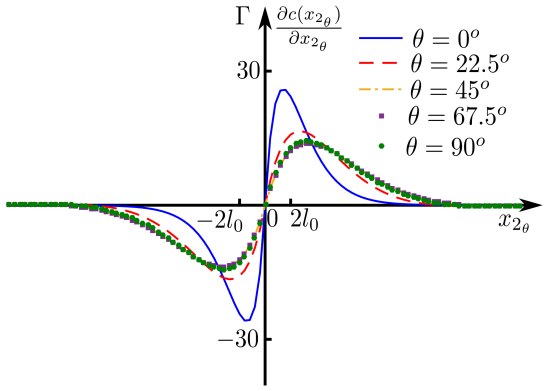

(b)

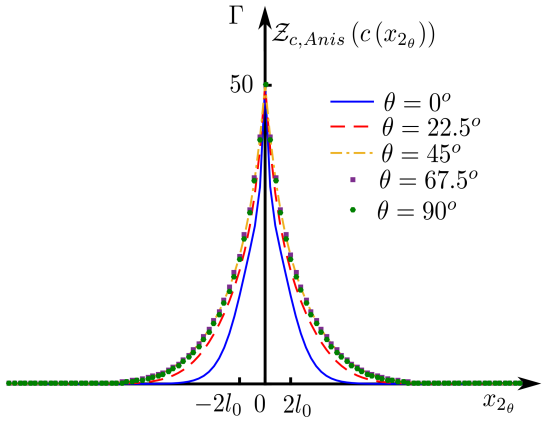

(c)

Figure 5.3: Orthotropic symmetry: (a) Phase field approximation $c\,(x_{2_\theta})$ (b) First derivative of phase field $\frac{\partial c(x_{2_\theta})}{\partial x_{2_\theta}}$ and (c) Crack density functional $\mathcal{Z}_{c,Anis}\,(c(x_{2_\theta}))$. Γ represents the position of the crack (see also Fig. 5.1).

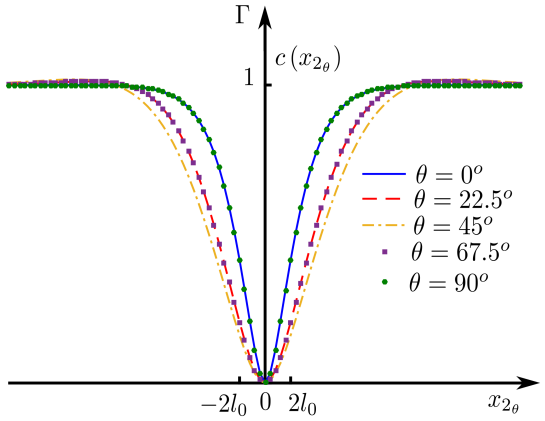

(a)

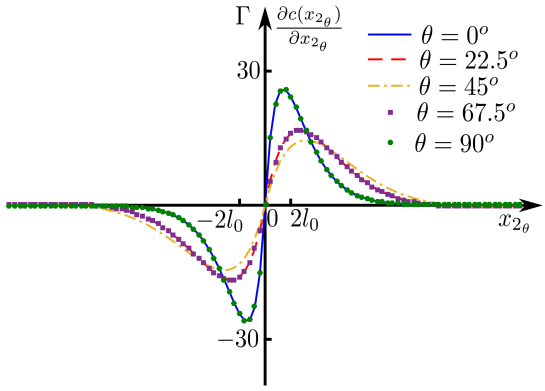

(b)

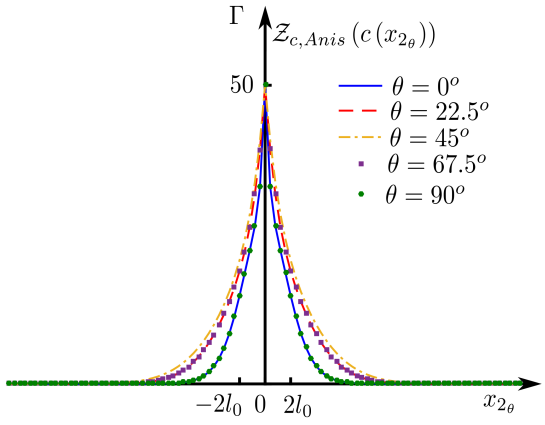

(c)

Figure 5.4: Cubic symmetry: (a) Phase field approximation $c\,(x_{2_\theta})$ (b) First derivative of phase field $\frac{\partial c(x_{2_\theta})}{\partial x_{2_\theta}}$ and (c) Crack density functional $\mathcal{Z}_{c,Anis}\,(c(x_{2_\theta}))$. Γ represents the position of the crack (see also Fig. 5.1).

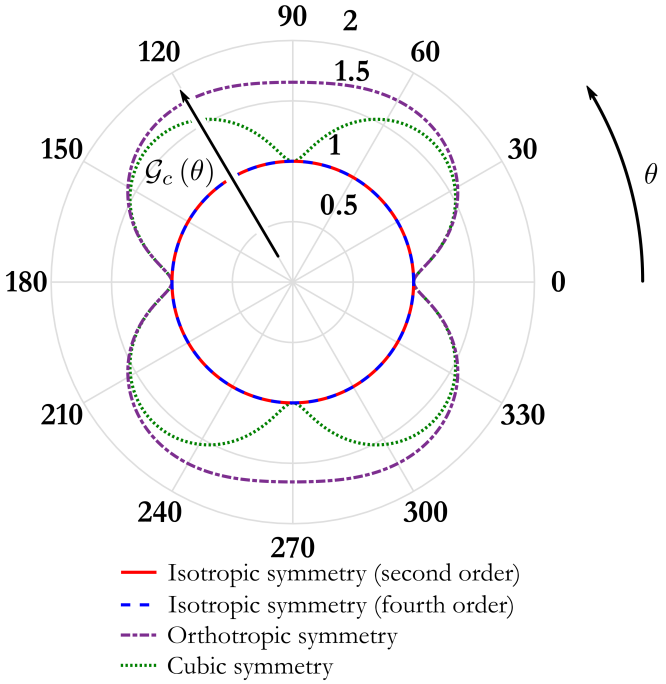

(a)

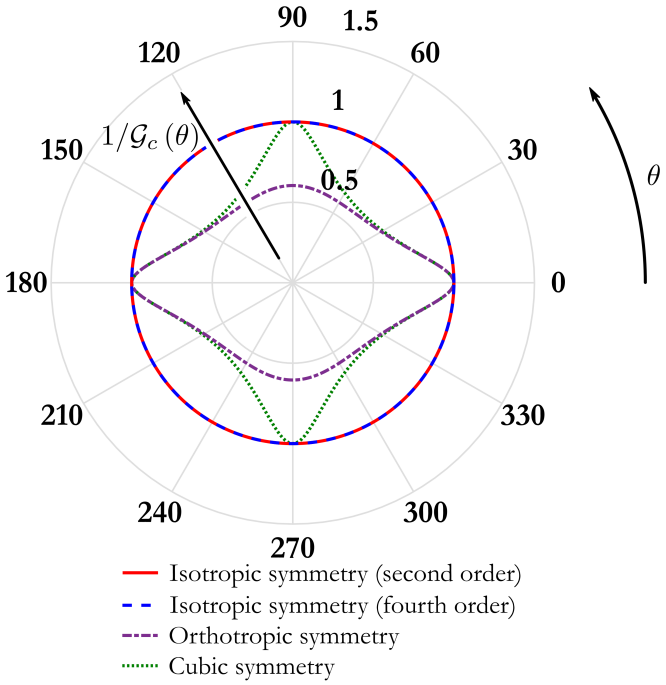

(b)

Figure 5.5: Polar plots: (a) Surface energy densities $\mathcal{G}_c(\theta)$ and (b) their reciprocals $1/\mathcal{G}_c(\theta)$ in polar coordinates.

In this work, the cases of both cubic and orthotropic symmetry are considered for the surface energy density. Thus, in two-dimensional case, the tensor $\boldsymbol{\gamma}$ reduces to Eq. (5.16) for cubic and Eq. (5.15) for orthotropic symmetry.

Examples of materials that possess cubic symmetry are single-crystals (Face Centered Cubic-FCC and Body-Centered Cubic-BCC) e.g. nickel (Sung and Chen, 2015), minerals e.g. oxides, sulphides, silicates and halides (Tromans and Meech, 2002) and polycrystalline materials e.g. solar-grade polycrystalline silicon (Liu and Juhre, 2018). Anisotropic materials with orthotropic symmetry are wood (Xu et al., 1996), sheet metals e.g. dual phase high strength CR340LA (Li et al., 2016), uni-directional fibre-reinforced composite laminae e.g. unidirectional carbon-fibre reinforced epoxy HTA/6376 (Cahill et al., 2014), biological (Gültekin et al., 2018) and bone tissues (Doblaré et al., 2004).

In Fig. 5.6, the distribution of the surface energy density $\mathcal{G}_c(\theta)$ and its reciprocal $1/\mathcal{G}_c(\theta)$ is shown for the case of increasing values of component γ_{1111} while all other components are kept constant. When $\gamma_{1111} = \gamma_{2222}$ the case of four-fold symmetry, i.e., cubic symmetry is manifested whereas in the case of $\gamma_{1111} \neq \gamma_{2222}$ the case of two-fold symmetry, i.e., orthotropic symmetry is revealed. Increasing values of component γ_{1111} result in increasing surface energy density values along the $90\,\mathrm{deg}$ and $270\,\mathrm{deg}$ fracture directions.

Similarly, increasing values of component γ_{2222} when all other components of the anisotropic fracture tensor are kept constant results in increasing values of the surface energy density along the $0\,\mathrm{deg}$ and $180\,\mathrm{deg}$ directions of fracture as shown in Fig. 5.7.

Thus, the values of the normal components of the tensor $\boldsymbol{\gamma}$ control the extreme values of the corresponding surface energy density. The effect of the shear components of the tensor, i.e., $\gamma_{1122}(=\gamma_{2211})$ and γ_{1212} is illustrated in Figs. 5.8 and 5.9, respectively. Both parameters control the extreme values of both the surface energy density and its reciprocal at a rotated coordinate system with respect to

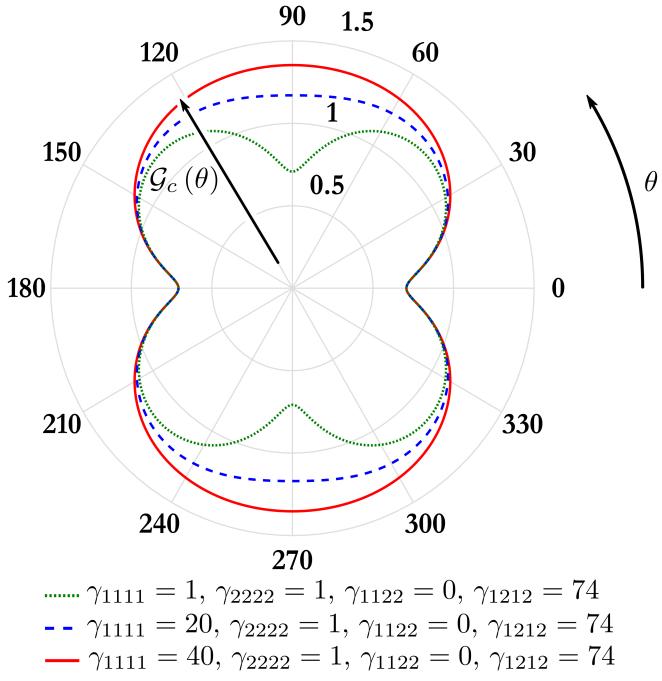

(a)

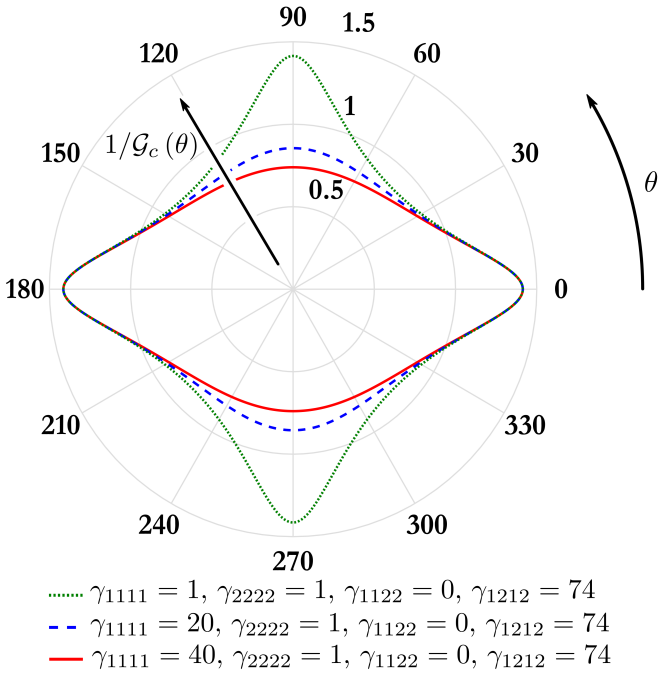

(b)

Figure 5.6: Polar plots of (a) surface energy density $\mathcal{G}_c(\theta)$ and (b) reciprocal of surface energy density $1/\mathcal{G}_c(\theta)$ for increasing values of component γ_{1111}.

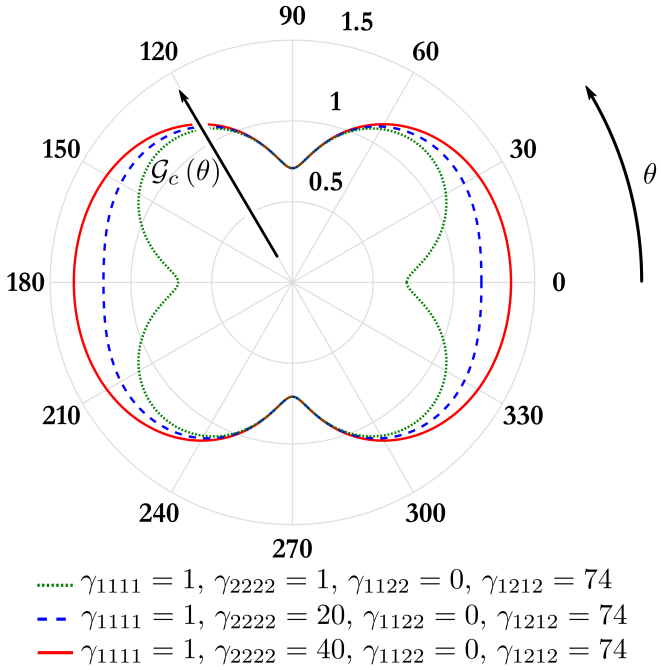

(a)

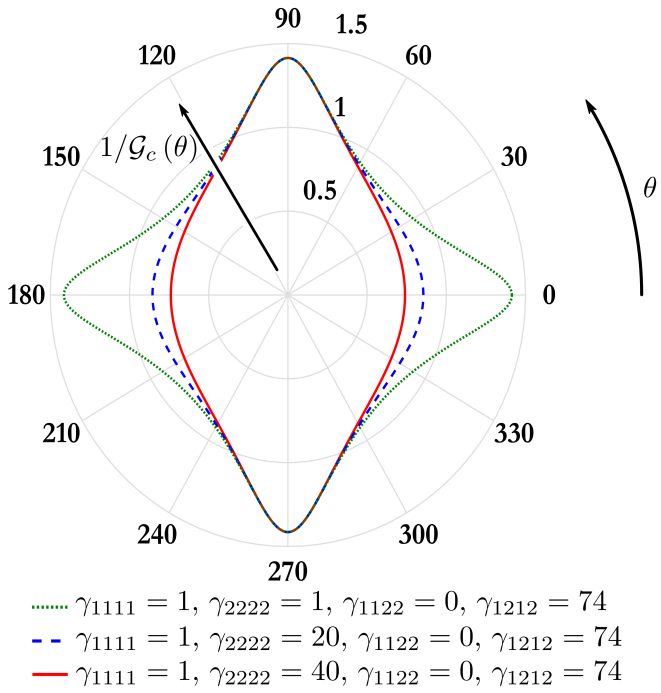

(b)

Figure 5.7: Polar plots of (a) surface energy density $\mathcal{G}_c(\theta)$ and (b) reciprocal of surface energy density$1/\mathcal{G}_c(\theta)$ for increasing values of component γ_{2222}.

the origin.

5.2.4.1 Convex and Non-convex reciprocals of surface energy density $1/\mathcal{G}_c(\theta)$

According to the choice of anisotropic parameters γ_{ijkl} the reciprocal of surface energy density $1/\mathcal{G}_c(\theta)$ can be either convex or non-convex. This can be illustrated by plotting the reciprocal of surface energy density in polar coordinates. Non-convex reciprocal plots of surface energy density lead to *strong* anisotropic materials with forbidden directions for the crack paths. Convex reciprocal plots results in *weak* anisotropic materials with no forbidden crack paths. A way to identify the forbidden portions of a reciprocal plot was suggested by Li et al. (2015) by introducing the surface stiffness of the surface energy, i.e.

$$\mathcal{S}^r(\theta) = \frac{\partial^2 \mathcal{G}_c(\theta)}{\partial \theta} + \mathcal{G}_c(\theta). \tag{5.18}$$

This can be justified by the fact that the energy change due to crack propagation is a function of the surface stiffness, i.e. $\dot{\Psi}_f \backsim \mathcal{S}^r(\theta)$. Hence, the sign of $\dot{\Psi}_f$ depends upon the sign of the quantity in Eq. (5.18). Indeed if $\mathcal{S}^r(\theta) > 0$ then $\dot{\Psi}_f > 0$ and the surface energy is stable against, whereas if $\mathcal{S}^r(\theta) < 0$ and $\dot{\Psi}_f > 0$ the surface energy is unstable. Further details can be found in Müller and Métois (2008). In 3D, such an analytical criterion does not exist and geometrical criteria are used for the forbidden orientation instead (Sekerka, 2005).

The forbidden directions are defined for all $\theta \in [0, 2\pi]$ where the surface stiffness is negative $\mathcal{S}^r(\theta) < 0$. In the same manner a crack can propagate in directions where $\mathcal{S}^r(\theta) > 0$. The influence of non-convexity in the resulting crack path is investigated in Section 5.3.3.1.

To better illustrate the influence of the convexity on the forbidden directions, two examples for the surface energy densities are considered one non-convex

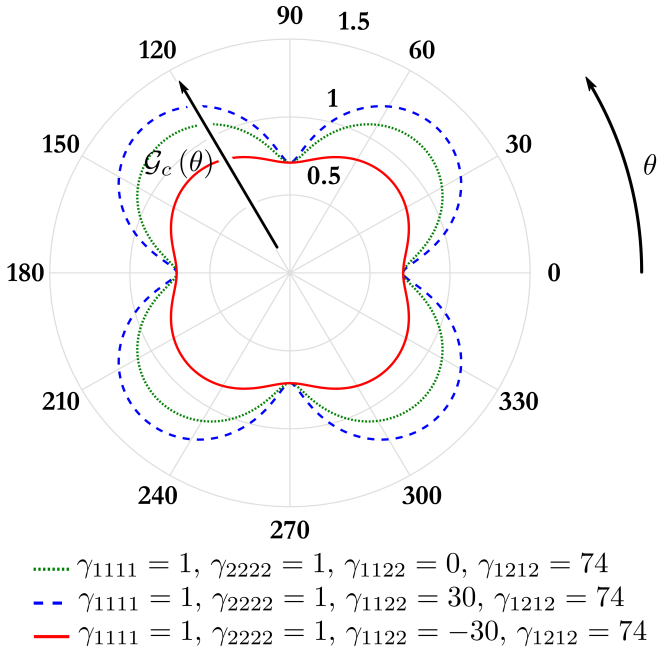

(a)

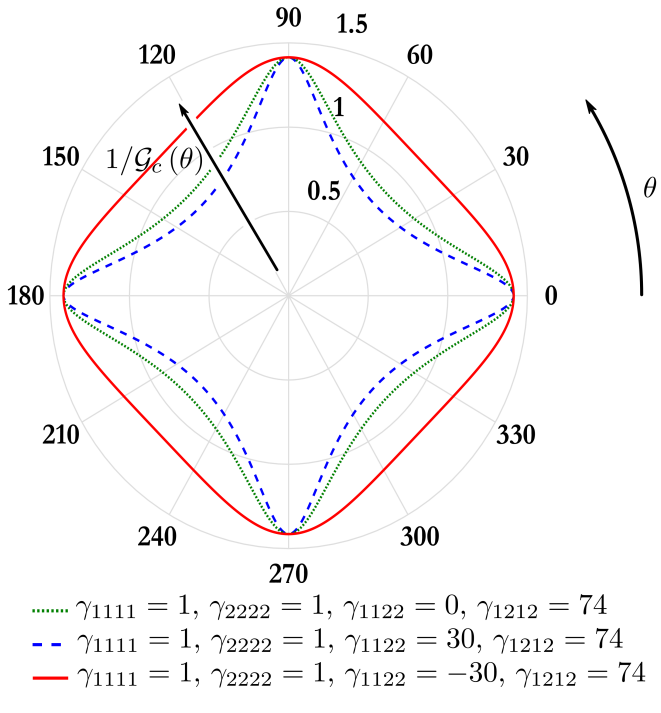

(b)

Figure 5.8: Polar plots of (a) surface energy density $\mathcal{G}_c(\theta)$ and (b) reciprocal of surface energy density $1/\mathcal{G}_c(\theta)$ for increasing values of component γ_{1122}.

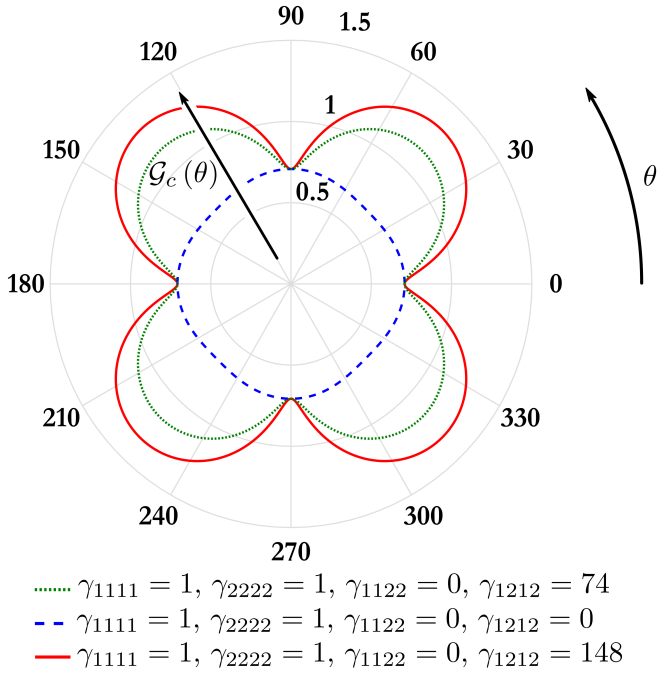

(a)

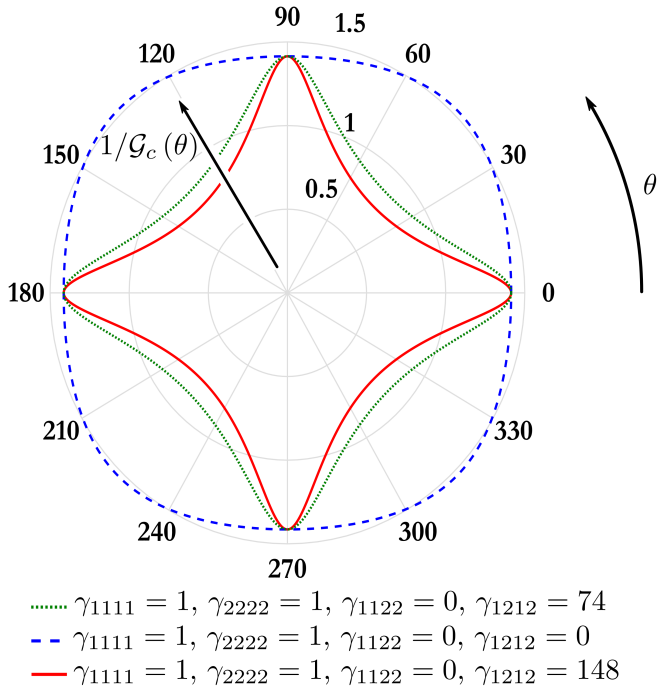

(b)

Figure 5.9: Polar plots of (a) surface energy density $\mathcal{G}_c(\theta)$ and (b) reciprocal of surface energy density $1/\mathcal{G}_c(\theta)$ for increasing values of component γ_{1212}.

and one with convex reciprocal. Figs. 5.10(a), 5.11(a), 5.12(a) and 5.13(a) are refereed to the non-convex case whereas Figs. 5.10(b), 5.11(b), 5.12(b) and 5.13(b) to the convex one. The non-convex polar plots are reproduced with anisotropic parameters $\gamma_{1111} = \gamma_{2222} = 1$, $\gamma_{1122} = 0$ and $\gamma_{1212} = 74$ while the convex polar plots with $\gamma_{1111} = \gamma_{2222} = 1$, $\gamma_{1122} = 0$ and $\gamma_{1212} = 0$. The length scale parameter is chosen to be $l_0 = 0.01$ m and $\bar{\mathcal{G}}_c = 0.50$ kN/m.

Figs. 5.10(a), (b) and 5.11(a), (b) represent the surface energy densities $\mathcal{G}_c(\theta)$ and their reciprocals $1/\mathcal{G}_c(\theta)$, respectively. Similarly, their second derivatives $\frac{\partial^2 \mathcal{G}_c(\theta)}{\partial \theta}$ and their surface stiffness $\mathcal{S}^r(\theta)$ are presented in Figs. 5.12(a), (b) and 5.13(a), (b) for the non-convex and convex case, respectively. The positive ($\mathcal{S}^r(\theta) > 0$) and negative ($\mathcal{S}^r(\theta) < 0$) surface stiffness is also marked in Figs. 5.10, 5.11 and 5.13 with blue and red colour, respectively. As it can be seen in Figs. 5.10(b), 5.11(b) and 5.13(b), in convex case there are only blue portions of the curves since the surface stiffness is always positive.

5.2.5 Derivation of coupled strong form

The strong form of the anisotropic brittle fracture problem is established herein by employing the same methodology introduced in Section 2.6.2.1 for the isotropic second-order phase field model. Hence, the energy balance equation of the anisotropic brittle fracture problem is defined as

$$\dot{\mathcal{K}}(\dot{\mathbf{u}}) + \dot{\mathcal{W}}^{int}(\dot{\mathbf{u}}, \dot{c}, \nabla\dot{c}) - \dot{\mathcal{W}}^{ext}(\dot{\mathbf{u}}) = 0 \tag{5.19}$$

where the rate of internal work functional $\dot{\mathcal{W}}^{int}(\dot{\mathbf{u}}, \dot{c}, \nabla\dot{c})$ is evaluated as

$$\dot{\mathcal{W}}^{int}(\dot{\mathbf{u}}, \dot{c}, \nabla\dot{c}) = \frac{d\Psi_s}{dt} = \frac{d}{dt}\int_{\Omega} \left(\psi_{el} + \bar{\mathcal{G}}_c \mathcal{Z}_{c,Anis}\right) d\Omega. \tag{5.20}$$

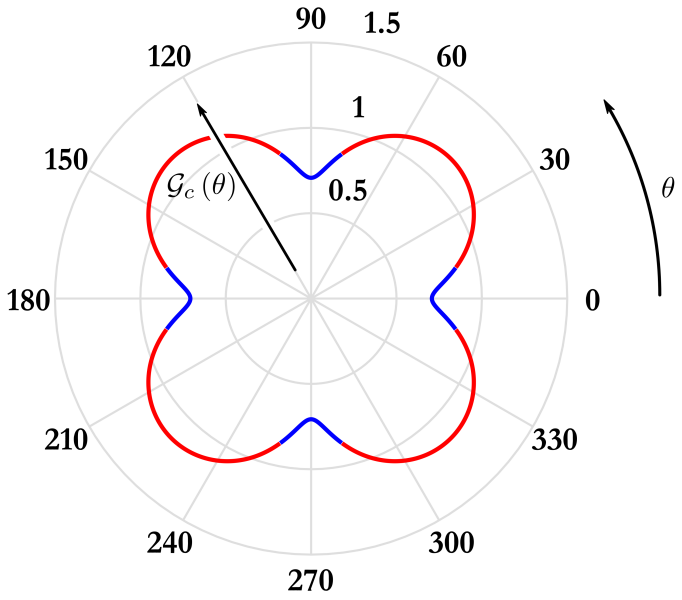

(a)

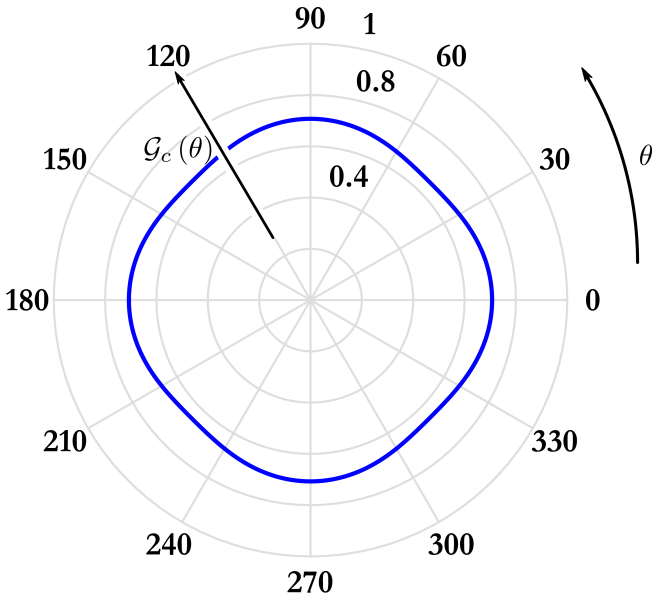

(b)

Figure 5.10: Polar plots of (a) a non-convex and (b) a convex surface energy density. In Subfigs. (a) and (b), the red portions of the curves are refereed to $\mathcal{S}^r(\theta) < 0$ while the blue to $\mathcal{S}^r(\theta) > 0$.

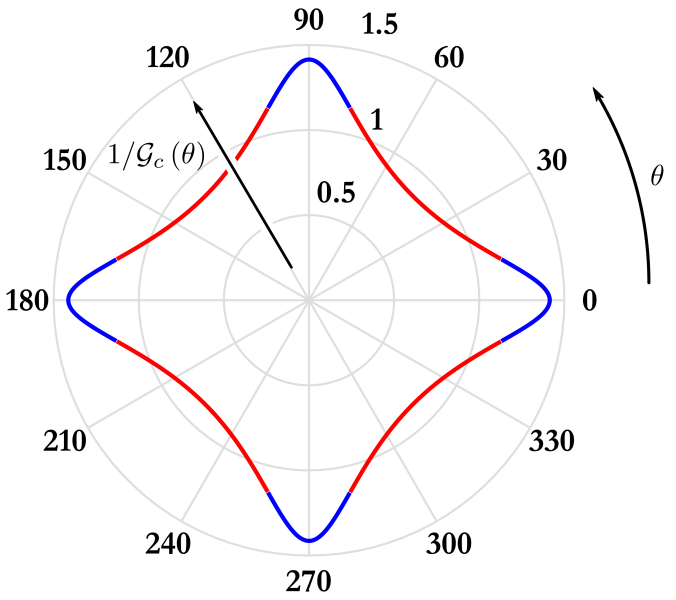

(a)

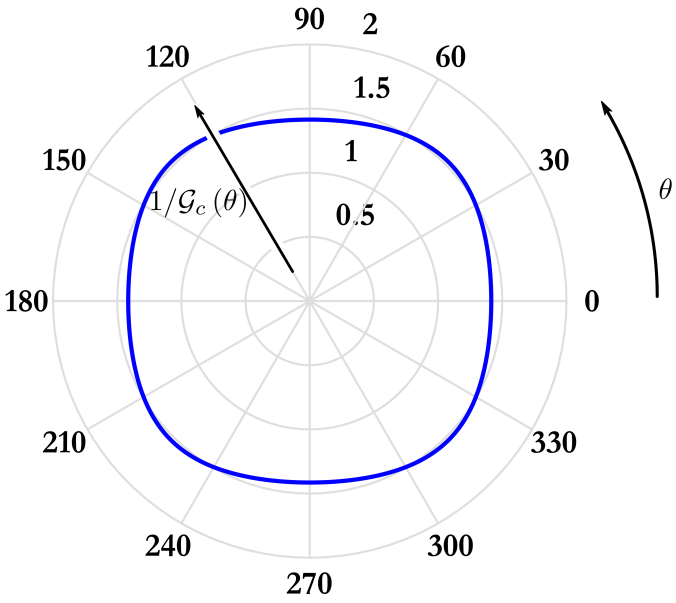

(b)

Figure 5.11: Polar plots of the reciprocals $1/\mathcal{G}_c(\theta)$ of (a) the non-convex (see 5.10(a)) and (b) convex (see 5.10(b)) surface energy densities. The red portions of the curves are refereed to $\mathcal{S}^r(\theta) < 0$ while the blue to $\mathcal{S}^r(\theta) > 0$.

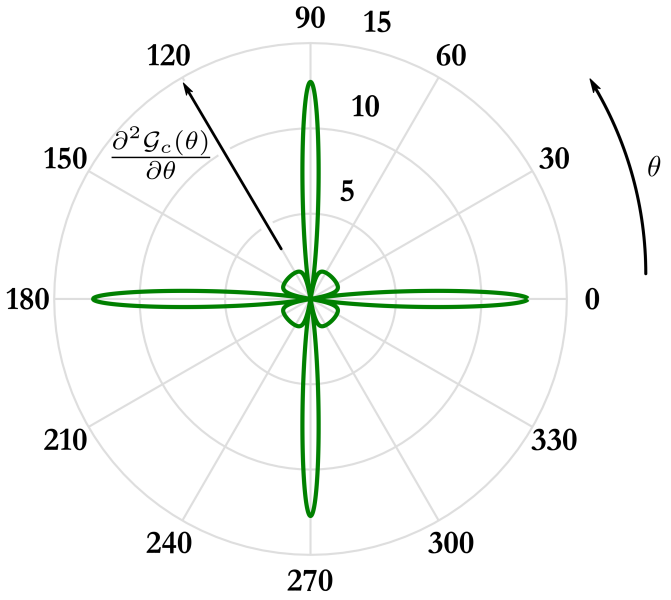

(a)

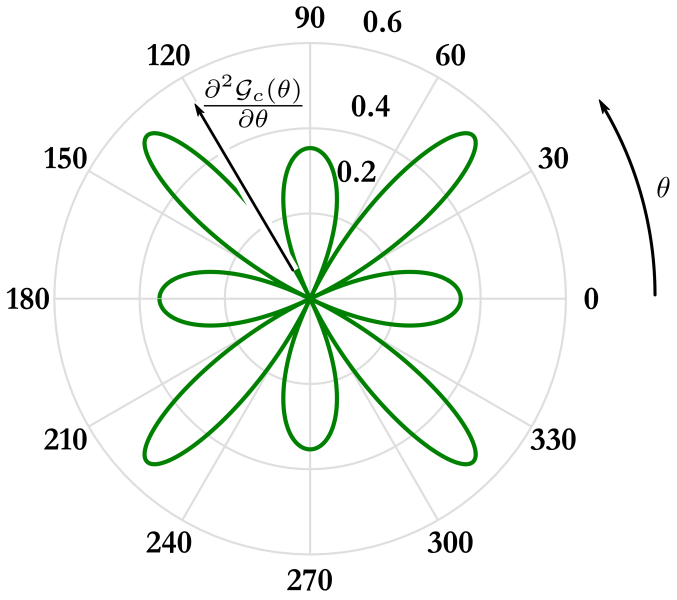

(b)

Figure 5.12: Polar plots of the second derivatives $\frac{\partial^2 \mathcal{G}_c(\theta)}{\partial \theta}$ of (a) the non-convex (see 5.10(a)) and (b) convex (see 5.10(b)) surface energy densities.

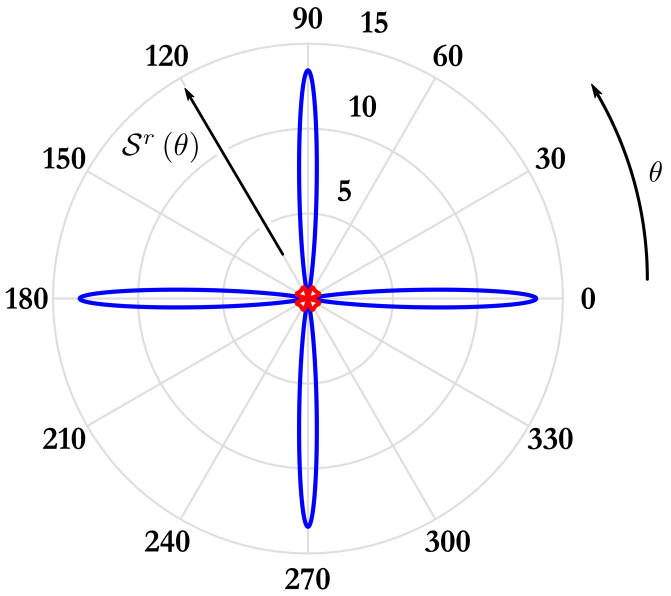

(a)

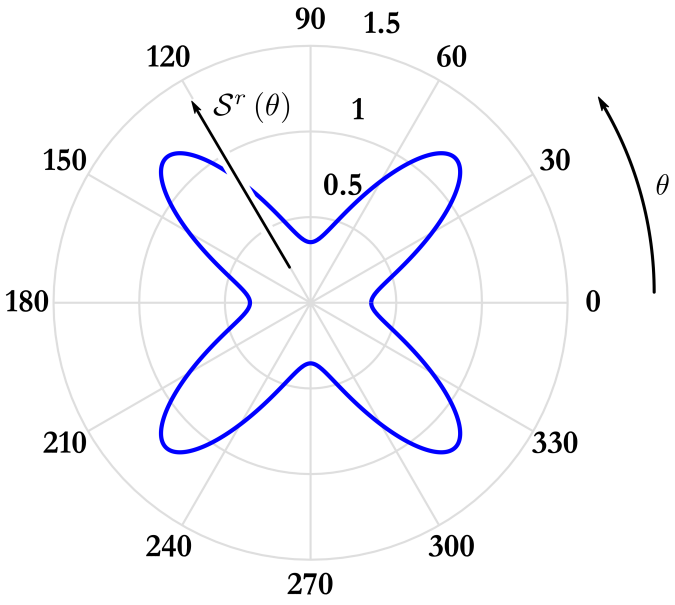

(b)

Figure 5.13: Polar plots of the surface stiffness $\mathcal{S}^r(\theta)$ of (a) the non-convex (see 5.10(a)) and (b) convex (see 5.10(b)) surface energy densities. The red portions of the curves are refereed to $\mathcal{S}^r(\theta) < 0$ while the blue to $\mathcal{S}^r(\theta) > 0$.

Applying the divergence theorem and performing the necessary algebraic manipulation, the balance of energy equation (5.19) becomes

$$\begin{aligned}
&\int_{\partial\Omega_{\bar{t}}} \left([\boldsymbol{\sigma}\mathbf{n} - \bar{\mathbf{t}}] \cdot \dot{\mathbf{u}}\right) d\partial\Omega + \int_{\Omega} \left([\rho\ddot{\mathbf{u}} - \nabla\cdot\boldsymbol{\sigma} - \mathbf{b}] \cdot \dot{\mathbf{u}}\right) d\Omega + \\
&\int_{\partial\Omega} \left(\left[\bar{\mathcal{G}}_c l_0 2\nabla c - \bar{\mathcal{G}}_c l_0^3 \sum_{ijkl} \gamma_{ijkl} \left(\frac{\partial^3 c}{\partial x_j \partial x_k \partial x_l} \right) - \bar{\mathcal{G}}_c l_0^3 \sum_{ijkl} \gamma_{ijkl} \left(\frac{\partial^3 c}{\partial x_i \partial x_j \partial x_k} \right) \right] \cdot \mathbf{n}\dot{c} \right) d\partial\Omega + \\
&\int_{\partial\Omega} \left(\left[\bar{\mathcal{G}}_c l_0^3 \sum_{ijkl} \gamma_{ijkl} \left(\frac{d}{dt} \left(\frac{\partial c}{\partial x_i} \right) \frac{\partial^2 c}{\partial x_k \partial x_l} \right) + \bar{\mathcal{G}}_c l_0^3 \sum_{ijkl} \gamma_{ijkl} \left(\frac{\partial^2 c}{\partial x_i \partial x_j} \frac{d}{dt} \left(\frac{\partial c}{\partial x_l} \right) \right) \right] \cdot \mathbf{n} \right) d\partial\Omega + \\
&\int_{\Omega} \left[\psi_{el_c} + \frac{\bar{\mathcal{G}}_c \left(c-1\right)}{2l_0} - \bar{\mathcal{G}}_c l_0 2\Delta c + 2\bar{\mathcal{G}}_c l_0^3 \sum_{ijkl} \gamma_{ijkl} \left(\frac{\partial^4 c}{\partial x_i \partial x_j \partial x_k \partial x_l} \right) \right] \dot{c}\, d\Omega = 0
\end{aligned} \tag{5.21}$$

where $\boldsymbol{\sigma}$ is the stress field derived from relation (2.50) whereas $\mathbf{n}$ is the outward unit normal vector of the boundary and $\psi_{el_c} = \partial\psi_{el}/\partial c = 2\left(1-k_f\right)c\psi_{el}^{+}$ is the derivative of elastic strain energy density with respect to the phase field c. The methodology employed for deriving Eq. (5.21) is presented in Appendix B.

Since Eq. (5.21) must hold for arbitrary values of $\dot{\mathbf{u}}$, $\dot{c}$ and $\nabla\dot{c}\cdot\mathbf{n}$ the resulting strong form is eventually derived as

$$\begin{cases}
\nabla\cdot\boldsymbol{\sigma} + \mathbf{b} = \rho\ddot{\mathbf{u}} & \text{on } [{}^{(0)}\Omega, {}^{(t)}\Omega] \\
\left(\dfrac{4l_0\left(1-k_f\right)\mathcal{H}}{\bar{\mathcal{G}}_c} + 1 \right) c - 4l_0^2\Delta c & \\
\qquad + 4l_0^4 \displaystyle\sum_{ijkl} \gamma_{ijkl} \frac{\partial^4 c}{\partial x_i \partial x_j \partial x_k \partial x_l} = 1 & \text{on } [{}^{(0)}\Omega, {}^{(t)}\Omega]
\end{cases} \tag{5.22}$$

where $\mathcal{H}$ is the history field defined as the maximum value of the tensile part of the elastic energy density ψ_{el}^{+} obtained in the domain $[0,t]$ that satisfies the Kuhn-Tucker conditions (Eqs. (2.59)).

Finally, the coupled field equations (5.22) are subject to the set of boundary and initial conditions presented in Eq. (5.23)

$$
\begin{cases}
\boldsymbol{\sigma}\mathbf{n} = \bar{\mathbf{t}}, & \text{on } [{}^{(0)}\partial\Omega_{\bar{\mathbf{t}}}, {}^{(t)}\partial\Omega_{\bar{\mathbf{t}}}] \\
\mathbf{u} = \bar{\mathbf{u}}, & \text{on } [{}^{(0)}\partial\Omega_{\bar{\mathbf{u}}}, {}^{(t)}\partial\Omega_{\bar{\mathbf{u}}}] \\
\mathbf{u} = {}^{(0)}\mathbf{u}, & \text{on } {}^{(0)}\Omega \\
\dot{\mathbf{u}} = {}^{(0)}\dot{\mathbf{u}}, & \text{on } {}^{(0)}\Omega \\
\ddot{\mathbf{u}} = {}^{(0)}\ddot{\mathbf{u}}, & \text{on } {}^{(0)}\Omega \\
\left[4l_0^2 \nabla c - 2l_0^4 \sum_{ijkl} \gamma_{ijkl} \left(\dfrac{\partial^3 c}{\partial x_j \partial x_k \partial x_l} \right) \right. & \\
\left. -2l_0^4 \sum_{ijkl} \gamma_{ijkl} \left(\dfrac{\partial^3 c}{\partial x_i \partial x_j \partial x_k} \right) \right] \cdot \mathbf{n} = 0 & \text{on } [{}^{(0)}\partial\Omega, {}^{(t)}\partial\Omega] \\
2l_0^4 \sum_{ijkl} \gamma_{ijkl} \left(\frac{\partial^2 c}{\partial x_k \partial x_l} \right) + 2l_0^4 \sum_{ijkl} \gamma_{ijkl} \left(\frac{\partial^2 c}{\partial x_i \partial x_j} \right) = 0, & \text{on } [{}^{(0)}\partial\Omega, {}^{(t)}\partial\Omega] \\
c = {}^{(0)}c, & \text{on } {}^{(0)}\Omega.
\end{cases}
\tag{5.23}
$$

5.3 Material Point Method for anisotropic brittle fracture

5.3.1 Discrete equations

The governing coupled Eqs. (5.22) are approximated with the MPM following the methodology introduced in Section 4.2. In this, the discrete equilibrium equations remain the same, as described in Section 4.2.1. Phase field discrete equation for anisotropic brittle fracture within a MPM setting are introduced in Section 5.3.1.1.

5.3.1.1 Anisotropic phase field discrete equations

The discrete form of the anisotropic phase field governing equations introduced in the second of Eqs. (5.22) is derived with the methodology employed in Section 4.2.2. In particular, the phase field strong form introduced in the second of Eqs. (5.22) becomes

$$\begin{aligned}\int_\Omega \Big(\frac{4l_0(1-k_f)\mathcal{H}}{\bar{\mathcal{G}}_c}+1\Big)cq\,d\Omega + \int_\Omega 4l_0^2(\nabla c:\nabla q)\,d\Omega \\ + \int_\Omega 4l_0^4\sum_{ijkl}\gamma_{ijkl}\left(\frac{\partial^2 c}{\partial x_i\partial x_j}\frac{\partial^2 q}{\partial x_k\partial x_l}\right)d\Omega \\ = \int_\Omega q\,d\Omega\end{aligned} \tag{5.24}$$

where c is the phase field and q are the corresponding weighting functions. The phase field c and the corresponding weighting functions q are defined with respect to the following spaces, i.e.,

$$\mathcal{Y} = \{c \in H^1(\Omega)\}$$

and

$$\mathcal{Q} = \{q \in H^1(\Omega)\},$$

respectively. Introducing the MPM approximation (Eq. (3.42)) into Eq. (5.24), the following expression is retrieved

$$\begin{aligned}\sum_{p=1}^{N_p}\mathcal{F}_p c_p q_p \Omega_p + \sum_{p=1}^{N_p} 4l_{0_p}^2(\nabla c_p:\nabla q_p)\Omega_p \\ + \sum_{p=1}^{N_p} 4l_{0_p}^4\sum_{ijkl}\gamma_{ijkl_p}\left(\frac{\partial^2 c_p}{\partial x_i\partial x_j}\frac{\partial^2 q_p}{\partial x_k\partial x_l}\right)\Omega_p = \sum_{p=1}^{N_p} q_p\Omega_p\end{aligned} \tag{5.25}$$

where c_p, q_p and γ_{ijkl_p} are the phase field, weighting functions and tensor components evaluated at the material point p. Parameter $\mathcal{F}_p$ in Eq. (5.25) is expressed as

$$\mathcal{F}_p = \frac{4l_{0_p}(1-k_{f_p})\mathcal{H}_p}{\bar{\mathcal{G}}_{c_p}} + 1 \tag{5.26}$$

where l_{0_p}, k_p, $\mathcal{H}_p$ and $\bar{\mathcal{G}}_{c_p}$ are the length scale parameter, model parameter, history field and critical fracture energy density of material point $\mathbf{x}_p$.

Both c_p and q_p are interpolated at the nodal points of the background mesh, using the higher-order B-spline interpolation functions as in the case of the displacement field. Use of high-order B-spline functions is required in this case, as second derivatives of the phase field appear on the variational expression (5.24). Thus, the interpolation relations considered assume the following form for the test functions and their first and second derivatives, i.e.,

$$q_p = \sum_{I=1}^{N_n} N_I(\mathbf{x}_p) q_I \tag{5.27}$$

$$\nabla q_p = \sum_{I=1}^{N_n} \nabla N_I(\mathbf{x}_p) q_I \tag{5.28}$$

and

$$\Delta q_p = \sum_{I=1}^{N_n} \Delta N_I(\mathbf{x}_p) q_I, \tag{5.29}$$

respectively. In Eqs. (5.27)-(5.29), $N_I(\mathbf{x}_p)$ are the background mesh shape functions pertinent to the phase field interpolation, q_I are nodal values of the corresponding test functions and Δ is the Laplace operator.

Similarly, the material point phase field is interpolated at the nodal values of its parent cell c_I according to Eq. (5.30)

$$c_p = \sum_{I=1}^{N_n} N_I(\mathbf{x}_p) c_I \tag{5.30}$$

whereas a similar interpolation scheme is assumed for its first

$$\nabla c_p = \sum_{I=1}^{N_n} \nabla N_I(\mathbf{x}_p) c_I \tag{5.31}$$

and second derivative

$$\Delta c_p = \sum_{I=1}^{N_n} \Delta N_I(\mathbf{x}_p) c_I, \tag{5.32}$$

respectively. Substituting, Eqs. (5.27),(5.28) and (5.29) into the discrete expression (5.25), the following relation is established

$$R_I^{c,Anis}(c) = S_I^{c,Anis} - F_I^c = 0, \quad I = 1\ldots, N_n \tag{5.33}$$

where

$$\begin{aligned} S_I^{c,Anis} = \sum_{p=1}^{N_p} \mathcal{F}_p c_p N_I(\mathbf{x}_p)\Omega_p + \sum_{p=1}^{N_p} 4l_{0_p}^2(\nabla c_p \cdot \nabla N_I(\mathbf{x}_p))\Omega_p \\ + \sum_{p=1}^{N_p} 4l_{0_p}^4 \sum_{ijkl} \gamma_{ijkl_p} \left(\frac{\partial^2 c_p}{\partial x_i \partial x_j} \frac{\partial^2 N_I(\mathbf{x}_p)}{\partial x_k \partial x_l} \right) \Omega_p \end{aligned} \tag{5.34}$$

and

$$F_I^c = \sum_{p=1}^{N_p} N_I(\mathbf{x}_p)\Omega_p, \tag{5.35}$$

respectively whereas $R_I^{c,Anis}(c)$ denotes the residual nodal values for the phase field.

Furthermore, introducing the phase field interpolation schemes (Eqs. (5.30) to (5.32)) and performing the necessary algebraic manipulation, the material point discrete phase field equations for the case of anisotropic fracture are cast in the following convenient form

$$\mathbf{K}^{c,Anis}\mathbf{c} = \mathbf{F}^c \tag{5.36}$$

where $\mathbf{K}^{c,Anis}$ is an $(N_n \times N_n)$ coefficient matrix whose $K_{I,J}^{c,Anis}$ component is expressed as

$$\begin{aligned} K_{I,J}^{c,Anis} = \sum_{p=1}^{N_p} \Bigg(\mathcal{F}_p N_J(\mathbf{x}_p) N_I(\mathbf{x}_p) + 4l_{0_p}^2 \Big(\nabla N_J(\mathbf{x}_p) \cdot \nabla N_I(\mathbf{x}_p) \Big) \\ + 4l_{0_p}^4 \sum_{ijkl} \gamma_{ijkl_p} \left(\frac{\partial^2 N_J(\mathbf{x}_p)}{\partial x_i \partial x_j} \frac{\partial^2 N_I(\mathbf{x}_p)}{\partial x_k \partial x_l} \right) \Bigg) \Omega_p. \end{aligned} \tag{5.37}$$

Vector $\mathbf{c}$ is the $(N_n \times 1)$ vector of unknown nodal phase fields and $\mathbf{F}^c$ is the $(N_n \times 1)$ vector whose F_I^c component is defined from relation (5.35).

5.3.2 Anisotropic PF-MPM solution scheme

In this work, a staggered iterative scheme is adopted for the solution of the system of coupled discrete equations (4.1) and (5.36), as described in Section 4.3. The anisotropic PF-MPM pseudo-code is provided in Algorithm 2.

To evaluate the anisotropic phase field coefficient matrix (see Eq. (5.37)), the derivatives of basis functions are evaluated in the material principal axes. Thus, if $(\nabla \mathbf{N}(\mathbf{x}_p))$ and $(\boldsymbol{\Delta} \mathbf{N}(\mathbf{x}_p))$ are the first and second derivatives of basis functions in global axes, then $(\nabla \mathbf{N}_{\phi_p}(\mathbf{x}_p))$ and $(\boldsymbol{\Delta} \mathbf{N}_{\phi_p}(\mathbf{x}_p))$ are the corresponding quantities in the material principal axes of the p^{th} material point. In the two-dimensional case, coordinate transformation from the global system $\mathbf{x} = \{x_1, x_2\}^T$ to the material principal system $\mathbf{x}_{\phi_p} = \{x_{1_{\phi_p}}, x_{2_{\phi_p}}\}^T$ is achieved through relation (5.38) below

$$\begin{Bmatrix} x_{1_{\phi_p}} \\ x_{2_{\phi_p}} \end{Bmatrix} = \begin{bmatrix} \cos(\phi_p) & -\sin(\phi_p) \\ \sin(\phi_p) & \cos(\phi_p) \end{bmatrix} \begin{Bmatrix} x_1 \\ x_2 \end{Bmatrix} \Leftrightarrow \mathbf{x}_{\phi_p} = \mathbf{R}_p \mathbf{x} \tag{5.38}$$

and

$$\mathbf{R}_p = \begin{bmatrix} \cos(\phi_p) & -\sin(\phi_p) \\ \sin(\phi_p) & \cos(\phi_p) \end{bmatrix} \tag{5.39}$$

where ϕ_p is the material orientation of the material point (counter clockwise).

5.3.3 Numerical examples

In this Section, a series of benchmark tests are examined with the proposed anisotropic PF-MPM scheme. For verification purposes, both the PF-MPM as well as its Finite Element counter part (PF-FEM) have been implemented in an in-house Fortran code.

Data: Define computational grid, material point properties (${}^{(0)}\mathbf{x}_p$, ${}^{(0)}\Omega_p$, ν_p, l_{0_p}, k_{f_p}, $\bar{\mathcal{G}}_{c_p}$, γ_{ijkl_p}, ϕ_p, ${}^{(0)}\mathcal{H}_p$, ${}^{(0)}\boldsymbol{\sigma}_p$, ${}^{(0)}\boldsymbol{\varepsilon}_p$)

for *each time step* $m = 1, 2, .., N_{steps}$ **do**

Reset the computational grid: Find active part of Eulerian Grid, N_n, N_{dofs}, N_{cells};

Compute: $\mathbf{N}({}^{(m)}\mathbf{x}_p)$, $\nabla\mathbf{N}({}^{(m)}\mathbf{x}_p)$, $\boldsymbol{\Delta}\mathbf{N}({}^{(m)}\mathbf{x}_p)$ and $\mathbf{B}({}^{(m)}\mathbf{x}_p)$, for all material points (see Section 3.9.9 and Eq. (3.54)). ;

Compute: $\nabla\mathbf{N}({}^{(m)}\mathbf{x}_{\phi_p})$ and $\boldsymbol{\Delta}\mathbf{N}({}^{(m)}\mathbf{x}_{\phi_p})$, for all material points. ;

Define: $\delta\mathbf{R}^{u(1)} = \boldsymbol{\Delta}\mathbf{F}^{ext}$;

for *each staggered iteration* $k = 1, 2, .., N_{staggs}$ **do**

Compute: ${}^{(m)}\mathbf{F}^{c(k)}$ (see Eq. (5.35)). ;

Compute: $\mathbf{K}^{c,Anis}$ (see Eq. (5.37)) according to $\mathbf{N}({}^{(m)}\mathbf{x}_p)$, $\nabla\mathbf{N}({}^{(m)}\mathbf{x}_{\phi_p})$ and $\boldsymbol{\Delta}\mathbf{N}({}^{(m)}\mathbf{x}_{\phi_p})$. ;

Solve: $\mathbf{K}^{c,Anis}\,{}^{(m)}\mathbf{c}^{(k)} = {}^{(m)}\mathbf{F}^{c(k)}$;

Map phase field (${}^{(m)}\mathbf{c}^{(k)}$) from grid nodes to material points. Evaluate: ${}^{(m)}c_p^{(k)}$, ${}^{(m)}\nabla c_p^{(k)}$, ${}^{(m)}\Delta c_p^{(k)}$, ${}^{(m)}g_p^{(k)}$, for all material points (see Eq. (5.30), (5.31),(5.32) and (2.48)). ;

Initialize $\boldsymbol{\Delta}\mathbf{u}^{(0)} = \mathbf{0}$;

for *each inner iteration* $j = 1, 2, .., N_{iters}$ **do**

Compute: $\mathbf{K}^u$ (see Eq. (3.59), for constitutive matrix see Eq. (2.51)) ;

Solve: $\mathbf{K}^u\delta\mathbf{u}^{(j)} = \delta\mathbf{R}^{u(j)}$, with displacement control. ;

Compute: $\boldsymbol{\Delta}\mathbf{u}^{(j)} = \boldsymbol{\Delta}\mathbf{u}^{(j-1)} + \delta\mathbf{u}^{(j)}$;

Compute: $\boldsymbol{\Delta}\boldsymbol{\varepsilon}_p^{(j)}$, for all material points (see Eq. (3.56)). ;

Compute: ${}^{(m)}\boldsymbol{\varepsilon}_p^{(j)} = {}^{(m-1)}\boldsymbol{\varepsilon}_p^{(j)} + \boldsymbol{\Delta}\boldsymbol{\varepsilon}_p^{(j)}$, for all material points. ;

Compute: ${}^{(m)}\boldsymbol{\sigma}_p^{(j)}$, for all material points (see Eq. (2.50)) ;

Compute: $\boldsymbol{\Delta}\mathbf{F}^{int(j)} = \{\boldsymbol{\Delta}\mathbf{F}_I^{int}\}$, $\boldsymbol{\Delta}\mathbf{F}_I^{int} = \sum_{p=1}^{N_p} {}^{(m)}\Omega_p^{(j)}\,{}^{(m)}\boldsymbol{\sigma}_p^{(j)} - {}^{(m-1)}\boldsymbol{\sigma}_p^{(j)} \cdot \mathbf{B}_I({}^{(m)}\mathbf{x}_p)$;

Compute Residual (Displacement-Field): $\delta\mathbf{R}^{u(j)} = \boldsymbol{\Delta}\mathbf{F}^{ext} - \boldsymbol{\Delta}\mathbf{F}^{int(j)}$;

Convergence Check (Displacement Field): If $\|\delta\mathbf{R}^{u(j)}\| \leq tol_u$ or $j \geq N_{iters}$ then "exit" from loop else $j = j + 1$ go to next inner iteration. ;

end

Compute: ${}^{(m)}\psi_{el_p}^{+}$, for all material points (see Eq. (2.77))

$\rightarrow {}^{(m)}\mathcal{H}_p = \begin{cases} {}^{(m)}\psi_{el_p}^{+}, & \text{for } {}^{(m)}\psi_{el_p}^{+} > {}^{(m-1)}\mathcal{H}_p \\ {}^{(m-1)}\mathcal{H}_p, & \text{otherwise} \end{cases}$;

Compute Residual (Phase Field): ${}^{(m)}\mathbf{R}^{c,Anis(k)}$ (see Eq. (5.33)) according to ${}^{(m)}c_p^{(k)}$, ${}^{(m)}\nabla c_p^{(k)}$, ${}^{(m)}\Delta c_p^{(k)}$, ${}^{(m)}\mathcal{H}_p$;

Convergence Check (Phase Field): If $\|\,{}^{(m)}\mathbf{R}^{c,Anis(k)}\| \leq tol_c$ or $k \geq N_{staggs}$ then "exit" from loop else $k = k + 1$ go to next staggered iteration. ;

end

Compute: $\boldsymbol{\Delta}\mathbf{u}_p = \sum_{I=1}^{N_n} N_I({}^{(m)}\mathbf{x}_p)\boldsymbol{\Delta}\mathbf{u}_I^{(j)}$, for all material points. ;

Compute: ${}^{(m)}\mathbf{u}_p = {}^{(m-1)}\mathbf{u}_p + \boldsymbol{\Delta}\mathbf{u}_p$, for all material points. ;

Compute: ${}^{(m)}\mathbf{x}_p = {}^{(m-1)}\mathbf{x}_p + \boldsymbol{\Delta}\mathbf{u}_p$, for all material points. ;

end

Algorithm 2: Anisotropic Phase Field Material Point Method pseudo-code (Staggered Solution Algorithm).

5.3.3.1 Square plate under pure tension

In this example, the case of a square plate under pure tension is examined. This example is used to examine the effect of the material orientation on the direction of the propagating crack. The geometry and boundary conditions of the problem are shown in Fig. 5.14(a). Displacements in segment BC are restrained along Y whereas a pin support is considered at point O restraining displacement in both directions. A load is applied at point A along Y. All points in segment AB - with the exception of B - are restrained so that their corresponding displacement components along Y are equal. The restraint is achieved by using a Penalty method with penalty parameter $\alpha = 1000000$ (see Appendix A for imposing kinematical constrains with Penalty method in MPM). Plane strain conditions are assumed with the elastic isotropic properties of the material, $E = 1000000$ kN/m^2 and $\nu = 0.3$ for the Young modulus and Poisson's ratio, respectively.

To gain insight into the influence of surface energy on the crack path, two cases are considered, namely that of cubic and orthotropic symmetry. The corresponding material properties are presented in Table 5.1. Furthermore, the polar plots of their surface energy density $\mathcal{G}_c(\theta)$ and their reciprocals $1/\mathcal{G}_c(\theta)$ for material orientation $\phi = 0$ are shown in Figs. 5.14(b) and 5.14(c), respectively. For cubic symmetry the maximum and minimum surface energy density are $\mathcal{G}_{c_{max}} = 1.1575$ kN/m and $\mathcal{G}_{c_{min}} = 0.7071$ kN/m, respectively. For the case of orthotropic symmetry these are $\mathcal{G}_{c_{max}} = 1.2292$ kN/m and $\mathcal{G}_{c_{min}} = 0.7071$ kN/m, respectively.

A displacement control Newton Raphson scheme is utilized with the maximum value of the monitored displacement $u = 0.006$ m. A force based convergence criterion is employed with a corresponding tolerance $tol_u = 1e-7$. A staggered solution procedure has been implemented with a single prediction step ($N_{staggs} = 1$)

The problem is solved using both the PF-FEM method and the PF-MPM method. Results obtained by both solution approaches also agree with the results provided in Li et al. (2015) where a purely meshless solution procedure was adopted. The Finite Element mesh used here comprises 29929 quadratic C^1-continuous cells with a mesh size $h = 0.00578$ m. A 3x3 quadrature rule is used for the quadratic basis functions as suggested in Hughes et al. (2010). The PF-MPM mesh consists of 32041 background quadratic C^1-continuous cells with a mesh size $h = 0.00578$ m. The initial cell density utilized is 3x3 $= 9$ material points per cell. All the simulation parameters are summarized in Table 5.1.

Eleven different material orientation angles are considered, namely

$$\phi = \{-50^o, -40^o, -30^o, -20^o, -10^o, 0^o, +10^o, +20^o, +30^o, +40^o, +50^o\} \quad (5.40)$$

The resulting load displacement paths for the case of $\phi = 0^o$ and $\phi = -50^o$ are shown in Figs. 5.15(a) and 5.16(a) for the case of cubic and orthotropic symmetry, respectively. Results between the MPM and FEM are in perfect agreement, as also shown by the corresponding relative error shown in Figs. 5.15(b) and 5.16(b). The relative error is defined by Eq. (4.19) and it is smaller than 1% for both angles. However, as the imposed displacement increases the error increases accordingly. This is attributed to the fact that in PF-MPM the position of sampling points, i.e., the material points, is updated. Conversely, the crack geometry is also updated. The variation of the ultimate limit load as a function of the material orientation angle is shown in Figs. 5.17(a) and 5.17(b) for cubic and orthotropic symmetry, respectively. Results derived from the MPM implementation agree with FEM.

Figs. 5.18(a)-(g) and 5.18(b)-(h) represent the phase field evolution for cubic symmetry and different values of material orientation ϕ for both PF-FEM and PF-MPM, respectively. Similarly, Figs. 5.19(a)-(g) and 5.19(b)-(h) represent the

phase field for orthotropic symmetry of both PF-FEM and PF-MPM, respectively.

The figures show that when $\phi < 45^o$, the crack path evolves in the lower half of the plate for both the cases of cubic and orthotropic symmetry (see Figs. 5.18(a)-(e), 5.18(b) -(f) and 5.19(a)-(e), 5.19(b)-(f)). However, when the material orientation angle increases, i.e., when $45 < \phi < 90^o$, then the crack path propagates along the higher half of the plate for cubic symmetry (see Figs. 5.18(g), 5.18(h)) and in the lower half of the plate for orthotropic symmetry (see Figs. 5.19(g), 5.19(h)). This pattern is anticipated due to four-fold and two-fold symmetry aspects of cubic symmetry and orthotropic materials, respectively.

Material Parameters					
Elastic Material Properties			Anisotropic Material Properties		
E	1000000	[kN/m^2]	γ_{1111}	1.00 (Cubic symmetry) 20.00 (Orthotropic symmetry)	[–]
ν	0.30	[–]	γ_{2222}	1.00	[–]
			γ_{1122}	0.00	[–]
			γ_{1212}	74.00	[–]
			l_0	0.01	[m]
			$\mathcal{G}_c$	0.50	[kN/m]
			$\mathcal{G}_{c_{max}}$	1.1575 (Cubic symmetry) 1.2292 (Orthotropic symmetry)	[kN/m]
			$\mathcal{G}_{c_{min}}$	0.7071 (Cubic symmetry) 0.7071 (Orthotropic symmetry)	[kN/m]
			ϕ	-50,-40,-30,-20,- 10,0,+10,+20,+30,+40,+50	[Deg]
Finite Element Method Model					
Number Of Control Points			30625		
Number Of Cells			173x173=29929		
Cell spacing			0.00578		[m]
$q_\xi = q_\eta$			2nd		
$\Xi = H$			$\{0, 0, 0, 0.00578, 0.01156, ..., 0.9884, 0.9942, 1, 1, 1\}$		
Quadrature rule			3x3		
Material Point Method Model					
Number Of Control Points			32761		
Number Of Cells			179x179=32041		
Cell spacing			0.00578		[m]
$q_\xi = q_\eta$			2nd		
$\Xi = H$			$\{0, 0, 0, 0.00559, 0.01117, ..., 0.9888, 0.9944, 1, 1, 1\}$		
Initial Cell density			3x3		
Solution Algorithm Parameters					
Δu			0.006		[mm]
N_{steps}			1000		
tol_u			1e-7		
N_{staggs}			1		
Penalty parameter α			1000000		

Table 5.1: Square plate under pure tension: Simulation parameters.

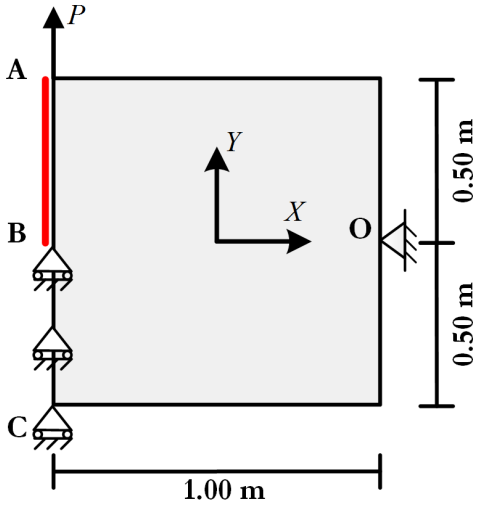

(a)

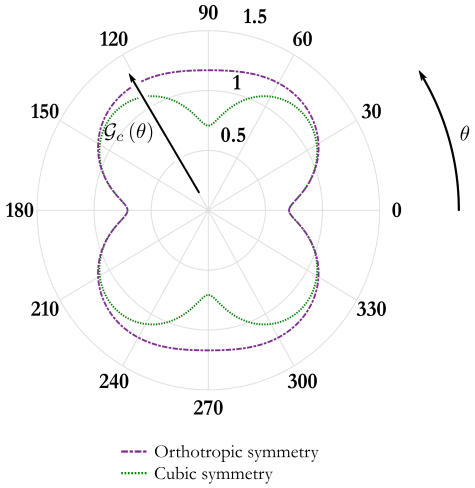

(b)

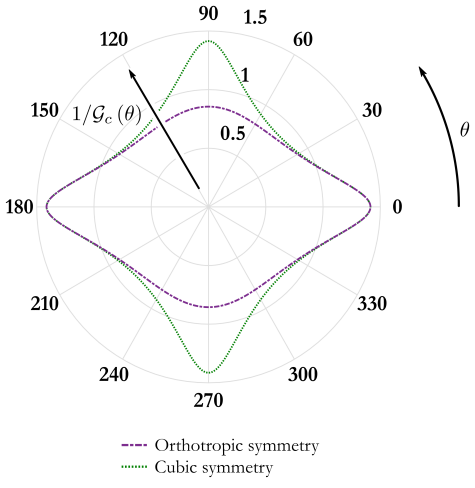

(c)

Figure 5.14: Square plate under pure tension: (a) Geometry and boundary conditions. (b) Surface energy densities and (c) their Reciprocals for material orientation $\phi = 0$ in polar coordinates.

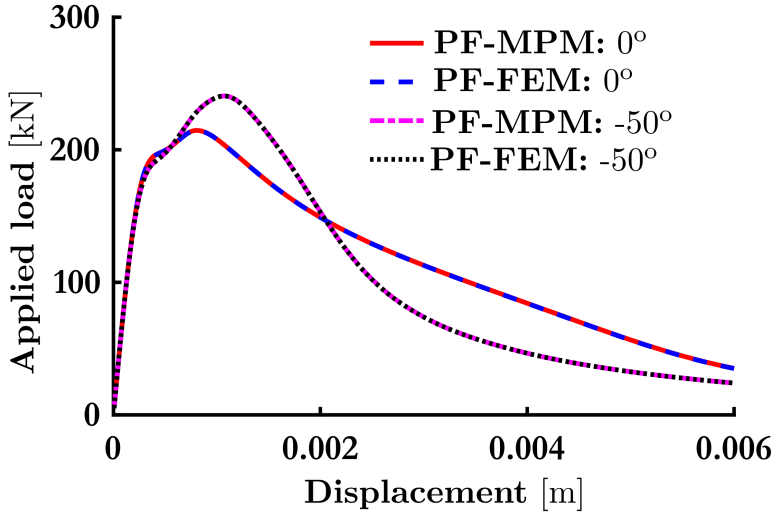

(a)

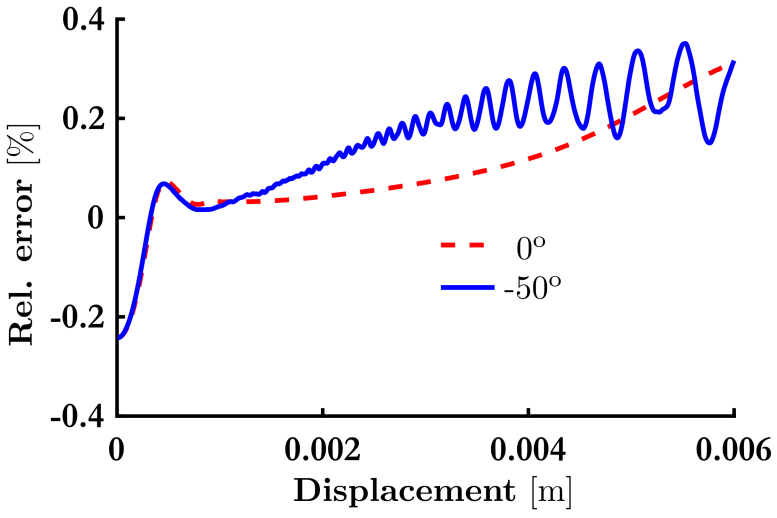

(b)

Figure 5.15: Square plate under pure tension: (a) PF-FEM vs PF-MPM comparison and (b) relative error for cubic symmetry.

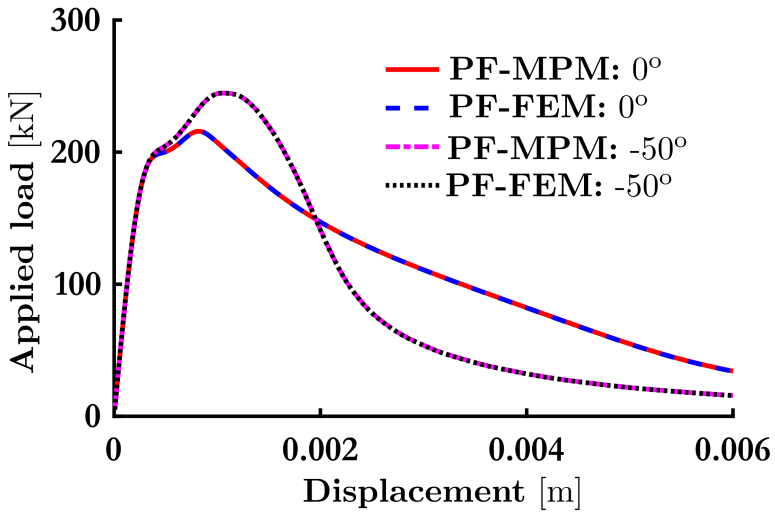

(a)

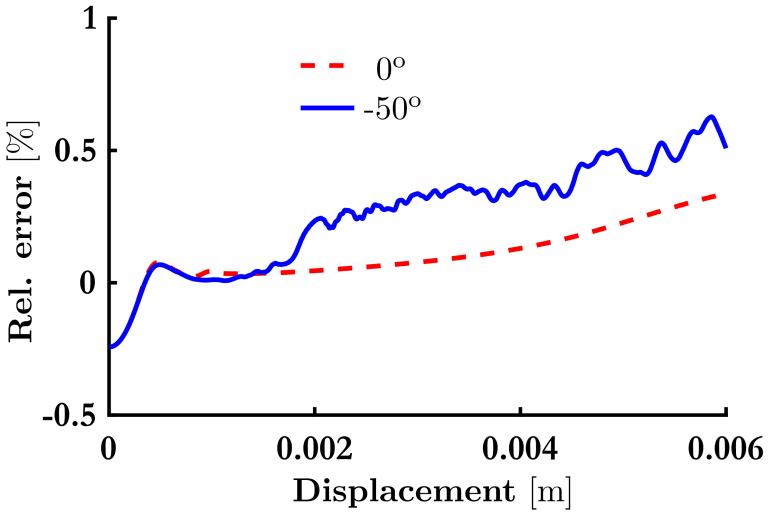

(b)

Figure 5.16: Square plate under pure tension: (a) PF-FEM vs PF-MPM comparison and (b) relative error for orthotropic symmetry.

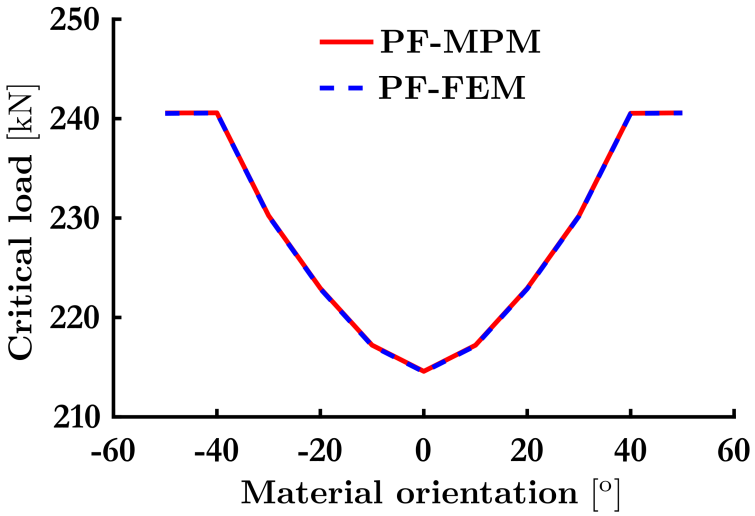

(a)

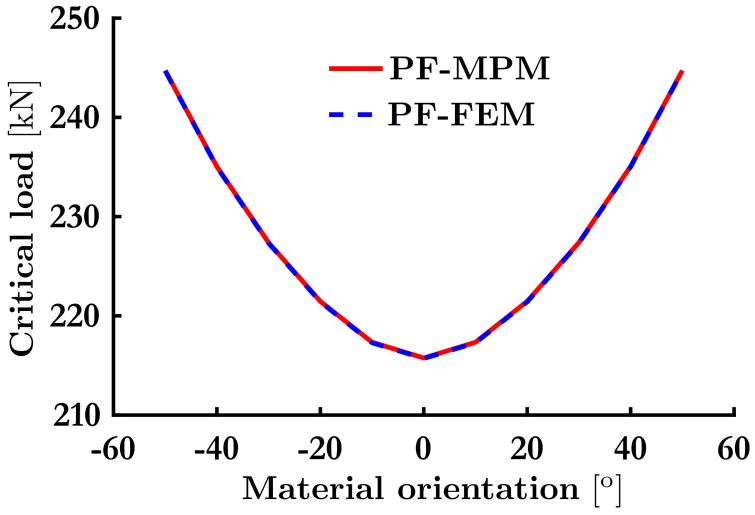

(b)

Figure 5.17: Square plate under pure tension: Critical Load vs Material Orientation for (a) cubic symmetry and (b) orthotropic symmetry.

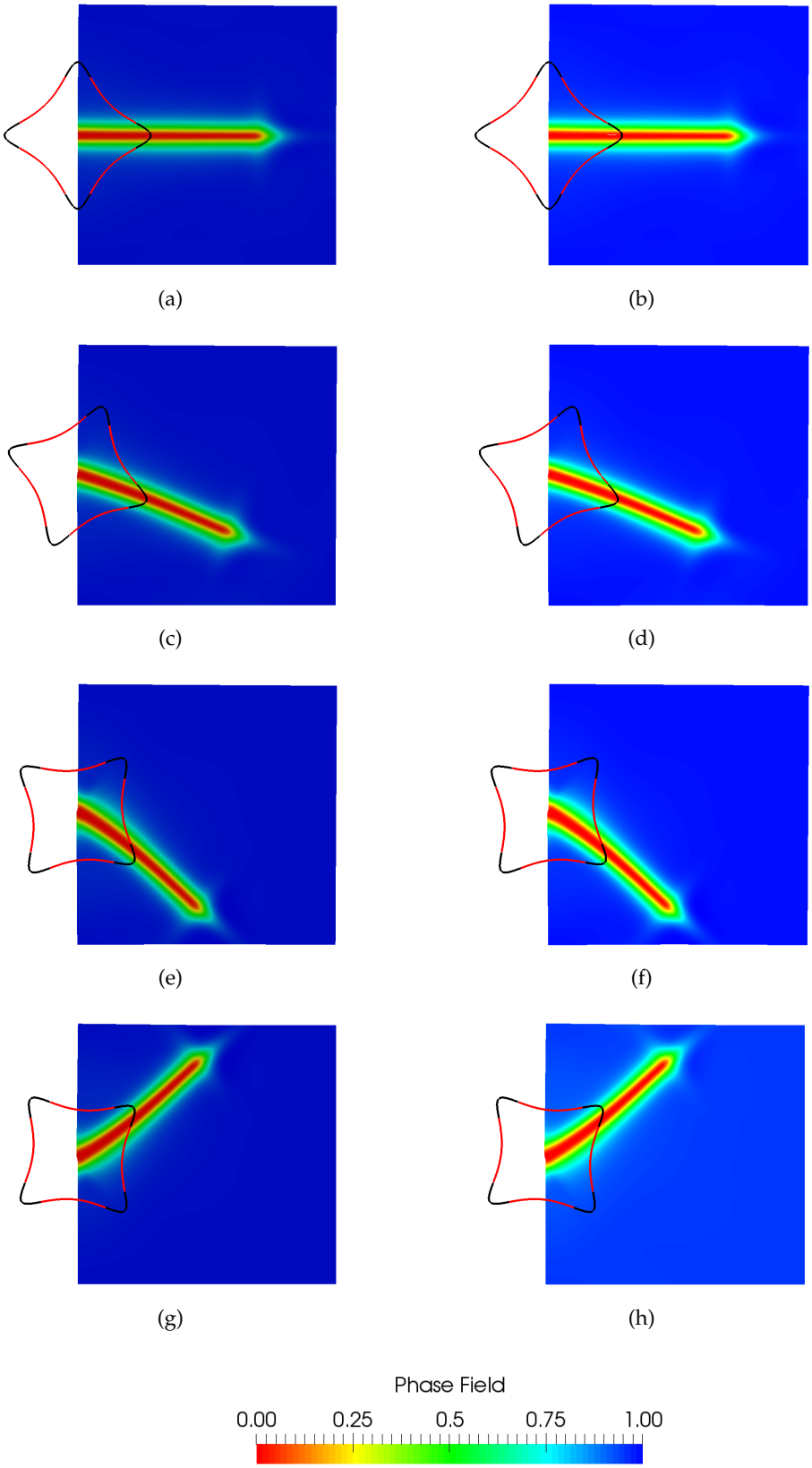

Figure 5.18: Square plate under pure tension: Phase field for $u = 0.006$ m and cubic symmetry. Finite Element Method for material orientation (a) 0^o, (c) $+20^o$, (e) $+40^o$ and (g) $+50^o$. Material Point Method for material orientation (b) 0^o, (d) $+20^o$, (f) $+40^o$ and (h) $+50$.

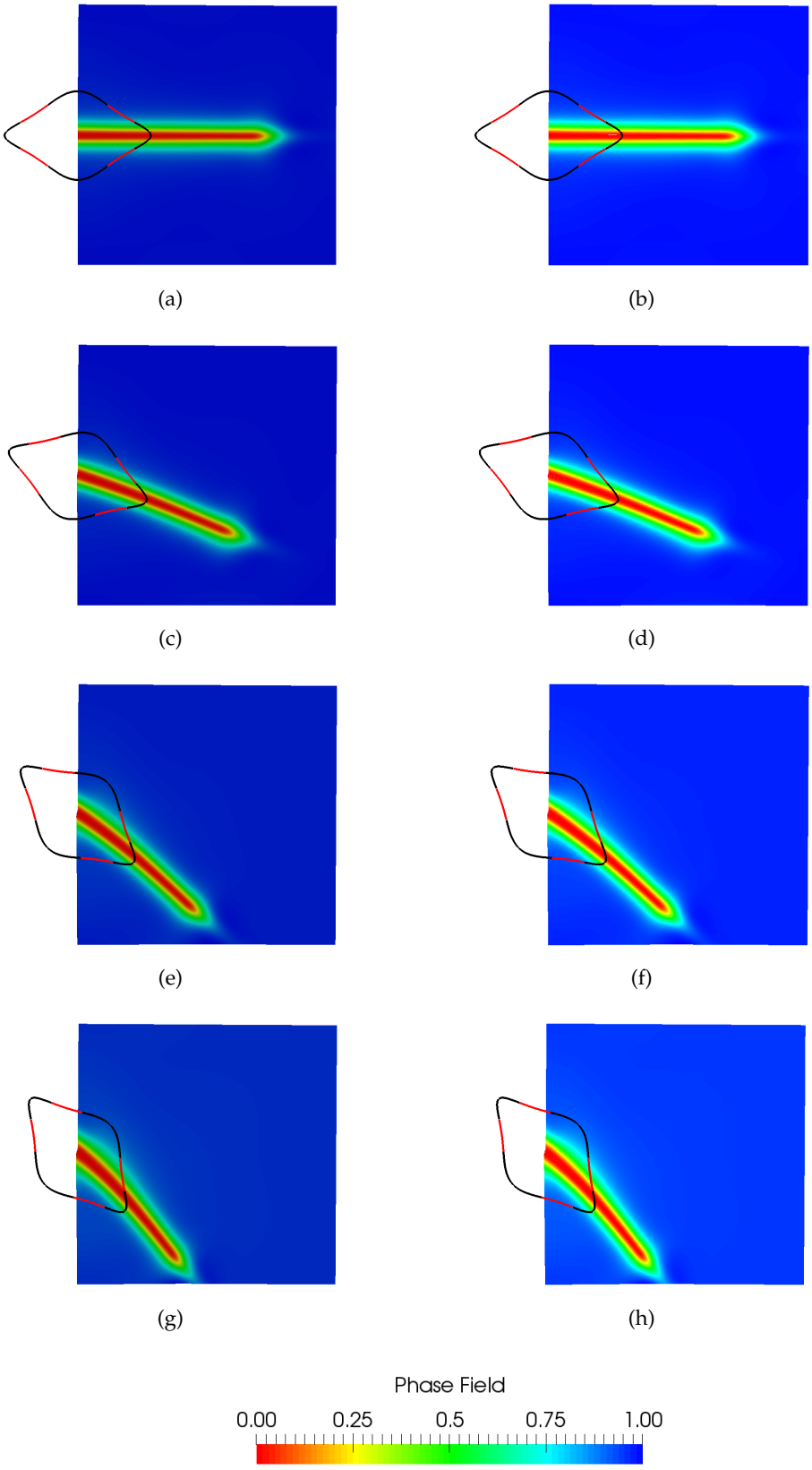

Figure 5.19: Square plate under pure tension: Phase field for $u = 0.006$ m and orthotropic symmetry. Finite Element Method for material orientation (a) 0^o, (c) $+20^o$, (e) $+40^o$ and (g) $+50^o$. Material Point Method for material orientation (b) 0^o, (d) $+20^o$, (f) $+40^o$ and (h) $+50$.

5.3.3.2 Three-point layered bending test

The case of a three point bending test on a composite beam is considered in this example. This example demonstrates the ability of the PF-MPM in simulating composite structures with different material anisotropic properties. The geometry and boundary conditions of the specimen are shown in Fig. 5.20(a). Plane strain conditions are assumed. The beam comprises two layers, namely A and B. The two layers have similar material properties as shown in Table 5.2. The elastic isotropic material properties are the same as in the previous example (see Section 5.3.3.1).

Cubic symmetry is considered for the surface energy density in both layers. The polar plots of the surface energy density and its reciprocal are shown in Figs. 5.20(b) and 5.20(c), respectively. The anisotropic parameters considered are presented in Table 5.2. Three different scenaria are examined for the material orientation of the two layers. In cases 1 and 2 the material orientations of both layers are $\phi = 0^o$ (case 1) and $\phi = -15^o$ (case 2), respectively. In case 3 the material orientation of layer A is $\phi = -15^o$ and layer B is $\phi = +15^o$.

A displacement control non-linear static analysis scheme is utilized with a constant displacement increment $\Delta u \approx 0.0033$ mm at midspan for 1500 steps. Staggered solution algorithm is utilized with a single prediction step ($N_{staggs} = 1$). A PF-FEM analysis is also made for verification purposes. The simulation parameters of both PF-MPM and PF-FEM are summarized into Table 5.2.

The corresponding load paths are shown in Fig. 5.21. The two methods demonstrate very good agreement for all three cases. In Figs. 5.22(a), 5.22(c) and 5.22(e) the phase field distribution retrieved from PF-FEM for case 1, case 2 and case 3, respectively is shown. The corresponding results from the PF-MPM are shown in Figs. 5.22(b), 5.22(d) and 5.22(f). All the results in Fig. 5.22 are retrieved at a vertical displacement $u = 5$ mm.

The crack paths derived from both methods are practically identical. In case 1 - with a material orientation angle - $\phi = 0^o$ - (see Figs. 5.22(a) and 5.22(b)), the crack propagates along the Y axis, exactly as in the case of isotropic surface energy. However, in case 2 (see Figs. 5.22(c) and 5.22(d)) the anisotropic surface energy forces the crack to diverge from the Y axis. Finally, in case 3 (see Figs. 5.22(e) and 5.22(f)) a crack 'kick' is observed in the interface of two layers as a result of their different material orientations ϕ. The evolution of the hydrostatic stress for case 3 and PF-MPM implementation is shown in Fig. 5.23 for three time steps, $u = 4.6$ mm, $u = 4.7$ mm and $u = 5$ mm, respectively. From these figures it can be verified that the crack propagates only due to tension as a result of the strain energy density ψ_{el} decomposition (see Eq. (2.43)).

Material Parameters							
Elastic Material Properties				Anisotropic Material Properties			
	Layer A	Layer B				Layer A	Layer B	
E	1000000	1000000	[kN/m^2]	γ_{1111}		1.00	1.00	[–]
ν	0.30	0.30	[–]	γ_{2222}		1.00	1.00	[–]
				γ_{1122}		0.00	0.00	[–]
				γ_{1212}		74.00	74.00	[–]
				l_0		0.005	0.005	[m]
				$\bar{\mathcal{G}}_c$		0.50	0.50	[kN/m]
				$\mathcal{G}_{c_{max}}$		1.1575	1.1575	[kN/m]
				$\mathcal{G}_{c_{min}}$		0.7071	0.7071	[kN/m]
					Case 1	0	0	
				ϕ	Case 2	-15	-15	[Deg]
					Case 3	-15	+15	
Finite Element Method Model								
Number Of Control Points				41584				
Number Of Cells				450x90=40500				
Cell spacing				0.0022				[m]
$q_\xi = q_\eta$				2nd				
Ξ				$\{0, 0, 0, 0.0022, 0.0044, ..., 0.9955, 0.9977, 1, 1, 1\}$				
H				$\{0, 0, 0, 0.0111, 0.0222, ..., 0.9777, 0.9888, 1, 1, 1\}$				
Quadrature rule				3x3				
Material Point Method Model								
Number Of Control Points				44884				
Number Of Cells				456x96=43776				
Cell spacing				0.0022				[m]
$q_\xi = q_\eta$				2nd				
Ξ				$\{0, 0, 0, 0.0021, 0.0043, ..., 0.9956, 0.9978, 1, 1, 1\}$				
H				$\{0, 0, 0, 0.0104, 0.0208, ..., 0.9791, 0.9895, 1, 1, 1\}$				
Initial Cell density				3x3				
Solution Algorithm Parameters								
Δu				0.0033				[mm]
N_{steps}				1500				
tol_u				1e-7				
N_{staggs}				1				

Table 5.2: Three point layered bending test: Simulation parameters.

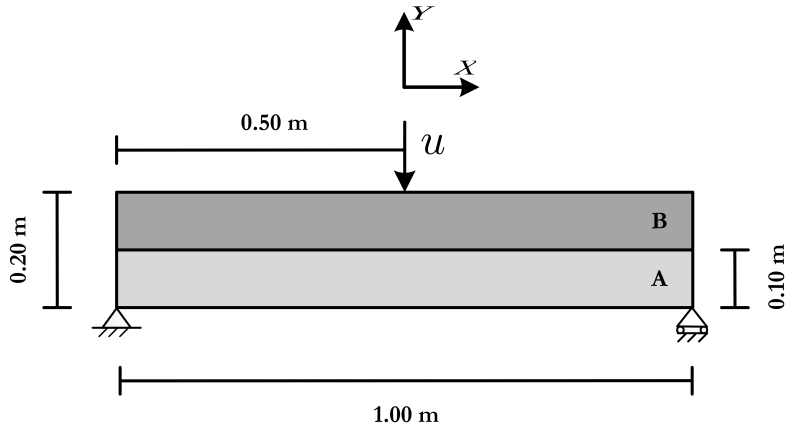

(a)

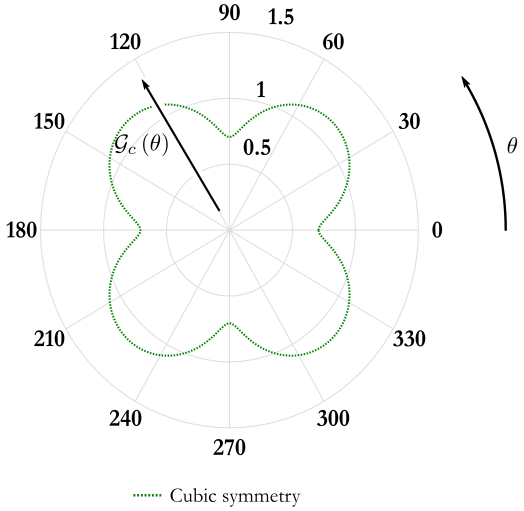

(b)

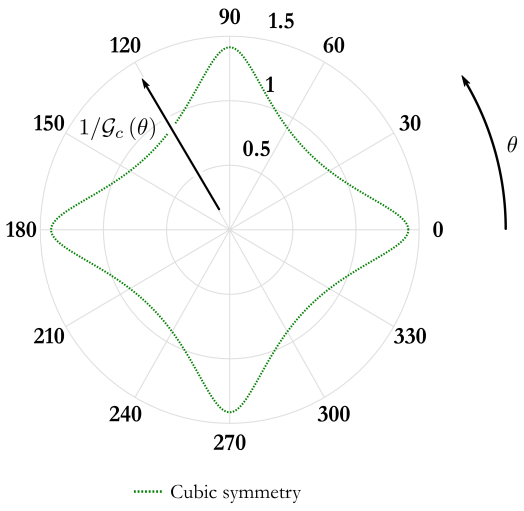

(c)

Figure 5.20: Three point layered bending test: (a) Geometry and boundary conditions. (b) Surface energy density and (c) its Reciprocal for material orientation $\phi = 0$ in polar coordinates.

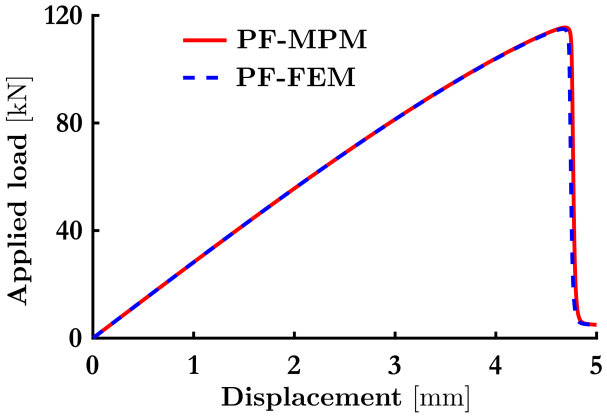

(a)

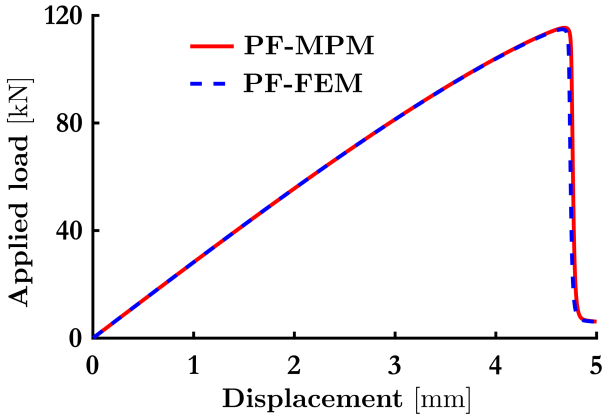

(b)

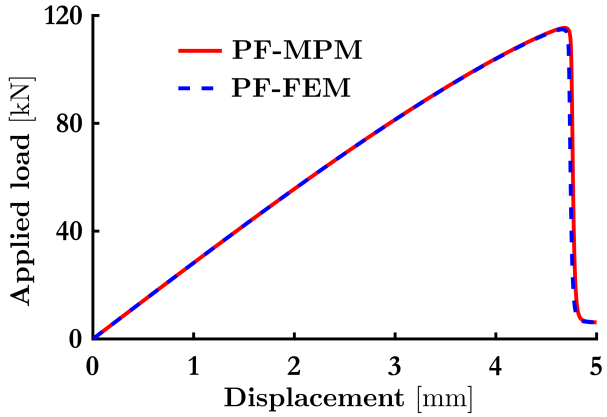

(c)

Figure 5.21: Three point layered bending test: Load displacement paths for (a) case 1 (b) case 2 (c) case 3.

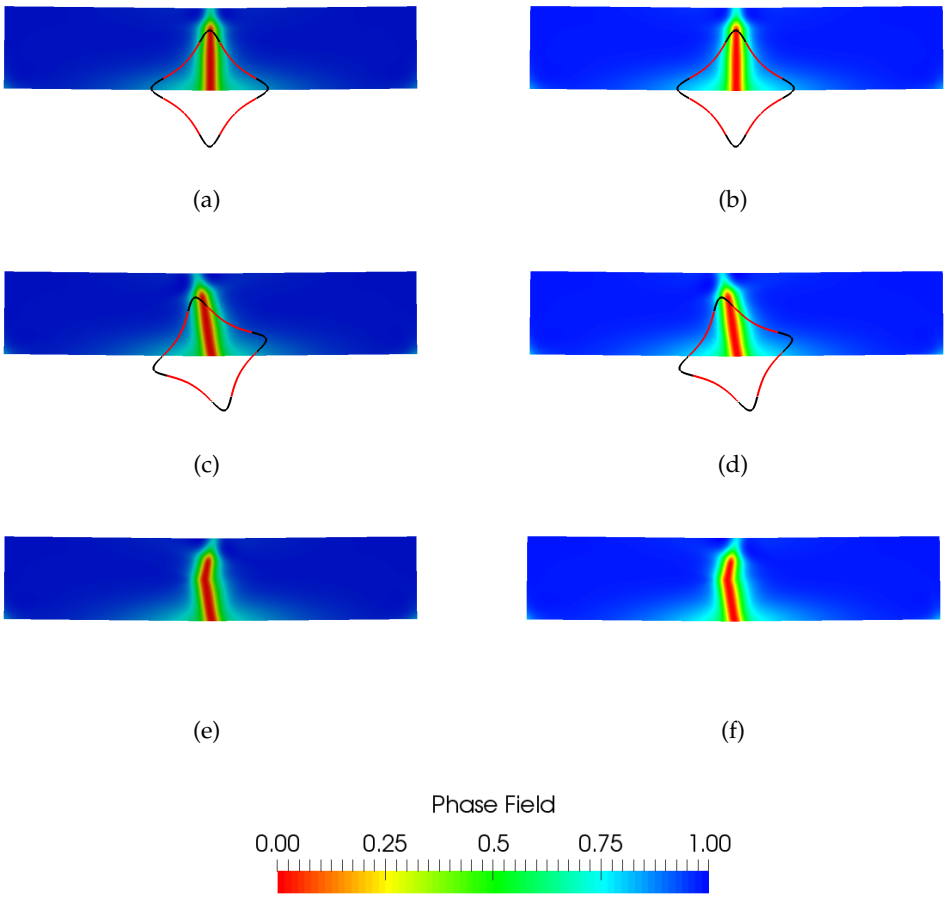

Figure 5.22: Three point layered bending test: Phase field for $u = 5$ mm. Finite Element Method for (a) case 1, (c) case 2 and (e) case 3, respectively. Material Point Method for (b) case 1, (d) case 2 and (f) case 3, respectively.

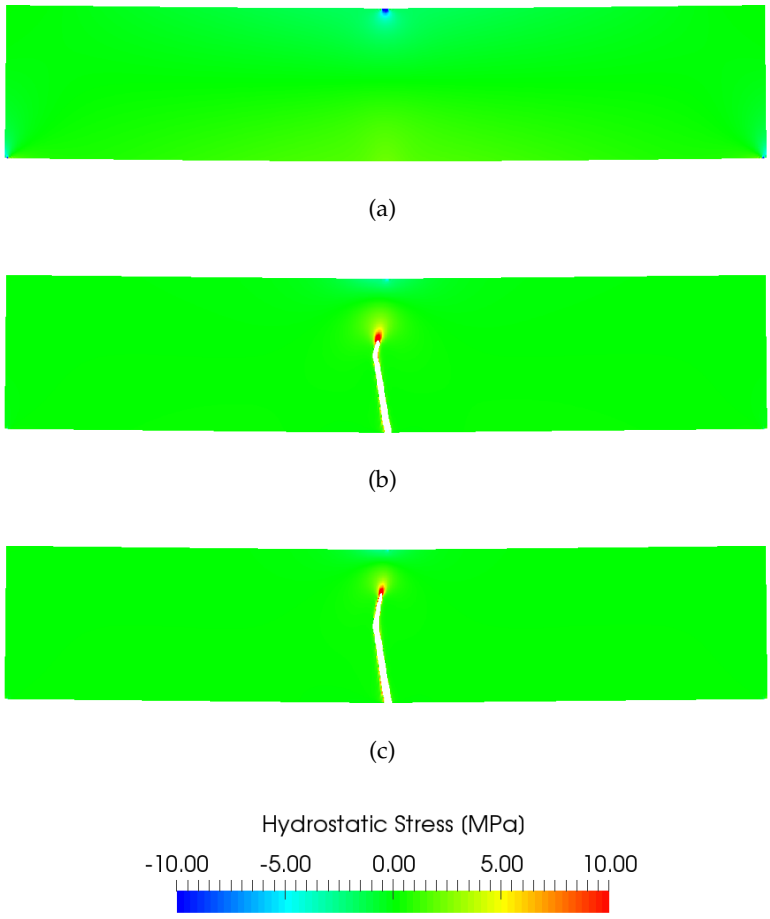

Figure 5.23: Three point layered bending test: Hydrostatic Stress (case 3) for (a) $u = 4.6$ mm, (b) $u = 4.7$ mm and (c) $u = 5.0$ mm, respectively. Material Points with $c_p < 0.02$ have been removed.

5.4 Conclusions

A robust framework for the resolution of evolving fractures in brittle anisotropic materials is introduced in this chapter. The method employed is based on a phase field approximation of the fracture energy defined on the basis of a fourth order anisotropic functional. The phase field is subsequently coupled to the material stress field by introducing the former as a degradation parameter on the elastic energy density of the material. Through a purely variation framework, the coupled partial differential equations of the problem are introduced.

A MPM approach is used to derive the discrete governing coupled equations of the problem. The latter are then solved in a staggered fashion. In this work, the specific cases of both cubic symmetry and orthotropy are examined in representative examples. Based on these, the proposed methodology is verified by means of comparison against the standard Phase Field Finite Element implementation. Results demonstrate that the MPM performs extremely well in resolving fracture propagation problems.

This chapter will thus form the basis for subsequent derivations pertaining to large displacement dynamic problems where Material Point Methods have proven advantageous as compared to Finite Element Methods (see chapter 6).

Chapter 6

Material Point Method for dynamic brittle fracture

Part of this chapter is submitted for publication and is currently under review (Kakouris and Triantafyllou, 2018b).

6.1 Introduction

Fracture of materials subjected to dynamic loading is commonly associated with complex yet intriguing phenomena, i.e., crack merging, branching and arrest (Ravi-Chandar and Knauss, 1984; Ravi-Chandar, 1998). These phenomena become even more pronounced in the case of anisotropy and high-rate loading conditions, e.g., impact. Anisotropy governs the fracture response of both natural and manufactured materials (see Chapter 5). Furthermore, the response of such materials under impact loading is receiving considerable attention as it pertains to numerous industrial applications particularly within the automotive and aerospace sector, see, e.g., Turner et al. (2018), Chen et al. (2015), and Lin et al. (2018).

Numerical simulation of fracture propagation under such conditions can provide valuable insight on the underlying mechanical processes while also providing a framework for optimum design of materials considering their post-fracture response under impact loading. However, robust and accurate simulation of impact driven dynamic fracture is a challenging task as it requires the fusion of robust fracture propagation modelling with contact induced non-linearities and large displacement kinematics.

Mesh based methods are prone to mesh distortion errors when large displacement kinematics are involved. Furthermore, contact problems, and in particular, dynamic impact problems require a fine mesh resolution to adequately account for the deformability of the contact surface, that in turn affects the accuracy of the resulting crack path. However, due to their corresponding kinematical assumptions, mesh based methods are computationally appealing when compared to purely particle based methods such as the discrete element method.

Very recently, Hesch et al. (2016) have developed a method to resolve contact problems involving isotropic phase field fracture. In this formulation, a Finite Element based mortar contact algorithm in conjunction with a hierarchical refinement scheme is employed that reduces computational costs although relying on the predefinition of contact areas. Therefore, an adaptive hierarchical refinement is needed for arbitrary impact fracture problems to resolve the local contact features.

The MPM has been introduced as a promising alternative to particle based methods that can efficiently deal with contact and large displacement problems. Taking advantage of the good qualities of phase field modelling in naturally resolving complex crack paths, a novel PF-MPM methodology is introduced in this chapter for robust modelling of dynamic brittle fracture of both isotropic and anisotropic materials in 2D problems only. The proposed method is further extended to account for frictional contact fracture problems. In this work, the

MPM contact algorithm utilized by Bardenhagen et al. (2000) and Huang et al. (2011) is adopted.

More specifically, in this work, multiple fields, termed discrete fields, are introduced in the non-deforming Eulerian mesh so that each contact body belongs to a different field. The phase field governing equations are independently solved for each contact body. Then, the solution of equations of motion is implemented within a predictor-corrector algorithm. The equilibrium governing equations are initially solved for each body separately and then the solution is corrected according to their contact conditions.

This MPM contact algorithm is not computationally taxing in comparison to Finite Element based contact algorithms. Since the interaction of contact surfaces is implemented through materials points within a fixed computational mesh. As a result, tracking or refining of contact areas is not required. These evolve naturally, according to corresponding material point displacements.

6.2 Governing equations for phase field fracture due to impact

6.2.1 Problem Statement

In this Section, the governing equations for contact induced brittle fracture are introduced. For brevity, the case of two bodies is presented herein. In Fig. 6.1(a), two deformable domains, namely Ω_1 and Ω_2 are considered such that $\Omega_1 \cup \Omega_2 = \Omega$. Their external boundaries are defined as $\partial\Omega_1$ and $\partial\Omega_2$, respectively.

At time t the two bodies are in contact along the surface $\partial\Omega_{1\bar{f}} = \partial\Omega_{2\bar{f}} = \partial\Omega_{\bar{f}} \subseteq \partial\Omega$. Furthermore, two crack paths are defined, i.e., Γ_1 and Γ_2 at Ω_1 and Ω_2, respectively, under the action of a set of tractions/ pressures $\bar{\mathbf{t}}$ and body forces $\mathbf{b} = \{b_1, b_2, b_3\}^T$.

When the two bodies are in contact, a contact force $\bar{\mathbf{f}}_1^{cont}$ is applied to body Ω_1 from body Ω_2. This is defined in component form according to Eq. (6.1)

$$\bar{\mathbf{f}}_1^{cont} = \bar{\mathbf{f}}_1^{nor} + \bar{\mathbf{f}}_1^{tan} = \bar{f}_1^{nor} \cdot \mathbf{n}_1^{cont} + \bar{f}_1^{tan} \cdot \mathbf{s}_1^{cont} \tag{6.1}$$

where $\bar{\mathbf{f}}_1^{nor}$ and $\bar{\mathbf{f}}_1^{tan}$ are the normal and tangential contact force vectors whereas $\bar{f}_1^{nor}$ and $\bar{f}_1^{tan}$ are their corresponding components. The normal and tangential surface unit vectors on contact surface $\partial\Omega_{1\bar{f}}$ are denoted as $\mathbf{n}_1^{cont}$ and $\mathbf{s}_1^{cont}$, respectively. Similarly, a contact force $\bar{\mathbf{f}}_2^{cont}$ is applied from Ω_1 to Ω_2 with components $\bar{\mathbf{f}}_2^{nor}$, $\bar{\mathbf{f}}_2^{tan}$ and normal and tangential surface unit vectors $\mathbf{n}_2^{cont}$ and $\mathbf{s}_2^{cont}$ being defined accordingly.

6.2.2 Derivation of coupled strong form for impact-fracture problems: A discrete field formulation

In this work, a discrete field approach is adopted for the robust and efficient numerical treatment of contact dynamics between deformable bodies whereby each body is treated independently as discrete field. In the general case, it is assumed that the entire domain consists of a set of independent discrete fields $\{\mathcal{D} \mid \mathcal{D} = 1, 2, \ldots, N_{\mathcal{D}}\}$, where $N_{\mathcal{D}} \in \mathbb{Z}^+$ is the total number of discrete fields and $\mathcal{D}$ indexes the $\mathcal{D}^{th}$ discrete field. Furthermore, all corresponding quantities that belong to discrete field $\mathcal{D}$, i.e., body $\Omega_{\mathcal{D}}$, are denoted with the subscript $\mathcal{D}$. Hence, in the two body case considered in this Section $\{\mathcal{D} \mid \mathcal{D} = 1, 2\}$.

Within the discrete field setting, the contact forces arising from the interaction of the discrete fields are treated as additional external forces. Hence, the energy balance equation (5.19), is re-defined for each discrete field $\mathcal{D}$ as

$$\dot{\mathcal{K}}_{\mathcal{D}}\left(\dot{\mathbf{u}}_{\mathcal{D}}\right) + \dot{\mathcal{W}}_{\mathcal{D}}^{int}\left(\dot{\mathbf{u}}_{\mathcal{D}}, \dot{c}_{\mathcal{D}}, \nabla\dot{c}_{\mathcal{D}}\right) - \dot{\mathcal{W}}_{\mathcal{D}}^{ext}\left(\dot{\mathbf{u}}_{\mathcal{D}}\right) - \dot{\mathcal{W}}_{\mathcal{D}}^{cont}\left(\dot{\mathbf{u}}_{\mathcal{D}}\right) = 0 \tag{6.2}$$

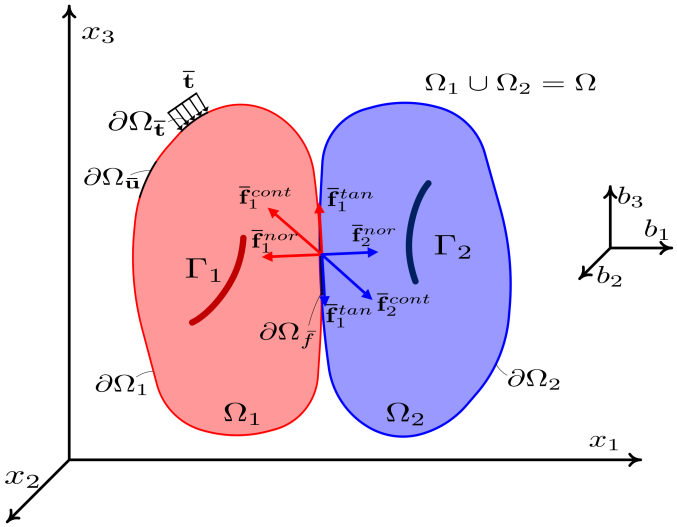

(a)

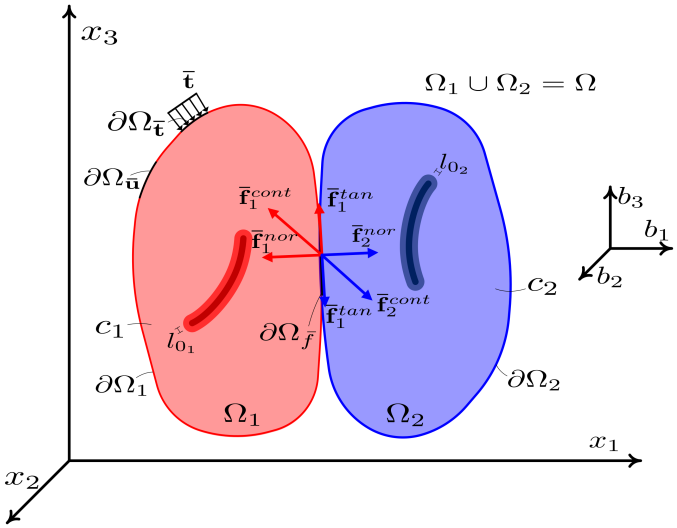

(b)

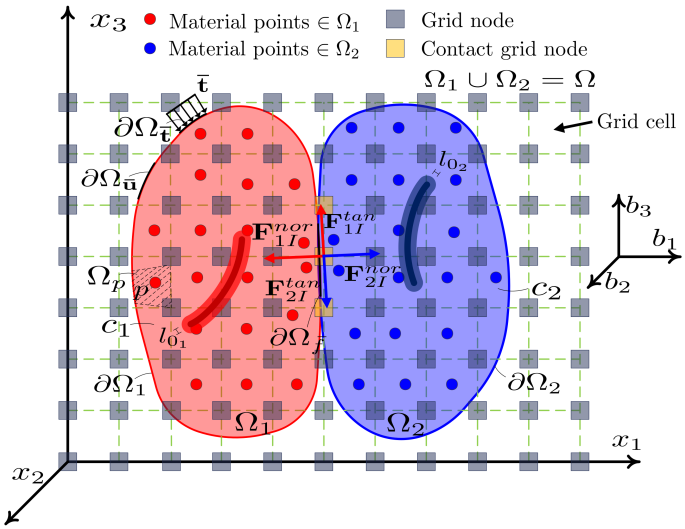

(c)

Figure 6.1: (a) Two bodies ($\Omega_1 \cup \Omega_2 = \Omega$) into contact with two crack paths Γ_1 and Γ_2 (b) Phase Field approximation of the crack paths and (c) Phase Field Material Point Method approximation.

where $\dot{\mathcal{W}}_{\mathcal{D}}^{cont}\left(\dot{\mathbf{u}}_{\mathcal{D}}\right)$ is the rate of work done by contact forces and is expressed as

$$\dot{\mathcal{W}}_{\mathcal{D}}^{cont}\left(\dot{\mathbf{u}}_{\mathcal{D}}\right) = \int_{\partial\Omega_{\mathcal{D}\bar{f}}} \left(\bar{\mathbf{f}}_{\mathcal{D}}^{cont} \cdot \dot{\mathbf{u}}_{\mathcal{D}}\right) d\partial\Omega_{\mathcal{D}\bar{f}}. \tag{6.3}$$

Thus, the coupled strong form introduced in Eqs. (5.22) is now defined for the discrete field $\mathcal{D}$ as

$$\begin{cases} \nabla \cdot \boldsymbol{\sigma}_{\mathcal{D}} + \mathbf{b}_{\mathcal{D}} = \rho_{\mathcal{D}} \ddot{\mathbf{u}}_{\mathcal{D}} & \text{on } \Omega_{\mathcal{D}} \\ \left(\dfrac{4l_{0_{\mathcal{D}}}\left(1-k_{f_{\mathcal{D}}}\right)\mathcal{H}_{\mathcal{D}}}{\bar{\mathcal{G}}_{c_{\mathcal{D}}}} + 1\right) c_{\mathcal{D}} - 4l_{0_{\mathcal{D}}}^2 \Delta c_{\mathcal{D}} \\ \qquad + 4l_{0_{\mathcal{D}}}^4 \displaystyle\sum_{ijkl} \gamma_{ijkl_{\mathcal{D}}} \frac{\partial^4 c_{\mathcal{D}}}{\partial x_i \partial x_j \partial x_k \partial x_l} = 1 & \text{on } \Omega_{\mathcal{D}}. \end{cases} \tag{6.4}$$

The set of boundary and initial conditions introduced in Eqs. (5.23) are modified for each discrete field $\mathcal{D}$ accordingly as

$$\begin{cases} \boldsymbol{\sigma}_{\mathcal{D}} \cdot \mathbf{n}_{\mathcal{D}} = \bar{\mathbf{t}}_{\mathcal{D}}, & \text{on } \partial\Omega_{\bar{\mathbf{t}}_{\mathcal{D}}} \\ \mathbf{u}_{\mathcal{D}} = \bar{\mathbf{u}}_{\mathcal{D}}, & \text{on } \partial\Omega_{\bar{\mathbf{u}}_{\mathcal{D}}} \\ \mathbf{u}_{\mathcal{D}} = {}^{(0)}\mathbf{u}_{\mathcal{D}}, & \text{on } {}^{(0)}\Omega_{\mathcal{D}} \\ \dot{\mathbf{u}}_{\mathcal{D}} = {}^{(0)}\dot{\mathbf{u}}_{\mathcal{D}}, & \text{on } {}^{(0)}\Omega_{\mathcal{D}} \\ \ddot{\mathbf{u}}_{\mathcal{D}} = {}^{(0)}\ddot{\mathbf{u}}_{\mathcal{D}}, & \text{on } {}^{(0)}\Omega_{\mathcal{D}} \\ \left[4l_{0_{\mathcal{D}}}^2 \nabla c_{\mathcal{D}} - 2l_{0_{\mathcal{D}}}^4 \displaystyle\sum_{ijkl} \gamma_{ijkl_{\mathcal{D}}} \left(\frac{\partial^3 c}{\partial x_j \partial x_k \partial x_l}\right)\right. \\ \quad \left. -2l_{0_{\mathcal{D}}}^4 \displaystyle\sum_{ijkl} \gamma_{ijkl_{\mathcal{D}}} \left(\frac{\partial^3 c_{\mathcal{D}}}{\partial x_i \partial x_j \partial x_k}\right)\right] \cdot \mathbf{n} = 0, & \text{on } \partial\Omega_{\mathcal{D}} \\ 2l_{0_{\mathcal{D}}}^4 \sum_{ijkl} \gamma_{ijkl_{\mathcal{D}}} \left(\frac{\partial^2 c_{\mathcal{D}}}{\partial x_k \partial x_l}\right) + 2l_{0_{\mathcal{D}}}^4 \sum_{ijkl} \gamma_{ijkl_{\mathcal{D}}} \left(\frac{\partial^2 c_{\mathcal{D}}}{\partial x_i \partial x_j}\right) = 0, & \text{on } \partial\Omega_{\mathcal{D}} \\ c_{\mathcal{D}} = {}^{(0)}c_{\mathcal{D}}, & \text{on } {}^{(0)}\Omega_{\mathcal{D}} \\ \boldsymbol{\sigma}_{\mathcal{D}} \cdot \mathbf{n}_{\mathcal{D}}^{cont} = \bar{\mathbf{f}}_{\mathcal{D}}^{cont}, & \text{on } \partial\Omega_{\mathcal{D}\bar{f}} \end{cases} \tag{6.5}$$

where the last boundary condition is due to the contact forces that in this implementation are considered as forces applied externally to the discrete field

$\mathcal{D}$.

Furthermore, the coupled field equations (6.4) are subjected to the kinematic constraints presented in Eqs. (6.6a) to (6.6e) and (6.7a) to (6.7e) at contact surface $\partial\Omega_{\bar{f}}$ (Yastrebov, 2013). The kinematic constraints of Eqs. (6.6a) to (6.6e) correspond to the normal contact laws

$$\begin{cases} \mathbf{n}_1^{cont} = -\mathbf{n}_2^{cont}, & \text{collinearity,} \quad \text{on } \partial\Omega_{\bar{f}} & \text{(6.6a)} \\ \bar{\mathbf{f}}_1^{nor} = -\bar{\mathbf{f}}_2^{nor}, & \text{collinearity,} \quad \text{on } \partial\Omega_{\bar{f}} & \text{(6.6b)} \\ \bar{f}^{nor} \leq 0, & \text{non-tension,} \quad \text{on } \partial\Omega_{\bar{f}} & \text{(6.6c)} \\ \gamma_n \leq 0, & \text{impenetrability,} \quad \text{on } \partial\Omega_{\bar{f}} & \text{(6.6d)} \\ \gamma_n \bar{f}^{nor} = 0, & \text{complementarity,} \quad \text{on } \partial\Omega_{\bar{f}} & \text{(6.6e)} \end{cases}$$

whereas Eq. (6.7a) to (6.7e) correspond to the tangential contact and friction laws, where the Coulomb friction model is adopted.

$$\begin{cases} \mathbf{s}_1^{cont} = -\mathbf{s}_2^{cont}, & \text{collinearity,} \quad \text{on } \partial\Omega_{\bar{f}} & \text{(6.7a)} \\ \bar{\mathbf{f}}_1^{tan} = -\bar{\mathbf{f}}_2^{tan}, & \text{collinearity,} \quad \text{on } \partial\Omega_{\bar{f}} & \text{(6.7b)} \\ |\bar{f}^{tan}| \leq \mu_f |\bar{f}^{nor}|, & \text{coulomb friction,} \quad \text{on } \partial\Omega_{\bar{f}} & \text{(6.7c)} \\ |\gamma_s| \geq 0, & \text{slip/non-slip,} \quad \text{on } \partial\Omega_{\bar{f}} & \text{(6.7d)} \\ |\gamma_s| \left(|\bar{f}^{tan}| - \mu_f |\bar{f}^{nor}| \right) = 0, & \text{complementarity,} \quad \text{on } \partial\Omega_{\bar{f}}. & \text{(6.7e)} \end{cases}$$

Kinematic constraints (6.6a), (6.7a) and (6.6b) and (6.7b) are imposed to satisfy Newton's third law at contact surface $\partial\Omega_{\bar{f}}$. The condition (6.6c) is imposed on the normal component of the contact force that is defined according to Eq. (6.8)

$$\bar{f}^{nor} = \bar{\mathbf{f}}_1^{cont} \cdot \mathbf{n}_1^{cont} = \bar{\mathbf{f}}_2^{cont} \cdot \mathbf{n}_2^{cont} \tag{6.8}$$

and implies a non-tension, i.e., non-stick, condition at the contact surface $\partial\Omega_{\bar{f}}$.

Furthermore, the impenetrability condition (6.6d) is imposed to ensure no penetration between the contact surfaces $\partial\Omega_{1\bar{f}}$ and $\partial\Omega_{2\bar{f}}$ when the two bodies are

in contact. In condition (6.6d), γ_n is defined as

$$\gamma_n = \dot{\mathbf{u}}_1^{rel} \cdot \mathbf{n}_1^{cont} = \dot{\mathbf{u}}_2^{rel} \cdot \mathbf{n}_2^{cont} \tag{6.9}$$

where $\dot{\mathbf{u}}_1^{rel} = (\dot{\mathbf{u}}_1 - \dot{\mathbf{u}}_2) = -\dot{\mathbf{u}}_2^{rel}$ is the relative velocity of the two bodies Ω_1 and Ω_2 (i.e. $\dot{\mathbf{u}}_1^{rel}$ is the velocity of body Ω_1 relative to body Ω_2).

Condition $\gamma_n = 0$ is satisfied when the relative velocity is zero, i.e. $\dot{\mathbf{u}}_1^{rel} = -\dot{\mathbf{u}}_2^{rel} = 0$ (e.g. the two bodies are in contact and their contact surfaces move together with the same velocity). Condition $\gamma_n < 0$ implies that the relative velocity lays on a different semi plane from the normal contact vector. Thus, the two bodies move in opposite directions, i.e. their contact surfaces $\partial\Omega_{1\bar{f}}$ and $\partial\Omega_{2\bar{f}}$ are separated. In this case $\bar{f}^{nor} = 0$, hence the complementarity condition (6.6e) is always satisfied. Conditions (6.6c), (6.6d) and (6.6e) as well as the relation of variables $\bar{f}^{nor}$ and γ_n are summarized in Fig. 6.2(a).

The kinematic constraint (6.7c) is imposed on the tangential component of contact force that is defined by

$$\bar{f}^{tan} = \bar{\mathbf{f}}_1^{cont} \cdot \mathbf{s}_1^{cont} = \bar{\mathbf{f}}_2^{cont} \cdot \mathbf{s}_2^{cont} \tag{6.10}$$

to account for the friction law at contact surface. The Coulomb friction model is utilized in this work where μ_f is the friction coefficient between the two bodies. In this, the condition $|\bar{f}^{tan}| = \mu_f |\bar{f}^{nor}|$ is satisfied when slip occurs at the contact surface whereas $|\bar{f}^{tan}| < \mu_f |\bar{f}^{nor}|$ when it does not. This means that the tangential component of contact force should be reduced according to Coulomb's friction model to allow for sliding at the contact surface.

Condition (6.7d) holds when either slip or no slip occurs at contact surface. In Eq. (6.7d), γ_s is defined as

$$\gamma_s = \dot{\mathbf{u}}_1^{rel} \cdot \mathbf{s}_1^{cont} = \dot{\mathbf{u}}_2^{rel} \cdot \mathbf{s}_2^{cont}. \tag{6.11}$$

In particular, $|\gamma_s| = 0$ holds when the relative velocity is zero, i.e. $\dot{\mathbf{u}}_1^{rel} = -\dot{\mathbf{u}}_2^{rel} = 0$ (e.g. the two bodies are in contact and their contact surfaces move together with the same velocity). At that case there is no slip at the contact surface, i.e. $|\bar{f}^{tan}| < \mu_f |\bar{f}^{nor}|$. When $|\gamma_s| > 0$, slip occurs. In this case, it holds that $|\bar{f}^{tan}| = \mu_f |\bar{f}^{nor}|$.

According to the aforementioned, the complementarity condition (6.7e) is always satisfied. Conditions (6.7c), (6.7d) and (6.7e) are summarized in Figs. 6.2(b) and 6.2(c). The relation between the variables $\bar{f}^{tan}$ and γ_s (i.e. slip/no slip conditions) is shown in Fig. 6.2(b) while the Coulomb's cone for the two-dimensional problem is presented in Fig. 6.2(c).

6.3 Material Point Method for impact fracture problems

Dynamic fracture under impact naturally involves large displacement kinematics especially in the pre- and post-fracture regime, e.g., in the case of high velocity projectile impact problems. To accurately resolve the pre and post fracture kinematics, the Material Point Method is used in this work to solve the system of coupled governing Eqs. (6.4).

In the Material Point Method framework employed herein, the entire domain $\Omega = \Omega_1 \cup \Omega_2$ is discretized into a set of material points $\mathcal{P} = \{p \mid p = 1, 2, \ldots, N_p\}$, where $N_p \in \mathbb{Z}^+$ is the total number of material points whereas p indexes the p^{th} material point. It is assumed herein that $N_{\mathcal{D}p}$ material points belong to discrete field $\mathcal{D}$, i.e. body $\Omega_{\mathcal{D}}$ (see Fig. 6.1(c)).

According to the MPM approximation, the mass density $\rho_{\mathcal{D}}$ and domain volume $\Omega_{\mathcal{D}}$ corresponding to discrete field $\mathcal{D}$ are additively decomposed into the corresponding material point contributions according to Eqs. (6.12) and (6.13),

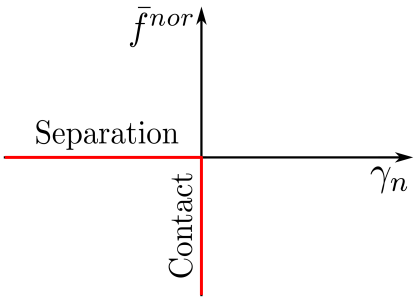

(a)

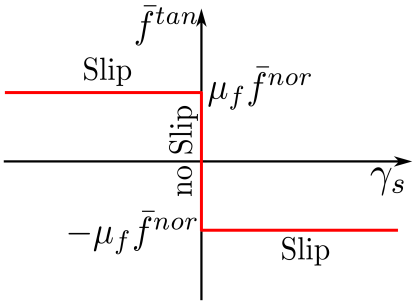

(b)

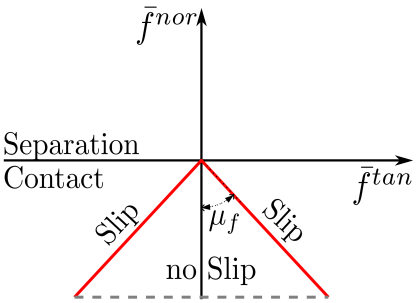

(c)

Figure 6.2: Kinematic contact constraints: (a) Normal contact law (b) Tangential friction law (c) Coulomb's cone for the two-dimensional problem.

respectively, i.e.,

$$\rho_{\mathcal{D}}\left(\mathbf{x}_{\mathcal{D}},t\right)=\sum_{p=1}^{N_p}\rho_{\mathcal{D}p}\Omega_{\mathcal{D}p}\delta\left(\mathbf{x}_{\mathcal{D}}-\mathbf{x}_{\mathcal{D}p}\right) \tag{6.12}$$

and

$$\Omega_{\mathcal{D}}\left(\mathbf{x}_{\mathcal{D}},t\right)=\sum_{p=1}^{N_p}\Omega_{\mathcal{D}p}\delta\left(\mathbf{x}_{\mathcal{D}}-\mathbf{x}_{\mathcal{D}p}\right). \tag{6.13}$$

6.3.1 Discrete equations

6.3.1.1 Equilibrium discrete equations

Defining appropriate trial solution and weighting function spaces for the displacement field, i.e.,

$$\mathcal{V}=\{\mathbf{u}\in H^1\left(\Omega\right)\ \ |\ \mathbf{u}=\bar{\mathbf{u}}\text{ on }\partial\Omega_{\bar{u}}\}$$

and

$$\mathcal{U}=\{\mathbf{w}\in H^1\left(\Omega\right)\ \ |\ \mathbf{w}=0\text{ on }\partial\Omega_{\bar{u}}\},$$

respectively, the discrete form of equilibrium equations introduced in the first of Eqs. (6.4) is expressed for each discrete field $\mathcal{D}$ as

$$\begin{aligned}\int_{\Omega_{\mathcal{D}}}\left(\rho_{\mathcal{D}}\ddot{\mathbf{u}}_{\mathcal{D}}\cdot\mathbf{w}_{\mathcal{D}}\right)d\Omega_{\mathcal{D}}+\int_{\Omega_{\mathcal{D}}}\left(\boldsymbol{\sigma}_{\mathcal{D}}:\nabla\mathbf{w}_{\mathcal{D}}\right)d\Omega_{\mathcal{D}}=\int_{\partial\Omega_{\mathcal{D}\bar{t}}}\left(\bar{\mathbf{t}}_{\mathcal{D}}\cdot\mathbf{w}_{\mathcal{D}}\right)d\partial\Omega_{\mathcal{D}\bar{t}}+\\ \int_{\Omega_{\mathcal{D}}}\left(\mathbf{b}_{\mathcal{D}}\cdot\mathbf{w}_{\mathcal{D}}\right)d\Omega_{\mathcal{D}}+\int_{\partial\Omega_{\mathcal{D}\bar{f}}}\left(\bar{\mathbf{f}}_{\mathcal{D}}^{cont}\cdot\mathbf{w}_{\mathcal{D}}\right)d\partial\Omega_{\mathcal{D}\bar{f}}\end{aligned} \tag{6.14}$$

where $\mathbf{w}$ are weighting functions that satisfy the homogeneous essential boundary conditions of the problem.

Substituting the material point approximation introduced in Eqs. (6.12) and (6.13) into Eq. (6.14), Eq. (6.15) is established

$$\sum_{p=1}^{N_p}(\rho_{\mathcal{D}p}\ddot{\mathbf{u}}_{\mathcal{D}p}\cdot\mathbf{w}_{\mathcal{D}p})\Omega_{\mathcal{D}p}+\sum_{p=1}^{N_p}(\boldsymbol{\sigma}_{\mathcal{D}p}:\nabla\mathbf{w}_{\mathcal{D}p})\Omega_{\mathcal{D}p}=\int_{\partial\Omega_{\mathcal{D}\bar{t}}}(\bar{\mathbf{t}}_{\mathcal{D}}\cdot\mathbf{w}_{\mathcal{D}})\,d\partial\Omega_{\mathcal{D}\bar{t}}+\sum_{p=1}^{N_p}(\mathbf{b}_{\mathcal{D}p}\cdot\mathbf{w}_{\mathcal{D}p})\Omega_{\mathcal{D}p}+\int_{\partial\Omega_{\mathcal{D}\bar{f}}}(\bar{\mathbf{f}}_{\mathcal{D}}^{cont}\cdot\mathbf{w}_{\mathcal{D}})\,d\partial\Omega_{\mathcal{D}\bar{f}}. \tag{6.15}$$

Next, making use of the interpolation schemes for the weighting functions $\mathbf{w}_{\mathcal{D}p}$ and their spatial derivatives $\nabla\mathbf{w}_{\mathcal{D}p}$ from Eq. (3.45) and Eq. (3.46), respectively and further assuming that it should hold for every set of nodal values $\mathbf{w}_{\mathcal{D}I}$ the following equilibrium equation is finally established

$$\mathbf{R}^{u}_{\mathcal{D}I}(\mathbf{u}_{\mathcal{D}})=\mathbf{F}^{irt}_{\mathcal{D}I}+\mathbf{F}^{int}_{\mathcal{D}I}-\mathbf{F}^{ext}_{\mathcal{D}I}-\mathbf{F}^{cont}_{\mathcal{D}I}=0,\quad I=1\ldots,N_n \tag{6.16}$$

In Eq. (6.16), $\mathbf{R}^{u}_{\mathcal{D}I}$ is the nodal residual force vector at grid node I and $N_n\in\mathbb{Z}^+$ is the total number of grid nodes.

Similarly, $\mathbf{F}^{irt}_{\mathcal{D}I}$, $\mathbf{F}^{int}_{\mathcal{D}I}$ and $\mathbf{F}^{ext}_{\mathcal{D}I}$ correspond to the nodal inertia, internal and external force vectors evaluated at grid node I. These quantities are computed by Eqs. (3.51), (3.52) and (3.53), respectively. Finally, $\mathbf{F}^{cont}_{\mathcal{D}I}$ corresponds to the contact force nodal vector defined as

$$\mathbf{F}^{cont}_{\mathcal{D}I}=\int_{\partial\Omega_{\mathcal{D}\bar{f}}}(\bar{\mathbf{f}}^{cont}_{\mathcal{D}}N_I(\mathbf{x}))\,d\partial\Omega_{\mathcal{D}\bar{f}}. \tag{6.17}$$

Substituting, the acceleration approximation, introduced in Eq. (3.49), in Eq. (6.16) the following equation of motion is established for each discrete field $\mathcal{D}$.

$$\mathbf{M}^{u}_{\mathcal{D}}\ddot{\mathbf{u}}_{\mathcal{D}}+\mathbf{F}^{int}_{\mathcal{D}}=\mathbf{F}^{ext}_{\mathcal{D}}+\mathbf{F}^{cont}_{\mathcal{D}} \tag{6.18}$$

where $\mathbf{M}^{u}_{\mathcal{D}}$ is the global lumped mass matrix of the structure whose $M^{u}_{\mathcal{D}I}$ component is evaluated from relation (3.58).

Eq. (6.18) lends itself conveniently into an explicit predictor-corrector time integration scheme as will be further discussed in Section 6.3.2 .

6.3.1.2 Anisotropic phase field discrete equations

The discrete form of the anisotropic phase field governing equations introduced in the second of Eqs. (6.4) can also be derived with the same procedure as in Section 5.3.1.1. Therefore, the nodal phase field residual vector, introduced in Eq. (5.33), is re-written for the discrete field $\mathcal{D}$ as

$$R_{\mathcal{D}I}^{c,Anis}(c_{\mathcal{D}}) = S_{\mathcal{D}I}^{c,Anis} - F_{\mathcal{D}I}^{c,Anis} = 0, \quad I = 1\ldots, N_n. \tag{6.19}$$

Similarly, the compact form, introduced in Eq. (5.36), is re-formulated as

$$\mathbf{K}_{\mathcal{D}}^{c,Anis}\mathbf{c}_{\mathcal{D}} = \mathbf{F}_{\mathcal{D}}^{c}. \tag{6.20}$$

6.3.2 Anisotropic PF-MPM solution scheme for impact fracture problems

In this work, a staggered solution procedure is employed to numerically solve the coupled Eqs. (6.18) and (6.20). The two sets of equations are treated independently, by allowing the equation of motion to be solved either implicitly or explicitly (see also Sections 4.3 and 5.3.2). Although an explicit time integration scheme is utilized herein to integrate Eqs. (6.18) in the time domain (Bardenhagen et al., 2000; Huang et al., 2011), an implicit time integration scheme can also be employed in a straightforward manner (Cummins and Brackbill, 2002; Nezamabadi et al., 2015; Chen et al., 2017). The complete staggered solution algorithm is described in Section 6.3.2.4 in detail.

6.3.2.1 Explicit time integration scheme

The momentum formulation of MPM algorithm is employed herein to numerically solve the equation of motion (6.18) (Sulsky et al., 1995). Hence, the equation of motion (6.18) at time t is rewritten for the grid node I in the following form

$$ {}^{(t)}M^{u}_{\mathcal{D}I}\,{}^{(t)}\ddot{\mathbf{u}}_{\mathcal{D}I} + {}^{(t)}\mathbf{F}^{int}_{\mathcal{D}I} = {}^{(t)}\mathbf{F}^{ext}_{\mathcal{D}I} + {}^{(t)}\mathbf{F}^{cont}_{\mathcal{D}I}. \tag{6.21} $$

Considering, a forward Euler integration scheme, the acceleration field is expressed as

$$ {}^{(t)}\ddot{\mathbf{u}}_{\mathcal{D}I} = ({}^{(t+\Delta t)}\dot{\mathbf{u}}_{\mathcal{D}I} - {}^{(t)}\dot{\mathbf{u}}_{\mathcal{D}I})/\Delta t. \tag{6.22} $$

where Δt is the corresponding time step. In view of Eq. (6.22), Eq. (6.21) is rewritten as

$$ \begin{aligned} {}^{(t)}M^{u}_{\mathcal{D}I}\,{}^{(t+\Delta t)}\dot{\mathbf{u}}_{\mathcal{D}I} = {}^{(t)}M^{u}_{\mathcal{D}I}\,{}^{(t)}\dot{\mathbf{u}}_{\mathcal{D}I} + \Delta t\left({}^{(t)}\mathbf{F}^{ext}_{\mathcal{D}I} + {}^{(t)}\mathbf{F}^{cont}_{\mathcal{D}I} - {}^{(t)}\mathbf{F}^{int}_{\mathcal{D}I}\right) \Leftrightarrow \\ {}^{(t+\Delta t)}\mathbf{p}_{\mathcal{D}I} = {}^{(t)}\mathbf{p}_{\mathcal{D}I} + \Delta t\left({}^{(t)}\mathbf{F}^{ext}_{\mathcal{D}I} + {}^{(t)}\mathbf{F}^{cont}_{\mathcal{D}I} - {}^{(t)}\mathbf{F}^{int}_{\mathcal{D}I}\right) \end{aligned} \tag{6.23} $$

where ${}^{(t+\Delta t)}\mathbf{p}_{\mathcal{D}I}$ and ${}^{(t)}\mathbf{p}_{\mathcal{D}I}$ are the nodal momentum at time $t+\Delta t$ and t, respectively.

At time t the nodal momentums ${}^{(t)}\mathbf{p}_{\mathcal{D}I}$ are unknown; hence, these are mapped from material points to grid node I using Eq. (6.24)

$$ {}^{(t)}\mathbf{p}_{\mathcal{D}I} = {}^{(t)}M^{u}_{\mathcal{D}I}\,{}^{(t)}\dot{\mathbf{u}}_{\mathcal{D}I} = \sum_{p=1}^{N_p} N_I({}^{(t)}\mathbf{x}_p) M_{\mathcal{D}p}\,{}^{(t)}\dot{\mathbf{u}}_{\mathcal{D}p}. \tag{6.24} $$

Similarly, the nodal internal forces ${}^{(t)}\mathbf{F}^{int}_{\mathcal{D}I}$ are evaluated as

$$ {}^{(t)}\mathbf{F}^{int}_{\mathcal{D}I} = \sum_{p=1}^{N_p} ({}^{(t)}\boldsymbol{\sigma}_{\mathcal{D}p} \cdot \nabla N_I({}^{(t)}\mathbf{x}_p))\,{}^{(t)}\Omega_{\mathcal{D}p}. \tag{6.25} $$

Eq. (6.23) is numerically solved using a predictor-corrector algorithm introduced by Bardenhagen et al. (2000) and further improved by Huang et al. (2011).

In this, the trial momentums are initially evaluated for each discrete field $\mathcal{D}$, neglecting the contact forces ${}^{(t)}\mathbf{F}^{cont}_{\mathcal{D}I}$, as

$$ {}^{(t+\Delta t)}\mathbf{p}^{trl}_{\mathcal{D}I} = {}^{(t)}\mathbf{p}_{\mathcal{D}I} + \Delta t \left({}^{(t)}\mathbf{F}^{ext}_{\mathcal{D}I} - {}^{(t)}\mathbf{F}^{int}_{\mathcal{D}I} \right). \tag{6.26} $$

The corresponding trial nodal velocities ${}^{(t+\Delta t)}\dot{\mathbf{u}}^{trl}_{\mathcal{D}I}$ are then computed accordingly as

$$ {}^{(t+\Delta t)}\dot{\mathbf{u}}^{trl}_{\mathcal{D}I} = \frac{{}^{(t+\Delta t)}\mathbf{p}^{trl}_{\mathcal{D}I}}{{}^{(t)}M^{u}_{\mathcal{D}I}}. \tag{6.27} $$

The trial velocities correspond to the velocities of each discrete field $\mathcal{D}$ when no contact force is exerted between them.

The predicted trial velocities ${}^{(t+\Delta t)}\dot{\mathbf{u}}^{trl}_{\mathcal{D}I}$ (evaluated from Eq. (6.27)) are then corrected according to Eq. (6.28)

$$ {}^{(t+\Delta t)}\dot{\mathbf{u}}_{\mathcal{D}I} = {}^{(t+\Delta t)}\dot{\mathbf{u}}^{trl}_{\mathcal{D}I} + \Delta t \frac{{}^{(t)}\mathbf{F}^{cont}_{\mathcal{D}I}}{{}^{(t)}M^{u}_{\mathcal{D}I}} \tag{6.28} $$

where ${}^{(t+\Delta t)}\dot{\mathbf{u}}_{\mathcal{D}I}$ is the vector of corrected nodal velocities at time $t+\Delta t$. To evaluate the corrected nodal velocities using Eq. (6.28), the contact forces ${}^{(t)}\mathbf{F}^{cont}_{\mathcal{D}I}$ must be evaluated first. The procedure for evaluating the contact forces between two discrete fields is presented in Section 6.3.2.2.

6.3.2.2 Contact force evaluation

The contact force vector ${}^{(t)}\mathbf{F}^{cont}_{\mathcal{D}I}$ is the sum of a normal ${}^{(t)}\mathbf{F}^{nor}_{\mathcal{D}I}$ and a tangential ${}^{(t)}\mathbf{F}^{tan}_{\mathcal{D}I}$ force vector. Hence, the corresponding components of these vectors, i.e. ${}^{(t)}F^{nor}_{\mathcal{D}I}$ and ${}^{(t)}F^{tan}_{\mathcal{D}I}$, should be initially computed taking into account the kinematic contact constraints presented in Eqs. (6.6a) to (6.6e) and (6.7a) to (6.7e). Their evaluation is performed through the following procedure.

The nodal centre of mass velocities are calculated using Eq. (6.29) below

$$ {}^{(t+\Delta t)}\dot{\mathbf{u}}_I^{cm} = \frac{\sum_{\mathcal{D}=1}^{N_\mathcal{D}} {}^{(t+\Delta t)}\mathbf{p}_{\mathcal{D}I}^{trl}}{\sum_{\mathcal{D}=1}^{N_\mathcal{D}} {}^{(t)}M_{\mathcal{D}I}^{u}} = \frac{\sum_{\mathcal{D}=1}^{N_\mathcal{D}} {}^{(t)}M_{\mathcal{D}I}^{u}\, {}^{(t+\Delta t)}\dot{\mathbf{u}}_{\mathcal{D}I}^{trl}}{\sum_{\mathcal{D}=1}^{N_\mathcal{D}} {}^{(t)}M_{\mathcal{D}I}^{u}}. \tag{6.29} $$

These correspond to the velocities that each discrete field $\mathcal{D}$ would have if these were to move as a single field (non-slip contact). The normal component of contact force ${}^{(t)}F_{\mathcal{D}I}^{nor,s}$ is evaluated considering the impenetrability condition Eq. (6.6d) at the I^{th} contact grid node as

$$ {}^{(t+\Delta t)}\gamma_{nI} = \left({}^{(t+\Delta t)}\dot{\mathbf{u}}_{1I} - {}^{(t+\Delta t)}\dot{\mathbf{u}}_{2I} \right) \cdot {}^{(t)}\mathbf{n}_{1I}^{cont} = 0. \tag{6.30} $$

As aforementioned in Section 6.2.2, when two bodies come into contact at the I^{th} grid node, it holds that $\gamma_{nI} = 0$. Substituting relation (6.28) into (6.30), considering the equilibrium of contact forces on the contact surface

$$ {}^{(t)}\mathbf{F}_{1I}^{cont} = - {}^{(t)}\mathbf{F}_{2I}^{cont} \tag{6.31} $$

and also Eq. (6.29), the normal component of contact force is expressed as

$$ {}^{(t)}F_{\mathcal{D}I}^{nor,s} = \frac{{}^{(t)}M_{\mathcal{D}I}^{u}}{\Delta t} \left({}^{(t+\Delta t)}\dot{\mathbf{u}}_I^{cm} - {}^{(t+\Delta t)}\dot{\mathbf{u}}_{\mathcal{D}I}^{trl} \right) \cdot {}^{(t)}\mathbf{n}_{\mathcal{D}I}^{cont}. \tag{6.32} $$

The surface unit normal vector is computed by using the mass gradients (Huang et al., 2011; Nezamabadi et al., 2015; Homel and Herbold, 2017; Chen et al., 2017) as

$$ {}^{(t)}\hat{\mathbf{n}}_{\mathcal{D}I}^{cont} = \frac{\sum_{p=1}^{N_p} \nabla N_I({}^{(t)}\mathbf{x}_p) M_{\mathcal{D}p}}{\| \sum_{p=1}^{N_p} \nabla N_I({}^{(t)}\mathbf{x}_p) M_{\mathcal{D}p} \|}. \tag{6.33} $$

However, as also mentioned in Huang et al. (2011), Eq. (6.33) should be modified to satisfy the collinearity conditions (6.6a) and (6.7a) at contact surface $\partial\Omega_{\bar{f}}$ as

$$ {}^{(t)}\mathbf{n}_{1I}^{cont} = - {}^{(t)}\mathbf{n}_{2I}^{cont} = \frac{{}^{(t)}\hat{\mathbf{n}}_{1I}^{cont} - {}^{(t)}\hat{\mathbf{n}}_{2I}^{cont}}{\| {}^{(t)}\hat{\mathbf{n}}_{1I}^{cont} - {}^{(t)}\hat{\mathbf{n}}_{2I}^{cont} \|} \tag{6.34} $$

to insure momentum conservation.

To satisfy the non-tensional constraint (Eq. (6.6c)) during contact, the normal component should be modified as

$$^{(t)}F^{nor}_{\mathcal{D}I} = \min(0, {}^{(t)}F^{nor,s}_{\mathcal{D}I}). \tag{6.35}$$

Similarly, the tangential component of contact force is evaluated considering the non-slip condition introduced in Eq. (6.7d) as

$$^{(t+\Delta t)}\gamma_{sI} = \left({}^{(t+\Delta t)}\dot{\mathbf{u}}_{1I} - {}^{(t+\Delta t)}\dot{\mathbf{u}}_{2I}\right) \cdot {}^{(t)}\mathbf{s}^{cont}_{1I} = 0. \tag{6.36}$$

Substituting relation (6.28) into (6.36) and then making use of Eqs. (6.31) and (6.29), the tangential component of contact force is expressed as

$$^{(t)}F^{tan,s}_{\mathcal{D}I} = \frac{{}^{(t)}M^{u}_{\mathcal{D}I}}{\Delta t}\left({}^{(t+\Delta t)}\dot{\mathbf{u}}^{cm}_{I} - {}^{(t+\Delta t)}\dot{\mathbf{u}}^{trl}_{\mathcal{D}I}\right) \cdot {}^{(t)}\mathbf{s}^{cont}_{\mathcal{D}I} \tag{6.37}$$

where the surface unit tangential vector $\mathbf{s}^{cont}_{\mathcal{D}I}$ can be derived as the unit vector that forms an orthogonal basis with $\mathbf{n}^{cont}_{\mathcal{D}I}$. The tangential component can be further modified to account for sliding at the contact grid node I, considering the Coulomb friction model, as

$$^{(t)}F^{tan}_{\mathcal{D}I} = \min\left(\mu_f|\,{}^{(t)}F^{nor}_{\mathcal{D}I}|, |\,{}^{(t)}F^{tan,s}_{\mathcal{D}I}|\right) \text{sign}\left({}^{(t)}F^{tan,s}_{\mathcal{D}I}\right). \tag{6.38}$$

Therefore, the contact force is eventually evaluated as

$$^{(t)}\mathbf{F}^{cont}_{\mathcal{D}I} = {}^{(t)}F^{nor}_{\mathcal{D}I} \cdot {}^{(t)}\mathbf{n}^{cont}_{\mathcal{D}I} + {}^{(t)}F^{tan}_{\mathcal{D}I} \cdot {}^{(t)}\mathbf{s}^{cont}_{\mathcal{D}I} \tag{6.39}$$

when the impenetrability condition

$$\left({}^{(t+\Delta t)}\dot{\mathbf{u}}^{trl}_{\mathcal{D}I} - {}^{(t+\Delta t)}\dot{\mathbf{u}}^{cm}_{\mathcal{D}I}\right) \cdot {}^{(t)}\mathbf{n}^{cont}_{\mathcal{D}I} > 0 \tag{6.40}$$

is satisfied at contact grid node I.

Finally, once the contact force vector is computed from Eq. (6.39), the initially predicted nodal velocities ${}^{(t+\Delta t)}\dot{\mathbf{u}}^{trl}_{\mathcal{D}I}$ should be corrected according to Eq. (6.28).

6.3.2.3 Material point properties update

The corrected nodal velocities ${}^{(t+\Delta t)}\dot{\mathbf{u}}_{\mathcal{D}I}$ are utilized to update the material point properties. Hence, the total strains at p^{th} material point are evaluated as

$$ {}^{(t+\Delta t)}\boldsymbol{\varepsilon}_{\mathcal{D}p} = {}^{(t)}\boldsymbol{\varepsilon}_{\mathcal{D}p} + \frac{1}{2}\Delta t \sum_{I=1}^{N_n} \left(\nabla N_I({}^{(t)}\mathbf{x}_p)\, {}^{(t+\Delta t)}\dot{\mathbf{u}}_{\mathcal{D}I} + \left(\nabla N_I({}^{(t)}\mathbf{x}_p)\, {}^{(t+\Delta t)}\dot{\mathbf{u}}_{\mathcal{D}I} \right)^T \right) \tag{6.41} $$

and the total stresses from Eq. (2.50). Finally, the displacement, velocity and acceleration of all material points are updated as

$$ {}^{(t+\Delta t)}\mathbf{u}_{\mathcal{D}p} = {}^{(t)}\mathbf{u}_{\mathcal{D}p} + \Delta t \sum_{I=1}^{N_n} \left(N_I({}^{(t)}\mathbf{x}_p)\, {}^{(t+\Delta t)}\dot{\mathbf{u}}_{\mathcal{D}I} \right) \tag{6.42} $$

$$ {}^{(t+\Delta t)}\dot{\mathbf{u}}_{\mathcal{D}p} = {}^{(t)}\dot{\mathbf{u}}_{\mathcal{D}p} + \Delta t \sum_{I=1}^{N_n} \left(N_I({}^{(t)}\mathbf{x}_p) \frac{{}^{(t)}\mathbf{F}^{ext}_{\mathcal{D}I} + {}^{(t)}\mathbf{F}^{cont}_{\mathcal{D}I} - {}^{(t)}\mathbf{F}^{int}_{\mathcal{D}I}}{{}^{(t)}M^u_{\mathcal{D}I}} \right) \tag{6.43} $$

and

$$ {}^{(t)}\ddot{\mathbf{u}}_{\mathcal{D}p} = \sum_{I=1}^{N_n} \left(N_I({}^{(t)}\mathbf{x}_p) \frac{{}^{(t)}\mathbf{F}^{ext}_{\mathcal{D}I} + {}^{(t)}\mathbf{F}^{cont}_{\mathcal{D}I} - {}^{(t)}\mathbf{F}^{int}_{\mathcal{D}I}}{{}^{(t)}M^u_{\mathcal{D}I}} \right), \tag{6.44} $$

respectively. The material point positions are also updated as

$$ {}^{(t+\Delta t)}\mathbf{x}_{\mathcal{D}p} = {}^{(t)}\mathbf{x}_{\mathcal{D}p} + \Delta t \sum_{I=1}^{N_n} \left(N_I({}^{(t)}\mathbf{x}_p)\, {}^{(t+\Delta t)}\dot{\mathbf{u}}_{\mathcal{D}I} \right). \tag{6.45} $$

6.3.2.4 Staggered solution algorithm

The solution procedure is implemented within a set of N_{steps} incremental steps $(m = 0, ..., N_{steps} - 1)$. At each increment m, the active part of Eulerian Grid is detected according to the material point footprints. Therefore, the total number

of grid nodes N_n, unconstrained degrees of freedom N_{dofs} and active cells N_{cells} are obtained (see Figs. 3.9 and 3.10).

Next, the higher-order B-splines basis functions, i.e. $\mathbf{N}\left({}^{(m)}\mathbf{x}_p\right)$, $\nabla\mathbf{N}\left({}^{(m)}\mathbf{x}_p\right)$ and $\Delta\mathbf{N}\left({}^{(m)}\mathbf{x}_p\right)$, are evaluated at material points in global axes. To account for the material orientation $\phi_{\mathcal{D}p}$ at p^{th} material point the first and second spatial derivatives of basis functions should also be computed in material principal axes, i.e. $\nabla\mathbf{N}_{\phi_p}\left({}^{(m)}\mathbf{x}_p\right)$ and $\Delta\mathbf{N}_{\phi_p}\left({}^{(m)}\mathbf{x}_p\right)$ (see Section 5.3.2 for details).

Then, the contact grid nodes are detected among the discrete fields according to Remark 1.

Remark 1. *Two discrete fields are in contact at grid node I when at least one material point from both discrete fields is projected into grid node I. In particular, the pair of discrete fields, $\mathcal{D}=1$ and $\mathcal{D}=2$ are in contact when the velocity of the $p=1$ material point, that belongs to discrete field $\mathcal{D}=1$, and the $p=2$ material point, that belongs to discrete field $\mathcal{D}=2$, are both interpolated at the grid node I. In this case, the grid node I is a contact grid node for this pair of discrete fields.*

Next, the outward normal ${}^{(m)}\mathbf{n}^{cont}_{\mathcal{D}I}$ and tangential ${}^{(m)}\mathbf{s}^{cont}_{\mathcal{D}I}$ unit vectors are computed at the contact grid nodes. Mass, momentum and internal forces are projected from material points to grid nodes; thus, the quantities ${}^{(m)}M^{u}_{\mathcal{D}I}$, ${}^{(m)}\mathbf{p}_{\mathcal{D}I}$ and ${}^{(m)}\boldsymbol{F}^{int}_{\mathcal{D}I}$ are obtained. Finally, the solution of the coupled Eqs. (6.23) and (6.20) is obtained within a set of N_{staggs} staggered iterations $(k=1,...,N_{staggs})$.

In the employed staggered scheme, the phase field Eq. (4.16) is initially solved for a specific value of the history field ${}^{(m)}\mathcal{H}^{(k)}_{\mathcal{D}p}$. The basis functions $\boldsymbol{N}\left({}^{(m)}\mathbf{x}_p\right)$ and their spatial derivatives evaluated with respect to the material principal axes are utilized to compute the phase field coefficient matrix $\boldsymbol{K}^{c}_{\mathcal{D}}$ from relation (4.17). Thus, the phase field nodal values ${}^{(m)}c^{(k)}_{\mathcal{D}I}$ are obtained for each discrete field $\mathcal{D}$. Next, the phase field nodal values are mapped back onto the material points and the degradation function ${}^{(m)}g^{(k)}_{\mathcal{D}p}$ is computed at each material point. Next, the equation of motion (6.23) is integrated in time employing the

predictor-corrector algorithm described in Section 6.3.2.1 and updated values for the history field ${}^{(m)}\mathcal{H}_{\mathcal{D}p}^{(k)}$ are obtained.

Finally, the phase field nodal residual vector ${}^{(m)}R_I^{c(k)}$ is evaluated according to the updated value of history field ${}^{(m)}\mathcal{H}_{\mathcal{D}p}^{(k)}$ and its convergence checked as $\| {}^{(h)}\mathbf{R}^{c(k)} \| \leq tol_c$ or $k \geq N_{staggs}$ where tol_c and $\| \cdot \|$ are the phase field tolerance value and the Euclidean norm, respectively. The staggered algorithm is continued until convergence is achieved. After convergence, the material point properties are updated and the algorithm proceeds to the next increment h.

The solution procedure is summarized into Algorithm 3 where $E_{\mathcal{D}p}$ and $\nu_{\mathcal{D}p}$ are the Young's modulus and Poisson ratio at material points. Four conditions, namely **C.1** to **C.4**, are also included in Algorithm 3. These are employed to verify that the kinematic constraints introduced in Eqs. (6.6a)-(6.6e) and (6.7a)-(6.7e) are satisfied at contact grid nodes.

6.4 Numerical examples

In this Section, a set of two-dimensional numerical examples is presented. The numerical examples demonstrate the accuracy of the proposed PF-MPM against the standard PF-FEM as well as its computational efficiency in impact-fracture problems. Both the isotropic and anisotropic phase field models are examined within both single and multi discrete-field examples.

Quadratic B-splines (C^1) are utilized for the background grid as described in Section 3.9.9. The initial cell density is chosen to be at least 3x3 $= 9$ material points per cell element. Higher-order B-splines are employed not only to compute the anisotropic phase field matrix in Eq. (5.37), but also to improve the accuracy of MPM from the so-called "cell-crossing error" (see Section 3.9.8).

In all cases examined in this work, stability of the explicit integration scheme is established on the basis of the following upper bound for the time increment

Data: Define dynamic parameters, computational grid, material point properties $(\Delta t, {}^{(0)}\mathbf{x}_{\mathcal{D}p}, {}^{(0)}\Omega_{\mathcal{D}p}, E_{\mathcal{D}p}, \nu_{\mathcal{D}p}, {}^{(0)}\rho_{\mathcal{D}p}, l_{0_{\mathcal{D}p}}, k_{f_{\mathcal{D}p}}, \bar{\mathcal{G}}_{c_{\mathcal{D}p}}, \gamma_{ijkl_{\mathcal{D}p}}, \phi_{\mathcal{D}p}, {}^{(0)}\mathcal{H}_{\mathcal{D}p}, {}^{(0)}\boldsymbol{\varepsilon}_{\mathcal{D}p}, {}^{(0)}\boldsymbol{\sigma}_{\mathcal{D}p}, {}^{(0)}\mathbf{u}_{\mathcal{D}p}, {}^{(0)}\dot{\mathbf{u}}_{\mathcal{D}p}, {}^{(0)}\ddot{\mathbf{u}}_{\mathcal{D}p}, {}^{(0)}\mathbf{x}_{\mathcal{D}p})$

for *each time step* $m = 0, .., N_{steps} - 1$ **do**

Reset the computational grid: Find active part of Eulerian Grid, N_n, N_{dofs}, N_{cells};

Compute: $\mathbf{N}({}^{(m)}\mathbf{x}_p)$, $\nabla\mathbf{N}({}^{(m)}\mathbf{x}_p)$ and $\Delta\mathbf{N}({}^{(m)}\mathbf{x}_p)$, for all material points. ;

Compute: $\nabla\mathbf{N}_{\phi_p}({}^{(m)}\mathbf{x}_p)$ and $\Delta\mathbf{N}_{\phi_p}({}^{(m)}\mathbf{x}_p)$, for all material points. ;

Detect contact grid nodes (see Remark 1);

Compute: ${}^{(m)}\mathbf{n}^{cont}_{\mathcal{D}I}$ and ${}^{(m)}\mathbf{s}^{cont}_{\mathcal{D}I}$ vectors (see Eqs. (6.34));

C.1: Check collinearity conditions for all contact nodes (see Eqs. (6.6a) and (6.7a));

Map mass, momentum and internal forces from material points to grid nodes: ${}^{(m)}M^{u}_{\mathcal{D}I}$, ${}^{(m)}\mathbf{p}_{\mathcal{D}I}$ and ${}^{(m)}\mathbf{F}^{int}_{\mathcal{D}I}$ (see Eqs. (3.58), (6.24) and (6.25)) ;

for *each staggered iteration* $k = 1, 2, .., N_{staggs}$ **do**

Compute: ${}^{(m)}\mathbf{F}^{c(k)}_{\mathcal{D}}$ (see Eq. (5.35) according to $\mathbf{N}({}^{(m)}\mathbf{x}_p)$. ;

Compute: ${}^{(m)}\mathbf{K}^{c,Anis(k)}_{\mathcal{D}}$ (see Eq. (5.37)) according to $\mathbf{N}({}^{(m)}\mathbf{x}_p)$, $\nabla\mathbf{N}_{\phi_p}({}^{(m)}\mathbf{x}_p)$, $\Delta\mathbf{N}_{\phi_p}({}^{(m)}\mathbf{x}_p)$ and ${}^{(m)}\mathcal{H}^{(k)}_{\mathcal{D}p}$. ;

Solve: ${}^{(m)}\mathbf{K}^{c,Anis(k)}_{\mathcal{D}}\,{}^{(m)}\mathbf{c}^{(k)}_{\mathcal{D}} = {}^{(m)}\mathbf{F}^{c(k)}_{\mathcal{D}}$;

Map phase field $({}^{(m)}\mathbf{c}^{(k)}_{\mathcal{D}})$ from grid nodes to material points. Evaluate: ${}^{(m)}c^{(k)}_{\mathcal{D}p}$, ${}^{(m)}\nabla c^{(k)}_{\mathcal{D}p}$, ${}^{(m)}\Delta c^{(k)}_{\mathcal{D}p}$, ${}^{(m)}g^{(k)}_{\mathcal{D}p}$, for all material points (see Eqs. (5.30), (5.31),(5.32) and (2.48)). ;

Update trial momentum: ${}^{(m+1)}\mathbf{p}^{trl(k)}_{\mathcal{D}I}$ (see Eq. (6.26));

Compute: ${}^{(m+1)}\dot{\mathbf{u}}^{trl(k)}_{\mathcal{D}I}$ and ${}^{(m+1)}\dot{\mathbf{u}}^{cm(k)}_{\mathcal{D}I}$ (see Eqs. (6.27) and (6.29)). ;

if *Eq. (6.40) is satisfied at contact grid node I* **then**

Compute: ${}^{(m)}F^{nor(k)}_{\mathcal{D}I}$, ${}^{(m)}F^{tan(k)}_{\mathcal{D}I}$ and ${}^{(m)}\mathbf{F}^{cont(k)}_{\mathcal{D}I}$ (see Eqs. (6.35), (6.38) and (6.39)) ;

end

C.2: Check collinearity conditions for all contact nodes (see Eq. (6.6b) and Eq. 6.7b);

Correct velocities: ${}^{(m+1)}\dot{\mathbf{u}}^{(k)}_{\mathcal{D}I}$ (see Eq. (6.28));

C.3: Check impenetrability and complementarity (normal) conditions for all contact nodes (see Eqs. (6.6d) and (6.6e)) ;

C.4: Check slip/non-slip and complementarity (tangential) conditions for all contact nodes (see Eqs. (6.7d) and (6.7e)) ;

Compute: ${}^{(m+1)}\boldsymbol{\varepsilon}^{(k)}_{\mathcal{D}p}$ and ${}^{(m+1)}\boldsymbol{\sigma}^{(k)}_{\mathcal{D}p}$, for all material points (see Eq. (6.41) and (2.50)) ;

Compute: ${}^{(m+1)}\psi^{+(k)}_{el_{\mathcal{D}p}}$, for all material points (see Eq. (2.77))

$\rightarrow {}^{(m)}\mathcal{H}^{(k)}_{\mathcal{D}p} = \begin{cases} {}^{(m+1)}\psi^{+(k)}_{el_{\mathcal{D}p}}, & \text{for } {}^{(m+1)}\psi^{+(k)}_{el_{\mathcal{D}p}} > {}^{(m)}\mathcal{H}^{(k)}_{\mathcal{D}p} \\ {}^{(m)}\mathcal{H}^{(k)}_{\mathcal{D}p}, & \text{otherwise} \end{cases}$;

Compute Residual (Phase Field): ${}^{(h)}\mathbf{R}^{c,Anis(k)}$ (see Eq. (6.19)) according to ${}^{(m)}c^{(k)}_{\mathcal{D}p}$, ${}^{(h)}\nabla c^{(k)}_{\mathcal{D}p}$, ${}^{(m)}\Delta c^{(k)}_{\mathcal{D}p}$, ${}^{(m)}g^{(k)}_{\mathcal{D}p}$;

Convergence Check (Phase Field): If $\| {}^{(m)}\mathbf{R}^{c(k)} \| \leq tol_c$ or $k \geq N_{staggs}$ then "exit" from loop else $k = k + 1$ go to next staggered iteration. ;

end

Update material point properties: ${}^{(m+1)}\mathbf{u}^{c(k)}_{\mathcal{D}p}$, ${}^{(m+1)}\dot{\mathbf{u}}^{c(k)}_{\mathcal{D}p}$ and ${}^{(m)}\ddot{\mathbf{u}}^{c(k)}_{\mathcal{D}p}$ (see Eqs. (6.42), (6.43), (6.44) and (6.45)). ;

Update material point history field: ${}^{(m+1)}\mathcal{H}_{\mathcal{D}p} = {}^{(m)}\mathcal{H}_{\mathcal{D}p}$;

end

Algorithm 3: Anisotropic Phase Field Material Point Method pseudo-code for impact-fracture problems (Staggered Solution Algorithm with Explicit time integration).

Δt

$$\Delta t \leq \Delta \tilde{t}_{cr} \tag{6.46}$$

where

$$\Delta \tilde{t}_{cr} = \alpha_c \cdot \Delta t_{cr} \tag{6.47}$$

and Δt_{cr} corresponds to the critical time step prescribed by the Courant-Friedrichs-Lewy (CFL) condition and it is defined by

$$\Delta t_{cr} = \frac{h}{\dot{u}_c}. \tag{6.48}$$

In Eq. (6.48), h is the cell spacing and $\dot{u}_c$ is the sound of speed in linearly elastic materials defined by

$$\dot{u}_c = \frac{E(1-\nu)}{(1+\nu)(1-2\nu)\rho}. \tag{6.49}$$

Parameter $\alpha_c \in [0.8, 0.98]$ in Eq. (6.46) depends on the non-linearities of the system (Zhang et al., 2016). In all the numerical experiments, we consider $\alpha_c = 0.80$.

In all numerical experiments presented the phase field residual tolerance was set to $tol_c = 10^{-6}$ and a single staggered iteration was required for solution convergence. This is due to the small time step, imposed by the stability requirements (Eq. (6.46)).

6.4.1 Cylinder rolling - Verification of contact algorithm

In the first example, the MPM contact algorithm is verified against existing analytical solutions in the literature. Herein, a cylinder rolling on a fixed plate is examined. The geometry and boundary conditions of the problem are shown in Fig. 6.3(a). At time $t = 0$ the cylinder is left to roll on the plate considering only its self-weight. Three cases are considered, herein, for the friction coefficient,

namely case (i): $\mu_f = 0.05$, case (ii): $\mu_f = 0.30$ and case (iii): $\mu_f = 0.90$. The angle of the plate is chosen to be $\theta_r = 60^o$.

The centre-of-mass displacement of the cylinder $\mathbf{u_{cm}}$ (see Fig. 6.3(a)) is measured at each case and compared against the analytical solution (Chen et al., 2017), computed from Eq. (6.50) below

$$\mathbf{u_{cm}} = \begin{cases} \frac{1}{2}gt^2(\sin\theta_r - \mu_f \cos\theta_r) & \tan\theta_r > 3\mu_f \textbf{ (roll and slip)} \\ \\ \frac{1}{3}gt^2 \sin\theta_r & \tan\theta_r \leq 3\mu_f \textbf{ (roll without slip)} \end{cases} \tag{6.50}$$

where g is the gravitational acceleration, i.e. $g = 9.81$ m/sec^s. According to the choice of the plate inclination and the friction coefficient, the cylinder can be either roll without slip or roll and slip on the plate. All the material and simulation parameters are presented in Table 6.1.

The centre-of-mass displacement over time is shown in Fig. 6.3(b). From Fig. 6.3(b), it is verified that the MPM contact algorithm agrees well with the analytical solutions for all cases. Furthermore, the cylinder rolling response over time is shown in Fig. 6.4. Roll without slip is only noticed in case (iii) whereas in cases (i) and (ii) both roll and slip is observed.

6.4.2 Plate under impact loading

A plate under impact loading is examined herein. The purpose of this example is to verify the proposed PF-MPM against the standard PF-FEM in dynamic brittle fracture problems. The ability of PF-MPM to simulate dynamic brittle fracture in anisotropic media is also demonstrated. The same problem has been previously analysed by Borden et al. (2012) with a Phase Field Finite Element implementation, considering a second order isotropic phase field formulation.

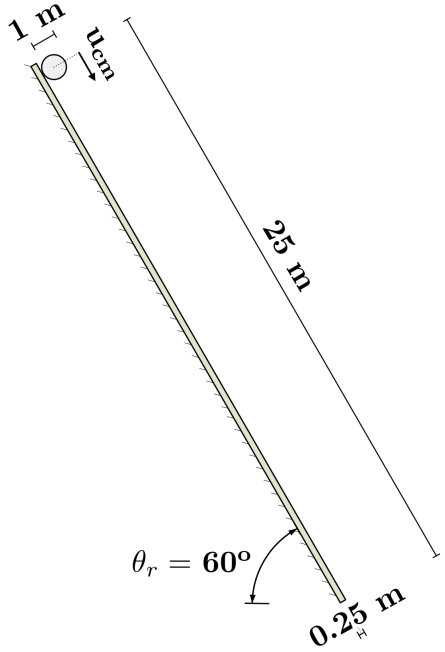

(a)

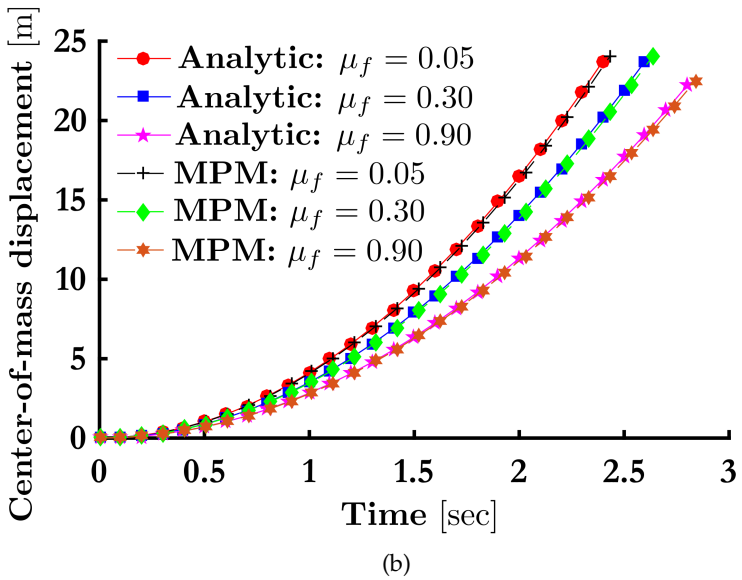

(b)

Figure 6.3: Cylinder rolling: (a) Geometry and boundary conditions (b) centre-of-mass displacement $\mathbf{u_{cm}}$ over time for MPM simulation and its corresponding analytical solution for cases (i): $\mu = 0.05$, (ii): $\mu = 0.30$ and (iii): $\mu = 0.90$.

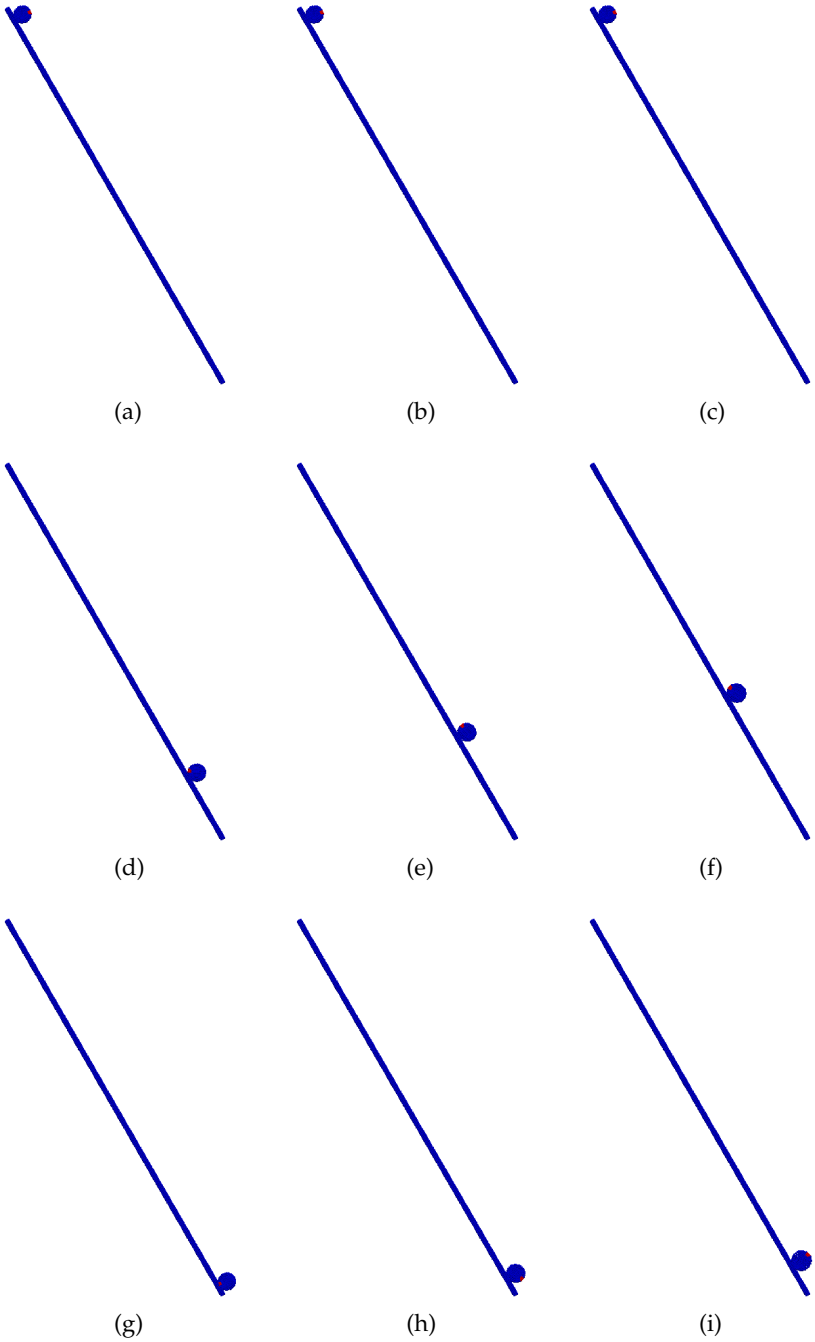

Figure 6.4: Cylinder rolling: Rolling response for (a), (d) and (g) case (i): $\mu_f = 0.05$, (b), (e) and (h) case (ii): $\mu_f = 0.30$ and (c), (f) and (i) case (iii): $\mu_f = 0.90$. The subfigs. (a)-(c) are refereed to time step $t = 0$ sec, the (d)-(f) to $t = 2.25$ sec and (g)-(i) to $t = 2.79$ sec.

Elastic Material Parameters			
	Cylinder	**Plate**	
E	1000	1000	[MN/m^2]
ν	0.30	0.30	[–]
ρ	1000	10000	[kg/m^3]
Material Point Method Model			
Number of Control Points	13668		
Number of Cells	400x32=12800		
Cell spacing	0.0625		[m]
$q_\xi = q_\eta$	2nd		
Ξ	$\{0,0,0,0.0025,0.0050,...,0.9950,0.9975,1,1,1\}$		
H	$\{0,0,0,0.03125,0.0625,...,0.9375,0.96875,1,1,1\}$		
Initial Cell density	3x3		
Number of Material Points	16848		
Discrete Fields			
Number of Discrete Fields	2		
μ_f	0.05	Case (i)	
	0.30	Case (ii)	
	0.90	Case (iii)	
Solution Algorithm Parameters			
Time Integrator	Explicit		
Δt	0.0000001		[sec]
Δt_{cr}	0.000000861		[sec]
$\Delta \tilde{t}_{cr}$	0.000000689		[sec]

Table 6.1: Cylinder rolling: Simulation parameters.

The geometry and boundary conditions are presented in Fig. 6.5(a). Herein, three cases are considered, i.e., (i) isotropic symmetry, (ii) cubic symmetry, and (iii) orthotropic symmetry. The material orientation is chosen to be $\phi = +30^o$ with respect to x axis (clockwise) as shown in Fig. 6.5(a).

The cell spacing is $h = 0.125$ mm and plane strain conditions are assumed. In case (i), all the anisotropic material parameters are chosen such that $\gamma_{ijkl} = 0$. Hence, the anisotropic phase field model reduces to the second order isotropic case. The maximum and minimum surface energy densities are equal to $\mathcal{G}_c(\theta) = \bar{\mathcal{G}}_c = \mathcal{G}_{c_{max}} = \mathcal{G}_{c_{min}} = 0.003$ N/mm. In case (ii) cubic symmetry of the surface energy density is considered with $\bar{\mathcal{G}}_c = 0.002121$ N/mm and anisotropic parameters $\gamma_{1111} = \gamma_{2222} = 1.00$, $\gamma_{1122} = 0.00$ and $\gamma_{1212} = 74.00$. These parameters result into maximum and minimum surface energy densities $\mathcal{G}_{c_{max}} = 0.0049$ N/mm and $\mathcal{G}_{c_{min}} = 0.003$ N/mm, respectively. In case (iii) the anisotropic parameter γ_{2222} is increased to $\gamma_{2222} = 80.00$ giving rise to orthotropic symmetry with maximum and minimum surface energy densities $\mathcal{G}_{c_{max}} = 0.0067$ N/mm and $\mathcal{G}_{c_{min}} = 0.003$ N/mm, respectively.

The surface energy densities and their reciprocals for material orientation $\phi =$

$+30^o$ are shown in Fig. 6.5(b) and Fig. 6.5(c), respectively. In cases (ii) and (iii), the parameter $\bar{\mathcal{G}}_c$ is chosen so that $\mathcal{G}_{c_{min}} = 0.003$ N/mm and to facilitate comparisons between all cases (see also, Figs. 6.5(b) and 6.5(c)).

A single discrete field is considered in this example. The solution procedure is implemented with a time step $\Delta t = 0.025$ μs for $N_{steps} = 3200$ steps. The critical time step is $\Delta\tilde{t}_{cr} = 0.026$ μs. The pressure is considered to be constant $\sigma = 1$ N/mm^2 during the analysis. The initial crack is modelled by introducing an initial history field at the corresponding material points as in Borden et al. (2012). In this, the initial history field is defined by

$$\mathcal{H}_p = \begin{cases} B_p \frac{\bar{\mathcal{G}}_{c_p}}{4l_{0_p}} \left(1 - \frac{d_p}{l_{0_p}}\right) & d_p \leq l_{0_p} \\ \\ 0 & d_p > l_{0_p} \end{cases} \tag{6.51}$$

where $B_p = 1000$ and d_p is the closest distance from the position of material point x_p to the line that represents the discrete crack. The Rayleigh wave speed is $\dot{u}_R = 2125$ m/s for the material parameters of that specimen (Freund, 1998). All simulation parameters are summarized in Table 6.2.

6.4.2.1 Case (i): Isotropy

Initially, the PF-MPM is compared against the PF-FEM with the results obtained in Borden et al. (2012) for the same cell spacing $h = 0.125$ mm.

The total energy time-histories for the two solutions are shown in Figs. 6.6(a) and 6.6(b) where the 2 methods demonstrate a very good agreement. The total fracture energy results (see Fig. 6.6(b)) are in good agreement with the results reported in Borden et al. (2012), although minor differences are observed, especially for time $t > 50$ μs. The total elastic strain energies (see Fig. 6.6(a)) also demonstrate very good agreement with some differences after $t > 30$ μs.

The evolution of the phase field is presented in Fig. 6.7 for specific time steps. In these, the occurrence of a branched crack is observed at approximately $t = 35$ μs. The evolution of the hydrostatic stress for the same timesteps is shown in Fig. 6.8. To demonstrate the influence of the surface energy density into the resulting crack paths, the reciprocal of the surface energy density is also plotted (black circle); the hydrostatic stresses are also shown in the same figure. Since the surface energy density is isotropic, hence independent of the material orientation, the crack naturally propagates along the vertical axis (see Figs. 6.7(b) and 6.8(b)) until branching occurs. Furthermore, crack branching is perfectly symmetrical due to structure, load symmetry and the isotropic phase field model.

The crack tip velocities for the two methods are presented in Fig. 6.6(c). As already mentioned in numerous works (see Borden et al. (2012), Hofacker and Miehe (2013), Schlüter et al. (2014)), the crack tip and the exact location of crack branching cannot be identified uniquely due to the smooth description of the crack. Therefore, the crack tip velocity is measured with the methodology employed in Borden et al. (2012) to facilitate verification. The results of both methods illustrate very good agreement. The crack widening and branching regions are almost the same for the two solutions and they are also shown in Fig. 6.6(c). Crack widening here refers to the broadening of the damage zone prior to branching in accordance with the definition introduced in Borden et al. (2012).

In Fig. 6.6(c), the crack tip velocity is clearly below the Rayleigh wave speed which is the crack speed limit as elaborated by Freund (1998) and Ravi-Chandar (1998). However, experimental studies have shown that cracks rarely propagate at speeds close to the Rayleigh wave speed. In fact, they propagate at a fraction of the Rayleigh wave speed, i.e. 60% $\dot{u}_R$ (Ravi-Chandar and Knauss, 1984). As shown in Fig. 6.6(c), the resulting crack tip velocities are below this limit.

6.4.2.2 Case (ii): Cubic symmetry

The evolution of the phase field and the hydrostatic stress for specific time steps is presented in Fig. 6.9 and 6.10, respectively. From Figs. 6.9(b) and 6.10(b), it is observed that due to the anisotropic cubic model and the material orientation $\phi = +30^o$ the crack does not initiate along the vertical axis. The crack propagates until the crack branches at approximately $t = 50$ μs. In this case, the branched crack is not symmetrical and it branches along its two preferential weak directions (see Figs. 6.10(c) and 6.10(d)). To further illustrate this, the reciprocal of the surface energy density is also plotted in Fig. 6.10.

6.4.2.3 Case (iii): Orthotropic symmetry

The evolution of the phase field and the hydrostatic stresses for several time steps in case (iii) are shown in Figs. 6.11 and 6.12, respectively. Opposite to the isotropic case, crack initiation does not occur along the the vertical axis as shown in Figs. 6.11(b) and 6.12(b). Indeed, the anisotropic orthotropic model and the material orientation trigger the crack to propagate along a weak direction that is not aligned with vertical axis, similar to case (ii). However, opposite to case (ii) no crack branching is observed in case (iii). This can be justified by the fact that there is only one preferential weak direction. As a result, the crack path continues to propagate at one half of the plate. To further illustrate the effect of anisotropy on the resulting crack path, the reciprocal of the surface energy density is also plotted in Fig. 6.12.

The energy time-histories for all cases are shown in Figs. 6.13(a) and 6.13(b). In all cases the crack initiates when the total elastic energy becomes approximately equal to $0.12\,\mathrm{J/m}$. It should be stressed that the total elastic strain energy evolves in an almost identical fashion in cases (ii) and (iii) until approximately $t = 50$ μs. After that, the two models diverge as a result of the crack branching in the case of cubic symmetry only.

The crack tip velocities for the three cases are shown in Fig. 6.13(c). The branched regions of both case (i) (isotropic) and (ii) (cubic) are also highlighted in Fig. 6.13(c). The crack branching in isotropic symmetry is observed earlier than in cubic symmetry with a corresponding decrease in crack speed. In all cases, the crack initiates at approximately $t = 10$ μs; the resulting crack tip velocities in all cases are comparable. This can be justified by the fact that the impact energy imposed as well as $\mathcal{G}_{c_{min}}$ are identical in all cases. In the orthotropic case, all the results are below the 60% $\dot{u}_R$ limit.

6.4.2.4 Crack branching and merging

The efficiency of phase field models to deal with complex crack paths, i.e. including crack branching and crack merging is demonstrated herein. The traction is increased to $\sigma = 2.3$ N/mm^2. All other model parameters are kept constant. The second order isotropic phase field model is used. The total duration of the analysis is $t_{tot} = 130$ μs within $N_{steps} = 5200$ steps. The evolution of the phase field for several time steps is presented in Fig. 6.14. In particular, Fig. 6.14(b) illustrates 5 branched cracks, i.e., 1 main, 2 secondary and 2 tertiary branches. More branched cracks are observed in Fig. 6.14(c) while in Fig. 6.14(d) 4 merged cracks are presented. The total strain energy together with the total fracture energy is shown in Fig. 6.16 whereas The evolution of the hydrostatic stress for that case is shown in Fig. 6.15 for several time steps

The crack tip velocity for that case is shown in Fig. 6.16(c). The crack tip velocity is measured along the paths $\mathbf{C}_{3,1}$, $\mathbf{C}_{3,2}$, $\mathbf{C}_{3,3}$ and $\mathbf{C}_{3,4}$ that are marked in Fig. 6.14(b). The increased impact loading, i.e. $\sigma = 2.3$ N/mm^2, leads to a crack initiation at approximately $t = 5$ μs. This occurs earlier than in case (i), where the first crack initiates at approximately $t = 10$ μs. The crack tip rapidly accelerates to the 60% $\dot{u}_R$ limit. Although, some points exceed the 60% $\dot{u}_R$ limit, the majority of measured points satisfy this condition while all points are clearly below the Rayleigh wave speed. In particular, the crack tip propagates with an

average speed close to the 60% $\dot{u}_R$ limit. The three branched regions are also illustrated in Fig. 6.16(c) where a decrease in crack speed is observed.

6.4.3 Collision of two rings

Herein, the collision of two rings is analysed with the geometry and boundary conditions of the problem shown in Fig. 6.17(a). The aim of this example is to demonstrate the robustness of the proposed method into resolving fragmentation problems and the interactions occurring between fragments.

The cell spacing is chosen to be $h = 0.50$ mm for the numerical implementation and plane stress conditions are assumed with thickness 2 mm. Two discrete fields are considered, i.e., field A (left ring) and B (right ring) with the friction coefficient between them, $\mu_f = 0.65$. The total number of material points is 325620. The elastic material parameters are chosen to be $E = 190000$ N/mm^2, $\nu = 0.30$ and $\rho = 8000$ kg/m^3 for both bodies. A time step $\Delta t = 0.0125$ μs for $N_{steps} = 50000$ is considered. The initial distance between the two rings is assumed to be $2h = 1.00$ mm.

The critical time step is $\Delta\tilde{t}_{cr} = 0.071$ μs. The initial distance between the two rings is assumed to be $2h = 1.00$ mm. An initial velocity is applied to the material points of the two rings as $\dot{\mathbf{u}}_{Ap_{(0)}} = \dot{\mathbf{u}}_{(0)}$ and $\dot{\mathbf{u}}_{Bp_{(0)}} = -\dot{\mathbf{u}}_{(0)}$. To examine the influence of the initial velocity on the resulting crack paths, two cases are considered, namely (i) $\dot{\mathbf{u}}_{(0)} = 0.01$ mm/μs and (ii) $\dot{\mathbf{u}}_{(0)} = 0.02$ mm/μs, respectively. The second order isotropic model is utilized for that problem, therefore $\gamma_{ijkl} = 0$ with length scale parameter $l_0 = 1.00$ mm, $k_f = 0.00$ and $\mathcal{G}_c(\theta) = \bar{\mathcal{G}}_c = \mathcal{G}_{c_{max}} = \mathcal{G}_{c_{min}} = 6.00$ N/mm. All simulation parameters are summarized in Table 6.3.

Material Parameters					
Elastic Material Properties			Anisotropic Material Properties		
E	32000	[N/mm^2]		0.00	Isotropic symmetry
			γ_{1111}	1.00	Cubic symmetry [–]
ν	0.20	[–]		1.00	Orthotropic symmetry
ρ	2450	[kg/m^3]		0.00	Isotropic symmetry
			γ_{2222}	1.00	Cubic symmetry [–]
$\dot{u}_R$	2125	[m/s]		80.00	Orthotropic symmetry
				0.00	Isotropic symmetry
			γ_{1122}	0.00	Cubic symmetry [–]
				0.00	Orthotropic symmetry
				0.00	Isotropic symmetry
			γ_{1212}	74.00	Cubic symmetry [–]
				74.00	Orthotropic symmetry
			l_0	0.25	[mm]
			k_f	0.00	[–]
				0.003	Isotropic symmetry
			$\bar{\mathcal{G}}_c$	0.002121	Cubic symmetry [N/mm]
				0.002121	Orthotropic symmetry
				0.003	Isotropic symmetry
			$\mathcal{G}_{c_{max}}$	0.0049	Cubic symmetry [N/mm]
				0.0067	Orthotropic symmetry
				0.003	Isotropic symmetry
			$\mathcal{G}_{c_{min}}$	0.003	Cubic symmetry [N/mm]
				0.003	Orthotropic symmetry
			ϕ	+30	[Deg]

Material Point Method Model		
Number of Control Points	265024	
Number of Cells	806x326=262756	
Cell spacing	0.125	[mm]
$q_\xi = q_\eta$	2nd	
Ξ	$\{0,0,0,0.001240,0.002481,...,0.997518,0.998759,1,1,1\}$	
H	$\{0,0,0,0.003067,0.006134,...,0.993865,0.996932,1,1,1\}$	
Initial Cell density	3x3	
Number of Material Points	2304000	
Discrete Fields		
Number of Discrete Fields	1	
Solution Algorithm Parameters		
Time Integrator	Explicit	
Δt	0.025	[μs]
N_{steps}	3200	
N_{staggs}	1	

Table 6.2: Plate under impact loading: Simulation parameters.

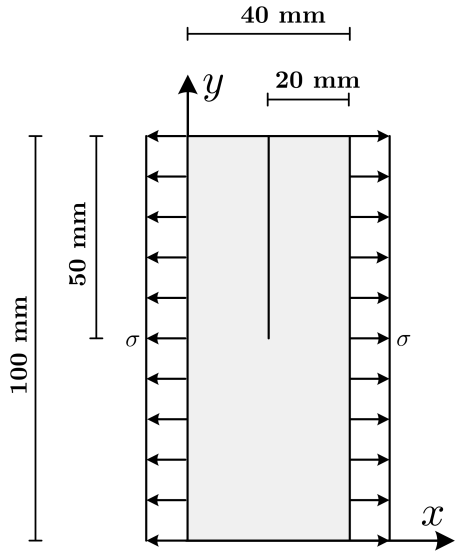

(a)

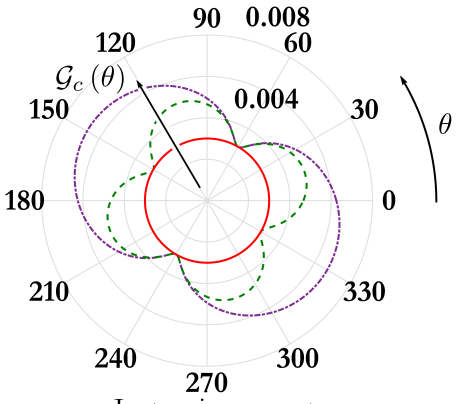

(b)

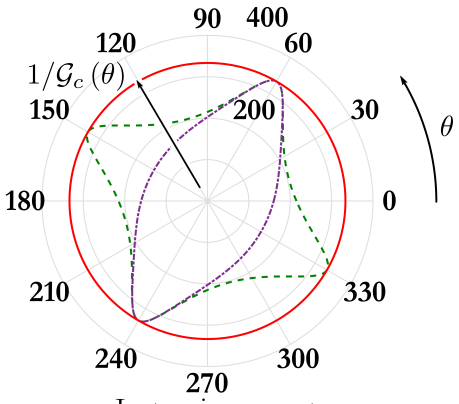

(c)

Figure 6.5: Plate under impact loading: (a) Geometry and boundary conditions. (b) Surface energy densities $\mathcal{G}_c(\theta)$ and (c) their reciprocals $1/\mathcal{G}_c(\theta)$ for material orientation $\phi = +30^o$ (with respect to x axis (clockwise)) in polar coordinates.

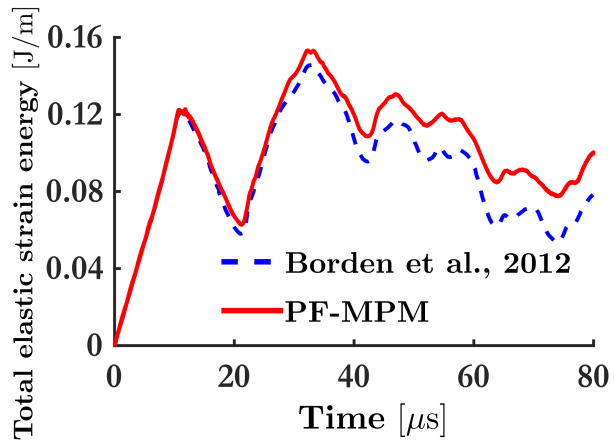

(a)

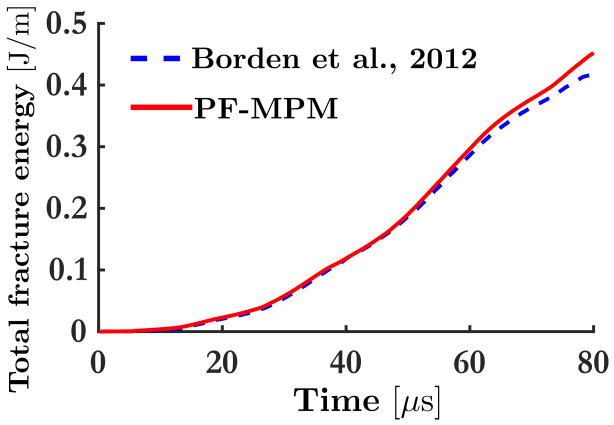

(b)

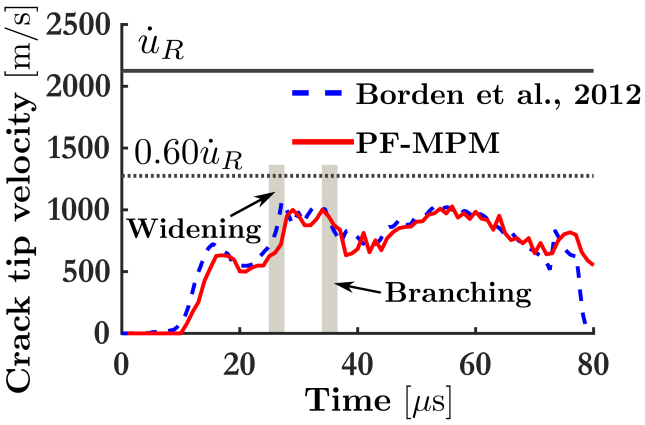

(c)

Figure 6.6: Plate under impact loading: (a) Total elastic strain energies, (b) Total fracture energies and (c) Crack tip velocities over time for Borden et al. (2012) and PF-MPM 2nd order isotropic model (case (i)). The traction is considered to be $\sigma = 1\ \mathrm{N/mm^2}$.

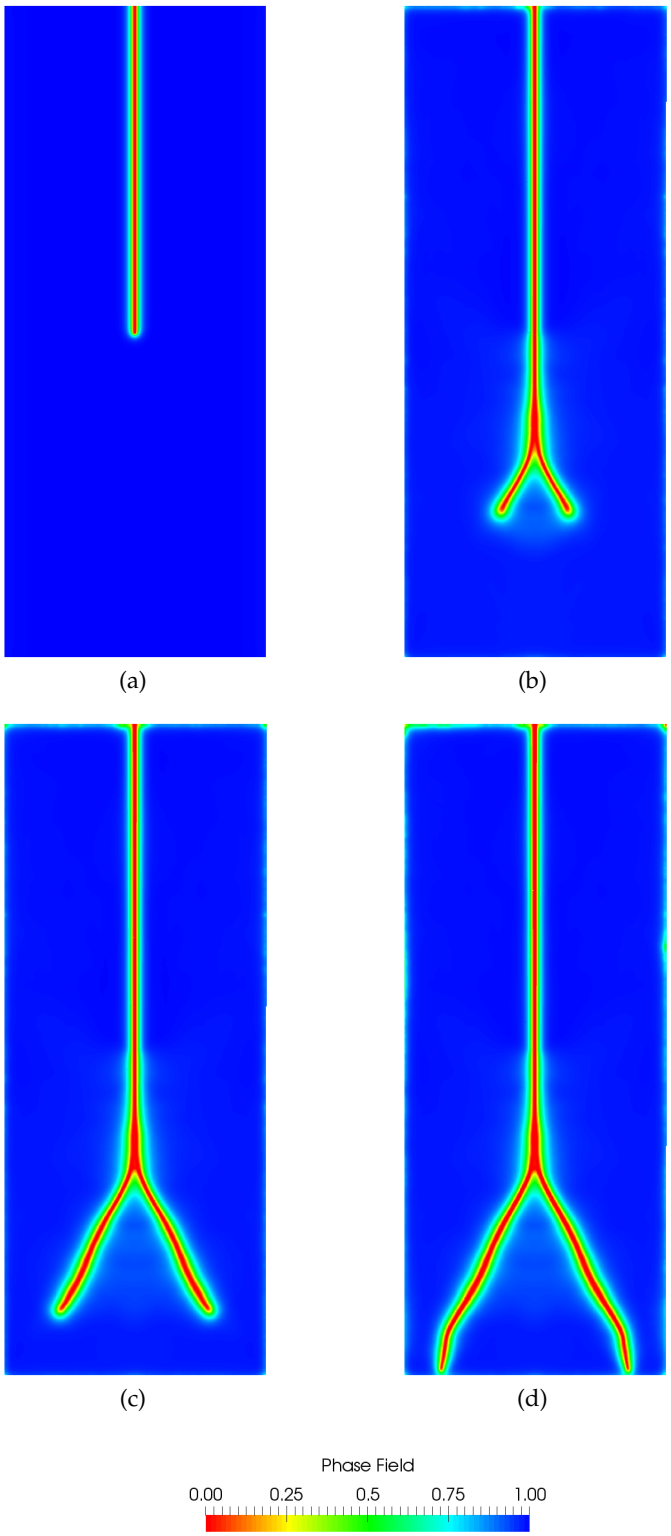

Figure 6.7: Plate under impact loading: Phase field for time steps (a) t=0 μs (b) t=50 μs (b) t=65 μs and (b) t=80 μs. Results for case (i): 2nd order isotropic phase field model and $\sigma = 1$ N/mm^2.

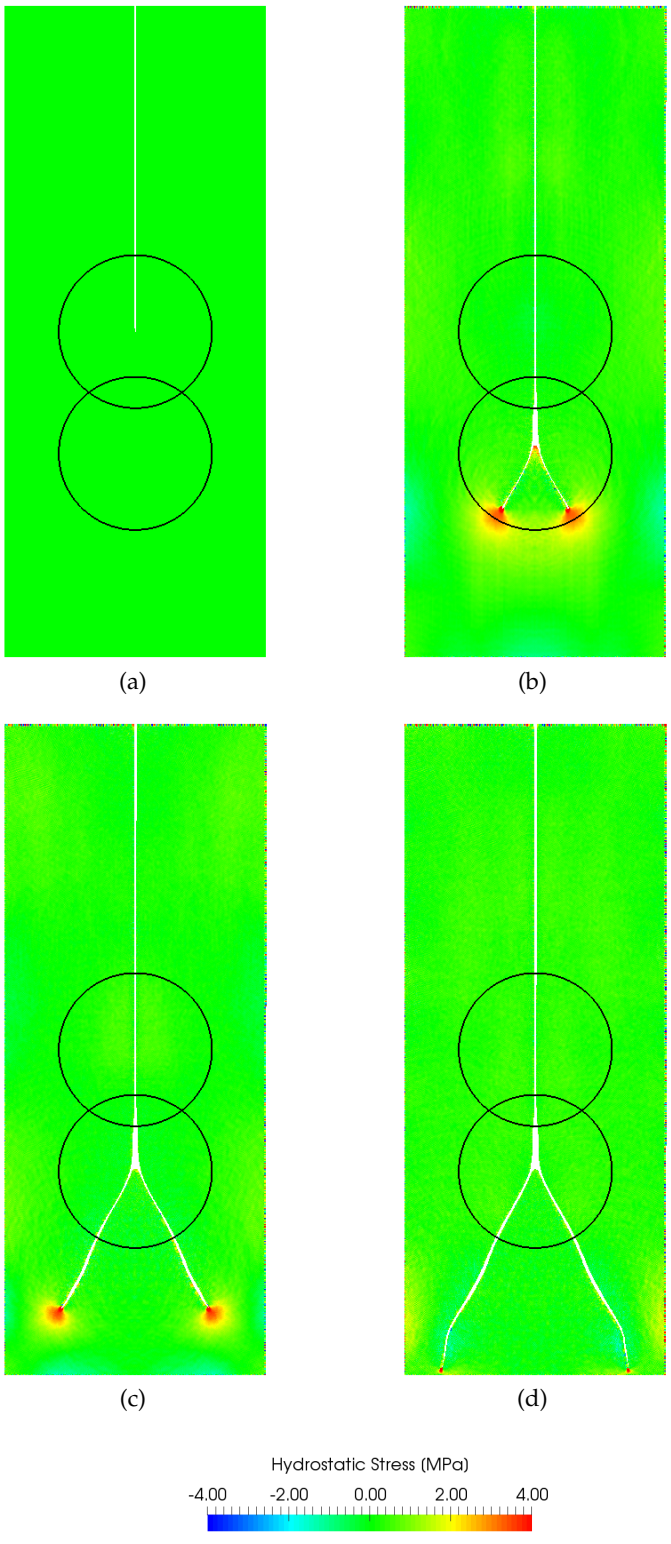

Figure 6.8: Plate under impact loading: Hydrostatic stress for time steps (a) t=0 μs (b) t=50 μs (c) t=65 μs and (d) t=80 μs. Results for case (i): 2nd order isotropic phase field model and $\sigma = 1$ N/mm^2. Material points with $c_p < 0.10$ have been removed.

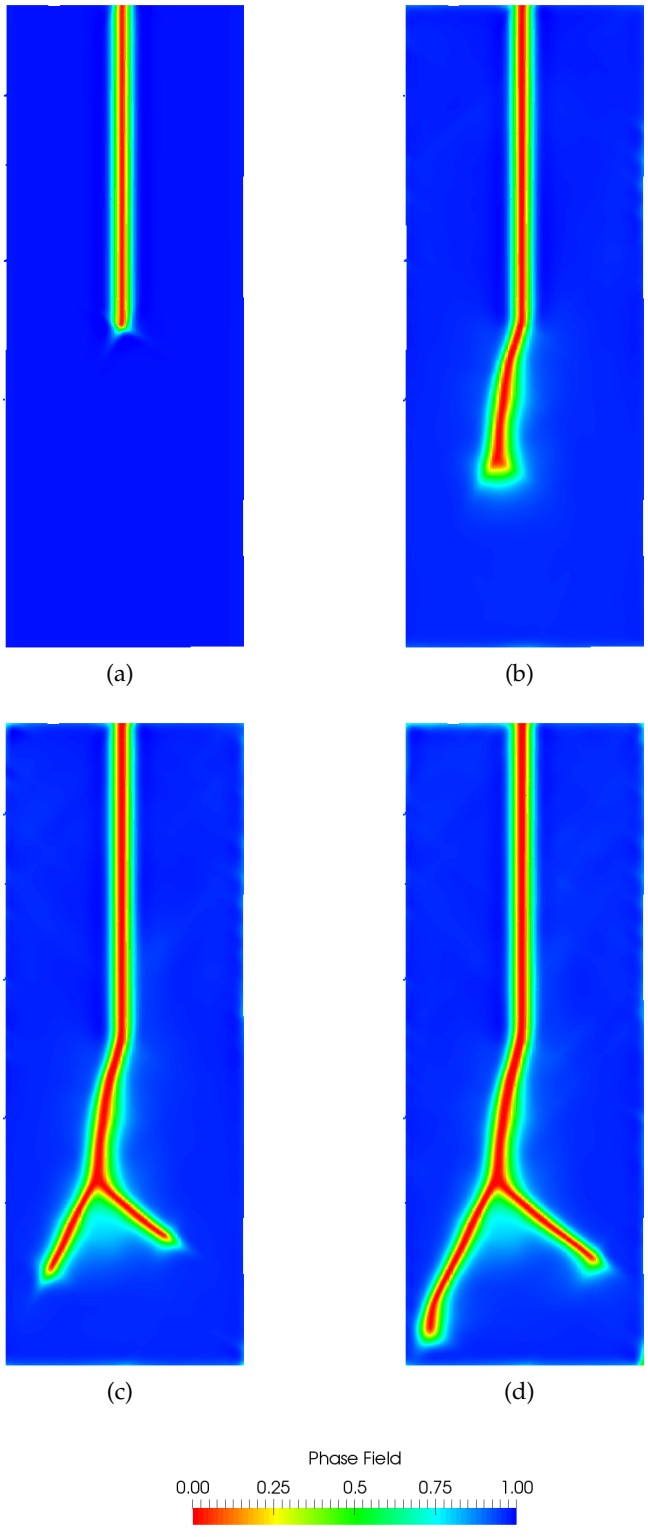

Figure 6.9: Plate under impact loading: Phase field for time steps (a) t=0 μs (b) t=50 μs (c) t=65 μs and (d) t=80 μs. Results for case (ii): 4th order anisotropic cubic phase field model and $\sigma = 1$ N/mm^2.

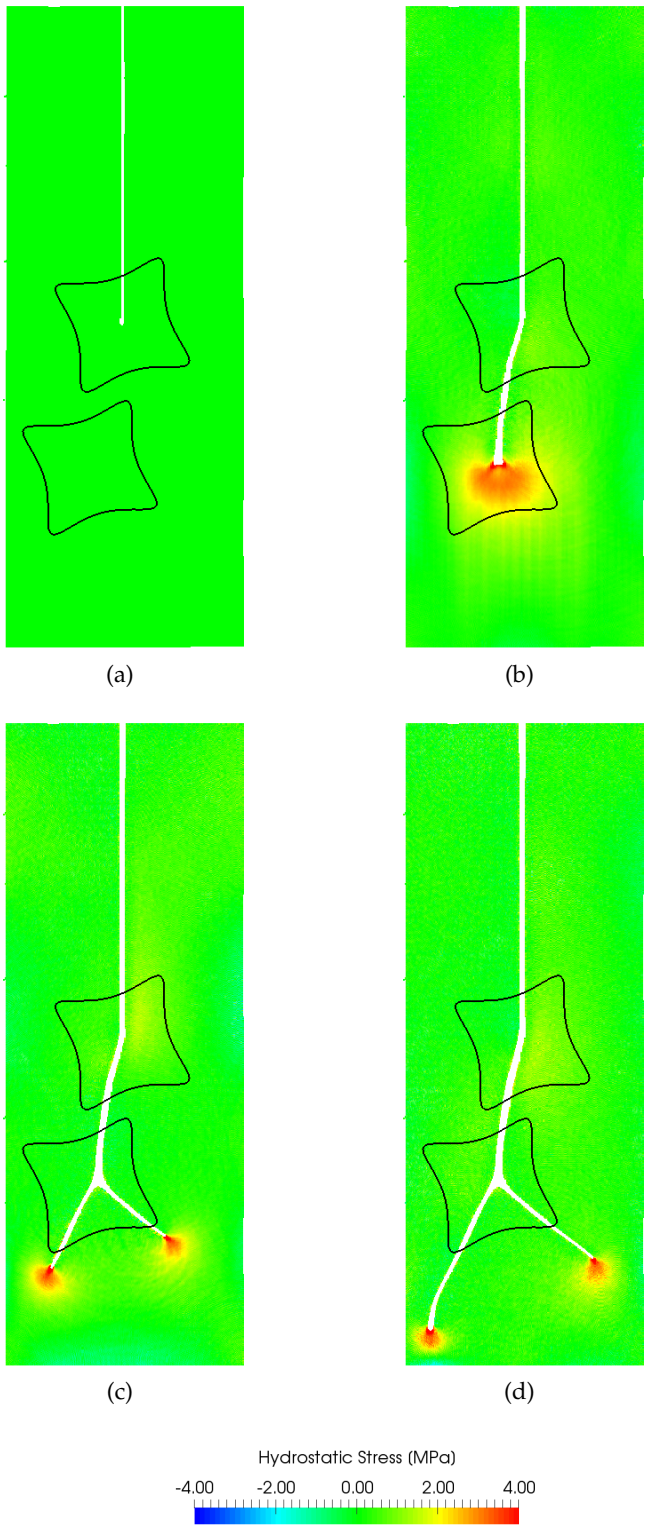

Figure 6.10: Plate under impact loading: Hydrostatic stress for time steps (a) t=0 μs (b) t=50 μs (c) t=65 μs and (d) t=80 μs. Results for case (ii): 4th order anisotropic cubic phase field model and $\sigma = 1$ N/mm^2. Material points with $c_p < 0.10$ have been removed.

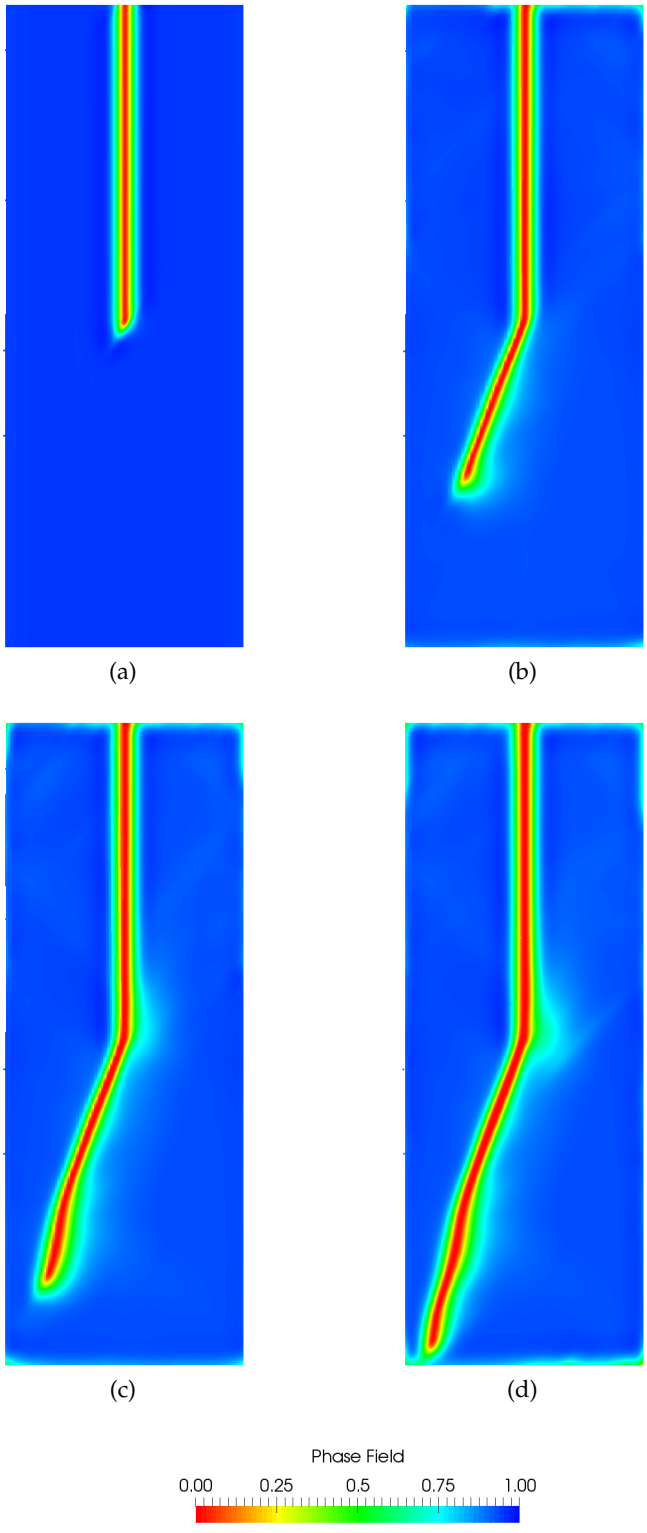

Figure 6.11: Plate under impact loading: Phase field for time steps (a) t=0 μs (b) t=50 μs (c) t=65 μs and (d) t=80 μs. Results for case (iii): 4th order anisotropic orthotropic phase field model and $\sigma = 1\,\mathrm{N/mm^2}$.

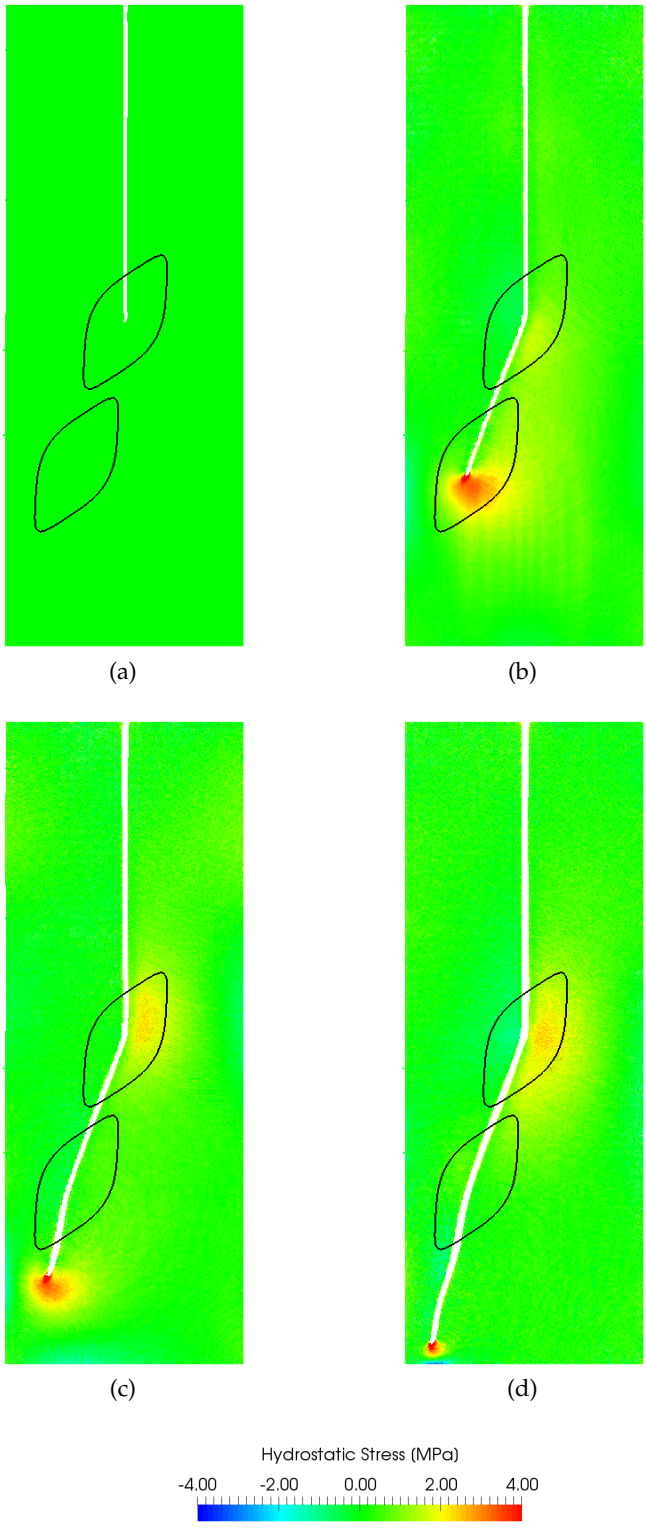

Figure 6.12: Plate under impact loading: Hydrostatic stress for time steps (a) t=0 μs (b) t=50 μs (c) t=65 μs and (d) t=80 μs. Results for case (iii): 4th order anisotropic orthotropic phase field model and $\sigma = 1$ N/mm^2. Material points with $c_p < 0.10$ have been removed.

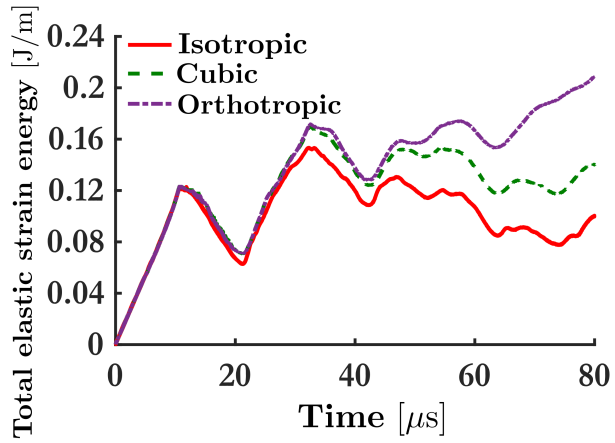

(a)

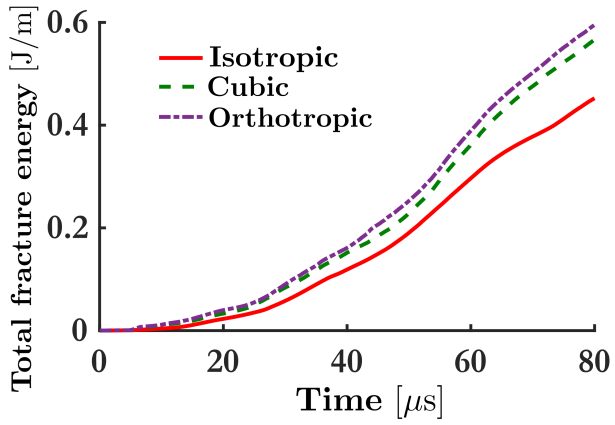

(b)

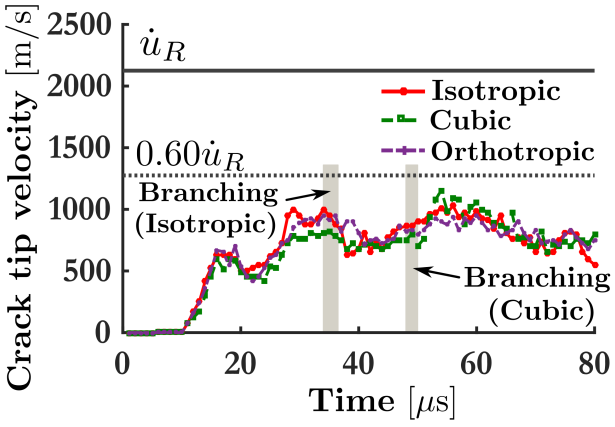

(c)

Figure 6.13: Plate under impact loading: (a) Total elastic strain energies, (b) Total fracture energies and (c) Crack tip velocities over time for PF-MPM 2nd order isotropic model (case (i)), PF-MPM 4th order cubic model (case (ii)) and PF-MPM 4th order orthotropic model (case (iii)). The traction is considered to be $\sigma = 1\,\mathrm{N/mm^2}$.

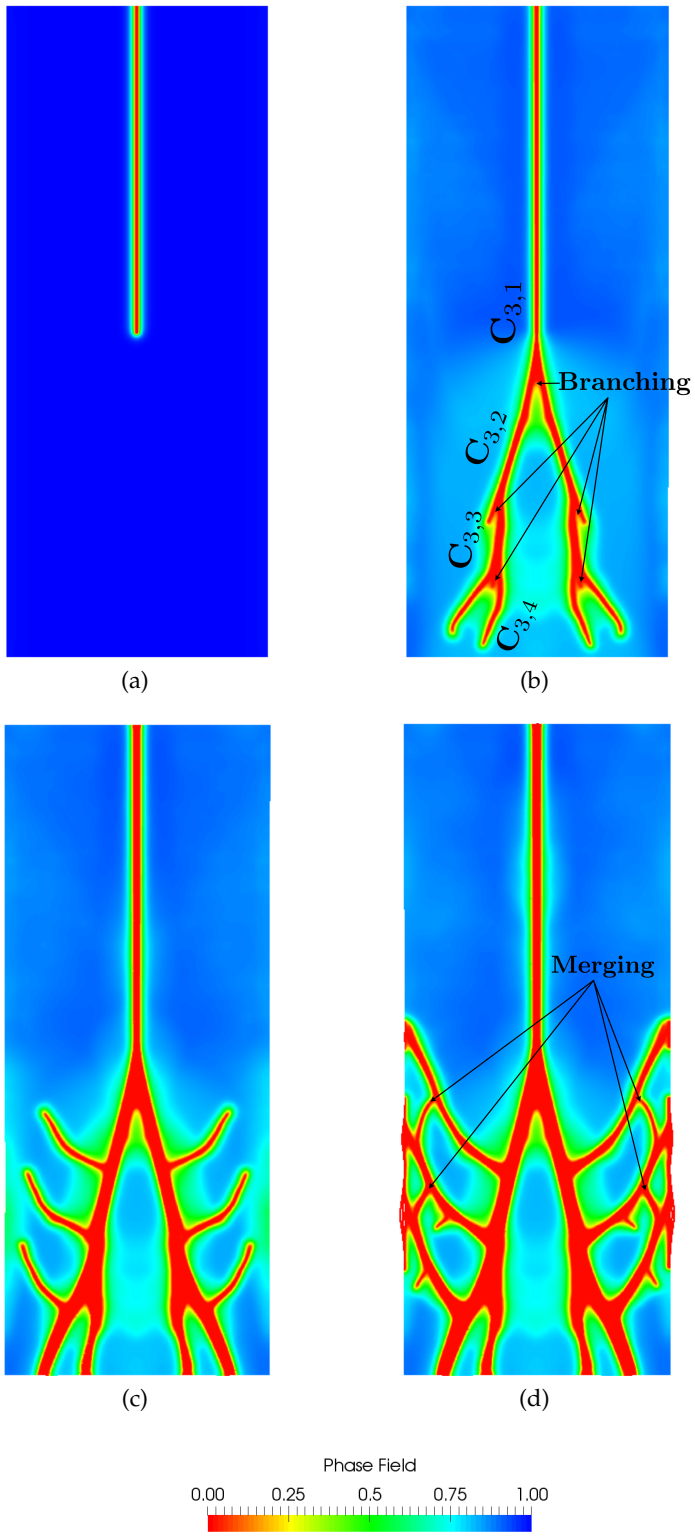

Figure 6.14: Plate under impact loading: Phase field for time steps (a) t=0 μs (b) t=50 μs (c) t=110 μs and (d) t=130 μs. Results for 2nd order isotropic phase field model and $\sigma = 2.3\ \mathrm{N/mm^2}$.

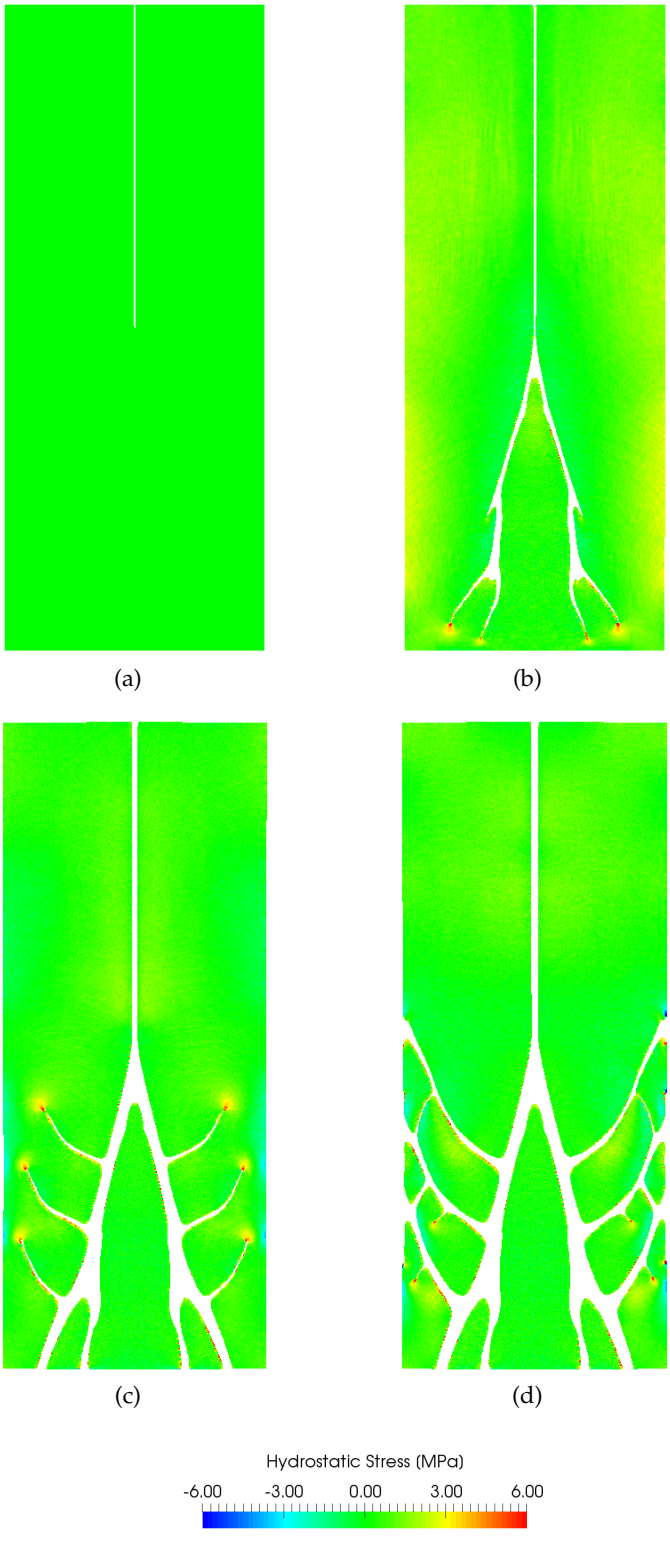

Figure 6.15: Plate under impact loading: Hydrostatic stress for time steps (a) t=0 μs (b) t=50 μs (c) t=110 μs and (d) t=130 μs. Results for 2nd order isotropic phase field model and $\sigma = 2.3$ N/mm^2. Material points with $c_p < 0.10$ have been removed.

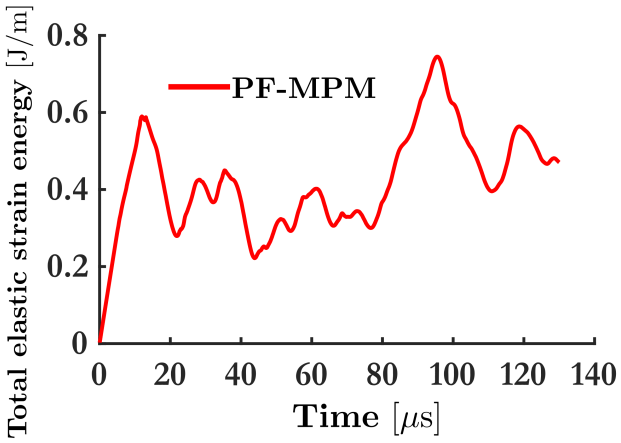

(a)

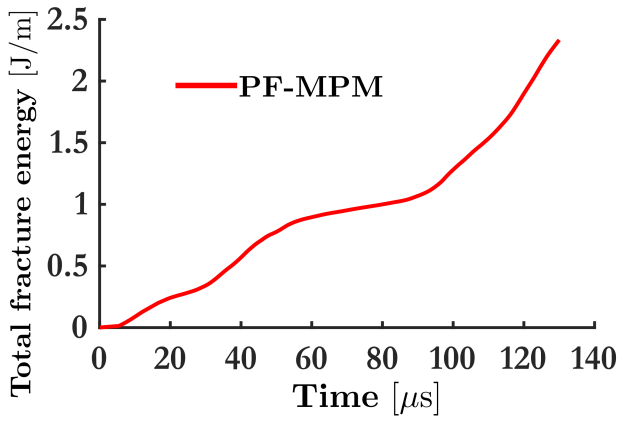

(b)

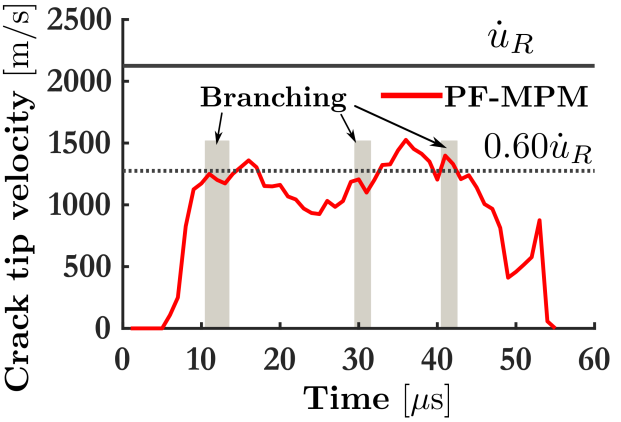

(c)

Figure 6.16: Plate under impact loading: (a) Total elastic strain energy, (b) Total fracture energy and (c) Crack tip velocity over time for PF-MPM 2nd order isotropic model. The traction is considered to be $\sigma = 2.3\,\mathrm{N/mm^2}$.

The total fracture energy time-history for both cases is shown in Fig. 6.17(b). The evolution of the phase field and the hydrostatic stress for points ((1)-(6)) labelled in Fig. 6.17(b) is shown in Figs. 6.20 and 6.21 for case (i) and in Figs. 6.22 and 6.23 for case (ii), respectively.

6.4.3.1 Case (i): $\dot{\mathbf{u}}_{(0)} = 0.01$ mm/μs

In case (i), a crack initiates at the contact surface of the two rings due to their initial impact (see Fig. 6.20(b)) followed by a second crack that initiates and fully propagates on the opposite side of each ring (see Fig. 6.20(c) and Fig. 6.20(d), respectively). Material degradation also occurs on the top and bottom surfaces of each ring. Crack opening gradually increases (see Fig. 6.20(e)) and eventually both rings are fully separated in two fragments (see Fig. 6.20(f)). As also shown in Fig. 6.20(b) the fracture process has been fully developed by point (4), hence the fracture energy remains constant along the path (4)-(6).

6.4.3.2 Case (ii): $\dot{\mathbf{u}}_{(0)} = 0.02$ mm/μs

Similar to case (i), in case (ii) a crack initiates at the contact surface of the two rings due to their initial impact (see Fig. 6.22(b)). Next, and opposite to case (i), two additional cracks simultaneously propagate of the top right (left) and bottom right (left) of each ring (see Fig. 6.22(c)). This is due to the increased impact velocity compared to case (i) where the corresponding points underwent material degradation only. Two more cracks are observed on the top left (right) and bottom left (right) at each ring (see Fig. 6.22(d)). The complete crack paths are presented in Fig. 6.22(e). After that point, the fracture energy remains constant; existing cracks do not propagate and new cracks are not initiated.

The final deformed configuration of the problem is shown in Fig. 6.22(f) where each ring is split into five fragments. The PF-MPM method naturally resolves

the large displacement motion of the fragments, accounting also for the non-stationarity of the contact surfaces (see, also, Figs. 6.23d, 6.22(e) and 6.22(f)). Using a phase field driven fracture approximation allows both, the crack paths and the contact surfaces to not be tracked algorithmically during the simulation process. Furthermore, this is accomplished with no mesh distortion induced errors, contrary to a FEM based approach.

6.4.3.3 Influence of time step Δt and staggered iterations N_{staggs}

A parametric study is conducted to investigate the sensitivity of the solution procedure on the time step Δt and the number of staggered iterations N_{staggs}. For this purpose, the fracture energy is chosen as a global index of the solution. Two time-steps, namely $\Delta t = 0.00625$ μs and $\Delta t = 0.003125$ μs are considered and both cases (i) and (ii) are examined. The resulting time-histories of the fracture energy are shown in Fig. 6.18.

In Fig. 6.18, it is obvious that the initial time step $\Delta t = 0.0125$ μs yields good convergence on the results and further deduction of the time step has minor influence. Similarly, the influence of staggered iterations on the fracture energy is presented in Figs. 6.19(a) and 6.19(b) for case (i) and (ii), respectively. The staggered iterations are increased from the initial $N_{staggs} = 1$ to $N_{staggs} = 2$ and then again to $N_{staggs} = 4$ with no influence on the results.

6.4.4 Disc-Beam impact fracture problem

In this case, a disc to beam impact fracture problem is examined. The aim of this example is to examine the influence of the anisotropy of the surface energy

Material Parameters							
Elastic Material Properties				Fracture Material Properties			
	A	**B**			**A**	**B**	
E	190000	190000	[N/mm^2]	γ_{ijkl}	0.00	0.00	[–]
ν	0.30	0.30	[–]	l_0	1.00	1.00	[mm]
ρ	8000	8000	[kg/m^3]	k_f	0.00	0.00	[–]
				$\mathcal{G}_c(\theta) = \bar{\mathcal{G}}_c$	6.00	6.00	[N/mm]
Material Point Method Model							
Number of Control Points				107724			
Number of Cells				380x280=106400			
Cell spacing				0.50			[mm]
$q_\xi = q_\eta$				2nd			
Ξ				$\{0, 0, 0, 0.00263, 0.0052, ..., 0.9947, 0.9973, 1, 1, 1\}$			
H				$\{0, 0, 0, 0.00357, 0.0071, ..., 0.9928, 0.9964, 1, 1, 1\}$			
Number of Material Points				325620			
Discrete Fields							
Number of Discrete Fields				2			
μ_f				0.65			
Solution Algorithm Parameters							
Time Integrator				Explicit			
Δt				0.0125			[μs]
N_{steps}				50000			
N_{staggs}				1			

Table 6.3: Collision of two rings: Simulation parameters.

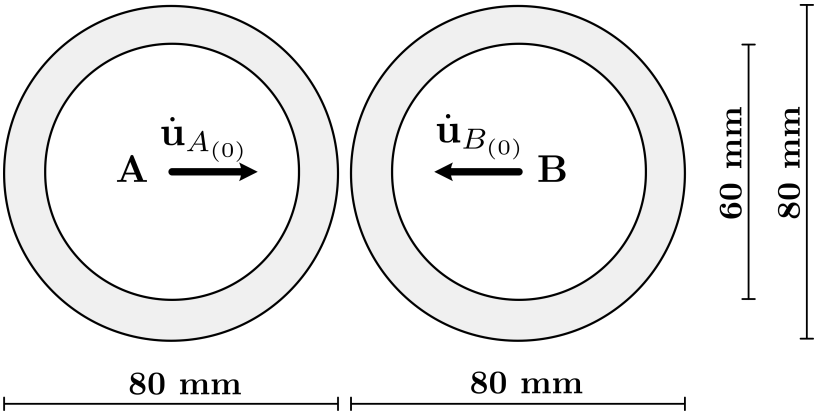

(a)

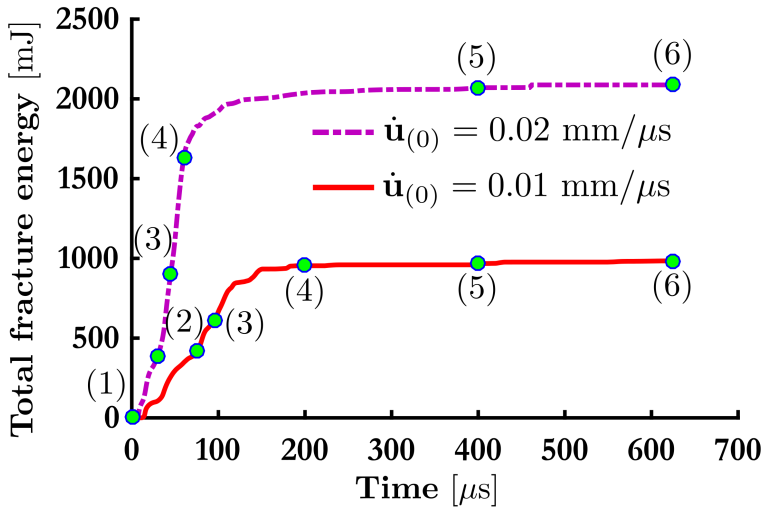

(b)

Figure 6.17: Collision of two rings: (a) Geometry and boundary conditions (b) Total fracture energy over time for case (i) $\dot{\mathbf{u}}_{(0)} = 0.01$ mm/μs and case (ii) $\dot{\mathbf{u}}_{(0)} = 0.02$ mm/μs.

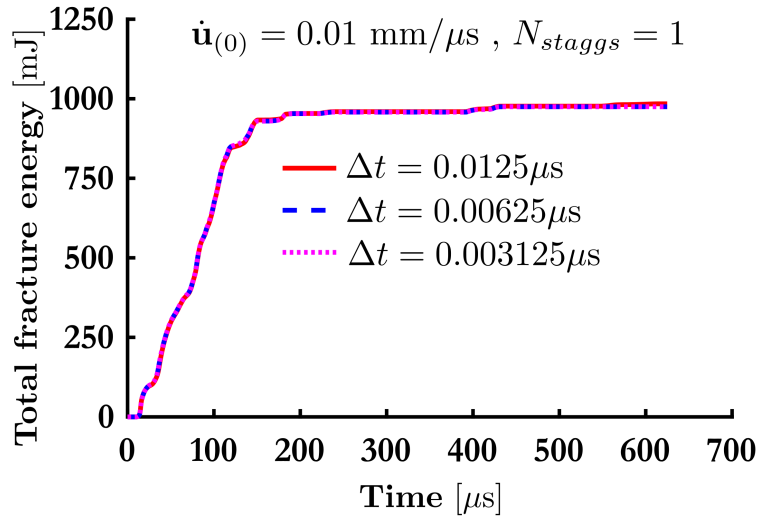

(a)

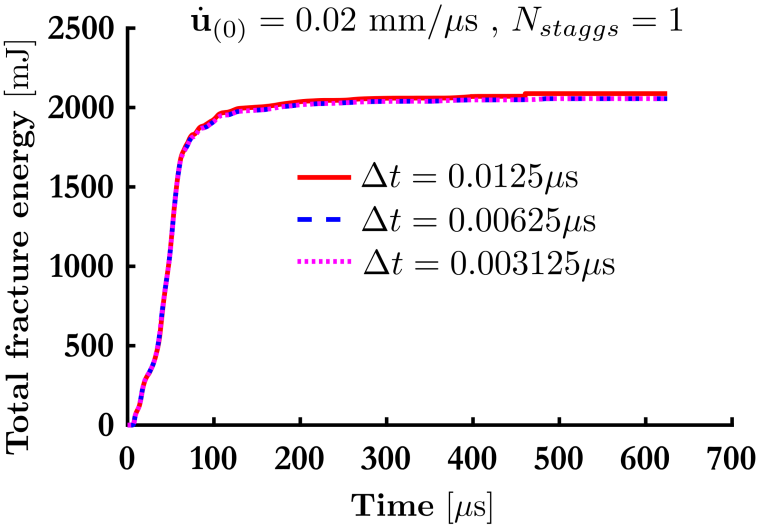

(b)

Figure 6.18: Collision of two rings: Influence of time step (Δt) on total fracture energy over time for (a) case (i) $\dot{\mathbf{u}}_{(0)} = 0.01$ mm/μs and (b) case (ii) $\dot{\mathbf{u}}_{(0)} = 0.02$ mm/μs.

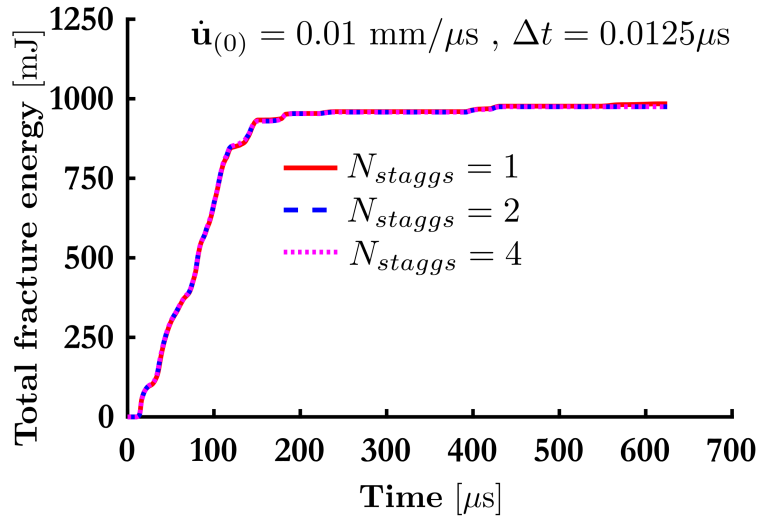

(a)

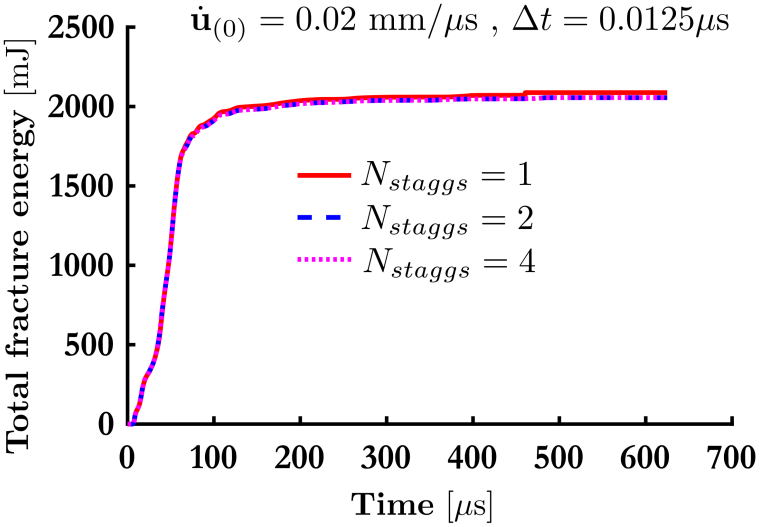

(b)

Figure 6.19: Collision of two rings: Influence of staggered iteration (N_{staggs}) on total fracture energy over time for (a) case (i) $\dot{\mathbf{u}}_{(0)} = 0.01$ mm/μs and (b) case (ii) $\dot{\mathbf{u}}_{(0)} = 0.02$ mm/μs.

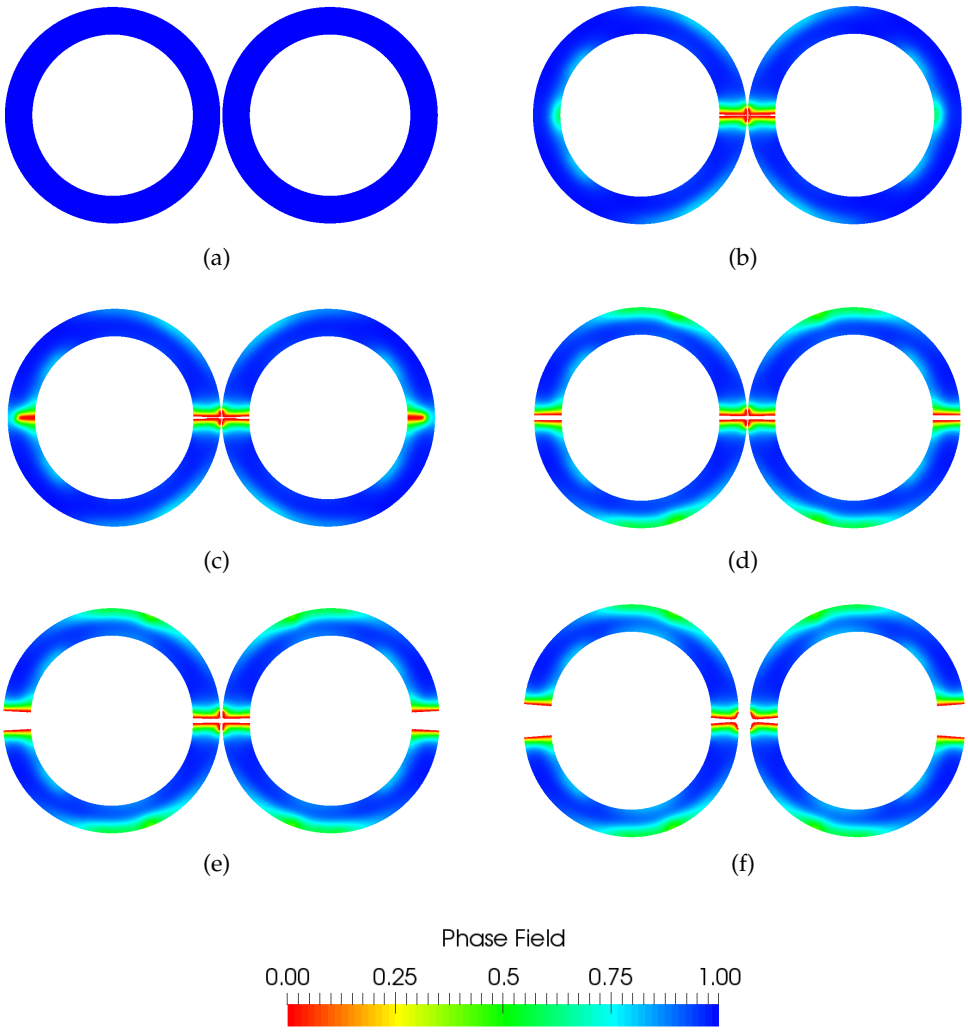

Figure 6.20: Collision of two rings - Case (i): Phase field for time steps (a) t=0 μs (b) t=75 μs (c) t=95 μs (d) t=200 μs (e) t=400 μs and (f) t=625 μs.

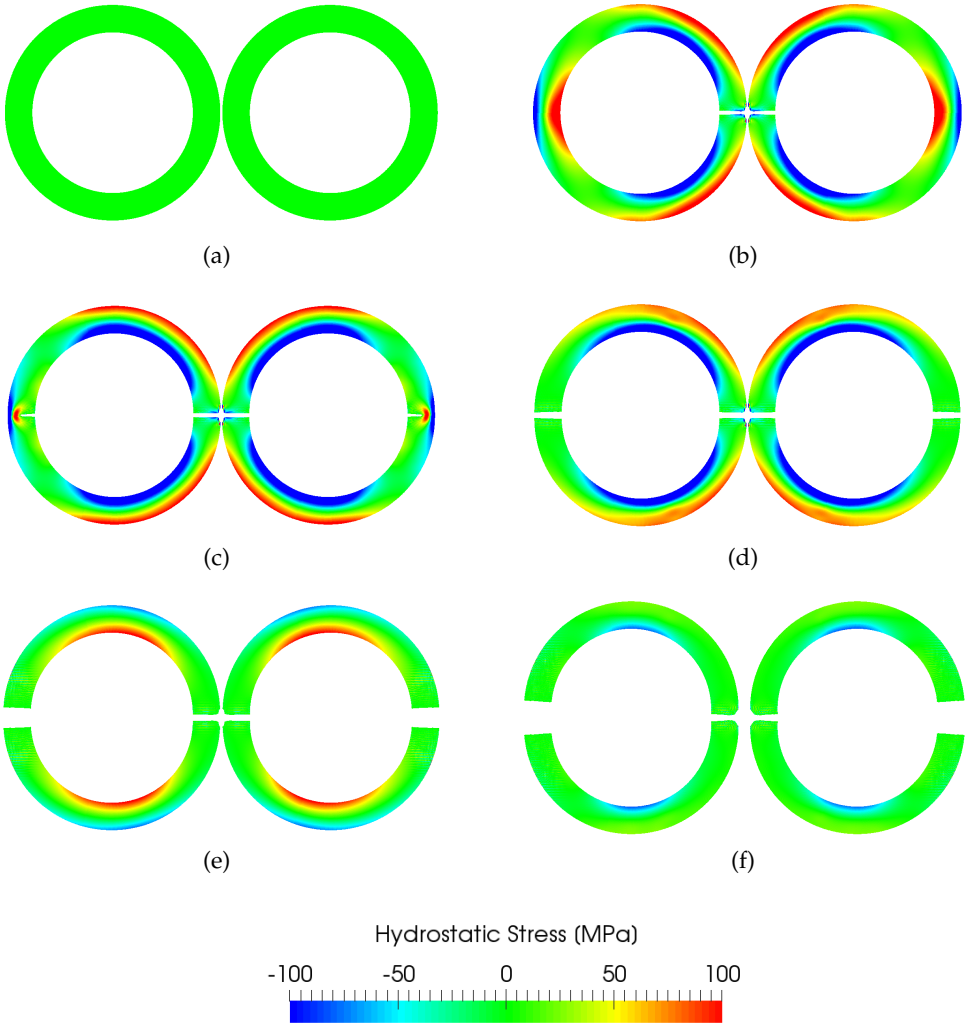

Figure 6.21: Collision of two rings - Case(i): Hydrostatic stresses for time steps (a) t=0 μs (b) t=75 μs (c) t=95 μs (d) t=200 μs (e) t=400 μs and (f) t=625 μs. Material points with $c_p < 0.05$ have been removed.

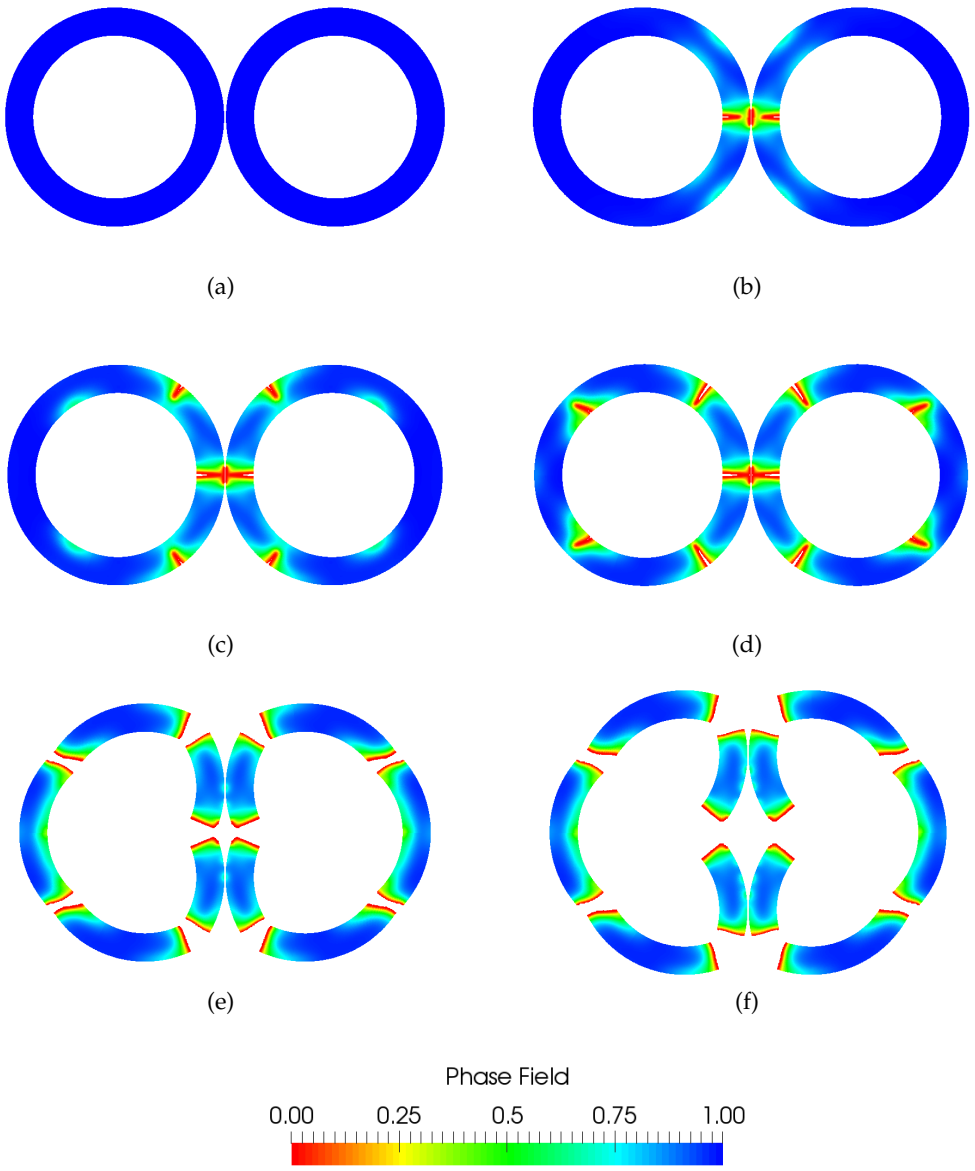

Figure 6.22: Collision of two rings - Case (ii): Phase field for time steps (a) t=0 μs (b) t=30 μs (c) t=45 μs (d) t=60 μs (e) t=400 μs and (f) t=625 μs.

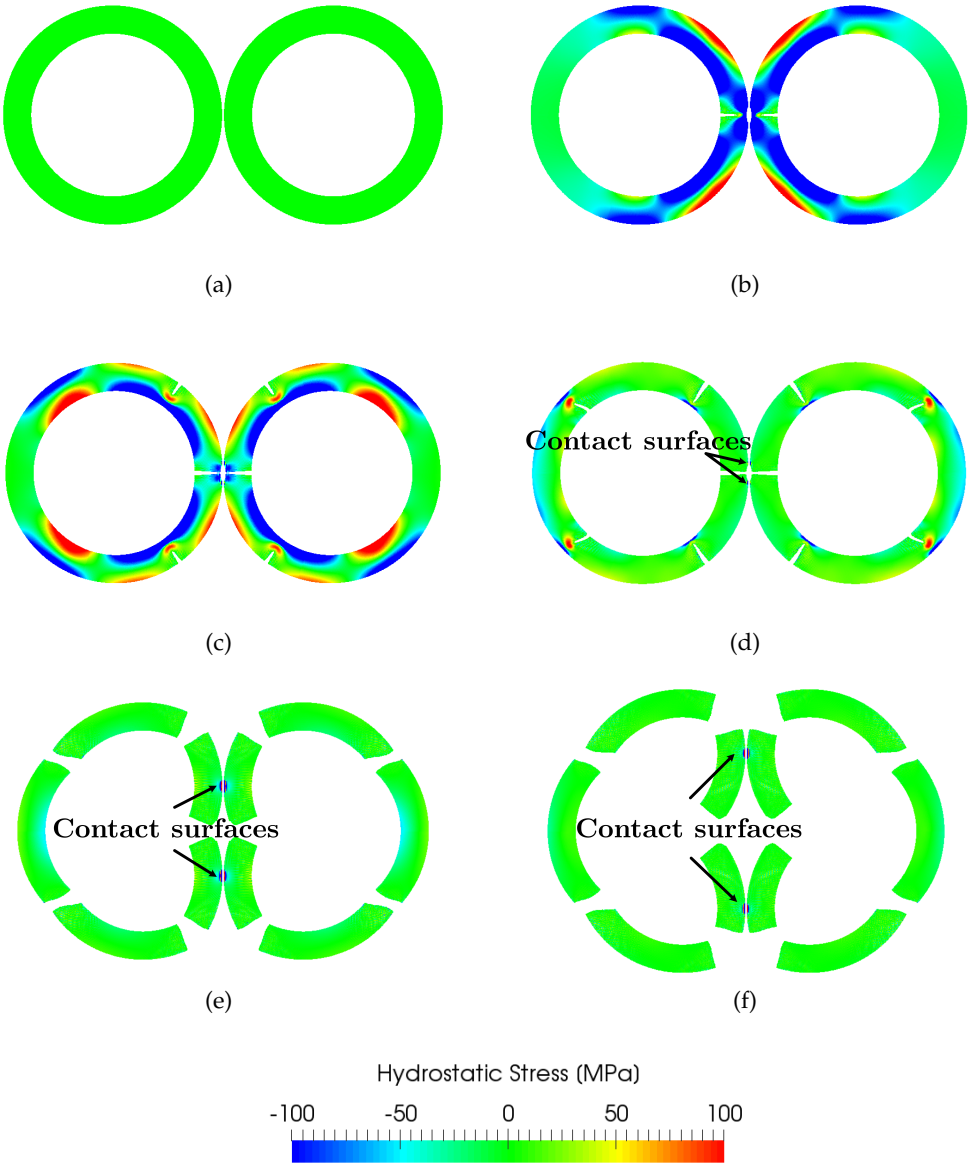

Figure 6.23: Collision of two rings - Case (ii): Hydrostatic stresses for time steps (a) t=0 μs (b) t=30 μs (c) t=45 μs (d) t=60 μs (e) t=400 μs and (f) t=625 μs. Material points with $c_p < 0.05$ have been removed.

density on impact fracture problems using the PF-MPM. Verification of the PF-MPM with analytical solutions is also made. Finally, a parametric study is presented where the influence of the material point and phase field parameters is examined on the response of the beam under impact.

The geometry and boundary conditions of the problem are presented in Fig. 6.24. To examine the dependence of the resulting crack patterns and overall response of the beam on the level of assumed material anisotropy, three cases are examined, namely case (i), case (ii) and case (iii) with different surface energy densities. The material orientation is considered to be $\phi = +45^o$ with respect to x axis (clockwise) for all cases.

The cell spacing is $h = 0.125$ mm and plane stress conditions are assumed with thickness 2 mm. Two discrete fields are considered in this example, namely A for the disc and B for the beam with the corresponding friction coefficient being $\mu_f = 0.65$. The total number of material points is 536796. An initial velocity is applied to all material points in the disc $\dot{\mathbf{u}}_{Ap_{(0)}} = 0.02$ mm/μs while the beam is at rest at this stage. The initial distance between the disc and the beam is considered to be $h = 0.125$ mm. The elastic material parameters are chosen to be $E = 190000$ N/mm^2, $\nu = 0.30$ and $\rho = 8000$ kg/m^3 for both bodies. The solution procedure is implemented with a time step $\Delta t = 0.0125$ μs. The critical time step is $\Delta \tilde{t}_{cr} = 0.018$ μs.

In case (i), the second order isotropic phase field model (i.e. $\gamma_{ijkl} = 0$) is chosen with surface energy density $\mathcal{G}_c(\theta) = \bar{\mathcal{G}}_c = \mathcal{G}_{c_{max}} = \mathcal{G}_{c_{min}} = 10.6066$ N/mm for the beam. In case (ii) , the second order isotropic phase field model is chosen again, but with a reduced surface energy density $\mathcal{G}_c(\theta) = \bar{\mathcal{G}}_c = \mathcal{G}_{c_{max}} = \mathcal{G}_{c_{min}} = 9.75$ N/mm for the beam. Finally, in case (iii) the fourth order orthotropic model is utilized with anisotropic parameters $\bar{\mathcal{G}}_c = 7.50$ N/mm, $\gamma_{1111} = 80.00$, $\gamma_{2222} = 1.00$, $\gamma_{1122} = 0.00$ and $\gamma_{1212} = 74.00$. These parameters result in maximum and minimum surface energy densities $\mathcal{G}_{c_{max}} = 23.6892$ N/mm and $\mathcal{G}_{c_{min}} = 10.6066$ N/mm, respectively for the beam. The surface energy density of the

disc is taken us sufficiently large (i.e. $\mathcal{G}_{c_A}(\theta) = 100\mathcal{G}_{c_B}(\theta)$) so that the disc remains undamaged in all cases. The length scale parameter is $l_0 = 0.25$ mm and $k_f = 0.00$ in all cases. In all cases reported in this Section, the projectile does not penetrate the beam, rather it bounces back and the beam undergoes free vibrations. All the simulation parameters are presented in Table 6.4.

6.4.4.1 Case (i): Isotropy - $\mathcal{G}_c(\theta) = 10.6066$ N/mm

The time history of the total fracture energy is shown in Fig. 6.25(a). In Fig. 6.25(a), the path points (1-7) are labelled to facilitate discussion on the material response. Phase field and hydrostatic stress snapshots corresponding to points (1-6) are shown in Figs. 6.26 and 6.27, respectively.

The disc initially comes into contact with the beam and fracture initiates at the contact surface (see. Fig. 6.26(b) and point (2) in Fig. 6.25(a)). Next, the right edge of the beam gradually degrades (see. 6.26(c) and point (3) in Fig. 6.25(a)) just before a crack initiates at the middle right-edge point. However, as the beam vibrates, the degradation continues at the left edge of the beam (see Fig. 6.26(d) and point (4) in Fig. 6.25(a)) a median crack develops and propagates just below the crack nucleation region (see Fig. 6.26(e) and point (5) in Fig. 6.25(a)). The complete crack path is shown in Fig. 6.26(f).

The results of Fig. 6.25(a) can be further examined in view of the total fracture energy evolution. The evolution of the total fracture energy from point (1) to (2) corresponds to damage initiating between the disc and the beam at their contact surface. Degradation at the right edge of the beam results in a further increase of the fracture energy corresponding to the path (2-3). Finally, the crack rapidly propagates from point (4) to (6). Hence, the total fracture energy corresponding to crack propagation is

$$\overset{(6)}{\underset{(4)}{\Psi_f}} = 311.82 - 94.29 = 217.53 \text{ mJ}.$$

This is in very good agreement with the analytical prediction (Sun and Jin, 2012) as $A_f \cdot \mathcal{G}_c(\theta) = 10 \cdot 2 \cdot 10.6066 = 212.13$ mJ, where A_f is the fracture surface. The slight increase of the total fracture energy from point (6) to (7) corresponds to the marginal degradation of the beam material during the free vibration regime of its response.

6.4.4.2 Case (ii): Isotropy - $\mathcal{G}_c(\theta) = 9.75$ N/mm

Even though the variation in $\mathcal{G}_c$ is small compared to case (i), it results in a significantly different material response. The total fracture energy time-history for case (ii) is shown in Fig. 6.25(b). The evolution of the phase field and the hydrostatic stress for points ((1)-(6)) labelled in Fig. 6.25(b) is shown in Figs. 6.28 and 6.29, respectively.

Similar to case (i), the disc initially comes into contact with the beam and causes damage at their contact surface. As a result, material degradation is observed at the right edge of the beam (see. Fig. 6.28(b) and point (2) in Fig. 6.25(b)) as in case (i). Next, a flexural crack initiates at the middle right-edge point of the beam due to maximum principal tensile stresses developing at the tensile fibre of the beam.

As the beam oscillates the maximum tension region alternates between the two edges and the crack arrests (see Fig. 6.28(c) and point (3) in Fig. 6.25(b)). A second crack then initiates at the left edge (see Fig. 6.28(d) and point (4) in Fig. 6.25b) and propagates (see Fig. 6.28e and point (5) in Fig. 6.25(b)) until the two cracks finally merge as shown in Fig. 6.28(f).

As in case (i), the evolution of the fracture energy (shown shown in Fig. 6.25(b)) is consistent with the observed response. The first crack (right crack) initiates at point (2) and stops at point (3). The second crack (left crack) propagates from

point (4) to (6). Therefore, the total fracture energy is

$$\Psi_f = {}^{(3)}_{(2)}\Psi_f + {}^{(6)}_{(4)}\Psi_f = (196.55 - 87.37) + (306.81 - 226.39)\ \text{mJ}.$$

This is again in very good agreement with the analytical prediction (Sun and Jin, 2012) as in this case $A_f \cdot \mathcal{G}_c(\theta) = 10 \cdot 2 \cdot 9.75 = 195$ mJ.

6.4.4.3 Case (iii): Orthotropy

Orthotropic anisotropy with a material orientation $\phi = +45^o$ results in two cracks at each beam edge (right and left) that do not coincide with the horizontal axis as in case (ii). The evolution of the phase field and the hydrostatic stress are represented for several time steps in Figs. 6.30 and 6.31, respectively. The characteristic points ((1)-(7)) of that analysis are shown in Fig. 6.25(c).

Similarly to the previous cases, damage initiation is observed at the contact surface (see Fig. 6.30(b) and point (2) in Fig. 6.25(c)). Next, degradation occurs at the left edge of the beam (see Fig. 6.30(c) and point (3) in Fig. 6.25(c)). The first crack (right crack) initiates at middle right-edge point of the beam and propagates along the material's week direction until it arrests in the vicinity of the beam's neutral axis (see Fig. 6.30(d) and point (4) in Fig. 6.25(c)). After impact, further degradation occurs due to the beam's free vibration resulting in degradation to its left edge (see Fig. 6.30(e) and point (5) in Fig. 6.25(c)). Finally, a second crack (left crack) initiates at the middle left-edge of the beam and propagates along the material's weak direction (see Fig. 6.30(f) and point (6) in Fig. 6.25(c)). Similar to the first crack, the second crack arrests in the vicinity of the beam's neutral axis. The final crack paths are shown in Fig. 6.31(f) where the two cracks do not merge as in case (ii).

6.4.4.4 Parametric study of case (i)

Case (i) is further investigated in terms of cell spacing h, time step Δt, cell density CD and staggered iterations N_{staggs}. Three cell spacings are examined, namely, $h = 0.50$ mm, $h = 0.25$ mm and $h = 0.125$ mm in combination with three length scale parameters $l_0 = 1.00$ mm, $l_0 = 0.50$ mm and $l_0 = 0.25$ mm (see Table 6.5). In all numerical simulations presented in Table 6.5, a cell density 3x3 material points per cell is used. Table 6.6 also presents the time step utilized for each analysis.

The fracture energy results are shown in Fig. 6.32 while the phase field and the final crack paths are shown in Fig. 6.35. In Figs. 6.35, all the results correspond to time step $\Delta t = 0.0125$ μs. Figs. 6.32(a), 6.32(b) and 6.32(c) investigate the influence of length scale parameter and time step for cell spacing $h = 0.50$ mm, $h = 0.25$ mm and $h = 0.125$ mm, respectively. The influence of time step size is also demonstrated in Figs. 6.32(a), 6.32(b) and 6.32(c). As it can be seen, the time step $\Delta t = 0.05$ μs, $\Delta t = 0.025$ μs and $\Delta t = 0.0125$ μs yield good accuracy for cell spacings $h = 0.50$ mm, $h = 0.25$ mm and $h = 0.125$ mm, respectively. These time steps are less than $0.80 \cdot \Delta t_{cr}$ (see Table 6.6) and further deduction of the time step size has no influence on the results. However, in the extensive numerical investigation conducted in this example, a time step greater than $0.80 \cdot \Delta t_{cr}$ causes instability problems and inaccurate results. The fracture energy tends to unrealistically increase to infinity after a few time steps and the material points are separated from the body. This numerical instability is treated by reducing the time step of the time integrator (Dokainish and Subbaraj, 1989).

Figs. 6.33(a), 6.33(b) and 6.33(c) investigate the influence of cell spacing for the length scale parameters $l_0 = 1.00$ mm, $l_0 = 0.50$ mm and $l_0 = 0.25$ mm, respectively. Figs. 6.33(a), 6.33(b) and 6.33(c) also verify that the numerical results rapidly converge when the resolution condition $l_0/h \geq 2$ is satisfied. Similarly, Fig. 6.33(c) illustrates that inaccurate results are produced when $l_0/h = 0.50$

(see Chapter 4 for more details in quasi-static examples). Furthermore, in Fig. 6.33(c) and for $h = 0.50$ mm cell spacing, the fracture energy reaches a plateau in a considerably low value than the other cases. This can be justified by the fact that crack initiation is never observed (see also Fig. 6.35(c)) due to insufficient crack regularization.

Fig. 6.33(c) also indicates that the initial selected cell density, i.e. 3x3 material points per cell, is enough and further refinement of the cell density has no influence on the results. Moreover, Fig. 6.34 shows the simulation results with more staggered iterations with no influence on the results again. Hence, the staggered approach adopted in the present PF-MPM scheme is suitable and yields good convergence. The only numerical restriction/instability derives from the time step size that should be less than $0.80 \cdot \Delta t_{cr}$.

In Fig. 6.32(c), the fracture energy results for $l_0 = 1.00$ mm and $l_0 = 0.50$ mm illustrate good agreement. However, the 'pattern' of fracture energy changes when $l_0 = 0.25$ mm. This can be explained by the fact that when the length scale parameter is $l_0 = 1.00$ mm and $l_0 = 0.50$ mm, the crack path initiates at the mid-right edge of the beam and propagates until its mid-left edge. However, when $l_0 = 0.25$ mm the mid-right edge is gradually degradated just before a crack initiates at that point. Then, due to the vibrations of the beam the crack finally initiates at its mid-left edge.

This demonstrates the dramatic influence of the length scale parameter on the results (see also Miehe et al. (2010b) for the influence of length scale parameter on crack paths for quasi-static FEM problems). An extremely small length-scale parameter l_0 in combination with a fine mesh is needed to recover the sharp limit of the crack. Moreover, the influence of length scale parameter is also demonstrated e.g. in Figs. 6.35(g), 6.35(h) and 6.35(i). The diffusion of damage around the crack is reduced when the l_0 is also reduced.

6.4.4.5 Discussion on observed fracture patterns

In this Section, the ability of the proposed method to simulate the incidence of Hertzian fracture as a function of the projectile velocity is demonstrated. As the developed method is only limited to brittle fracture, an accurate resolution of the process zone ahead of the crack tip is not feasible. Hence a numerical validation against experimental results is not attempted and is beyond the scope of this work.

Fracture patterns emerging from static indentation of a practically rigid disc against a deformable solid as well as from low and high speed impact tests have been the focus of extensive experimental investigations, see, e.g., (Ball and McKenzie, 1994; Jelagin and Larsson, 2008). The failure modes observed vary considerably with the velocity of the projectile, the flexibility of the impacted beam, and the interface properties Jelagin and Larsson (2008).

We focus here in case (i) with isotropic fracture energy equal to $\mathcal{G}_c(\theta) = 10.6066$ N/mm. The fracture patterns shown in Fig. 6.26 correspond to a median type of crack, with the crack at the left end nucleating due to impact and then propagating towards the right edge driven by the principal tensile stresses at the mid-span. To investigate the effect of the projectile velocity on the induced fracture pattern, a total of 33 analysis cases was performed keeping the geometry, the elastic and the fracture properties of the beam similar to those reported in Section 6.4.4.1. In each case the projectile velocity is varied from 0.02 mm/μs to 0.18 mm/μs at a step size of 0.005 mm/μs. All analysis parameters, the background cell size and the cell density are similar to Section 6.4.4.1.

We define the Hertzian cone index β with a value $\beta = 0$ corresponding to a cone not developing and $\beta = 1$ when a cone develops. This is plotted versus the projectile velocity in Fig. 6.36; a cone fracture pattern occurs for velocities larger than 0.10 mm/μs. Conversely, for velocities smaller than 0.10 mm/μs the crack pattern is consistent with the flexure failure mode described in Section

6.4.4.1. In Fig. 6.37, phase field snapshots are shown for six particular cases of projectile velocity. All snapshots correspond to time $t = 16\mu$s.

For the case of the lowest impact velocity considered in Fig. 6.37(a), the crack pattern involves a median crack propagating from the left and towards the right edge of the beam. Secondary, flexural cracks appear at the right edge of the beam. Such a response is consistent with experimental observations on brittle materials at low impact loads where a plastic band initiates at the impact zone prior to crack formation, see, e.g., Hagan and Swain (1978). In the framework presented herein, the material degradation prior to fracture assumes this role.

Increasing impact velocities result in a Hertz cone formation at the vicinity of the impact zone. Secondary cracks also propagate from the left edge. Of interest is also the evidently smooth transition from a median to a Hertz cone fracture pattern from Fig. 6.37(c) to Fig. 6.37(d).

6.4.5 Anisotropic plate with centred crack

In the final example, the crack paths derived with the PF-MPM are validated against experiments conducted in a composite material with anisotropic surface energy density Cahill et al. (2014). The case of the anisotropic rectangular plate shown in Fig. 6.38 is examined, made from a unidirectional HTA/ 6376 composite laminate and subjected to an initial velocity field $\dot{u}\left(\mathbf{x}\right)_{(0)} = 0.0002y$ mm/μs. The plate contains a pre-existing crack at its centre with length 25 mm.

In their experimental campaign, Cahill et al. (2014) have shown that cracks grow parallel to the fibre direction hence indicating that the damage originates only through matrix failure. We consider herein the case of fibre orientation at $\phi = +45^o$ as shown in Fig. 6.38. This allows us to use the same Young's modulus and Poisson's ratio along x and y. The elastic material properties considered

Material Parameters								
Elastic Material Properties				Fracture Material Properties				
	A	**B**			**A**	**B**		
E	190000	190000	[N/mm^2]		0.00	0.00	Case (i)	
				γ_{1111}	0.00	0.00	Case (ii)	[–]
ν	0.30	0.30	[–]		80.00	80.00	Case (iii)	
ρ	8000	8000	[kg/m^3]		0.00	0.00	Case (i)	
				γ_{2222}	0.00	0.00	Case (ii)	[–]
					1.00	1.00	Case (iii)	
					0.00	0.00	Case (i)	
				γ_{1122}	0.00	0.00	Case (ii)	[–]
					1.00	1.00	Case (iii)	
					0.00	0.00	Case (i)	
				γ_{1212}	0.00	0.00	Case (ii)	[–]
					74.00	74.00	Case (iii)	
				l_0	0.25	0.25		[mm]
				k_f	0.00	0.00		[–]
					1060.66	10.6066	Case (i)	
				$\bar{\mathcal{G}}_c$	975.00	9.75	Case (ii)	[N/mm]
					750.00	7.50	Case (iii)	
					1060.66	10.6066	Case (i)	
				$\mathcal{G}_{c_{max}}$	975.00	9.75	Case (ii)	[N/mm]
					2368.92	23.6892	Case (iii)	
					1060.66	10.6066	Case (i)	
				$\mathcal{G}_{c_{min}}$	975.00	9.75	Case (ii)	[N/mm]
					1060.66	10.6066	Case (iii)	
				ϕ	+45	+45		[Deg]

Material Point Method Model		
Number of Control Points	242004	
Number of Cells (Patches)	400x600=240000	
Cell (Patch) spacing	0.125	[mm]
$q_\xi = q_\eta$	2nd	
Ξ	$\{0, 0, 0, 0.0025, 0.0050, ..., 0.9950, 0.9975, 1, 1, 1\}$	
H	$\{0, 0, 0, 0.00167, 0.00333, ..., 0.99667, 0.99833, 1, 1, 1\}$	
Initial Cell density	3x3	
Number of Material Points	536796	
Discrete Fields		
Number of Discrete Fields	2	
μ_f	0.65	
Solution Algorithm Parameters		
Time Integrator	Explicit	
Δt	0.0125	[μs]
N_{staggs}	1	

Table 6.4: Disc-Beam impact fracture problem: Simulation parameters.

Cell density $CD = 3$x3			
l_0 [mm]	Cell spacing (h) [mm]		
	0.50	0.25	0.125
1.00			
0.50	$\Delta t = 0.05, 0.025$	$\Delta t = 0.025, 0.0125$	$\Delta t = 0.0125, 0.00625$
0.25			

Table 6.5: Disc-Beam impact fracture problem: Input data for each analysis and its corresponding time step size used.

	Cell spacing (h) [mm]		
	0.50	0.25	0.125
Δt_{cr} [μs]	0.088	0.044	0.022
$0.80 \cdot \Delta t_{cr}$ [μs]	0.070	0.035	0.017

Table 6.6: Disc-Beam impact fracture problem: Critical time step size for each cell spacing $h = 0.50$, $h = 0.25$ and $h = 0.125$.

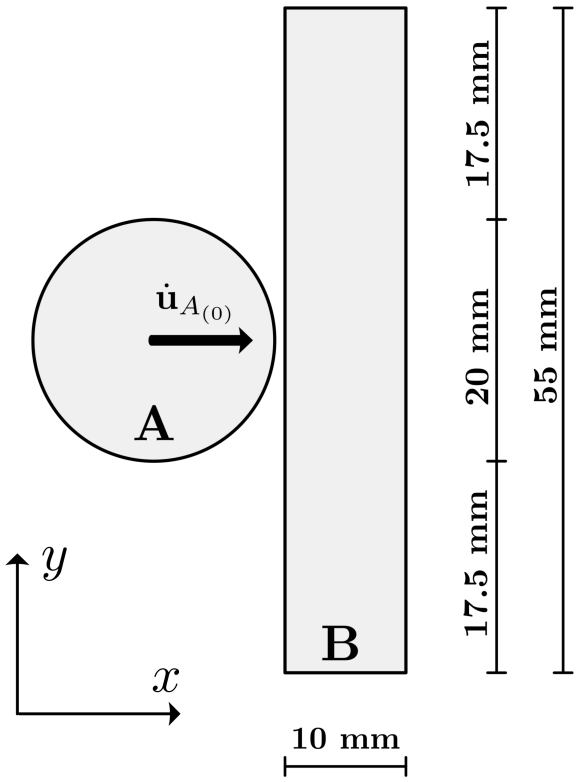

Figure 6.24: Disc-Beam impact fracture problem: Geometry. The sphere and the beam have all their boundaries free.

are $E = 14980$ N/mm^2 and $\nu = 0.36$.The mass density is $\rho = 1586$ kg/m^3. The length scale parameter is considered $l_0 = 1$ mm and the anisotropic parameters are taken to be $\gamma_{1111} = 1.00$, $\gamma_{2222} = 2900$, $\gamma_{1122} = 0.00$ and $\gamma_{1222} = 74.00$ and $\bar{\mathcal{G}}_c = 4.175$ N/mm. These parameters correspond to an orthotropic surface energy with $\mathcal{G}_{c_{min}} = 5.9067$ N/mm along the fibre orientation and $\mathcal{G}_{c_{max}} = 30.9044$ N/mm normal to the fibre.

The cell spacing is $h = 1.00$ mm and plane strain conditions are assumed. The total number of material points is 281250. The solution procedure is implemented with a time step $\Delta t = 0.0125$ μs for a total time of 25 μs. The critical time step is $\Delta \tilde{t}_{cr} = 0.201$ μs. All simulation parameters are summarized in Table 6.7.

The results for the numerical simulations together with the experimental observations are shown in Fig. 6.39. The reciprocal of the surface energy density

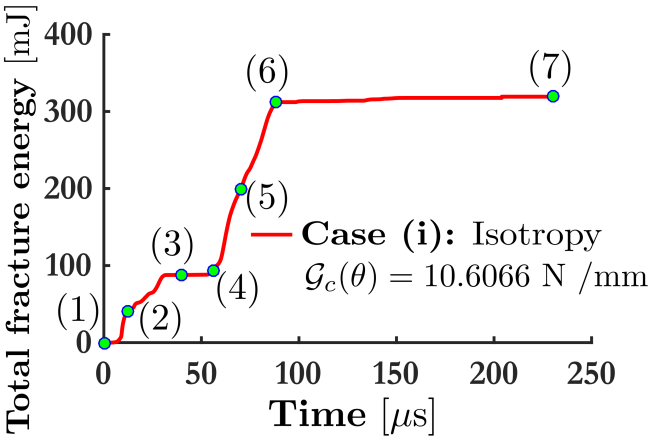

(a)

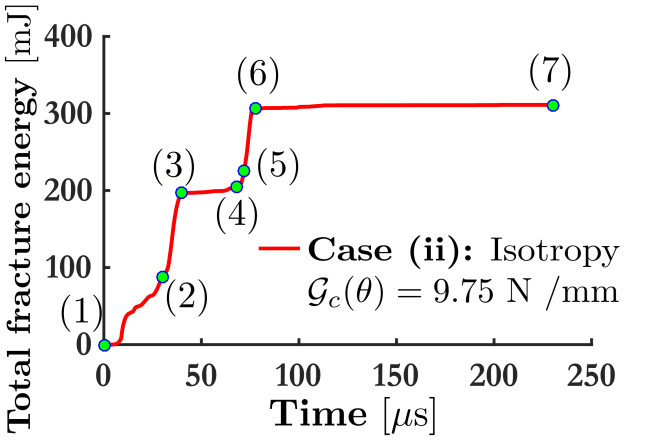

(b)

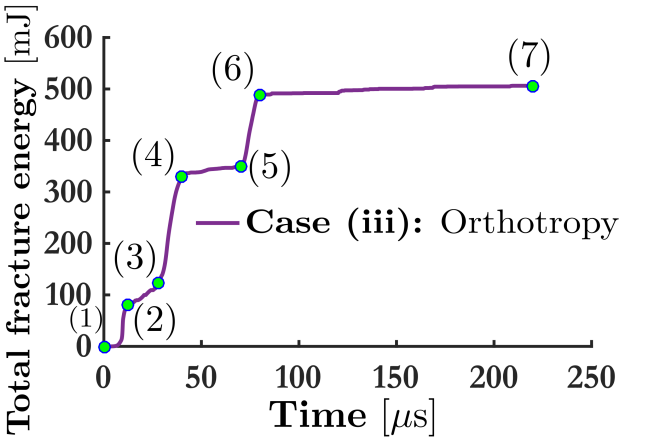

(c)

Figure 6.25: Disc-Beam impact fracture problem: Total fracture energy over time for (a) case (i): PF-MPM 2nd order isotropic model and $\mathcal{G}_c(\theta) = 10.6066$ N/mm (b) case (ii): PF-MPM 2nd order isotropic model and $\mathcal{G}_c(\theta) = 9.75$ N/mm and (c) case (iii): PF-MPM 4th order orthotropic model for the beam.

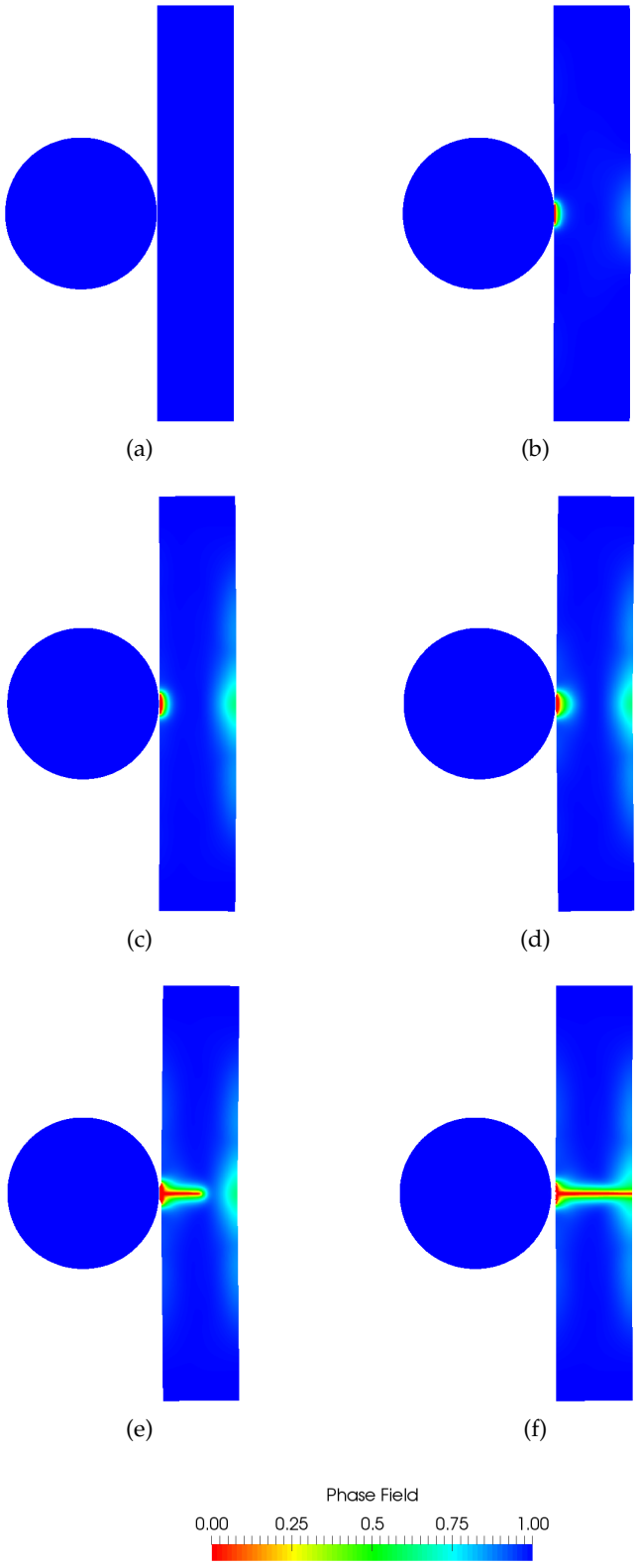

Figure 6.26: Disc-Beam impact fracture problem: Phase field for time steps (a) t=0 μs (b) t=12 μs (c) t=40 μs (d) t=56 μs (e) t=70 μs and (f) t=88 μs. Results for case (i): PF-MPM 2nd order isotropic model and $\mathcal{G}_c\left(\theta\right) = 10.6066$ N/mm for the beam.

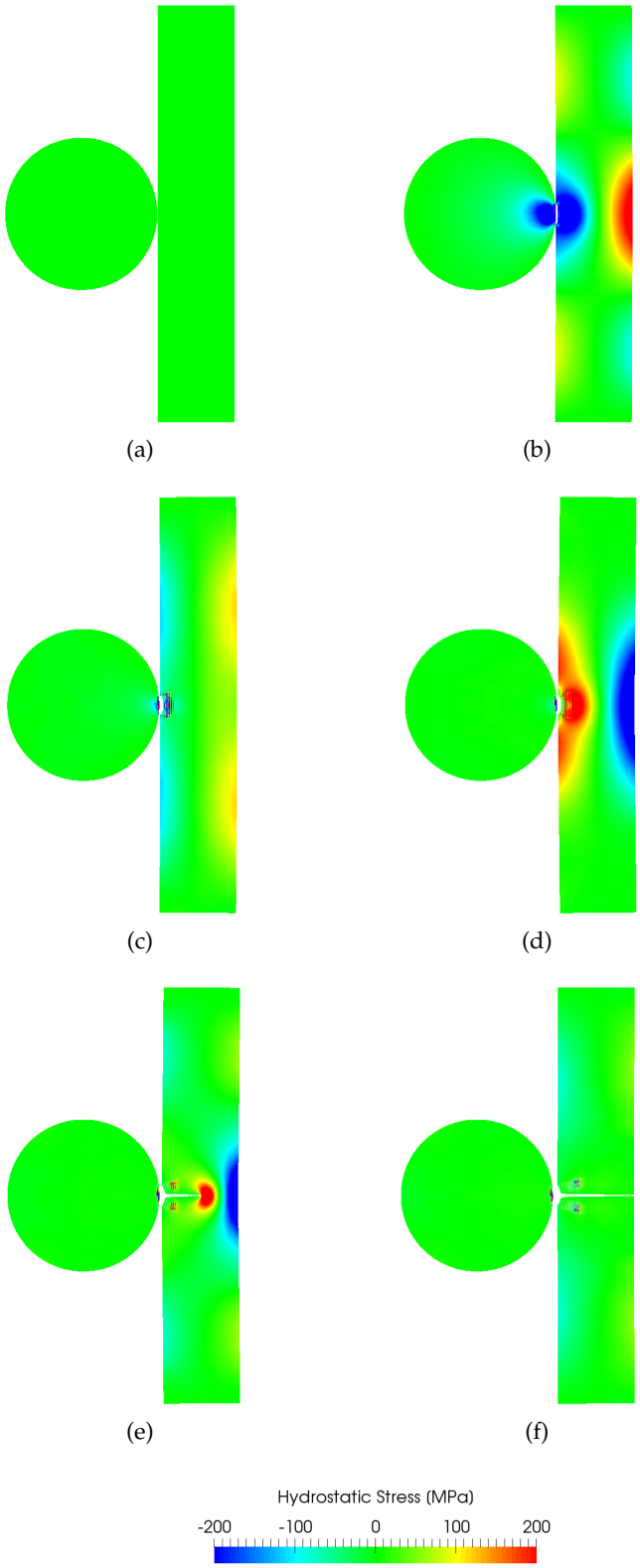

Figure 6.27: Disc-Beam impact fracture problem: Hydrostatic stresses for time steps (a) t=0 μs (b) t=12 μs (c) t=40 μs (d) t=56 μs (e) t=70 μs and (f) t=88 μs. Results for case (i): PF-MPM 2nd order isotropic model and $\mathcal{G}_c(\theta) = 10.6066$ N/mm for the beam. Material points with $c_p < 0.08$ have been removed.

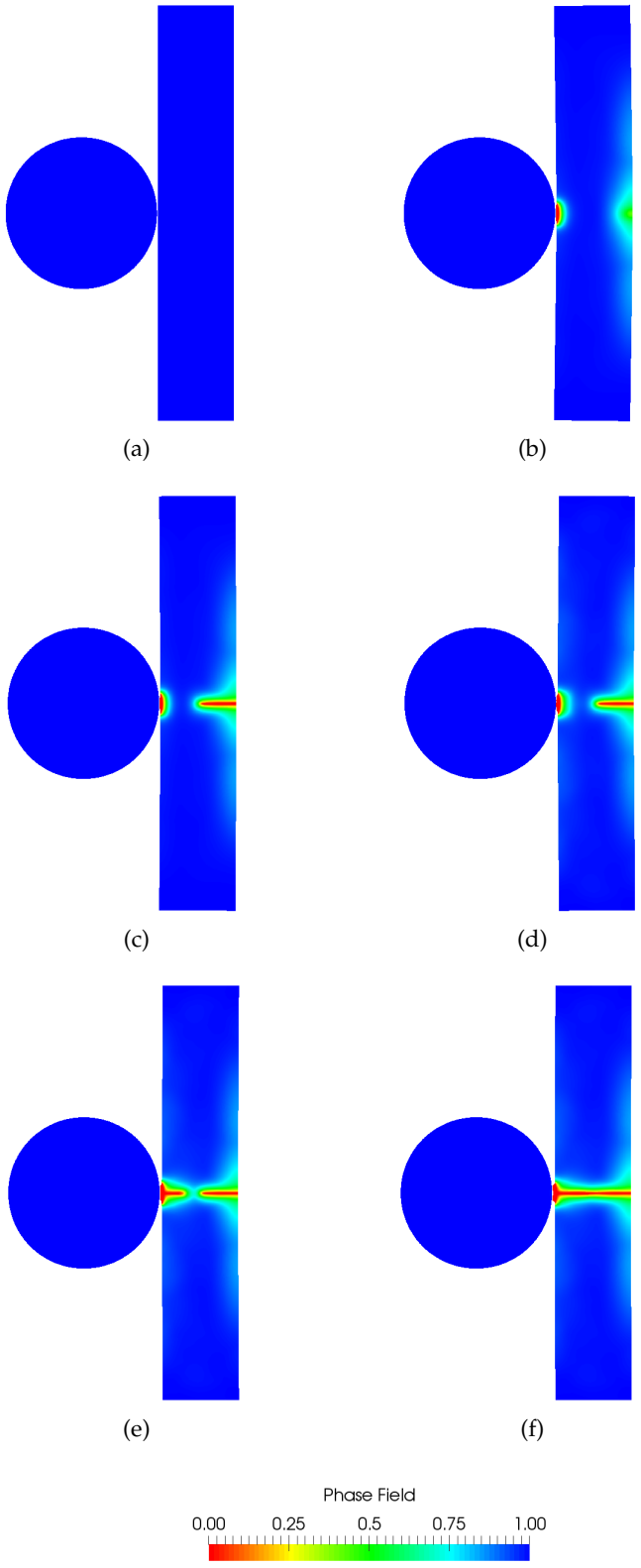

Figure 6.28: Disc-Beam impact fracture problem: Phase field for time steps (a) t=0 μs (b) t=30 μs (c) t=40 μs (d) t=68 μs (e) t=72 μs and (f) t=78 μs. Results for case (ii): PF-MPM 2nd order isotropic model and $\mathcal{G}_c(\theta) = 9.75$ N/mm for the beam.

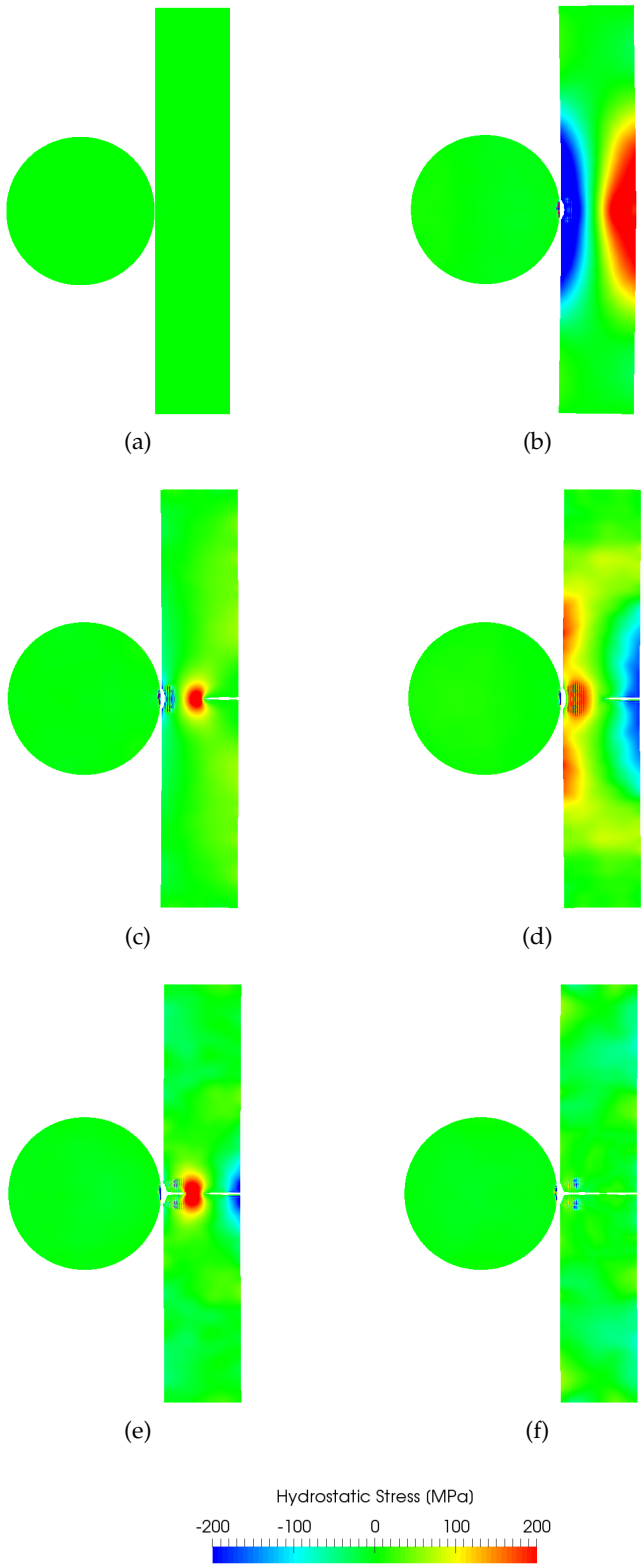

Figure 6.29: Disc-Beam impact fracture problem: Hydrostatic stresses for time steps (a) t=0 μs (b) t=30 μs (c) t=40 μs (d) t=68 μs (e) t=72 μs and (f) t=78 μs. Results for case (ii): PF-MPM 2nd order isotropic model and $\mathcal{G}_c(\theta) = 9.75$ N/mm for the beam. Material points with $c_p < 0.08$ have been removed.

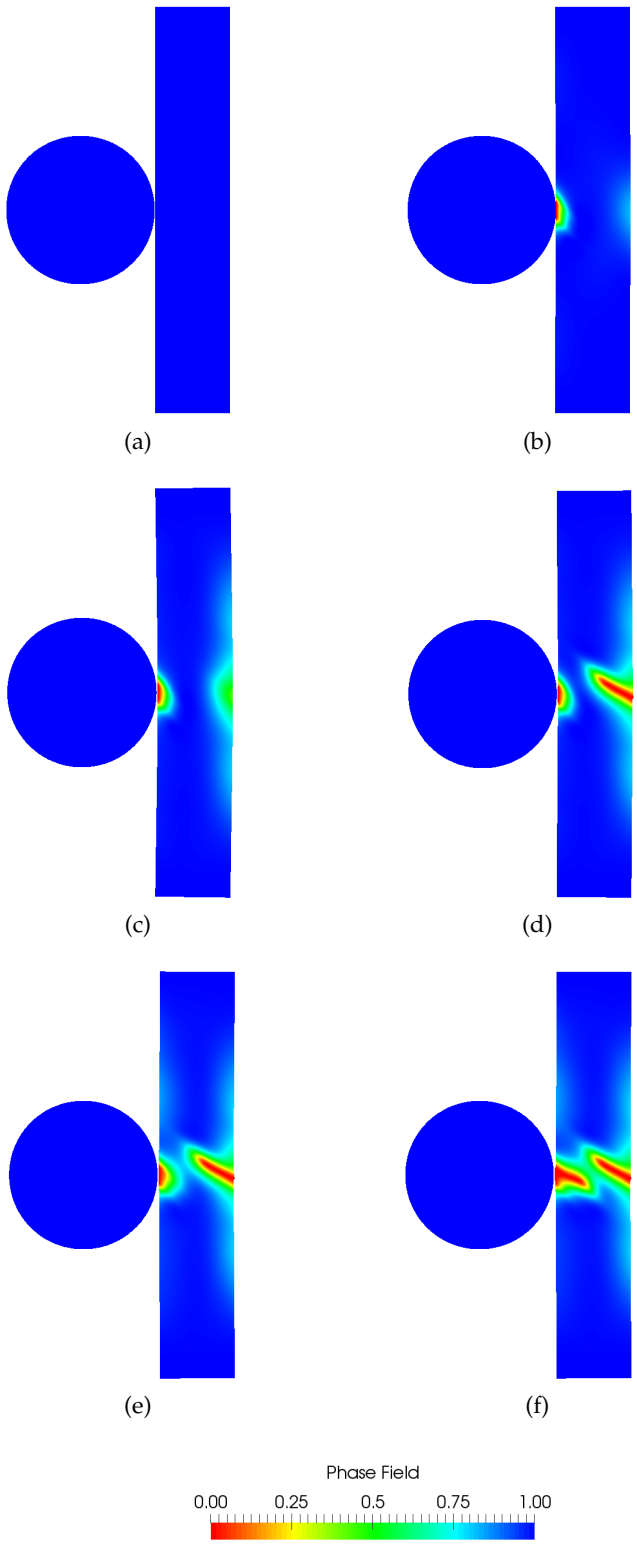

Figure 6.30: Disc-Beam impact fracture problem: Phase field for time steps (a) t=0 μs (b) t=12 μs (c) t=28 μs (d) t=40 μs (e) t=70 μs and (f) t=80 μs. Results for case (iii): PF-MPM 4th order orthotropic model.

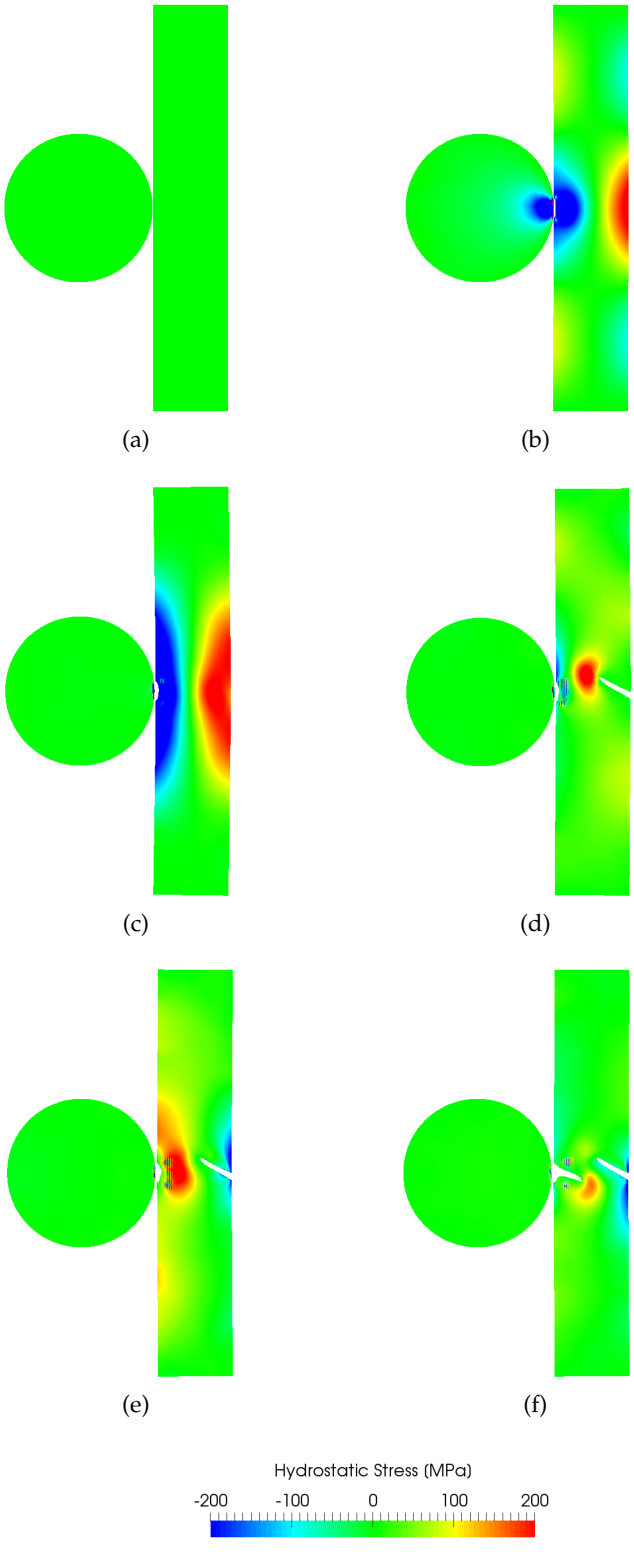

Figure 6.31: Disc-Beam impact fracture problem: Hydrostatic stresses for time steps (a) t=0 μs (b) t=12 μs (c) t=28 μs (d) t=40 μs (e) t=70 μs and (f) t=80 μs. Results for case (iii): PF-MPM 4th order orthotropic model. Material points with $c_p < 0.08$ have been removed.

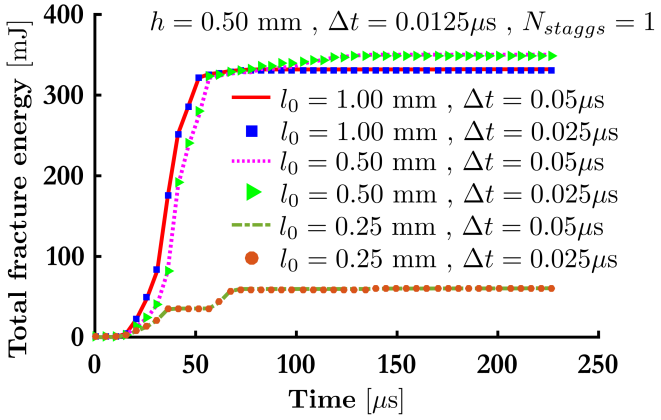

(a)

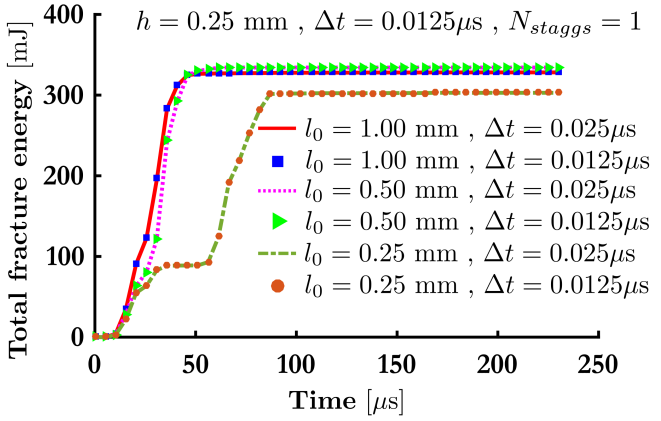

(b)

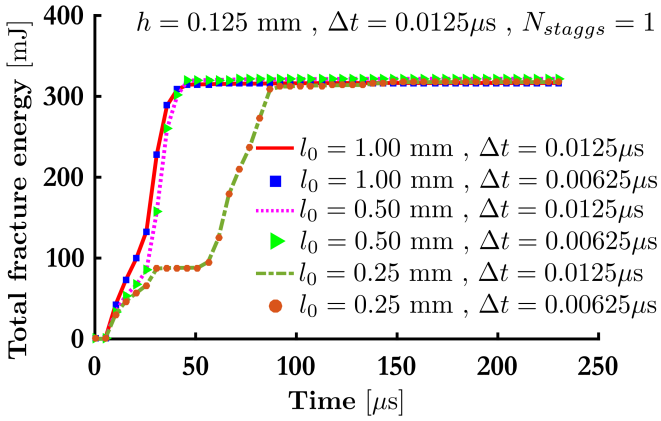

(c)

Figure 6.32: Disc-Beam impact fracture problem (Parametric study of case (i)): Total fracture energy over time. Sub-figs (a), (b) and (c) investigate the influence of length scale parameter (l_0) and time step (Δt) for cell spacing $h = 0.50$ mm, $h = 0.25$ mm and $h = 0.125$ mm, respectively.

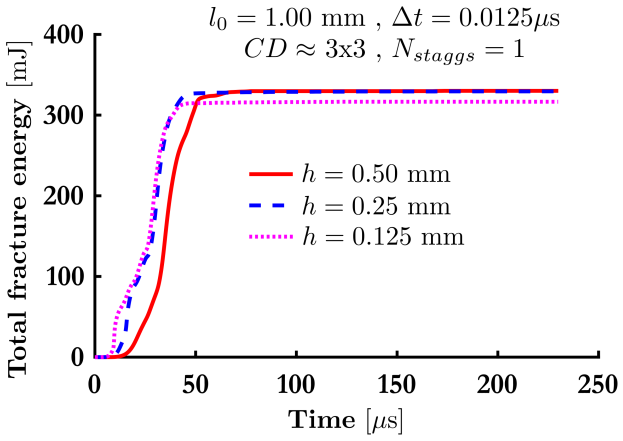

(a)

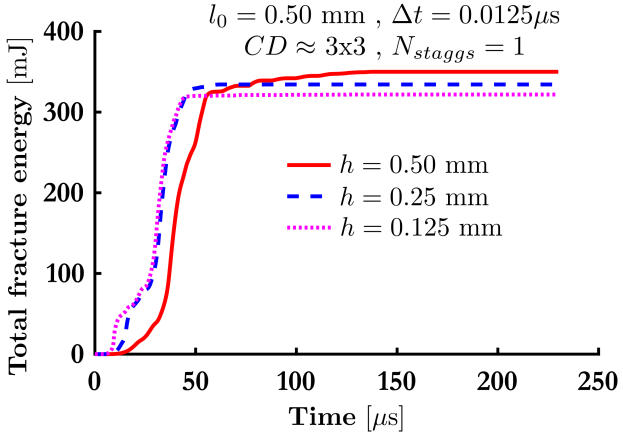

(b)

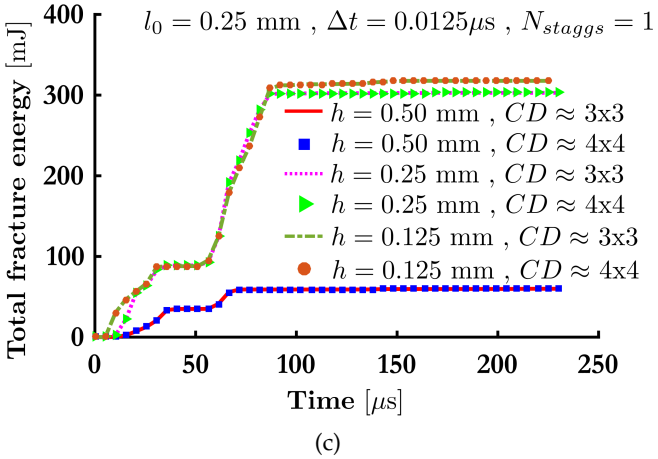

(c)

Figure 6.33: Disc-Beam impact fracture problem (Parametric study of case (i)): Total fracture energy over time. Sub-figs (a), (b) and (c) shown the influence of cell spacing for length scale parameter $l_0 = 1.00$ mm, $l_0 = 0.50$ mm and $l_0 = 0.25$ mm, respectively. In sub-fig (c), the influence of cell density is also illustrated for approximately 3x3 and 4x4 material points per cell.

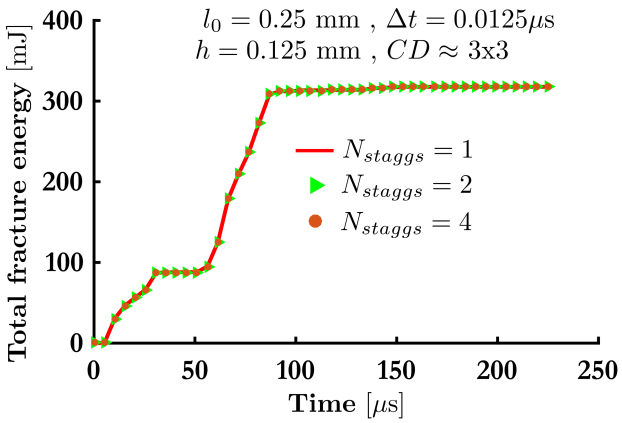

Figure 6.34: Disc-Beam impact fracture problem (Parametric study of case (i)): Total fracture energy over time. Influence of staggered iterations.

(black eclipse) is also plotted on these snapshots. In Figs. 6.39(b) and 6.39(c), the phase field evolves along the material orientation $\phi = +45^o$. The crack paths derived from our simulation agree well with the experimental crack paths presented in Fig. 6.39(d).

6.5 Conclusions

In this chapter, a novel numerical method is introduced for the treatment of dynamic brittle fracture in both isotropic and anisotropic elastic media. The evolution of crack paths is represented by means of phase field models within a MPM setting. Anisotropy is explicitly introduced in the fracture energy through a crack density functional. The method is further extended to account for frictional contact problems involving phase field fracture adopting a discrete field approach. A notable advantage of the proposed formulation is that both the equilibrium and phase field governing equations are solved independently for each discrete field rendering the method suitable for parallel implementation.

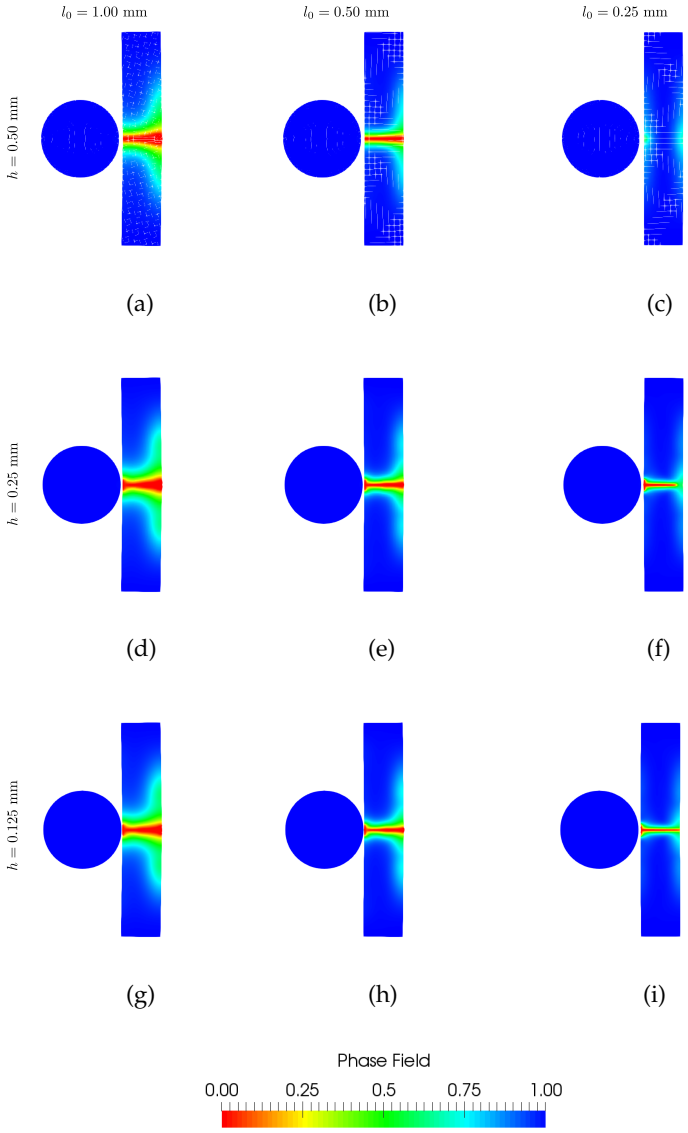

Figure 6.35: Disc-Beam impact fracture problem (Parametric study): Phase field for cell spacing $h = 0.50$ mm ((a)-(c)), $h = 0.25$ mm ((d)-(f)) and $h = 0.125$ mm ((g)-(i)). Sub-figs (a), (d) and (g) are for $l_0 = 1.00$ mm, (b), (e) and (h) for $l_0 = 0.50$ mm and (c), (f) and (i) for $l_0 = 0.25$ mm. Results for case (i).

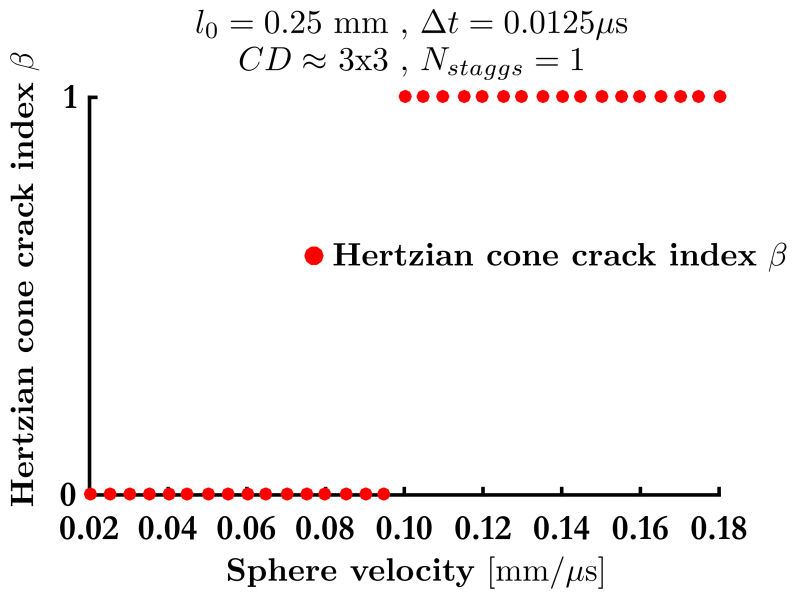

Figure 6.36: Hertzian cone crack index β versus projectile velocity.

Material Parameters					
Elastic Material Properties			Anisotropic Material Properties		
E	14980	[N/mm^2]	γ_{1111}	1.00	[–]
ν	0.36	[–]	γ_{2222}	2900	[–]
ρ	1586	[kg/m^3]	γ_{1122}	0.00	[–]
			γ_{1212}	74.00	
			l_0	1.00	[mm]
			k_f	0.00	[–]
			$\mathcal{G}_{c_{max}}$	30.9044	[N/mm]
			$\mathcal{G}_{c_{min}}$	5.9067	[N/mm]
			ϕ	+45	[Deg]
Material Point Method Model					
Number of Control Points			45904		
Number of Cells			150x300=45000		
Cell spacing			1.00		[mm]
$q_\xi = q_\eta$			2nd		
Ξ			$\{0,0,0,0.006666,0.013333,...,0.986666,0.993333,1,1,1\}$		
H			$\{0,0,0,0.003333,0.006666,...,0.993333,0.996666,1,1,1\}$		
Initial Cell density			3x3		
Number of Material Points			280800		
Discrete Fields					
Number of Discrete Fields			1		
Solution Algorithm Parameters					
Time Integrator			Explicit		
Δt			0.0125		[μs]
N_{steps}			2000		
N_{staggs}			1		

Table 6.7: Anisotropic plate with centre crack: Simulation parameters.

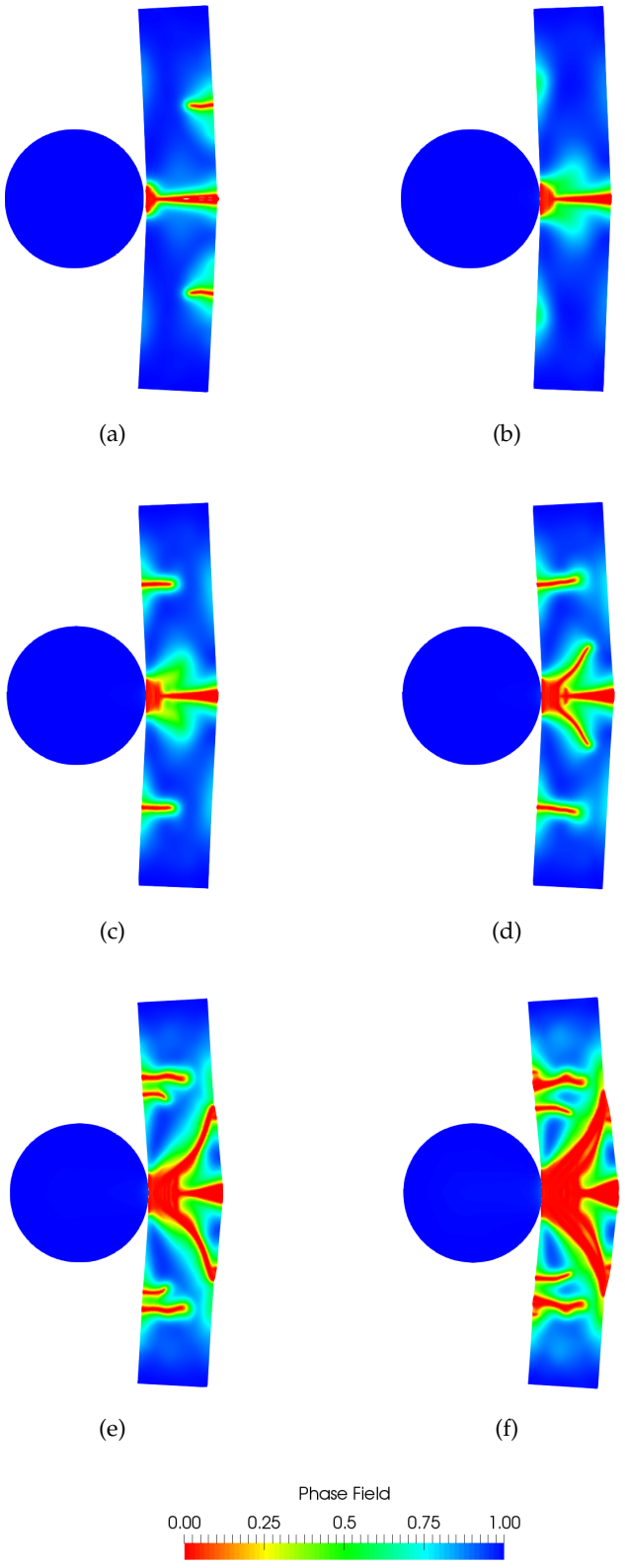

Figure 6.37: Fracture patterns for varying projectile velocities (a) $\dot{\mathbf{u}}_{Ap_{(0)}} = 0.05\,\text{mm}/\mu\text{s}$ (b) $\dot{\mathbf{u}}_{Ap_{(0)}} = 0.08\,\text{mm}/\mu\text{s}$ (c) $\dot{\mathbf{u}}_{Ap_{(0)}} = 0.095$ mm/μs (d) $\dot{\mathbf{u}}_{Ap_{(0)}} = 0.10$ mm/μs (e) $\dot{\mathbf{u}}_{Ap_{(0)}} = 0.14$ mm/μs (f) $\dot{\mathbf{u}}_{Ap_{(0)}} = 0.18$ mm/μs. All snapshots correspond to time $t = 16\mu$s.

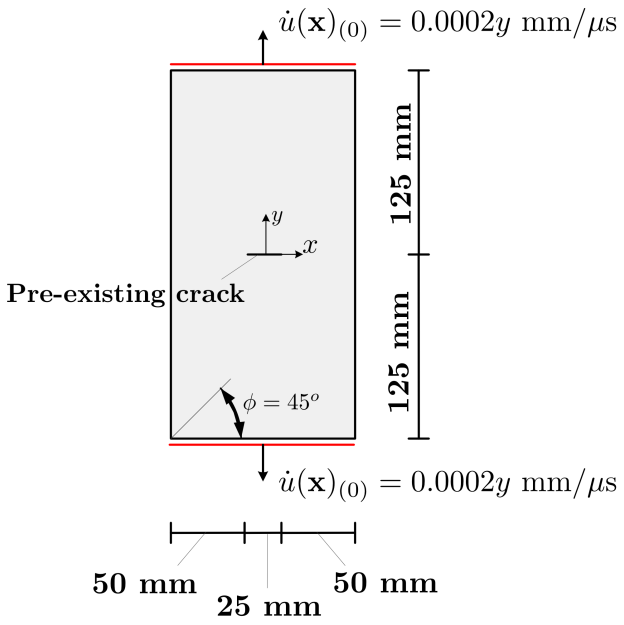

Figure 6.38: Anisotropic plate with centre crack: Geometry and boundary conditions.

The method is rather appealing for the case of phase field modelling where very fine meshes are commonly required due to the regularized crack topology. Rather than employing a uniform background mesh and material point density, multiple small scale problems can be solved separately for each discrete field at their corresponding background domain. In terms of contact driven fracture, contrary to standard FEM implementations that necessitate the algorithmic treatment of local contact features, these now naturally emerge from the interaction of material points within a fixed Eulerian mesh. Indeed, the fixed Eulerian grid is utilized to identify the contact surfaces using the material points' projection on the grid.

A set of representative numerical examples is presented where the computational advantages of PF-MPM are demonstrated. In the first example, the method is verified against the standard Phase Field Finite Element Method; the two methods are in good agreement. The influence of anisotropy is examined in terms of crack path, time history energy results and crack tip velocities. Benchmark problems with complex crack path i.e. crack branching and merging are

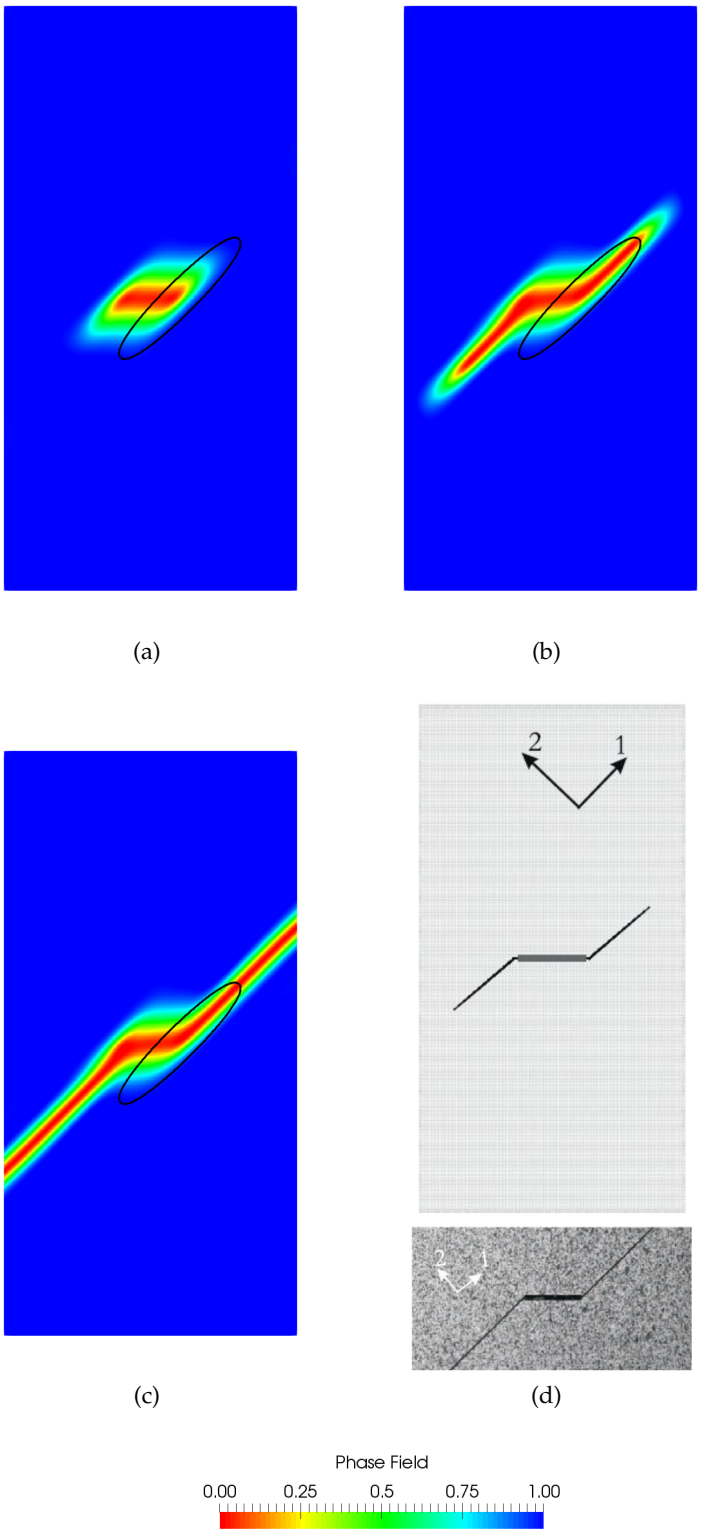

Figure 6.39: Anisotropic plate with centre crack: Phase field for time steps (a) t=0 μs (b) t=22 μs and (c) t=25 μs. The experimental observations are shown in (d) (Cahill et al. (2014)).

considered and the robustness of the method is established. It is shown that different loading velocities and fracture material parameters strongly influence the dynamic failure response of the structure and the resulting crack paths. Fracture energies computed from the proposed method are compared and indeed verified against the corresponding analytical predictions. Finally, crack paths derived from the method are validated, when possible, against experimental observations.

Chapter 7

An application of the PF-MPM to the study of rocking system dynamics

Part of this chapter is published in the 16th European Conference on Earthquake Engineering (Thessaloniki, Greece) (Kakouris et al., 2018).

7.1 Introduction to rocking mechanics

Rocking dynamics occur in systems whose connection with their support medium is achieved through a non-tensile interface where the shear forces are frictional. Examples of rocking systems can be found in a wide range of applications: from museum exhibits and hospital equipment to electrical devices and structural elements. The response of such systems when subjected to ground excitations is substantially different to the response of monolithic structures. A distinctive feature is the appearance of rigid body rotations and displacements during the motion. These are often dominant and hence the criteria of failure of such bodies are mainly kinematic, rather than the usual stress exceedance criteria used for typical structural systems.

As a reasonable consequence, the majority of relevant literature examines rocking systems under the assumptions of rigid support medium and body (Housner, 1963), or by assuming that the rocking body is flexible only in the lateral direction (Acikgoz and DeJong, 2012). However, the decelerations of the rocking body during the occurring impacts are often of the order of tenths of g. These large forces may induce large local stresses at the points of application that may deteriorate the contact surface or lead to local failures.

This mode of failure has often been ignored in the literature. This is mainly due to the computational complexity of the problem between large displacement kinematics and computational mechanics. The change of the contact surface during the rocking motion in combination with an impact and sliding contact problem pose substantial challenges for standard FE methods: they result in the need for re-meshing techniques, or very dense initial meshes. The latter solution in turn results in further increased demands from the time integration method used so as to ensure stability. Such an approach could potentially lead to the deceiving result that the underlying physical problem is chaotic, when in reality the issue often lies in the robustness of the computational treatment. Furthermore, mesh distortion errors that are inevitable in large kinematics Finite Element analyses hinder the fidelity of rocking body simulations where the deformability of the contact surfaces significantly affects the resulting contact forces.

To alleviate the previous problems and develop rocking models that allow the study of the stresses induced in rocking systems, a Material Point Method for simulating the rocking kinematics of deformable bodies is proposed. In this chapter, the developed model is used to study the dynamics of a relatively stiff body and support medium and the solutions obtained are compared versus existing models in the literature. Next, the influence of rocking body deformability is examined under earthquake loads. Finally, the proposed PF-MPM is utilized to examine the damage evolution in rocking systems.

7.2 Rigid Rocking models

The Inverted Pendulum Model (IPM), developed by Housner (1963), is potentially the most popular model for rocking bodies. The rocking body, the properties and the axes convention used in the following equations are defined in Fig. 7.1. The rigid body is defined by its mass m, half-width and half-height b and h, respectively. The occurring moment of inertia, about any of the bottom corners 0 and $0'$, is denoted as I_0 whereas $R = \sqrt{h^2 + b^2}$ is the distance from a corner to the centre of mass and the angle $\alpha = \tan^{-1}(b/h)$ describes the slenderness of the block.

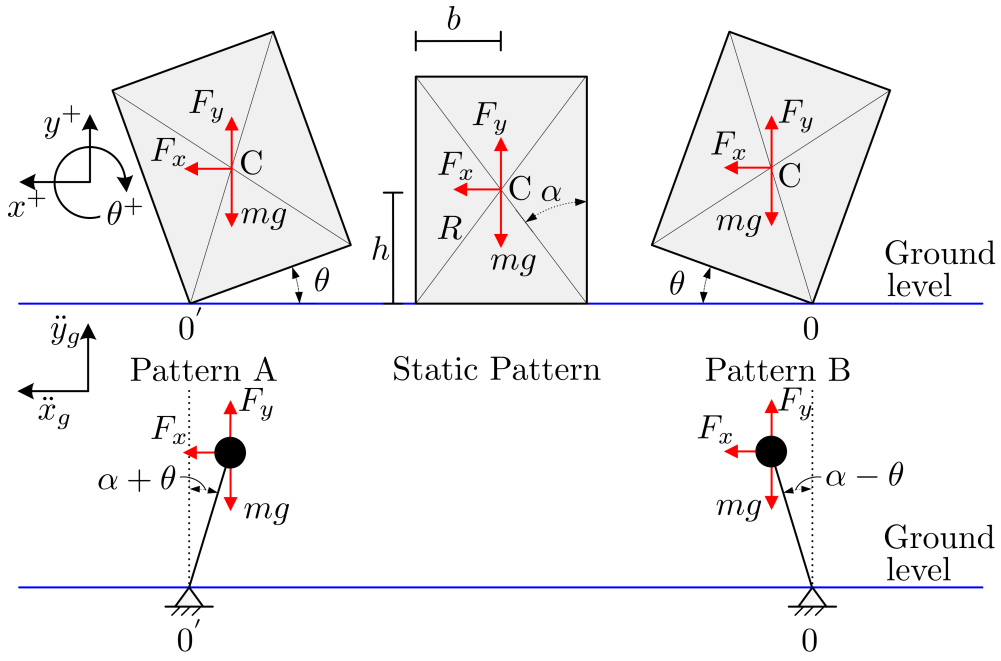

Figure 7.1: Inverted Pendulum Model (IPM defined by Housner (1963) for a free-standing rocking block).

The body rocks with respect to one of the corners depending on the sign of θ. Thus, it can be simulated by a pendulum whose pin is located at that corner as shown in Fig. 7.1. This further implies that the body is assumed not to slide, or experience free-flight, that the body and the ground are rigid, and that the response of the body is strictly planar.

When θ transitions through zero an impact occurs between the body and the

ground and as a result, the body may lose kinetic energy as it transitions, accordingly, from one pendulum pattern to the other. If it is further assumed that the angular momentum with respect to the future rocking corner is conserved, the reduction of energy factor, r, which relates the kinetic energy before and after impact is expressed as

$$r = \frac{\left(\dot{\theta}^{+}\right)^{2}}{\left(\dot{\theta}^{-}\right)^{2}} = \frac{1/2 I_0 \dot{\theta}_2^2}{1/2 I_0 \dot{\theta}_2^1} = \left[1 - \frac{mR^2}{I_0}\left(1 - \cos\left(2\alpha\right)\right)\right]^2 \tag{7.1}$$

where $\dot{\theta}^{+}$ and $\dot{\theta}^{-}$ are the angular velocity after and before impact, respectively. Hence, the IPM results in a discontinuity of the velocity state before and after the impact. It should further be noted that as discussed in Chatzis et al. (2017), the reduction of energy factor could well be within the value defined in equation (7.1) and unity, i.e., no loss of energy during impacts. To be able to alleviate that related uncertainty the contact interface mechanics have to be specified.

A means of achieving that while also introducing the deformability of the support medium is through the Winkler Model (WM) proposed in Chatzis and Smyth (2012b) for rocking bodies with a flat base. The model is illustrated in Fig. 7.2 below

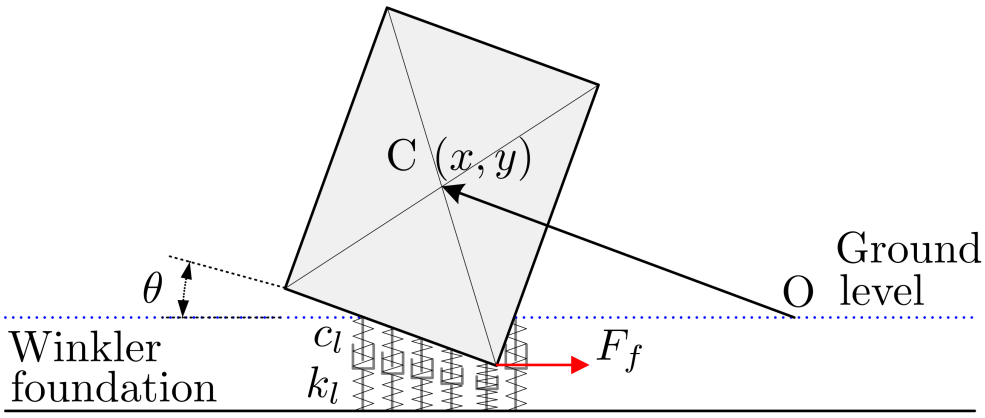

Figure 7.2: WM for rocking bodies on deformable media (Chatzis and Smyth, 2012b).

The support medium parameters used in the model are the distributed per

unit length stiffness k_l and damping coefficients c_l , while nonlinear horizontal springs are used for the frictional forces F_f. A Coulomb friction model is used that is defined by the coefficient of friction μ_f. The motion of the rigid body is described by the horizontal, vertical and rotational generalized coordinates (x,y and θ, respectively). As a result, the model allows for including the effects of impact, sliding and free flight without discontinuities in the states. Additionally, no assumption needs to be made regarding the impact duration as the dissipated energy is a parameter of the WM properties.

7.3 Material Point Method for rocking mechanics

Considering the advantages of MPM in contact mechanics (see Chapter 6), the overarching objective in this Section, is to, for the first time, simulate the rocking body - ground interaction by considering the actual dynamics of the two deformable bodies (rocking body, ground) in contact. Their interaction is derived from their contact and friction forces with minimal computational complexity and without increasing the computational demands.

7.3.1 Governing discrete equations

A discrete field approach is adopted, herein, for studying rocking dynamics. Therefore, the equilibrium discrete equations introduced in Section 6.3.1.1 are utilized. Those equations are integrated using the explicit time integration scheme described in Section 6.3.2.1.

7.3.2 Numerical examples

7.3.2.1 Rocking body response subjected into horizontal single sinusoidal ground acceleration

The rocking response of a body with dimensions $2b = 0.795$ m and $2h = 3.113$ m, shown in Fig. 7.3(a) resting on an elastic medium is simulated herein using the proposed MPM scheme. The purpose of this example is to verify the appropriateness of the MPM to simulate rocking system dynamics. The body is subjected to a horizontal ground acceleration prescribed by a single sinusoidal pulse defined in equation (7.2) as

$$\ddot{u}_g = \begin{cases} \alpha \sin(\omega t) & 0 \leq t < \frac{2\pi}{\omega} \\ \\ 0 & t \geq \frac{2\pi}{\omega} \end{cases} \tag{7.2}$$

where α and ω are the amplitude and the frequency of the excitation, respectively. The Young's modulus and Poisson ratio of the ground are $E = 260$ MPa and $\nu = 0.30$, respectively. The corresponding parameters for the body are chosen as $E = 5200$ MPa and $\nu = 0.30$. The parameters were chosen so that the body is substantially more rigid than the support medium. This allows for comparison versus previous work in the literature as the dimensions of the specific body under the assumption of it being rigid have been used in the works of Zhang and Makris (2001), Chatzis and Smyth (2012b) and Chatzis and Smyth (2012a). The mass density of the ground is $\rho = 1300$ kg/m^3 whereas the mass density of the rigid body is $\rho = 606.101$ kg/m^3. The latter allows for valid comparisons to be made against the mass per unit length used for this body in Chatzis and Smyth (2012b), i.e 1.5 tonnes/m. The friction coefficient between the rocking body and the ground is $\mu_f = 0.625$.

According to the MPM formulation introduced in Section 6.3 two discrete fields

are defined; one corresponding to the rigid body and one corresponding to the elastic medium. The former is discretized into 8928 material points whereas 7200 material points are used for the latter. Quadratic B-splines are utilized for the background grid with cell spacing 0.05 m and plane strain conditions are assumed. Initially, the material points are positioned in the Gauss positions of each parent cell; the cell density is 3x3. A time step $\Delta t = 0.00001$ sec is employed. The ground excitation is applied to MPM model employing D' Alembert's principle.

As initially shown in Zhang and Makris (2001), utilizing the IPM, a stability analysis on the body when subjected to single cycle acceleration pulses of varying frequency and amplitude (ω, α) offers useful information on the stability of the system. By varying the values of ω and α in the horizontal and vertical axes, respectively and by denoting for a given frequency the amplitudes at which a transition between survival and failure is observed the stability diagram of Fig. 7.3(b) can be generated. Failure in this context pertains to the toppling of the rocking body.

In such a diagram, three distinct regions can be observed: a region of survival, a closed region (loop) where the body topples having experienced a single impact with the ground, and an area of failure occurring for larger amplitudes where the body fails without having experienced an impact. The boundaries between those regions for the IPM are indicated in Fig. 7.3(b) with a magenta hexagram. Using a deformable WM for the support medium, for the same body Chatzis and Smyth (2012b) produced a stability diagram which also included the presence of the three regions. The WM predicted boundaries are also plotted in Fig. 7.3(b) with a golden square.

A set of 127 analyses is carried out with various pairs of (ω, α) to derive the stability diagram of Fig. 7.3(b) using the MPM. The axes are normalized as ω/p and α/α_g, respectively, where $p = 2.14$ and $\alpha_g = 2.5049$. In this work green dots, blue pentagrams, and red diamonds correspond to the result obtained

from the proposed MPM model and account for safe, failure with impact and failure without impact respectively. It should be noted the body is considered to survive, after experiencing two impacts without failure during its free vibration response. The body is considered to fail when $|\theta| \geq 85^{o}$ where θ is the angle between the rocking body and the ground. The obtained results are superimposed on the boundaries predicted by the IPM and WM models.

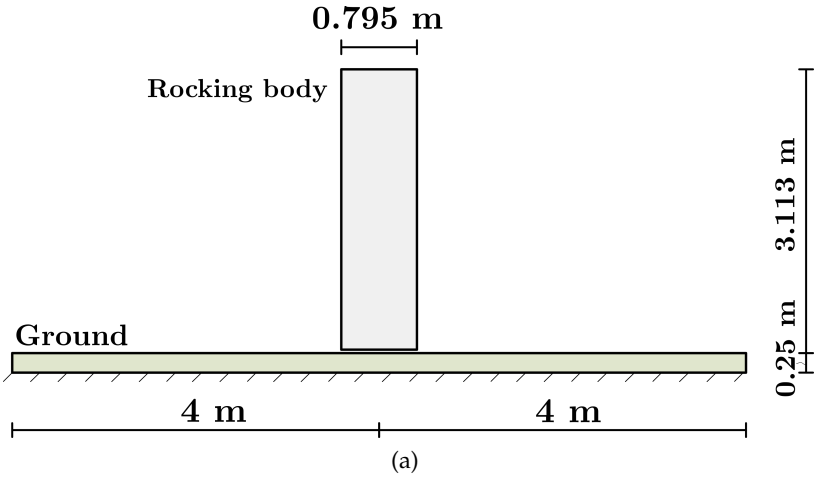

(a)

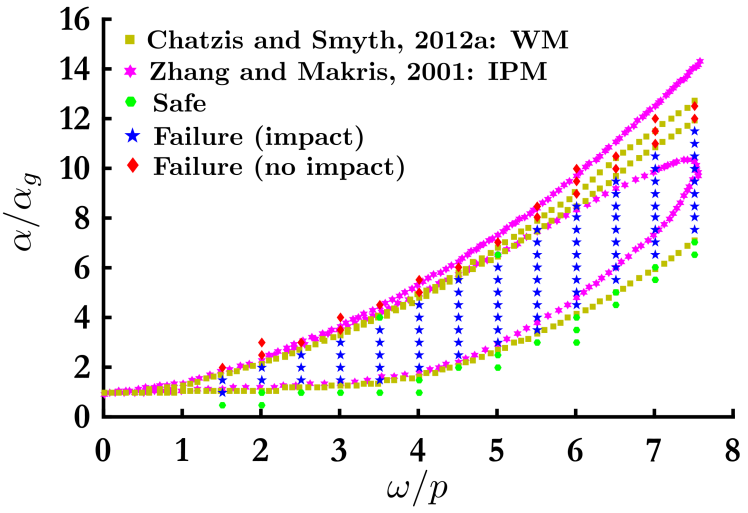

(b)

Figure 7.3: (a) Geometry and boundary conditions (b) Failure-safety analysis with the WM, IPM and MPM.

As shown in Fig. 7.3(b), the proposed MPM method demonstrates a very good agreement with the WM approach. The two methods predict that the failure with no impact regions extends to larger frequencies than those predicted by

the IPM model under the assumption of conserving angular momentum with respect to the future rocking corner. This phenomenon has been further explained in Chatzis et al. (2017) where it is argued that bodies with a flat base would not necessarily satisfy this assumption. Similarly to the WM, MPM does not need to adopt such an assumption, but rather relies on modelling the properties of the bodies in contact and accurately resolving the corresponding contact interfaces. It is further expected that the MPM model would show a better agreement to the results in Zhang and Makris (2001) if the same body had feet on the two corners, similarly to what has been demonstrated in Chatzis and Smyth (2012b) for the Concentrated Spring Model (CSMd).

It should further be stated that the stability diagram for the WM shown in Chatzis and Smyth (2012b) and in Fig. 7.3(b) uses an estimate of the properties on the contact interface stiffness and damping based on the model of Wolf (1994), which essentially simulates the support medium as an elastic half-space. It further appears that this model is also reasonable for the case studied here. However, the MPM does not need to make an assumption on the contact interface properties which is a further advantage of the model presented herein.

In the following, three individual cases are presented for each failure-safety condition. In the first case, the pair $\omega/p = 3$, $\alpha/\alpha_g = 1$ results in survival for the rocking body. A snapshot of the response of the rocking body is presented in Fig. 7.4 at chosen time instances. The ground excitation and rocking body angle time histories are presented in Fig. 7.5. In the second case, the frequency is the same ratio $\omega/p = 3$ while the amplitude is increased to $\alpha/\alpha_g = 2.5$. That pair leads the rocking body to toppling after having experience one impact with the ground. The complete rocking response is represented in Fig. 7.6. Similarly, the ground excitation and rocking angle time-histories are shown in Fig. 7.7.

In the third case, the amplitude is increased to $\alpha/\alpha_g = 3.5$. This amplitude seems to be adequate to overturn the rocking body without impact. The corresponding rocking motion is presented in Fig. 7.8 whereas the ground excitation

time-history and corresponding rocking angle are shown in Fig. 7.9.

7.3.2.2 Influence of rocking body deformability - Sensitivity analysis under earthquake loads

The rocking body of Section 7.3.2.1 is now subjected into horizontal earthquake loads. The 1999, Chi-Chi, Taiwan event, CHY101 recording is used herein (north component) with a peak ground acceleration (PGA) 3.90 m/s^2. It can be found in the P.E.E.R. ground motion database as RSN1244_CHICHI_CHY101-N (*Pacific-Earthquake-Engineering-Research-Center (P.E.E.R. Ground Motion Database)* 2018). The ground excitation and its corresponding spectral acceleration diagram (for damping 5%) are shown in Fig. 7.10(a) and Fig. 7.10(b), respectively. For brevity, acceleration recordings from $t = 20$ sec onwards are used since acceleration recorded prior to this cut-off point are negligible.

All the simulation parameters are kept constant as in the previous Section 7.3.2.1. The sensitivity of the response on the deformability of the rocking body is examined herein. In particular, the four cases shown in Table 7.1 are considered for the Young's modulus of the rocking body, namely, case (i) $E_a = E = 5200$ MPa case (ii) $E_b = E/10 = 520$ MPa case (iii) $E_c = E/100 = 52$ MPa and case (iv) $E_d = E/1000 = 5.2$ MPa. The rocking body angles with ground over time for all cases are presented in Fig. 7.10(c).

From Fig. 7.10(c), it is noticed that the stiffer the rocking body, the faster it fails. In particular, the rocking bodies fail at time 22.5360 sec, 20.6960 sec, 20.5840 sec and 18.0980 sec for the cases (i), (ii), (iii) and (d), respectively. The failure criterion that is used is the same as in Section 7.3.2.1, i.e. $|\theta| \geq 85^o$. The difference in its rocking response highlights the importance of accurately resolving the deformability of the rocking body. The MPM provides us with a significant advantage towards that goal.

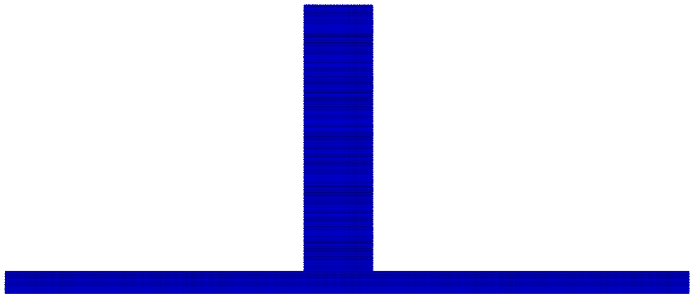

(a)

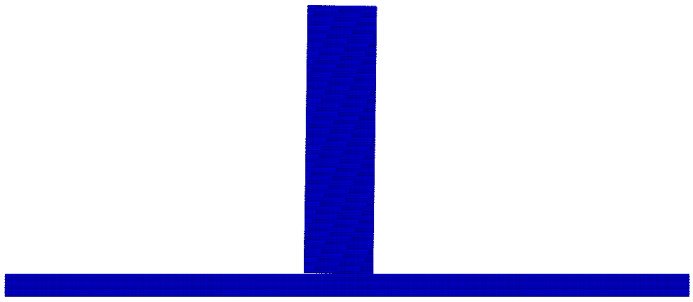

(b)

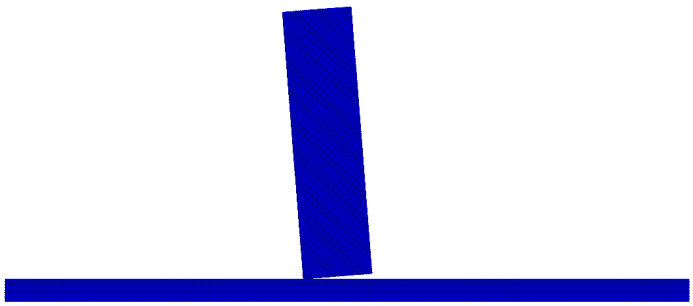

(c)

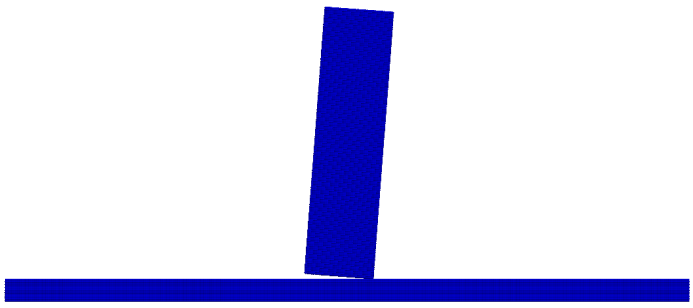

(d)

Figure 7.4: $\omega/p = 3$ and $\alpha/\alpha_g = 1$ (Safe): Rocking body response for (a) 0 sec (b) 0.47 sec (c) 1.20 sec and (d) 2.10 sec.

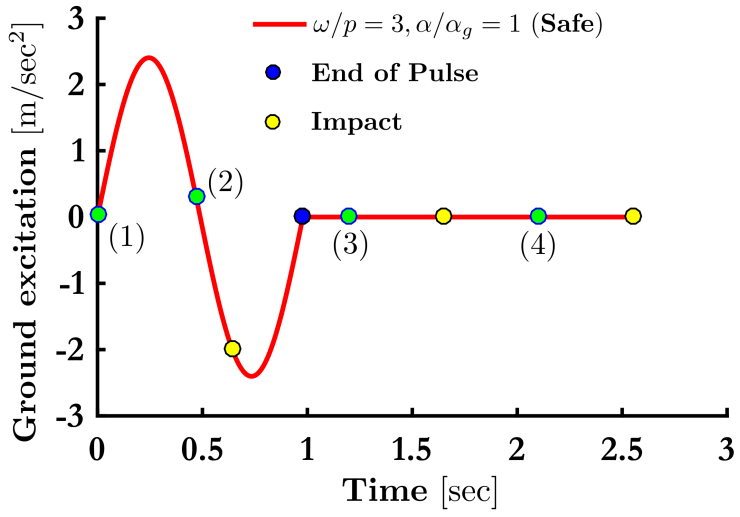

(a)

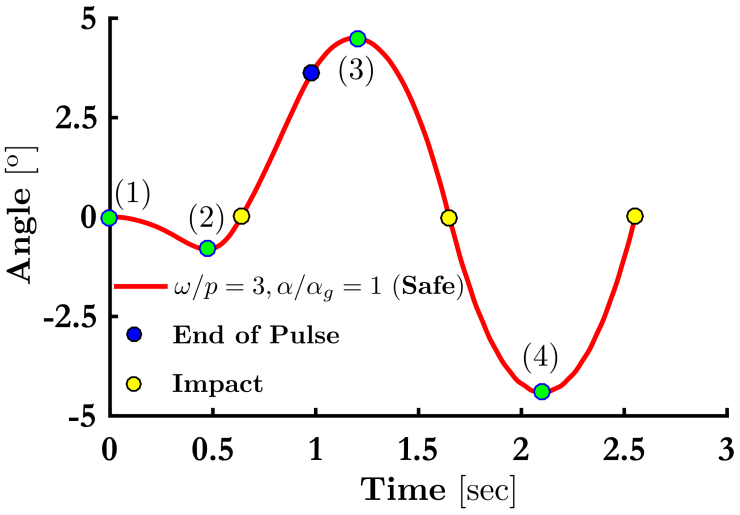

(b)

Figure 7.5: $\omega/p = 3$ and $\alpha/\alpha_g = 1$ (Safe): Plots over time for (a) ground excitation (acceleration pulse) (b) rocking body angle with ground - labels (1), (2), (3), (4) correspond to Fig. 7.4 sub-captions (a), (b), (c), (d).

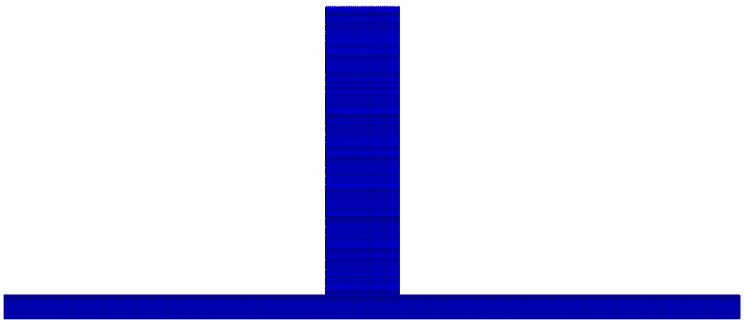

(a)

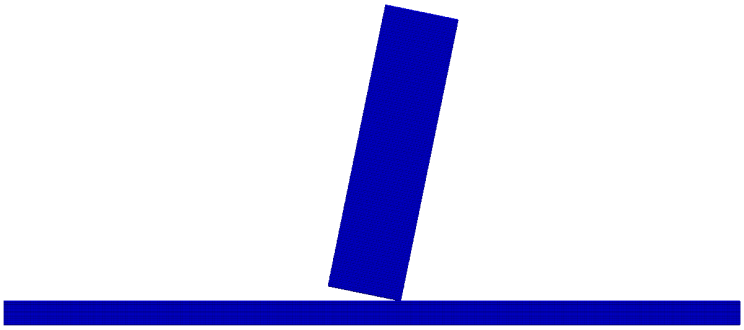

(b)

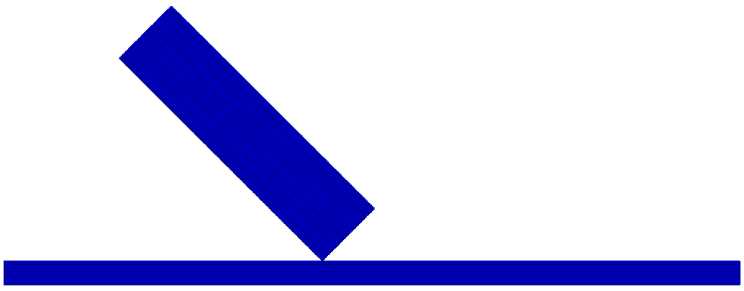

(c)

(d)

Figure 7.6: $\omega/p = 3$ and $\alpha/\alpha_g = 2.5$ (Failure (impact)): Rocking body response for (a) 0 sec (b) 0.73 sec (c) 2.51 sec and (d) 2.90 sec.

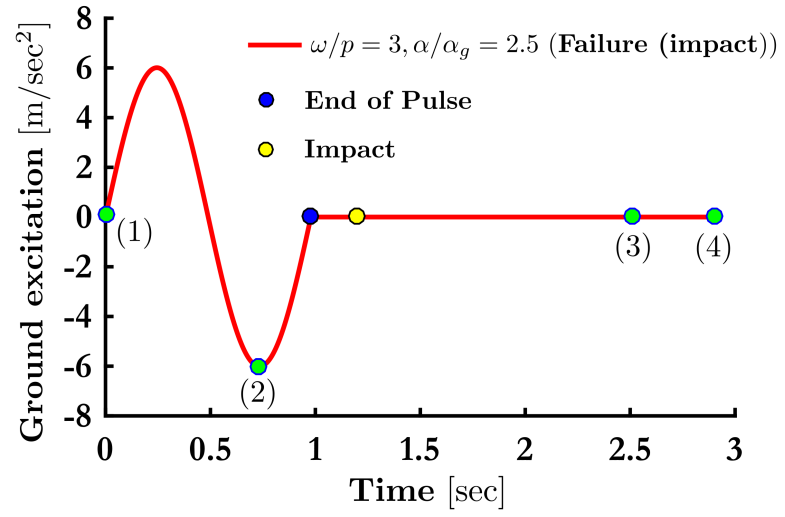

(a)

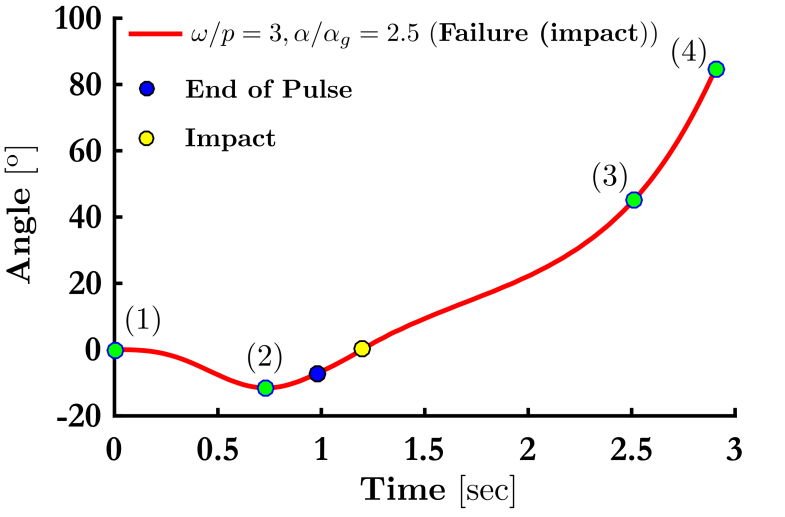

(b)

Figure 7.7: $\omega/p = 3$ and $\alpha/\alpha_g = 2.5$ (Failure (impact)): Plots over time for (a) ground excitation (acceleration pulse) (b) rocking body angle with ground - labels (1), (2), (3), (4) correspond to Fig. 7.6 sub-captions (a), (b), (c), (d).

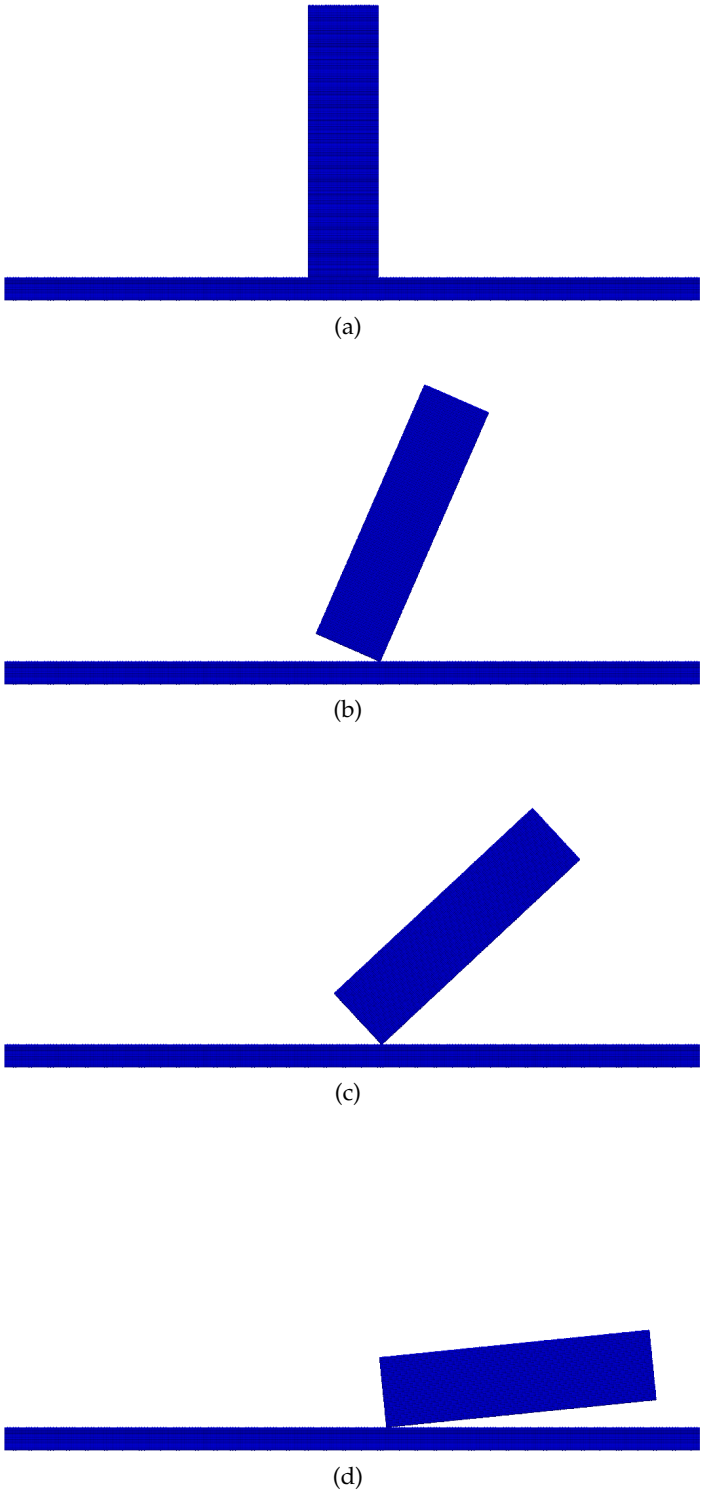

(a)

(b)

(c)

(d)

Figure 7.8: $\omega/p = 3$ and $\alpha/\alpha_g = 3.5$ (Failure (no impact)): Rocking body response for (a) 0 sec (b) 1.50 sec (c) 2.20 sec and (d) 2.58 sec.

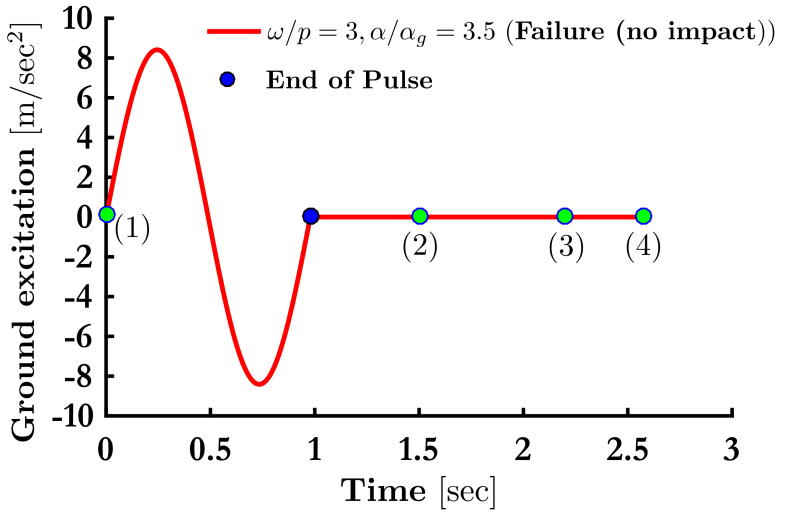

(a)

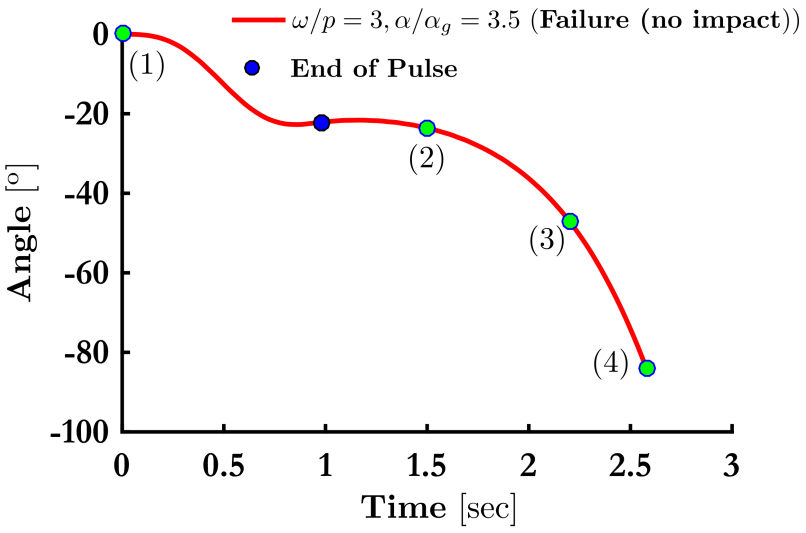

(b)

Figure 7.9: $\omega/p = 3$ and $\alpha/\alpha_g = 3.5$ (Failure (no impact)): Plots over time for (a) ground excitation (acceleration pulse) (b) rocking body angle with ground - labels (1), (2), (3), (4) correspond to Fig. 7.8 sub-captions (a), (b), (c), (d).

Finally, snapshots of rocking body motion for all the four cases are presented in Fig. 7.11 over time. In all cases, the rocking body rocks about its two bottom corners. In cases (i) and (ii) the rocking body eventually overturns about its left bottom corner whereas for the cases (ii) and (iii) about its right bottom corner.

Young's modulus	**Case (i)**	**Case (ii)**	**Case (iii)**	**Case (iv)**	
E	5200	$E/10 = 520$	$E/100 = 52$	$E/1000 = 5.2$	[MPa]

Table 7.1: Sensitivity analysis under earthquake loads: Young's modulus of the rocking body.

7.4 Material Point Method for studying crack propagation on rocking systems

In the previous Sections of this Chapter, the proposed MPM is verified against existing models in the literature. Furthermore, the importance of accurately resolving the deformability of the rocking body is shown to significantly affect its rocking response. In this Section, the proposed PF-MPM is utilized to simulate crack propagation on deformable rocking systems.

7.4.1 Governing discrete equations

As mentioned in Section 7.3, the response of a rocking system is considered as two deformable bodies in contact. Thus, the governing coupled equations introduced in Section 6.2 are used for the crack propagation on rocking systems. Furthermore, the numerical implementation introduced in Section 6.3 is adopted as summarized in pseudo-algorithm 3 on page 203.

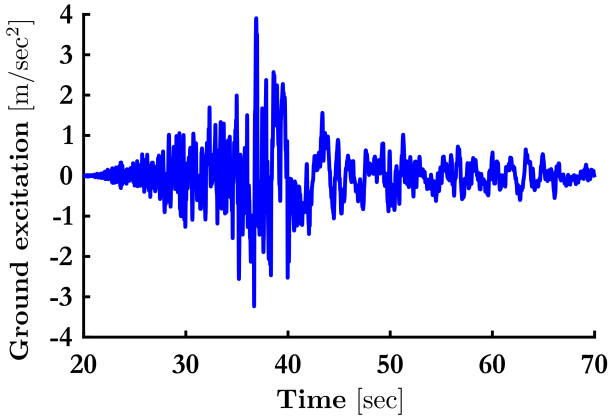

(a)

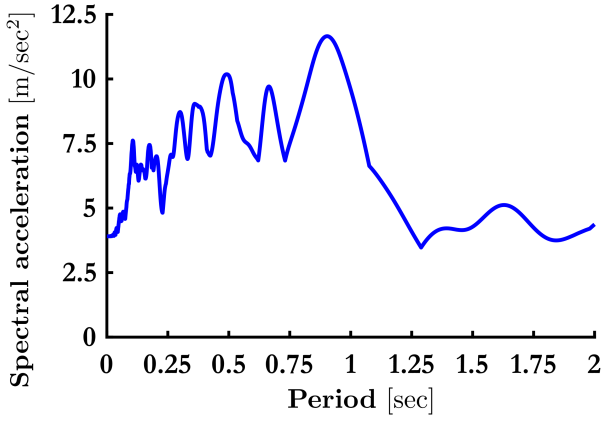

(b)

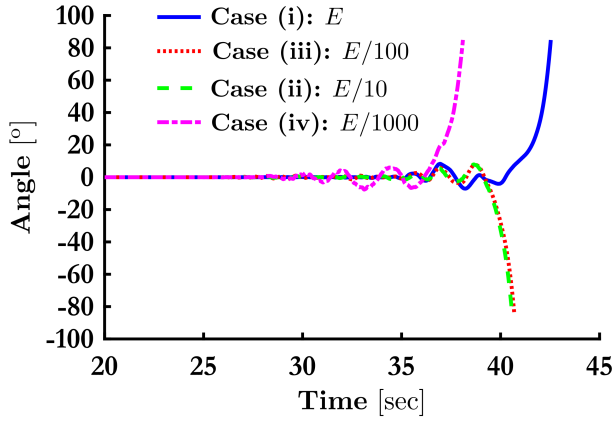

(c)

Figure 7.10: Chi-Chi ground motion record: (a) Acceleration time histories (b) Spectral accelerations and (c) rocking body angle with ground for Young's modulus: case (i) E (blue solid line) case (ii) $E/10$ (red dotted line) case (iii) $E/100$ (green dashed line) and case (iv) $E/1000$ (magenta dash-dot line).

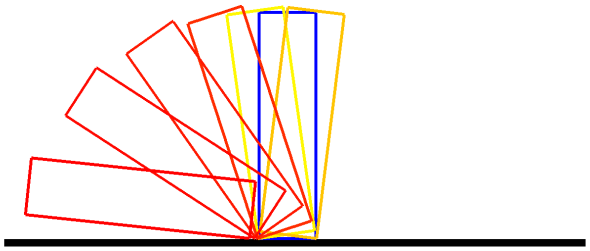

(a)

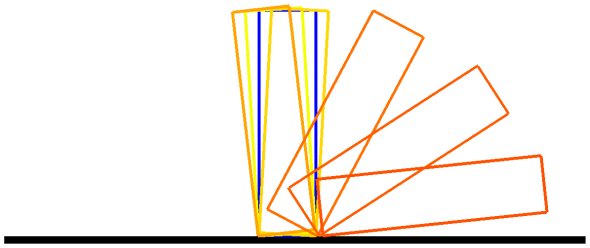

(b)

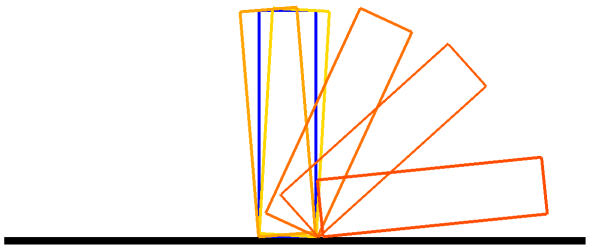

(c)

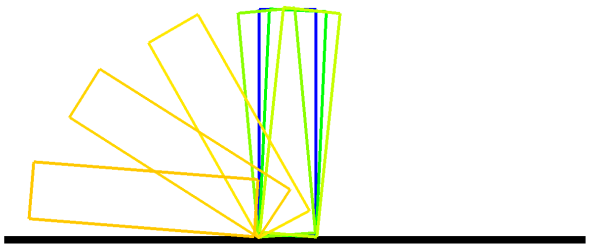

(d)

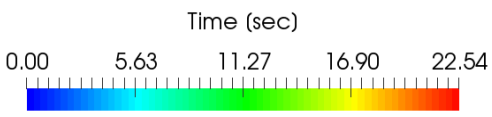

Figure 7.11: Chi-Chi ground excitation: Snapshots of rocking body motion for (a) case (i) E (b) case (ii) $E/10$ (c) case (iii) $E/100$ and (d) case (iv) $E/1000$.

7.4.2 Numerical example

7.4.2.1 Damage evolution in rocking structures: Circular Arch with Buttresses

In this example, a circular arch with two buttresses is examined. The aim of this example is to assess the potential of the PF-MPM in simulating damage evolution in rocking systems. The structure is subjected to the Chi-Chi, Taiwan earthquake ground motion (see Fig. 7.10(a)). Two cases are examined. In case (i), the buttresses can rock under the action of earthquake ground motion. In case (ii), the two buttresses are fixed in the ground. Thus, they are unable to experience rocking, uplift of sliding.

The geometry of the structure is shown in Fig. 7.12(a). The vault has circular shape with radius $R = 3.488$ m while the span is 6.4 m. The width of the buttresses is 0.80 m and the vault thickness is 0.20 m. The Young's modulus, Poisson ratio and the mass density of the ground are $E = 260$ MPa, $\nu = 0.30$ and $\rho = 1300$ kg/m^3, respectively. The structure is considered to comprise natural stone with corresponding parameters $E = 300$ MPa, $\nu = 0.25$ and $\rho = 1700$ kg/m^3. The fracture properties of both the ground and the structure are chosen as $l_0 = 0.20$ mm, $k_f = 0.00$ and $\gamma_{ijkl} = 0$. The surface energy density of the structure is considered to be $\mathcal{G}_c(\theta) = \bar{\mathcal{G}}_c = \mathcal{G}_{c_{max}} = \mathcal{G}_{c_{min}} = 2700$ N/m whereas the corresponding parameter for the ground and the buttresses is assumed to be sufficiently large (i.e. $\mathcal{G}_{c_g}(\theta) = 1000\mathcal{G}_{c_s}(\theta)$), so that no damage can occur on it.

Quadratic B-splines are utilized for the background grid with cell spacing 0.10 m and plane strain conditions are assumed. The circular arch with the two buttresses consists of 5886 material points whereas the ground is formulated by 12960 material points. To reduce the computational cost, the ground is included in the analysis of case (i) only. In case (ii), the ground material points are

removed for brevity and the fixed boundary conditions are directly applied on the bottom of each buttress at their corresponding grid nodes. The initial cell density of each parent cell is at least 3x3. The explicit time integration scheme is employed with time step $\Delta t = 0.00005$ sec and the ground excitation is applied by using the D' Alembert's principle as in Section 7.3.2.

The time history of the rocking angle with the ground for the left buttress for case (i) is presented in Fig. 7.12(b). From Fig. 7.12(b) and case (i), it is noticed that the buttress initially rocks with the ground experiencing small angles (i.e. less than 2^o). Then, the arc gradually degrades until the appearance of the first hinge on its left side at time $t = 31.75$ sec (see Fig. 7.13(b)). Next, two more hinges are observed, one approximately on the top of the arc (see Fig. 7.13(c)) and another on its right side 7.13(d) at time $t = 32$ and $t = 32.25$ sec. Finally, the collapse mechanism and the final state are presented in Figs. 7.13(e) and 7.13(f), respectively.

Similarly, the evolution of the phase field for several time steps and case (ii) is presented in Fig. 7.14. In this, none hinge is observed in the arc during the whole earthquake excitation. Its left (see Fig. 7.14(b)) and right (see Fig. 7.14(c)) side are only degradated with a minimum observed degradation value at approximately 0.80. Therefore, the rocking boundary conditions on the buttresses significantly affect the damage evolution of the structure as compared to the corresponding fixed supports.

7.5 Conclusions

In this Chapter, a MPM is presented for the simulation of rocking body dynamics. The method is rigorously established within a discrete field setting. In this, solution of the governing equations of motion is performed for each field individually while contact conditions between fields are explicitly introduced into

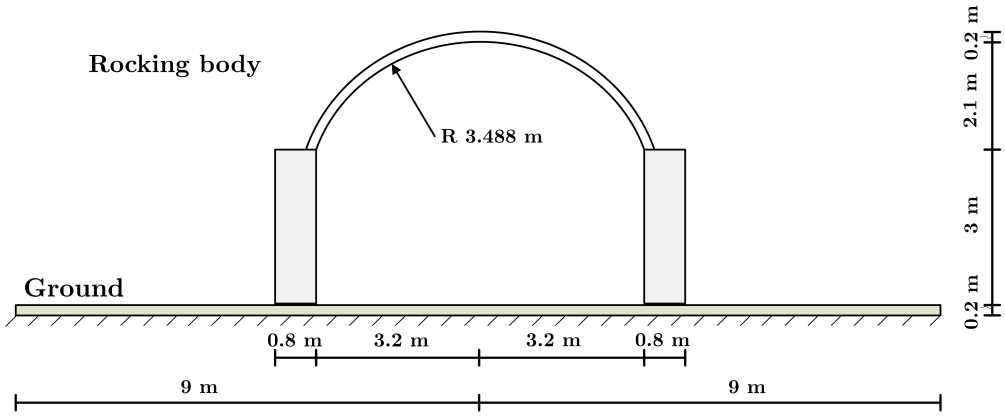

(a)

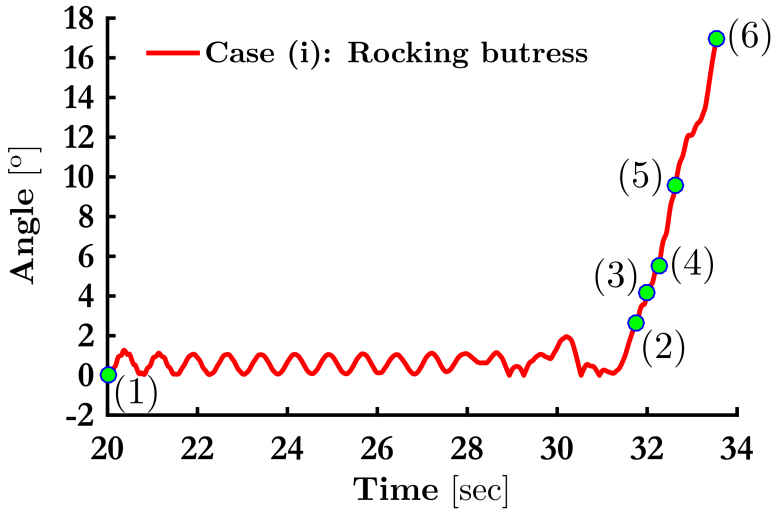

(b)

Figure 7.12: Circular Arch with Buttresses: (a) Geometry and boundary conditions (b) rocking body angle with ground for case (i): Buttresses can experience rocking with ground [labels (1) to (6) correspond to Fig. 7.13 sub-captions (a) to (f)].

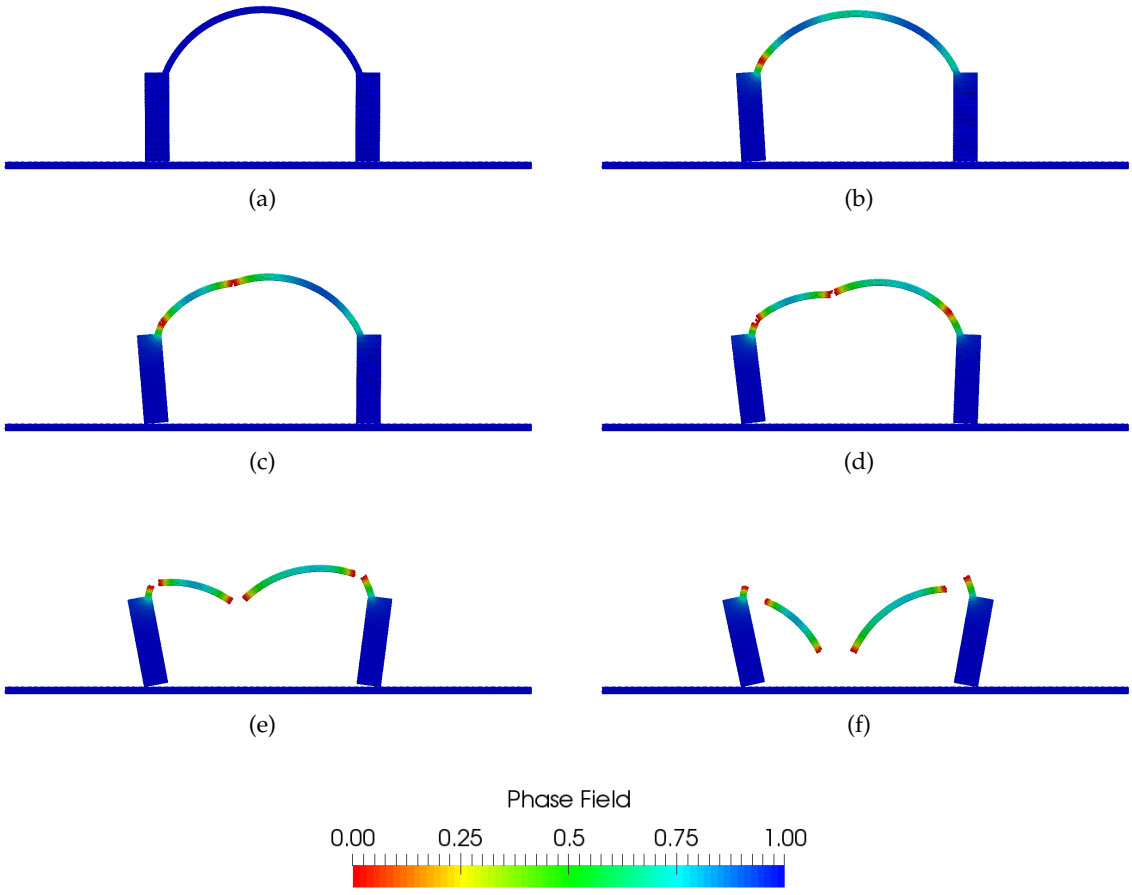

Figure 7.13: Circular Arch with Buttresses: Phase field for time step (a) $t = 20$ sec (initial state) (b) $t = 31.75$ sec (first hinge) (c) $t = 32$ sec (second hinge) (d) $t = 32.25$ sec (third hinge) (e) $t = 32.63$ sec (collapse) and (f) $t = 33.53$ sec (final state). Results for case (i): Buttresses can experience rocking with ground.

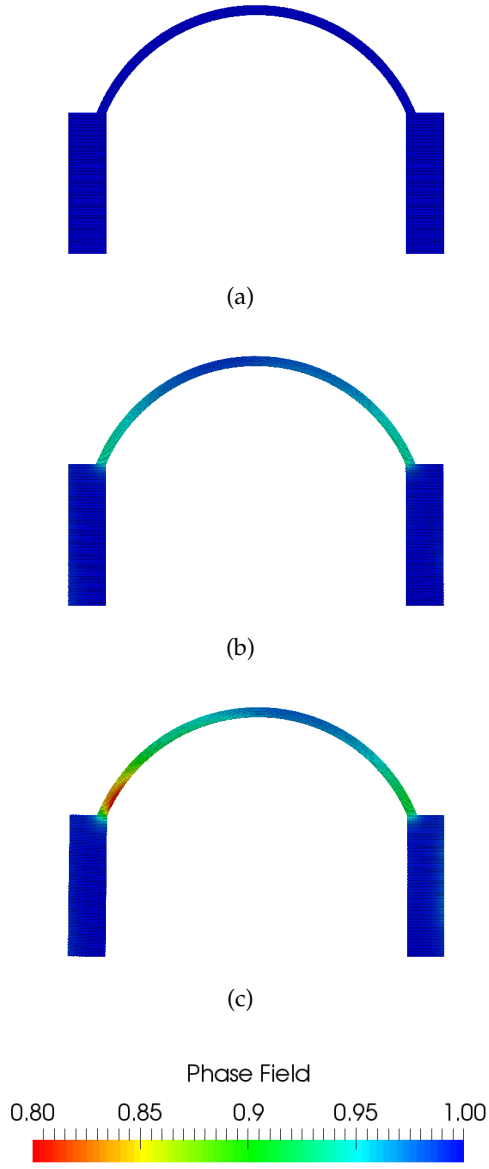

Figure 7.14: Circular Arch with Buttresses: Phase field for time step (a) $t = 0$ sec (b) $t = 31$ sec and (c) $t = 32$ sec. Results for case (ii): Buttresses are fixed on the ground.

the strong form of the problem through appropriate boundary conditions. Solution of the resulting governing equations is performed in an explicit manner using a predictor corrector algorithm.

Results obtained with the proposed numerical method for the case of a rigid body over an elastic half-space are compared against the Inverted Pendulum and Winkler rocking models. Results indicate that the numerical predictions are in good agreement with the estimates of both the Inverted Pendulum Model and the Winkler Model. As no assumption needs to be implied on either the stiffness of the rocking body or the contact interface properties, the proposed method provides an attractive alternative for the simulation of more complex problems, e.g., rocking of deformable and non-elastic bodies.

Chapter 8

Conclusions and Future work

8.1 Conclusions

This thesis proposes a novel computational method to simulate crack propagation in brittle materials, namely the Phase Field Material Point Method. Phase Field models have been shown to be extremely robust in resolving complex crack paths involving crack merging and branching.

In this work, MPM is employed as an alternative to standard grid based or meshless methods. In doing so, the proposed scheme can naturally treat large displacement driven fracture problems while at the same time avoiding mesh distortion errors. This is particularly important in impact driven fracture as well as fragmentation analysis where the proposed method demonstrates excellent performance.

To investigate the accuracy and the efficiency of the derived model over the standard computational approaches, the results are verified with the standard Phase Field Finite Element Method implementation and analytical solutions. The method is validated against experimental observations and measurements available in the literature.

The proposed model is initially developed for quasi-static brittle fracture. The influence of the length scale parameter, i.e. the diffusion of damage around

the crack is investigated on the material response. It is shown that the critical displacement and load are strongly influenced by the choice of length scale parameter. Furthermore, the mesh/grid sensitivity and cell density (i.e. number of material points per grid cell) are also examined. In this, the PF-MPM is found to also require a sufficient grid spacing to regularize the phase field smooth description as in PF-FEM. However, the cell density slightly influences the resulting load-displacement response of the material. The number of staggered iteration and the displacement increment are also examined in load-displacement paths. Similar with length scale parameter, the critical displacement and load are strongly dependent on these. Convergence in the material response is achieved by either decreasing the displacement increment or increasing the number of staggered iterations.

Following this, a fourth order phase field fracture model is employed. This allows for simulating the response of materials with anisotropic fracture energy. Within this setting, a family of both isotropic and anisotropic fourth order phase field models is derived. Benchmark tests conducted considering the case of cubic and orthotropic surface energy demonstrate that the resulting crack paths significantly depend on the material orientation. The proposed framework produces complex anisotropic fracture in a robust fashion and paves the way for the numerical investigation of such phenomena.

Finally, the proposed PF-MPM is originally upgraded within a dynamic setting with the objective of simulating dynamic fracture and impact induced fracture propagation problems. The resulting scheme is verified against a standard Phase Field Finite Element implementation where the two methods illustrate excellent agreement. The effect of anisotropy on the dynamic response of impacting bodies is also examined for the first time.

In particular, it is demonstrated that the material orientation and the weak directions of an anisotropic material strongly influence the resulting crack paths. The crack paths emerge either on material's weak directions or close to them.

Through extensive numerical testing, it is shown that the proposed method naturally treats complex crack geometries in a robust and efficient manner.

A significant advantage of the proposed method for the case of impact problems is that local contact features do not need to be tracked algorithmically. Instead, contact surface detection is performed at the fixed Eulerian grid. Thus, the derived computational tool can efficiently treat both arbitrary crack paths and contact surfaces without extra computational cost. The influence of surface energy anisotropy and loading conditions on the resulting crack paths is assessed through a set of benchmark problems. In this, it is shown that an amplified value of initial loading velocity leads to more complex crack paths.

Furthermore, the length scale parameter, cell spacing, cell density and number of staggered iterations are also examined on fracture energy time histories. It is demonstrated that the ratio of length scale parameter/cell spacing strongly influences the derived results as in quasi-static case. Similarly, the cell density slightly modifies the results. The number of staggered iterations is not critical in dynamic problems as it is to quasi-static case. Indeed, the simulations are restricted by the critical time step (CFL) and it is the critical parameter to achieve convergence on the results. The impact algorithms developed are also verified against analytical solutions and the results are shown to agree well.

Finally, the appropriateness of PF-MPM to simulate the response of rocking systems is studied. The method is found to be able to treat the rocking response of both rigid and deformable body in a robust and accurate manner. The proposed scheme does not rely on any assumption pertinent to the properties of the contact surfaces and the rocking bodies themselves.

Furthermore, deformable rocking bodies are also examined and the difference in their rocking response is highlighted. The damage evolution induced by rocking response is also examined, providing an appealing computational tool for complex soil-structure interaction analyses.

8.2 Future work

The following are research directions that could further improve the work presented in this thesis:

- Although Phase Field models offer advantages in simulating complex crack paths, they increase the number of unknowns to be considered. The accurate resolution of phase field evolution within its length scale effectively poses an upper bound on grid mesh size, hindering its computational efficiency especially in 3D problems. This is a common issue for both PF-MPM and PF-FEM. Hence, an adaptive mesh refinement strategy can be applied to reduce the computational demands. Alternatively, a multiscale formulation can also be applied to resolve the micro features of the material.

- In this work, a staggered iterative approach is adopted for all the benchmark problems. Both single and multi predictor-corrector schemes are examined. However, a staggered strategy sometimes requires a small time step to accurately solve the decoupled problem. Although the staggered scheme yields good results in the benchmark problems examined herein, a monolithic approach, i.e. solving the fully coupled problem, can be appealing when large time steps are permitted.

- The contact algorithm presented in this work is utilized within a staggered iterative approach combined with an explicit time integration scheme. Although this strategy is proven to be robust for parallel implementation, it is restricted by small time steps due to the Courant-Friedrichs-Levy (CFL) condition. Hence, the proposed PF-MPM can also be implemented within an implicit time integration scheme to overcome the above issue. However, an implicit time integration scheme introduces iterations at each time step. Thus, its efficiency in terms of computational costs should be further

examined against the proposed explicit scheme.

- In this work, the objective is to examine how the material anisotropy influences the evolution of crack paths. The material anisotropy is only examined in terms of its surface energy. Thus, generalization of the method can be made to also account for the anisotropic elastic material properties, i.e. the elastic stiffness tensor $\mathbf{D}$.

- The rocking bodies that are examined in this work, are assumed to resting on rigid support media. Yet, the proposed method can also simulate rocking response on deformable support media. Thus, a detailed analysis of how the deformability of support medium influences both its failure-safety condition (stability analysis examination) and the resulting crack paths at rocking body can be further exploited.

- The proposed PF-MPM presented in this work can be extended to account for isotropic and anisotropic ductile fracture, yielding a unified approach in fracture analysis of materials.

- The materials that are analysed in this work, are rate independent. However, the critical fracture energy density can be rate dependent in some materials. Thus, another future direction of this work is the extension of the proposed scheme to account for rate dependent materials.

- Finally, the proposed method can be extended to 3D problems.

Appendix A

Material Point penalty method for imposing kinematic constraints

In the following, we consider the case of the two dimensional problem shown in Fig. A.1. This involves 2 active cells with 6 active grid nodes totalling 12 degrees of freedom for the background Eulerian grid. Eight material points points are considered. Kinematic constraints need to be imposed on both displacement components of the material point p, namely $\mathbf{u}_p = \{u_{p_x}, u_{p_y}\}$.

As described in Section 3.9.4.1, in the MPM the displacement components of a material point are interpolated to the corresponding nodes of the active cell

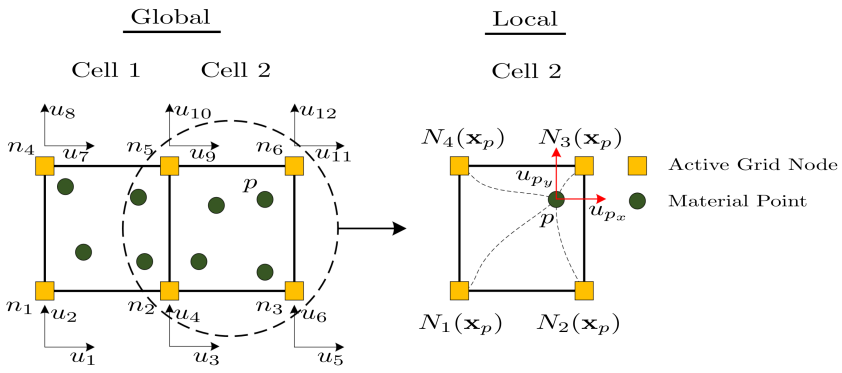

Figure A.1: Imposition of constraints with Penalty Method.

the material point resides. For the case of material point p shown in Fig. A.1, the interpolation expressions for both the horizontal and vertical components of the displacement vector are expressed in the following form

$$\begin{cases} u_{p_x} = N_1(\mathbf{x}_p)u_3 + N_2(\mathbf{x}_p)u_5 + N_3(\mathbf{x}_p)u_{11} + N_4(\mathbf{x}_p)u_9 \\ u_{p_y} = N_1(\mathbf{x}_p)u_4 + N_2(\mathbf{x}_p)u_6 + N_3(\mathbf{x}_p)u_{12} + N_4(\mathbf{x}_p)u_{10} \end{cases} \tag{A.1}$$

Following the standard procedure for the Penalty Method (Bathe, 2007), the following matrices are formulated

$$\mathbf{A} = \begin{bmatrix} 0 & 0 & N_1(\mathbf{x}_p) & 0 & N_2(\mathbf{x}_p) & 0 & 0 & 0 & N_4(\mathbf{x}_p) & 0 & N_3(\mathbf{x}_p) & 0 \\ 0 & 0 & 0 & N_1(\mathbf{x}_p) & 0 & N_2(\mathbf{x}_p) & 0 & 0 & 0 & N_4(\mathbf{x}_p) & 0 & N_3(\mathbf{x}_p) \end{bmatrix} \tag{A.2}$$

and

$$\mathbf{V} = \{u_{p_x}, u_{p_y}\} \tag{A.3}$$

where $\mathbf{A}$ is an $(N_{constr} \times N_{dofs})$ coefficient matrix whereas $\mathbf{V}$ is an $(1 \times N_{constr})$ coefficient vector. $N_{constr} \in \mathbb{Z}^+$ and $N_{dofs} \in \mathbb{Z}^+$ denotes to the total number of imposed constraints and total number of active unconstrained degree of freedom of the whole structure. Therefore, the incremental external forces as well as the incremental internal forces are modified according to equations (A.4) and (A.5) below

$$\boldsymbol{\Delta}\mathbf{F}^{ext} := \boldsymbol{\Delta}\mathbf{F}^{ext} + \alpha\mathbf{A}^T\mathbf{V}^T \tag{A.4}$$

$$\boldsymbol{\Delta}\mathbf{F}^{int} := \boldsymbol{\Delta}\mathbf{F}^{int} + \alpha\mathbf{A}^T\mathbf{A}\boldsymbol{\Delta}\mathbf{u} \tag{A.5}$$

where α is the Penalty Method parameter. If a direct solver is utilized then the global stiffness matrix of the structure is redefined according to equation (A.6) below

$$\mathbf{K}^u := \mathbf{K}^u + \alpha\mathbf{A}^T\mathbf{A} \tag{A.6}$$

This technique is extremely advantageous when the boundary conditions are not align with the background grid. Another alternative technique to deal with

boundary conditions that are not coincide with the background grid has recently introduced by Cortis et al. (2018) utilizing an implicit boundary method. Similar strategy is adapted to standard FEM when the essential boundary conditions should be applied on surfaces/edges that are not aligned with element edges.

Appendix B

Variational approach of the anisotropic phase field model

In the energy balance equation (5.19) the rate of the kinetic energy is evaluated as

$$\dot{\mathcal{K}}\left(\dot{\mathbf{u}}\right) = \frac{d}{dt}\int\limits_{\Omega}\frac{1}{2}\rho|\dot{\mathbf{u}}|^2 d\Omega = \int\limits_{\Omega}\left([\rho\ddot{\mathbf{u}}]\cdot\dot{\mathbf{u}}\right)d\Omega \tag{B.1}$$

Similarly, the rate of the external work is expressed as

$$\dot{\mathcal{W}}^{ext}\left(\dot{\mathbf{u}}\right) = \int_{\partial\Omega_{\bar{t}}}\left(\bar{\mathbf{t}}\cdot\dot{\mathbf{u}}\right)d\partial\Omega_{\bar{t}} + \int_{\Omega}\left(\mathbf{b}\cdot\dot{\mathbf{u}}\right)d\Omega \tag{B.2}$$

and the rate of the internal work is defined accordingly as

$$\dot{\mathcal{W}}^{int}\left(\dot{\mathbf{u}},\dot{c},\nabla\dot{c}\right) = \frac{d\Psi_s}{dt} = \frac{d}{dt}\int\limits_{\Omega}\left(\psi_{el} + \bar{\mathcal{G}}_c\mathcal{Z}_{c,Anis}\right)d\Omega \tag{B.3}$$

Applying the divergence theorem in equation (B.3), the rate of the internal work $\dot{\mathcal{W}}^{int}\left(\dot{\mathbf{u}},\dot{c},\nabla\dot{c}\right)$ assumes the following form

$$\dot{\mathcal{W}}^{int}\left(\dot{\mathbf{u}},\dot{c},\nabla\dot{c}\right) = \mathcal{B}_1 + \mathcal{B}_2 + \mathcal{B}_3 + \mathcal{B}_4 \tag{B.4}$$

where the components B_i, $i = 1 \dots 4$ assume the following expressions

$$\begin{aligned}\mathcal{B}_1 &= \frac{d}{dt}\int_\Omega \psi_{el} d\Omega \\ &= \int_{\partial\Omega} \left([\boldsymbol{\sigma}\mathbf{n}]\cdot\dot{\mathbf{u}}\right)\, d\partial\Omega - \int_\Omega \left([\nabla\cdot\boldsymbol{\sigma}]\cdot\dot{\mathbf{u}}\right)\, d\Omega + \int_\Omega \left(\psi_{el_c}\dot{c}\right)\, d\Omega\end{aligned} \tag{B.5}$$

$$\mathcal{B}_2 = \frac{d}{dt}\int_\Omega \left(\bar{\mathcal{G}}_c\left[\frac{(c-1)^2}{4l_0}\right]\right) d\Omega = \int_\Omega \left(\left[\bar{\mathcal{G}}_c\frac{(c-1)}{2l_0}\right]\dot{c}\right)\, d\Omega \tag{B.6}$$

$$\begin{aligned}\mathcal{B}_3 &= \frac{d}{dt}\int_\Omega \left(\bar{\mathcal{G}}_c\left[l_0|\nabla c|^2\right]\right)\, d\Omega \\ &= \int_{\partial\Omega} \left(\left[\bar{\mathcal{G}}_c l_0 2\nabla c\right]\cdot\mathbf{n}\dot{c}\right)\, d\partial\Omega - \int_\Omega \left(\left[\bar{\mathcal{G}}_c l_0 2\Delta c\right]\dot{c}\right)\, d\Omega\end{aligned} \tag{B.7}$$

and

$$\begin{aligned}\mathcal{B}_4 &= \frac{d}{dt}\int_\Omega \left(\bar{\mathcal{G}}_c\left[l_0^3\sum_{ijkl}\gamma_{ijkl}\frac{\partial^2 c}{\partial x_i\partial x_j}\frac{\partial^2 c}{\partial x_i\partial x_j}\right]\right)\, d\Omega \\ &= \int_\Omega \left(\bar{\mathcal{G}}_c\left[l_0^3\sum_{ijkl}\gamma_{ijkl}\frac{d}{dt}\left(\frac{\partial^2 c}{\partial x_i\partial x_j}\frac{\partial^2 c}{\partial x_k\partial x_l}\right)\right]\right)\, d\Omega \\ &= \int_\Omega \left(\bar{\mathcal{G}}_c\left[l_0^3\sum_{ijkl}\gamma_{ijkl}\left(\frac{d}{dt}\left(\frac{\partial^2 c}{\partial x_i\partial x_j}\right)\frac{\partial^2 c}{\partial x_k\partial x_l} + \frac{\partial^2 c}{\partial x_i\partial x_j}\frac{d}{dt}\left(\frac{\partial^2 c}{\partial x_k\partial x_l}\right)\right)\right]\right)\, d\Omega \\ &= \mathcal{T}_1 + \mathcal{T}_2,\end{aligned} \tag{B.8}$$

respectively, where

$$\mathcal{T}_1 = \int_\Omega \left(\bar{\mathcal{G}}_c\left[l_0^3\sum_{ijkl}\gamma_{ijkl}\left(\frac{d}{dt}\left(\frac{\partial^2 c}{\partial x_i\partial x_j}\right)\frac{\partial^2 c}{\partial x_k\partial x_l}\right)\right]\right)\, d\Omega \tag{B.9}$$

and

$$\mathcal{T}_2 = \int_\Omega \left(\bar{\mathcal{G}}_c\left[l_0^3\sum_{ijkl}\gamma_{ijkl}\left(\frac{\partial^2 c}{\partial x_i\partial x_j}\frac{d}{dt}\left(\frac{\partial^2 c}{\partial x_k\partial x_l}\right)\right)\right]\right)\, d\Omega \tag{B.10}$$

Components $\mathcal{T}_1$ and $\mathcal{T}_2$ are further expanded employing the divergence theorem into

$$\begin{aligned}
\mathcal{T}_1 &= \int_{\partial\Omega} \left(\left[\bar{\mathcal{G}}_c l_0^3 \sum_{ijkl} \gamma_{ijkl} \left(\frac{d}{dt} \left(\frac{\partial c}{\partial x_i} \right) \frac{\partial^2 c}{\partial x_k \partial x_l} \right) \right] \cdot \mathbf{n} \right) d\partial\Omega - \int_{\Omega} \left(\left[\bar{\mathcal{G}}_c l_0^3 \sum_{ijkl} \gamma_{ijkl} \left(\frac{d}{dt} \left(\frac{\partial c}{\partial x_i} \right) \frac{\partial^3 c}{\partial x_j \partial x_k \partial x_l} \right) \right] \right) d\Omega \\
&= \int_{\partial\Omega} \left(\left[\bar{\mathcal{G}}_c l_0^3 \sum_{ijkl} \gamma_{ijkl} \left(\frac{d}{dt} \left(\frac{\partial c}{\partial x_i} \right) \frac{\partial^2 c}{\partial x_k \partial x_l} \right) \right] \cdot \mathbf{n} \right) d\partial\Omega \\
&- \left(\int_{\partial\Omega} \left(\left[\bar{\mathcal{G}}_c l_0^3 \sum_{ijkl} \gamma_{ijkl} \left(\frac{dc}{dt} \frac{\partial^3 c}{\partial x_j \partial x_k \partial x_l} \right) \right] \cdot \mathbf{n} \right) d\partial\Omega - \int_{\Omega} \left(\left[\bar{\mathcal{G}}_c l_0^3 \sum_{ijkl} \gamma_{ijkl} \left(\frac{dc}{dt} \frac{\partial^4 c}{\partial x_i \partial x_j \partial x_k \partial x_l} \right) \right] \right) d\Omega \right) \\
&= \int_{\partial\Omega} \left(\left[\bar{\mathcal{G}}_c l_0^3 \sum_{ijkl} \gamma_{ijkl} \left(\frac{d}{dt} \left(\frac{\partial c}{\partial x_i} \right) \frac{\partial^2 c}{\partial x_k \partial x_l} \right) \right] \cdot \mathbf{n} \right) d\partial\Omega \\
&- \left(\int_{\partial\Omega} \left(\left[\bar{\mathcal{G}}_c l_0^3 \sum_{ijkl} \gamma_{ijkl} \left(\frac{\partial^3 c}{\partial x_j \partial x_k \partial x_l} \right) \right] \cdot \mathbf{n} \dot{c} \right) d\partial\Omega - \int_{\Omega} \left(\left[\bar{\mathcal{G}}_c l_0^3 \sum_{ijkl} \gamma_{ijkl} \left(\frac{\partial^4 c}{\partial x_i \partial x_j \partial x_k \partial x_l} \right) \right] \dot{c} \right) d\Omega \right)
\end{aligned} \tag{B.11}$$

and

$$\begin{aligned}
\mathcal{T}_2 &= \int_{\partial\Omega} \left(\left[\bar{\mathcal{G}}_c l_0^3 \sum_{ijkl} \gamma_{ijkl} \left(\frac{\partial^2 c}{\partial x_i \partial x_j} \frac{d}{dt} \left(\frac{\partial c}{\partial x_l} \right) \right) \right] \cdot \mathbf{n} \right) d\partial\Omega - \int_{\Omega} \left(\left[\bar{\mathcal{G}}_c l_0^3 \sum_{ijkl} \gamma_{ijkl} \left(\frac{\partial^3 c}{\partial x_i \partial x_j \partial x_k} \frac{d}{dt} \left(\frac{\partial c}{\partial x_l} \right) \right) \right] \right) d\Omega \\
&= \int_{\partial\Omega} \left(\left[\bar{\mathcal{G}}_c l_0^3 \sum_{ijkl} \gamma_{ijkl} \left(\frac{\partial^2 c}{\partial x_i \partial x_j} \frac{d}{dt} \left(\frac{\partial c}{\partial x_l} \right) \right) \right] \cdot \mathbf{n} \right) d\partial\Omega \\
&- \left(\int_{\partial\Omega} \left(\left[\bar{\mathcal{G}}_c l_0^3 \sum_{ijkl} \gamma_{ijkl} \left(\frac{\partial^3 c}{\partial x_i \partial x_j \partial x_k} \frac{dc}{dt} \right) \right] \cdot \mathbf{n} \right) d\partial\Omega - \int_{\Omega} \left(\left[\bar{\mathcal{G}}_c l_0^3 \sum_{ijkl} \gamma_{ijkl} \left(\frac{\partial^4 c}{\partial x_i \partial x_j \partial x_k \partial x_l} \frac{dc}{dt} \right) \right] \right) d\Omega \right) \\
&= \int_{\partial\Omega} \left(\left[\bar{\mathcal{G}}_c l_0^3 \sum_{ijkl} \gamma_{ijkl} \left(\frac{\partial^2 c}{\partial x_i \partial x_j} \frac{d}{dt} \left(\frac{\partial c}{\partial x_l} \right) \right) \right] \cdot \mathbf{n} \right) d\partial\Omega \\
&- \left(\int_{\partial\Omega} \left(\left[\bar{\mathcal{G}}_c l_0^3 \sum_{ijkl} \gamma_{ijkl} \left(\frac{\partial^3 c}{\partial x_i \partial x_j \partial x_k} \right) \right] \cdot \mathbf{n} \dot{c} \right) d\partial\Omega - \int_{\Omega} \left(\left[\bar{\mathcal{G}}_c l_0^3 \sum_{ijkl} \gamma_{ijkl} \left(\frac{\partial^4 c}{\partial x_i \partial x_j \partial x_k \partial x_l} \right) \right] \dot{c} \right) d\Omega \right),
\end{aligned} \tag{B.12}$$

respectively.

Substituting equations (B.11) and (B.12) in Eq. (B.8) the following expression is derived for $\mathcal{B}_4$

$$\begin{aligned}\mathcal{B}_4 = &\int_{\partial\Omega}\left(\left[\bar{\mathcal{G}}_c l_0^3 \sum_{ijkl}\gamma_{ijkl}\left(\frac{d}{dt}\left(\frac{\partial c}{\partial x_i}\right)\frac{\partial^2 c}{\partial x_k \partial x_l}\right) + \bar{\mathcal{G}}_c l_0^3 \sum_{ijkl}\gamma_{ijkl}\left(\frac{\partial^2 c}{\partial x_i \partial x_j}\frac{d}{dt}\left(\frac{\partial c}{\partial x_l}\right)\right)\right]\cdot\mathbf{n}\right) d\partial\Omega \\ &-\int_{\partial\Omega}\left(\left[\bar{\mathcal{G}}_c l_0^3 \sum_{ijkl}\gamma_{ijkl}\left(\frac{\partial^3 c}{\partial x_j \partial x_k \partial x_l}\right) + \bar{\mathcal{G}}_c l_0^3 \sum_{ijkl}\gamma_{ijkl}\left(\frac{\partial^3 c}{\partial x_i \partial x_j \partial x_k}\right)\right]\cdot\mathbf{n}\dot{c}\right) d\partial\Omega \\ &+2\int_{\Omega}\left(\left[\bar{\mathcal{G}}_c l_0^3 \sum_{ijkl}\gamma_{ijkl}\left(\frac{\partial^4 c}{\partial x_i \partial x_j \partial x_k \partial x_l}\right)\right]\dot{c}\right) d\Omega\end{aligned} \tag{B.13}$$

Substituting Eq. (B.13) in the energy balance equation (5.19) expression (5.21) is finally established.

Appendix C

Transformation of surface energy density to polar coordinates

The surface energy density and their corresponding reciprocal expression polar plots are evaluated according to the methodology introduced in Li et al. (2015). In this, the Cartesian coordinate system $\mathbf{x}\,(x_1, x_2)$ is transformed to $\mathbf{x}_\theta\,(x_{1_\theta}, x_{2_\theta})$ where the x_{1_θ}-axis is defined along the crack path Γ and x_{2_θ}-axis is the axis normal to the crack interface as shown in Fig. 5.1. Angle θ is the counter-clockwise angle between x_1-axis and x_{1_θ}.

Thus, a coordinate transformation from $\mathbf{x}\,(x_1, x_2)$ to $\mathbf{x}_\theta\,(x_{1_\theta}, x_{2_\theta})$ is performed through the transformation equation (C.1)

$$\left\{ \begin{array}{c} x_{1_\theta} \\ x_{2_\theta} \end{array} \right\} = \begin{bmatrix} \cos(\theta) & -\sin(\theta) \\ \sin(\theta) & \cos(\theta) \end{bmatrix} \left\{ \begin{array}{c} x_1 \\ x_2 \end{array} \right\} = \mathbf{x}_\theta = \mathbf{R}_\theta \mathbf{x} \tag{C.1}$$

with the inverse transformation defined as

$$\left\{ \begin{array}{c} x_1 \\ x_2 \end{array} \right\} = \begin{bmatrix} \cos(\theta) & \sin(\theta) \\ -\sin(\theta) & \cos(\theta) \end{bmatrix} \left\{ \begin{array}{c} x_{1_\theta} \\ x_{2_\theta} \end{array} \right\} = \mathbf{x} = \mathbf{R}_\theta^T \mathbf{x}_\theta \tag{C.2}$$

Assuming that $\partial c\left(\mathbf{x}\left(\mathbf{x}_\theta\right)\right)/\partial\mathbf{x} \approx \partial c\left(\mathbf{x}\left(x_{2_\theta}\right)\right)/\partial\mathbf{x}$ and applying the chain rule, the phase field first spatial derivatives are expressed as

$$\frac{\partial c}{\partial x_1} = \frac{\partial c}{\partial x_{1_\theta}}\frac{\partial x_{1_\theta}}{\partial x_1} + \frac{\partial c}{\partial x_{2_\theta}}\frac{\partial x_{2_\theta}}{\partial x_1} \approx \frac{\partial c}{\partial x_{2_\theta}}\frac{\partial x_{2_\theta}}{\partial x_1} = \frac{\partial c}{\partial x_{2_\theta}}\sin(\theta) \tag{C.3}$$

and

$$\frac{\partial c}{\partial x_2} = \frac{\partial c}{\partial x_{1_\theta}}\frac{\partial x_{1_\theta}}{\partial x_2} + \frac{\partial c}{\partial x_{2_\theta}}\frac{\partial x_{2_\theta}}{\partial x_2} \approx \frac{\partial c}{\partial x_{2_\theta}}\frac{\partial x_{2_\theta}}{\partial x_2} = \frac{\partial c}{\partial x_{2_\theta}}\cos(\theta), \tag{C.4}$$

respectively. Similarly, the second spatial derivatives are expressed as

$$\begin{aligned}\frac{\partial^2 c}{\partial {x_1}^2} = \frac{\partial}{\partial x_1}\left(\frac{\partial c}{\partial x_1}\right) = \frac{\partial}{\partial x_{1_\theta}}\left(\frac{\partial c}{\partial x_1}\right)\frac{\partial x_{1_\theta}}{\partial x_1} + \frac{\partial}{\partial x_{2_\theta}}\left(\frac{\partial c}{\partial x_1}\right)\frac{\partial x_{2_\theta}}{\partial x_1} \approx \\ \frac{\partial}{\partial x_{2_\theta}}\left(\frac{\partial c}{\partial x_1}\right)\frac{\partial x_{2_\theta}}{\partial x_1} = \frac{\partial^2 c}{\partial x_{2_\theta}^2}\sin^2(\theta)\end{aligned} \tag{C.5}$$

$$\begin{aligned}\frac{\partial^2 c}{\partial {x_2}^2} = \frac{\partial}{\partial x_2}\left(\frac{\partial c}{\partial x_2}\right) = \frac{\partial}{\partial x_{1_\theta}}\left(\frac{\partial c}{\partial x_2}\right)\frac{\partial x_{1_\theta}}{\partial x_2} + \frac{\partial}{\partial x_{2_\theta}}\left(\frac{\partial c}{\partial x_2}\right)\frac{\partial x_{2_\theta}}{\partial x_2} \approx \\ \frac{\partial}{\partial x_{2_\theta}}\left(\frac{\partial c}{\partial x_2}\right)\frac{\partial x_{2_\theta}}{\partial x_2} = \frac{\partial^2 c}{\partial x_{2_\theta}^2}\cos^2(\theta)\end{aligned} \tag{C.6}$$

and

$$\begin{aligned}\frac{\partial^2 c}{\partial x_1 \partial x_2} = \frac{\partial}{\partial x_1}\left(\frac{\partial c}{\partial x_2}\right) = \frac{\partial}{\partial x_{1_\theta}}\left(\frac{\partial c}{\partial x_2}\right)\frac{\partial x_{1_\theta}}{\partial x_1} + \frac{\partial}{\partial x_{2_\theta}}\left(\frac{\partial c}{\partial x_2}\right)\frac{\partial x_{2_\theta}}{\partial x_1} \approx \\ \frac{\partial}{\partial x_{2_\theta}}\left(\frac{\partial c}{\partial x_2}\right)\frac{\partial x_{2_\theta}}{\partial x_1} = \frac{\partial^2 c}{\partial x_{2_\theta}^2}\cos(\theta)\sin(\theta) \approx \frac{\partial^2 c}{\partial x_2 \partial x_1},\end{aligned} \tag{C.7}$$

respectively. Higher-order spatial derivatives are defined accordingly as

$$\frac{\partial^3 c}{\partial {x_1}^3} \approx \frac{\partial^3 c}{\partial x_{2_\theta}^3}\sin^3(\theta) \qquad \text{and} \qquad \frac{\partial^3 c}{\partial {x_2}^3} \approx \frac{\partial^3 c}{\partial x_{2_\theta}^3}\cos^3(\theta) \tag{C.8}$$

and

$$\begin{aligned}\frac{\partial^4 c}{\partial {x_1}^4} \approx \frac{\partial^4 c}{\partial x_{2_\theta}^4}\sin^4(\theta) \quad , \quad \frac{\partial^4 c}{\partial {x_2}^4} \approx \frac{\partial^4 c}{\partial x_{2_\theta}^4}\cos^4(\theta) \quad , \quad \frac{\partial^4 c}{\partial {x_1}^2 \partial {x_2}^2} \approx \frac{\partial^4 c}{\partial x_{2_\theta}^4}\cos^2(\theta)\sin^2(\theta) \\ \frac{\partial^4 c}{\partial x_1 \partial {x_2}^3} \approx \frac{\partial^4 c}{\partial x_{2_\theta}^4}\cos^3(\theta)\sin(\theta) \quad , \quad \frac{\partial^4 c}{\partial x_2 \partial {x_1}^3} \approx \frac{\partial^4 c}{\partial x_{2_\theta}^4}\sin^3(\theta)\cos(\theta)\end{aligned} \tag{C.9}$$

Employing equations (C.3) to (C.9), the functional $\mathcal{Z}_{c,Anis}$ of equation (5.3) is expressed in polar coordinates as

$$\mathcal{Z}_{c,Anis} = \left[\frac{(c-1)^2}{4l_0} + l_0|\nabla c|^2 + l_0^3 \sum_{ijkl} \gamma_{ijkl} \frac{\partial^2 c}{\partial x_i \partial x_j} \frac{\partial^2 c}{\partial x_k \partial x_l}\right] \approx \left[\frac{(c-1)^2}{4l_0} + l_0 \left(\frac{\partial c}{\partial x_{2_\theta}}\right)^2 + l_0^3 \gamma_\theta \left(\frac{\partial^2 c}{\partial x_{2_\theta}^2}\right)^2\right] \tag{C.10}$$

where γ_θ is defined from Eq. (5.9). Furthermore, the Euler-Lagrange equation is rewritten in the form

$$\begin{aligned} c - 1 - 4l_0^2 \Delta c + 4l_0^4 \sum_{ijkl} \gamma_{ijkl} \frac{\partial^4 c}{\partial x_i \partial x_j \partial x_k \partial x_l} = 0 \Rightarrow \\ \frac{d}{dx_{2_\theta}} \left(\frac{\partial \mathcal{Z}_{c,Anis}}{\partial(\partial c/\partial x_{2_\theta})}\right) - \frac{\partial \mathcal{Z}_{c,Anis}}{\partial c} = 0 \Leftrightarrow \\ c - 1 - 4l_0^2 \left(\frac{\partial^2 c}{\partial x_{2_\theta}^2}\right) + 4l_0^4 \gamma_\theta \left(\frac{\partial^4 c}{\partial x_{2_\theta}^4}\right) = 0 \end{aligned} \tag{C.11}$$

Equation (C.11) can then be numerically solved subject to the following boundary conditions, introduced in Eqs. (5.11) for fourth-order or Eqs. (5.12) for second order phase field models, respectively. Finally, the surface energy density $\mathcal{G}_c(\theta)$ is numerically evaluated from Eq. (5.17).

The maximum and minimum values of $\mathcal{G}_c(\theta)$ for $\theta \in [0, 2\pi]$ are defined as $\mathcal{G}_{c_{max}}$ and $\mathcal{G}_{c_{min}}$ respectively. The polar plot of surface energy density $\mathcal{G}_c(\theta)$ can be rotated by an arbitrary angle ϕ through the transformation equation (C.12)

$$\boldsymbol{\gamma}_\phi = \boldsymbol{Q}_\phi \boldsymbol{\gamma} \boldsymbol{Q}_\phi^T \tag{C.12}$$

where the rotation matrix $\boldsymbol{Q}_\phi$ is defined as

$$\boldsymbol{Q}_\phi = \begin{bmatrix} c^2 & s^2 & -2cs \\ s^2 & c^2 & 2cs \\ cs & -cs & c^2 - s^2 \end{bmatrix} \tag{C.13}$$

with $c = \cos(\phi)$, $s = \sin(\phi)$ the angle ϕ taken as positive in the clockwise direction. The pseudo-algorithm for the derivation of surface energy density $\mathcal{G}_c(\theta)$ and its reciprocal $1/\mathcal{G}_c(\theta)$ in polar coordinates is summarized in Algorithm 4.

Data: Define input material parameters (γ_{ijkl}, l_0, $\bar{\mathcal{G}}_c$, ϕ)
Define: $x_{lb} = 50 l_0$;
for $\theta = 0, .., 2\pi$ **do**
  Compute: $\boldsymbol{Q}_\phi$ (see Eq. (C.13)) ;
  Compute: $\boldsymbol{\gamma}_\phi$ (see Eq. (C.12)) ;
  Compute: γ_θ (see Eq. (5.9)) ;
  Define the boundary conditions: Use Eqs. (5.11) when $\gamma_{ijkl} \neq 0$ (fourth-order) or Eqs. (5.12) when $\gamma_{ijkl} = 0$ (second-order) ;
  Solve the differential equation (C.11) (third relation) and get $c(x_{2_\theta})$, $\frac{\partial c(x_{2_\theta})}{\partial x_{2_\theta}}$, $\frac{\partial^2 c(x_{2_\theta})}{\partial x_{2_\theta}^2}$;
  Compute: $\mathcal{Z}_{c,Anis}(x_{2_\theta})$ (see second of Eqs. (C.10)) ;
  Compute: $\mathcal{G}(\theta)$ (see last term of Eq. (5.17)) ;
  Compute: $1/\mathcal{G}(\theta)$;
end
Compute: $\mathcal{G}_{c_{max}} = \max_{\forall\theta\in[0,2\pi]}(\mathcal{G}(\theta))$ and $\mathcal{G}_{c_{min}} = \min_{\forall\theta\in[0,2\pi]}(\mathcal{G}(\theta))$;

Algorithm 4: Derivation of surface energy density $\mathcal{G}_c(\theta)$ and its reciprocal $1/\mathcal{G}_c(\theta)$ in polar coordinates.

Bibliography

Abe, K. et al. (2014). "Material Point Method for Coupled Hydromechanical Problems". In: *Journal of Geotechnical and Geoenvironmental Engineering* 140.3, p. 04013033.

Acikgoz, S. and M. J. DeJong (2012). "The interaction of elasticity and rocking in flexible structures allowed to uplift". In: *Earthquake Engineering & Structural Dynamics* 41.15, pp. 2177–2194.

Agathos, K., E. Chatzi, and S. P.A. Bordas (2016). "Stable 3D extended finite elements with higher order enrichment for accurate non planar fracture". In: *Computer Methods in Applied Mechanics and Engineering* 306.1, pp. 19–46.

Ai, W. and C. E. Augarde (2018a). "A multi-cracked particle method for complex fracture problems in 2D". In: *Mathematics and Computers in Simulation* 150, pp. 1–24.

— (2018b). "An adaptive cracking particle method providing explicit and accurate description of 3D crack surfaces". In: *Mathematics and Computers in Simulation* 114, pp. 1291–1309.

Allaire, G., N. Van Goethem, and F. Jouve (2007). *A level set method for the numerical simulation of damage evolution*. Technical Report: Note Ecole Polytechnique, Centre de Mathematiques Appliquees.

Ambati, M., T. Gerasimov, and L. De Lorenzis (2015a). "A review on phase-field models of brittle fracture and a new fast hybrid formulation". In: *Computational Mechanics* 55.2, pp. 383–405.

— (2015b). "Phase-field modeling of ductile fracture". In: *Computational Mechanics* 55.5, pp. 1017–1040.

Ambrosio, L. and V. M. Tortorelli (1990). "Approximation of functional depending on jumps by elliptic functional via Γ -convergence". In: *Communications on Pure and Applied Mathematics* 43.8, pp. 999–1036.

Amiri, F. et al. (2014a). "Phase-field modeling of fracture in linear thin shells". In: *Theoretical and Applied Fracture Mechanics* 69, pp. 102–109.

Amiri, F. et al. (2014b). "XLME interpolants, a seamless bridge between XFEM and enriched meshless methods". In: *Computational Mechanics* 53, pp. 45–57.

Amiri, F. et al. (2016). "Fourth order phase-field model for local max-ent approximants applied to crack propagation". In: *Computer Methods in Applied Mechanics and Engineering* 312.1, pp. 254–275.

Amor, H., J-J. Marigo, and C. Maurini (2009). "Regularized formulation of the variational brittle fracture with unilateral contact: Numerical experiments". In: *Journal of the Mechanics and Physics of Solids* 57.8, pp. 1209–1229.

Anderson, T. L. (1995). *Fracture Mechanics: Fundamentals and Applications*. CRC Press, Boca Raton, FL.

Arroyo, M. and M. Ortiz (2006). "Local maximum-entropy approximation schemes: a seamless bridge between finite elements and meshfree methods". In: *International Journal for Numerical Methods in Engineering* 65, pp. 2167–2202.

Arzani, H., A. Kaveh, and M. Taheri Taromsari (2017). "Optimum two-dimensional crack modeling in discrete least-squares meshless method by charged system search algorithm". In: *Scientia Iranica* 24.1, pp. 143–152.

Ast, J. et al. (2014). "Microcantilever bending experiments in NiAl - Evaluation, size effects, and crack tip plasticity". In: *Journal of Materials Research* 29.18, pp. 2129–2140.

Azocar, D., M. Elgueta, and M. C. Rivara (2010). "Automatic LEFM crack propagation method based on local Lepp-Deleuny mesh refinement". In: *Advances in Engineering Software* 41, pp. 111–119.

Babuška, I. and J. M. Melenk (1997). "The partition of unity method". In: *International Journal for Numerical Methods in Engineering* 40.4, pp. 727–758.

Ball, A. and H. McKenzie (1994). "On the low velocity impact behaviour of glass plates". In: *Le Journal de Physique IV* 4.C8, pp. 783–788.

Bandara, S. and K. Soga (2015). "Coupling of soil deformation and pore fluid flow using material point method". In: *Computers and Geotechnics* 63, pp. 199–214.

Barbieri, E. and M. Meo (2011). "A Meshless Cohesive Segments Method for Crack Initiation and Propagation in Composites". In: *Applied Composite Materials* 18, pp. 45–63.

Bardenhagen, S. G. and E. Kober (2004). "The generalized interpolation material point method". In: *Computer Modeling in Engineering and Sciences* 5.6, pp. 477–495.

Bardenhagen, S. G., J. U. Brackbill, and D. Sulsky (2000). "The material-point method for granular materials". In: *Computer Methods in Applied Mechanics and Engineering* 187.3, pp. 529–541.

Bardenhagen, S. G., J. A. Nairn, and H. Lu (2011). "Simulation of dynamic fracture with the Material Point Method using a mixed J-integral and cohesive law approach". In: *International Journal of Fracture* 170.1, pp. 49–66.

Barenblatt, G. I. (1962). "The Mathematical Theory of Equilibrium Cracks in Brittle Fracture". In: *Advances in Applied Mechanics* 7, pp. 55–129.

Bathe, K-J. (2007). *Finite element procedures*. Prentice Hall, Upper Saddle River, NJ.

Batra, R. C. and G. M. Zhang (2007). "Search algorithm, and simulation of elastodynamic crack propagation by modified smoothed particle hydrodynamics (MSPH) method". In: *Computational Mechanics* 40.3, pp. 531–546.

Belytschko, T. and T. Black (1999). "Elastic crack growth in finite elements with minimal remeshing". In: *International Journal for Numerical Methods in Engineering* 620, pp. 601–620.

Belytschko, T., Y. Y. Lu, and L. Gu (1994). "Element-free Galerkin methods". In: *International Journal for Numerical Methods in Engineering* 37.2, pp. 229–256.

Belytschko, T. et al. (2003). "Dynamic crack propagation based on loss of hyperbolicity and a new discontinuous enrichment". In: *International Journal for Numerical Methods in Engineering* 58, pp. 1873–1905.

Bernard, P., N. Moës, and N. Chevaugeon (2012). "Damage growth modeling using the Thick Level Set (TLS) approach: Efficient discretization for quasi-static loadings". In: *Computer Methods in Applied Mechanics and Engineering* 233-236, pp. 11–27.

Bittencourt, T. et al. (1996). "Quasi-automatic simulation of crack propagation for 2D LEFM problems". In: *Engineering Fracture Mechanics* 55, pp. 321–334.

Bobaru, F. and W. Hu (2012). "The Meaning, Selection, and Use of the Peridynamic Horizon and its Relation to Crack Branching in Brittle Materials". In: *International Journal of Fracture* 176.2, pp. 215–222.

Boor, C. D. (2001). *A Practical Guide to Splines.* Applied Mathematical Sciences. New York: Springer.

Borden, M. J. et al. (2012). "A phase-field description of dynamic brittle fracture". In: *Computer Methods in Applied Mechanics and Engineering* 217–220, pp. 77–95.

Borden, M. J. et al. (2014). "A higher-order phase-field model for brittle fracture: Formulation and analysis within the isogeometric analysis framework". In: *Computer Methods in Applied Mechanics and Engineering* 273, pp. 100–118.

Borden, M. J. et al. (2016). "A phase-field formulation for fracture in ductile materials: Finite deformation balance law derivation, plastic degradation, and stress triaxiality effects". In: *Computer Methods in Applied Mechanics and Engineering* 312.1, pp. 130–166.

Borst, R. de and V. Verhoosel (2016). "Gradient damage vs phase field approaches for fracture: Similarities and differences". In: *Computer Methods in Applied Mechanics and Engineering* 312, pp. 78–94.

Borst, R. de et al. (2012). *Nonlinear Finite Element Analysis of Solids and Structures*. Wiley, 2nd edition.

Bouchard, P., F. Bay, and Y. Chastel (2003). "Numerical modelling of crack propagation: automatic remeshing and comparison of different criteria". In: *Computer Methods in Applied Mechanics and Engineering* 192, pp. 3887–3908.

Bourdin, B., G. A. Francfort, and J-J. Marigo (2008). "The Variational Approach to Fracture". In: *Journal of Elasticity* 91.1-3, pp. 5–148.

Brackbill, J. U. and H. M. Ruppel (1986). "FLIP: A method for adaptively zoned, particle-in-cell calculations of fluid flows in two dimensions". In: *Journal of Computational Physics* 65, pp. 314–343.

Braides, A. (1998). *Approximation of Free-Discontinuity Problems*. Springer, Berlin.

Budyn, E. et al. (2004). "A method for multiple crack growth in brittle materials without remeshing". In: *International Journal for Numerical Methods in Engineering* 61, pp. 1741–1770.

Bulinga, M. (1998). "Energy Minimizing Brittle Crack Propagation". In: *Journal of Elasticity* 52, pp. 201–237.

Cahill, L. et al. (2014). "An experimental/numerical investigation into the main driving force for crack propagation in uni-directional fibre-reinforced composite laminae". In: *Composite Structures* 107, pp. 119–130.

Camacho, G. T. and M. Ortiz (1996). "Computational modelling of impact damage in brittle materials". In: *International Journal of Solids and Structures* 33.20, pp. 2899–2938.

Cazes, F. and N. Moës (2015). "Comparison of a phase-field model and of a thick level set model for brittle and quasi-brittle fracture". In: *International Journal for Numerical Methods in Engineering* 103.2, pp. 114–143.

Chandler, M. R. et al. (2016). "Fracture toughness anisotropy in shale". In: *Journal of Geophysical Research: Solid Earth* 121.3, pp. 1706–1729.

Charlton, T. J., W. M. Coombs, and C. E. Augarde (2017). "iGIMP: An implicit generalised interpolation material point method for large deformations". In: *Computers & Structures* 190, pp. 108–125.

Chatzis, M. N. and A. W. Smyth (2012a). "Modeling of the 3D rocking problem". In: *International Journal of Non-Linear Mechanics* 47.4, pp. 85–98.

Chatzis, M. N. and A. W. Smyth (2012b). "Robust Modeling of the Rocking Problem". In: *Journal of Engineering Mechanics* 138.3, pp. 247–262.

Chatzis, M. N., M. G. Espinosa, and A. W. Smyth (2017). "Examining the Energy Loss in the Inverted Pendulum Model for Rocking Bodies". In: *Journal of Engineering Mechanics* 143.5, p. 04017013.

Chen, S., M. Zang, and W. Xu (2015). "A three-dimensional computational framework for impact fracture analysis of automotive laminated glass". In: *Computer Methods in Applied Mechanics and Engineering* 294, pp. 72–99.

Chen, Z. et al. (2009). "Cohesive zone finite element-based modeling of hydraulic fractures". In: *Acta Mechanica Solida Sinica* 22, pp. 443–452.

Chen, Z.-P. et al. (2017). "A frictional contact algorithm for implicit material point method". In: *Computer Methods in Applied Mechanics and Engineering* 321, pp. 124–144.

Cheng, K. and T. Fries (2012). "Higher-order XFEM for curved strong and weak discontinuities". In: *International Journal for Numerical Methods in Engineering* 82, pp. 564–590.

Chessa, J., H. Wang, and T. Belytschko (2003). "On the construction of blending elements for local partition of unity enriched finite elements". In: *International Journal for Numerical Methods in Engineering* 57, pp. 1015–1038.

Coombs, W. M. et al. (2018). "Overcoming volumetric locking in material point methods". In: *Computer Methods in Applied Mechanics and Engineering* 333, pp. 1–21.

Cortis, M. et al. (2018). "Imposition of essential boundary conditions in the material point method". In: *International Journal for Numerical Methods in Engineering* 113.1, pp. 130–152. ISSN: 1097-0207.

Cummins, S. J. and J. U. Brackbill (2002). "An Implicit Particle-in-Cell Method for Granular Materials". In: *Journal of Computational Physics* 180.2, pp. 506–548.

Daphalapurkar, N. P. et al. (2007). "Simulation of dynamic crack growth using the generalized interpolation material point (GIMP) method". In: *International Journal of Fracture* 143.1, pp. 79–102.

Daux, C. et al. (2000). "Arbitrry branched and intersecting crcks with extended finite element method". In: *International Journal for Numerical Methods in Engineering* 48, pp. 1741–1760.

Doblaré, M., J. Garciá, and M. Gómez (2004). "Modelling bone tissue fracture and healing: a review". In: *Engineering Fracture Mechanics* 70, pp. 1809–1840.

Dokainish, M. A. and K. Subbaraj (1989). "A survey of direct time-integration methods in computational structural dynamics-I. Explicit methods". In: *Computers & Structures* 32.6, pp. 1371–1386.

Douillet-Grellier, T. et al. (2016). "Mixed-mode fracture modeling with smoothed particle hydrodynamics". In: *Computers and Geotechnics* 79, pp. 73–85.

Duarte, C. A. et al. (2001). "A generalized finite element method for the simulation of three-dimensional dynamic crack propagation". In: *Computer Methods in Applied Mechanics and Engineering* 190, pp. 2227–2262.

Duddu, R. (2014). "Numerical modeling of corrosion pit propagation using the combined extended finite element and level set method". In: *Computational Mechanics* 54.3, pp. 613–627.

Dugdale, D. S. (1960). "Yielding of Steel Sheets Containing Slits". In: *Journal of Mechanics and Physics of Solids* 8, pp. 100–104.

Erdogan, F. and G. C. Sih (1963). "On the Crack Entension in Plates Under Plane Loading and Transverse Shear". In: *Journal of Basic Engineering* 85, pp. 519–525.

Ferté, G., P. Massin, and N. Moës (2016). "3D crack propagation with cohesive elements in the extended finite element method". In: *Computer Methods in Applied Mechanics and Engineering* 300.1, pp. 347–374.

Fix, G. J. (1982). *Phase field methods for free boundary problems*. Carnegie Mellon University, U.S.

Francfort, G. A. and J.-J. Marigo (1998). "Revisiting brittle fracture as an energy minimization problem". In: *Journal of the Mechanics and Physics of Solids* 46.8, pp. 1319–1342.

Freund, L. B. (1998). *Dynamic Fracture Mechanics*. Cambridge University Press.

Fries, T. and T. Belytschko (2010). "The extended/generalized finite element method: an overview of the method and its applications". In: *International Journal for Numerical Methods in Engineering* 84, pp. 253–304.

Fries, T-P. and T. Belytschko (2006). "The intrinsic XFEM: a method for arbitrary discontinuities without additional unknowns". In: *International Journal for Numerical Methods in Engineering* 68.13, pp. 1358–1385.

Gan, Y. et al. (2018). "Enhancement of the material point method using B-spline basis functions". In: *International Journal for Numerical Methods in Engineering* 113.3, pp. 411–431.

Gerasimov, T. and L. De Lorenzis (2016). "A line search assisted monolithic approach for phase-field computing of brittle fracture". In: *Computer Methods in Applied Mechanics and Engineering* 312, pp. 276–303.

Griffith, A. A. (1921). "The Phenomena of Rupture and Flow in Solids". In: *Philosophical Transactions of the Royal Society of London A* 221, pp. 163–198.

Guilkey, J. E. and J. A. Weiss (2003). "Implicit time integration for the material point method: Quantitative and algorithmic comparisons with the finite element method". In: *International Journal for Numerical Methods in Engineering* 57.9, pp. 1323–1338.

Guilkey, J. E., J. B. Hoying, and J. A. Weiss (2006). "Computational modeling of multicellular constructs with the material point method". In: *Journal of Biomechanics* 39.11, pp. 2074–2086.

Gültekin, O., H. Dal, and G. A. Holzapfel (2018). "Numerical aspects of anisotropic failure in soft biological tissues favor energy-based criteria: A rate-dependent anisotropic crack phase-field model". In: *Computer Methods in Applied Mechanics and Engineering* 331, pp. 23–52.

Ha, Y. D. and F. Bobaru (2010). "Studies of dynamic crack propagation and crack branching with peridynamics". In: *International Journal of Fracture* 162, pp. 229–244.

Hagan, J. and M. Swain (1978). "The origin of median and lateral cracks around plastic indents in brittle materials". In: *Journal of Physics D: Applied Physics* 11.15, pp. 2091–2112.

Hansbo, A. and P. Hansbo (2004). "A finite element method for the simulation of strong and weak discontinuities in solid mechanics". In: *Computer Methods in Applied Mechanics and Engineering* 193, pp. 3523–3540.

Harlow, F. H. (1964). "The Particle-in-Cell Computing Method for Fluid Dynamics". In: *Methods of Computational Physics* 3, pp. 319–343.

Hesch, C. et al. (2016). "Hierarchical NURBS and a higher-order phase-field approach to fracture for finite-deformation contact problems". In: *Computer Methods in Applied Mechanics and Engineering* 301, pp. 242–258.

Hillerborg, A., M. Modeer, and P. E. Petersson (1976). "Analysis of Crack Formation and Crack Growth in Concrete by Means of Fracture Mechanics and Finite Elements". In: *Cement and Concrete Research* 6, pp. 773–781.

Hofacker, M. and C. Miehe (2013). "A phase field model of dynamic fracture: Robust field updates for the analysis of complex crack patterns". In: *International Journal for Numerical Methods in Engineering* 93.3, pp. 276–301.

Holzapfel, G. A., T. C. Gasser, and R. W. Ogden (2000). "A New Constitutive Framework for Arterial Wall Mechanics and a Comparative Study of Material Models". In: *Journal of elasticity and the physical science of solids* 61.1, pp. 1–48.

Homel, M. A. and E. B. Herbold (2017). "Field-gradient partitioning for fracture and frictional contact in the material point method". In: *International Journal for Numerical Methods in Engineering* 109.7, pp. 1013–1044.

Housner, G. W. (1963). "The behavior of inverted pendulum structures during earthquakes". In: *Bulletin of the Seismological Society of America* 53.2, pp. 403–417.

Huang, P. et al. (2011). "Contact algorithms for the material point method in impact and penetration simulation". In: *International Journal for Numerical Methods in Engineering* 85.4, pp. 498–517.

Hughes, T. J. R., J. A. Cottrell, and Y. Bazilevs (2005). "Isogeometric analysis: CAD, finite elements, NURBS, exact geometry and mesh refinement". In: *Computer Methods in Applied Mechanics and Engineering* 194.39-41, pp. 4135–4195.

Hughes, T. J. R., A. Reali, and G. Sangalli (2010). "Efficient quadrature for NURBS-based isogeometric analysis". In: *Computer Methods in Applied Mechanics and Engineering* 199.5-8, pp. 301–313.

Ingraffea, A. R. and V. Saouma (1985). "Numerical modelling of discrete crack propagation in reinforced and plain concrete". In: *Fracture Mechanics of Concrete. Martinus Nijhoff Publishers: Dordrecht*, pp. 171–225.

Jassim, I., D. Stolle, and P. Vermeer (2013). "Two-phase dynamic analysis by material point method". In: *International Journal for Numerical and Analytical Methods in Geomechanics* 37.15, pp. 2502–2522.

Jelagin, D. and P-L. Larsson (2008). "On indentation and initiation of fracture in glass". In: *International Journal of Solids and Structures* 45.10, pp. 2993–3008.

Kaczmarczyk, Ł., M. M. Nezhad, and C. Pearce (2014). "Three-dimensional brittle fracture: configurational-force-driven crack propagation". In: *International Journal for Numerical Methods in Engineering* 97.7, pp. 531–550.

Kakouris, E. G. and S. P. Triantafyllou (2017). "Phase-Field Material Point Method for Brittle Fracture". In: *International Journal for Numerical Methods in Engineering* 112.12, pp. 1750–1776.

Kakouris, E. G. and S. P. Triantafyllou (2018a). "Material point method for crack propagation in anisotropic media: a phase field approach". In: *Archive of Applied Mechanics* 88.1, pp. 287–316.

— (2018b). "Phase-field material point method for dynamic brittle fracture with isotropic and anisotropic surface energy". In: *Computer Methods in Applied Mechanics and Engineering (Submitted - under review)*.

Kakouris, E. G., M. N. Chatzis, and S. P. Triantafyllou (2018). "A Material Point Method for studing rocking systems." In: 16^{th} *European Conference on Earthquake Engineering, Thessaloniki, Greece.*

Klein, P. A. et al. (2001). "Physics-based modeling of brittle fracture: cohesive formulations and the application of meshfree methods". In: *Theoretical and Applied Fracture Mechanics* 37, pp. 99–166.

Konuk, I., A. Gürtner, and S. Yu (2009). "A Cohesive Element Framework for Dynamic Ice-Structure Interaction Problems - Part II: Implementation". In: *ASME 2009 28th International Conference on Ocean, Offshore and Arctic Engineering*. American Society of Mechanical Engineers, pp. 185–193.

Kuhn, C., A. Schlüter, and R. Müller (2015). "On degradation functions in phase field fracture models". In: *Computational Materials Science* 108, Part B, pp. 374–384.

Lancaster, P. and K. Salkauskas (1981). "Surfaces generated by moving least squares methods". In: *Mathematics of Computation* 37, pp. 141–158.

Lazzarin, P. et al. (2008). "Local strain energy density and fatique strength of welded joints under uniaxial and multiaxial loading". In: *Engineering Fracture Mechanics* 75, pp. 1875–1889.

Le Bellego, C. et al. (2003). "Calibration of nonlocal damage model from size effect tests". In: *European Journal of Mechanics - A/Solids* 22, pp. 33–46.

Lee, G., H-J. Chung, and C-K. Choi (2003). "Adaptive crack propagation analysis with the element-free Galerkin method". In: *International Journal for Numerical Methods in Engineering* 56, pp. 331–350.

Li, B. et al. (2015). "Phase-field modeling and simulation of fracture in brittle materials with strongly anisotropic surface energy". In: *International Journal for Numerical Methods in Engineering* 102.3-4, pp. 711–727.

Li, J. G. et al. (2014). "Sloshing impact simulation with material point method and its experimental validations". In: *Computers & Fluids* 103, pp. 86–99.

Li, T. et al. (2016). "Gradient damage modeling of brittle fracture in an explicit dynamics context". In: *International Journal for Numerical Methods in Engineering* 108.11, pp. 1381–1405.

Lian, Y. P., X. Zhang, and Y. Liu (2011). "Coupling of finite element method with material point method by local multi-mesh contact method". In: *Computer Methods in Applied Mechanics and Engineering* 200.47, pp. 3482–3494.

Liang, Y. et al. (2017). "Material point method with enriched shape function for crack problems". In: *Computer Methods in Applied Mechanics and Engineering* 322, pp. 541–562.

Lin, D. et al. (2018). "Numerical simulations of impact fracture behavior of an automotive windshield glazing: An intrinsic cohesive approach". In: *Composite Structures* 186, pp. 79–93.

Liu, M. (2010). "Smooth Particle Hydrodynamics (SPH): an Overview and Recent Developments". In: *Archives of Computational Methods in Engineering* 17, pp. 25–76.

Liu, W. K., S. Jun, and Y. F. Zhang (1995). "Reproducing kernel particle methods". In: *International Journal of Impact Engineering* 20, pp. 1081–1106.

Liu, Z. and D. Juhre (2018). "Phase-Field Modelling of Crack Propagation in Anisotropic Polycrystalline Materials". In: *Procedia Structural Integrity* 13, pp. 787–792.

Lu, H. et al. (2006). "Multiscale simulation from atomistic to continuum - coupling molecular dynamics (MD) with the material point method (MPM)". In: *Philosophical Magazine* 86.20, pp. 2971–2994.

Lucy, L. B. (1977). "A numerical approach to the testing of the fission hypothesis". In: *Astronomical Journal* 82, pp. 1013–1024.

Luding, S. (2008). "Introduction to Discrete Element Methods". In: *European Journal of Environmental and Civil Engineering* 12, pp. 785–826.

Matvienko, Y. (2012). "Maximum Average Tangential Stress Criterion for Prediction of the Crack Path". In: *International Journal of Fracture* 176, pp. 113–118.

Mazars, J. (1986). "A description of micro- and macroscale damage of concrete structures". In: *Engineering Fracture Mechanics* 25.5, pp. 729–737.

Meer, F. van der and L. Sluys (2015). "The Thick Level Set method: Sliding deformations and damage initiation". In: *Computer Methods in Applied Mechanics and Engineering* 285, pp. 64–82.

Miehe, C., M. Hofacker, and F. Welschinger (2010a). "A phase field model for rate-independent crack propagation: Robust algorithmic implementation based on operator splits". In: *Computer Methods in Applied Mechanics and Engineering* 199.45-48, pp. 2765–2778.

Miehe, C., F. Welschinger, and M. Hofacker (2010b). "Thermodynamically consistent phase-field models of fracture: Variational principles and multi-field FE implementations". In: *International Journal for Numerical Methods in Engineering* 83.10, pp. 1273–1311.

Miehe, C., F. Aldakheel, and A. Raina (2016). "Phase field modeling of ductile fracture at finite strains: A variational gradient-extended plasticity-damage theory". In: *International Journal of Plasticity* 84, pp. 1–32.

Moës, N. and T. Belytschko (2002). "Extended finite element method for cohesive crack growth". In: *Engineering Fracture Mechanics* 69.7, pp. 813–833.

Moës, N., J. Dolbow, and T. Belytschko (1999). "A finite element method for crack growth without remeshing". In: *International Journal for Numerical Methods in Engineering* 46.1, pp. 131–150.

Moës, N. et al. (2011). "A level set based model for damage growth: The thick level set approach". In: *International Journal for Numerical Methods in Engineering* 86, pp. 358–380.

Moreau, K. et al. (2015). "Explicit dynamics with a non-local damage model using the thick level set approach". In: *International Journal for Numerical Methods in Engineering* 102, pp. 808–838.

Most, T. and C. Bucher (2003). "Moving Least Squares-elements for stochastic crack propagation simulations coupled with stochastic finite elements". In:

Conference: 9th International Conference on Applications of Statistics and Probability in Civil Engineering At: San Francisco, USA.

Müller, P. and J. J. Métois (2008). "Anisotropy of the surface thermodynamic properties of silicon". In: *Thin Solid Films* 517, pp. 65–68.

Murakami, S. (2012). *Continuum Damage Mechanics*. Solid Mechanics and Its Applications, Springer Netherlands.

Murakami, S. and Y. Liu (1995). "Mesh-dependence in local approach to creep fracture". In: *International Journal of Damage Mechanics* 4, pp. 230–250.

Nairn, J. A. (2003). "Material Point Method Calculations with Explicit Cracks". In: *Computer Modeling in Engineering and Sciences* 4.6, pp. 649–663.

Nairn, J. A., C. Hammerquist, and Y. E. Aimene (2017). "Numerical Implementation of Anisotropic Damage Mechanics". In: *International Journal for Numerical Methods in Engineering* 112.12, pp. 1848–1868.

Nasseri, M. H. B. and B. Mohanty (2008). "Fracture toughness anisotropy in granitic rocks". In: *International Journal of Rock Mechanics and Mining Sciences* 45.2, pp. 167–193.

Nezamabadi, S. et al. (2015). "Implicit frictional-contact model for soft particle systems". In: *Journal of the Mechanics and Physics of Solids* 83, pp. 72–87.

Nguyen, T-T. et al. (2017). "Multi-phase-field modeling of anisotropic crack propagation for polycrystalline materials". In: *Computational Mechanics* 60.2, pp. 289–314.

Nguyen, V. P. et al. (2008). "Meshless methods: A review and computer implementation aspects". In: *Mathematics and Computers in Simulation* 79.3, pp. 763–813.

Nguyen, Vinh Phu et al. (2015). "Isogeometric analysis: An overview and computer implementation aspects". In: *Mathematics and Computers in Simulation* 117, pp. 89–116.

Nuismer, R. (1975). "An energy release rate criterion for mixed mode fracture". In: *International Journal of Fracture* 11, pp. 245–250.

Organ, D. et al. (1996). "Continuous meshless approximations for nonconvex bodies by diffraction and transparency". In: *Computational Mechanics* 18, pp. 225–235.

Pacific-Earthquake-Engineering-Research-Center (P.E.E.R. Ground Motion Database) (2018). URL: http://peer.berkeley.edu/products/strong_ground_motion_db.html.

Park, K. and G. H. Paulino (2011). "Cohesive Zone Models: A Critical Review of Traction-Separation Relationships Across Fracture Surfaces". In: *Applied Mechanics Reviews* 64.6, p. 060802.

Peerlings, R. et al. (2001). "A critical comparison of nonlocal and gradient-enhanced softening continua". In: *International Journal of Solids and Structures* 38, pp. 7723–7746.

Peerlings, R. H. et al. (1996). "Gradient-enhanced damage for quasi-brittle materials". In: *International Journal for Numerical Methods in Engineering* 39, pp. 3391–3403.

Peerlings, R. H. et al. (2002). "Localisation issues and nonlocal continum approaches to fracture". In: *European Journal of Mechanics - A/Solids* 21, pp. 175–189.

Pijaudier-Cabot, G. and Z. P. Bazant (1987). "Nonlocal damage theory". In: *Journal of Engineering Mechanics* 113.10, pp. 1512–1533.

Pijaudier-Cabot, G. and A. Huerta (1991). "Finite element analysis of bifurcation in nonlocall strain softening solids". In: *Computer Methods in Applied Mechanics and Engineering* 90, pp. 905–919.

Rabczuk, T. and G. Zi (2007). "A Meshfree Method based on the Local Partition of Unity for Cohesive Cracks". In: *Computational Mechanics* 39, pp. 743–760.

Rabczuk, T. et al. (2010). "A simple and robust three-dimensional cracking-particle method without enrichment". In: *Computer Methods in Applied Mechanics and Engineering* 199.37, pp. 2437–2455.

Radovitzky, R. et al. (2011). "A scalable 3D fracture and fragmentation algorithm based on a hybrid, discontinuous Galerkin, cohesive element method". In: *Computer Methods in Applied Mechanics and Engineering* 200.1, pp. 326–344.

Raina, A. and C. Miehe (2016). "A phase-field model for fracture in biological tissues". In: *Biomechanics and Modeling in Mechanobiology* 15.3, pp. 479–496.

Rangarajan, R. et al. (2015). "Simulating curvilinear crack propagation in two dimensions with universal meshes". In: *International Journal for Numerical Methods in Engineering* 102.3-4, pp. 632–670.

Rapaport, D. C. (2004). *The Art of Molecular Dynamics Simulation*. Cambridge University Press.

Ravi-Chandar, K. (1998). "Dynamic Fracture of Nominally Brittle Materials". In: *International Journal of Fracture* 90.1, pp. 83–102.

Ravi-Chandar, K. and W. G. Knauss (1984). "An experimental investigation into dynamic fracture: III. On steady-state crack propagation and crack branching". In: *International Journal of Fracture* 26.2, pp. 141–154.

Remmers, J. J. C., R. de Borst, and A. Needleman (2003). "A cohesive segments method for the simulation of crack growth". In: *Computational mechanics* 31.1-2, pp. 69–77.

Remmers, J. J. C., R. de Borst, and Alan Needleman (2008). "The simulation of dynamic crack propagation using the cohesive segments method". In: *Journal of the Mechanics and Physics of Solids* 56.1, 70–92], year = [2008.

Sadeghirad, A., R. M. Brannon, and J. Burghardt (2011). "A convected particle domain interpolation technique to extend applicability of the material point method for problems involving massive deformations". In: *International Journal for Numerical Methods in Engineering* 86.12, pp. 1435–1456.

Sadeghirad, A., R. M. Brannon, and J. E. Guilkey (2013). "Second-order convected particle domain interpolation (CPDI2) with enrichment for weak discontinuities at material interfaces". In: *International Journal for Numerical Methods in Engineering* 95.11, pp. 928–952.

Salen, A. L. and M. H. Aliabadi (1995). "Crack growth analysis in concrete using boundary element method". In: *Engineering Fracture Mechanics* 51, pp. 533–545.

Salzman, A., N. Moës, and N. Chevaugeon (2016). "On use of the thick level set method in 3D quasi-static crack simulation of quasi-brittle material". In: *International Journal of Fracture* 202, pp. 21–49.

Sanchez, J. et al. (2015). "Solving quasi-static equations with the material-point method". In: *International Journal for Numerical Methods in Engineering* 103.1, pp. 60–78.

Schillinger, D., M. J. Borden, and H. K. Stolarski (2015). "Isogeometric collocation for phase-field fracture models". In: *Computer Methods in Applied Mechanics and Engineering* 284, pp. 583–610.

Schlüter, A. et al. (2014). "Phase field approximation of dynamic brittle fracture". In: *Computational Mechanics* 54.5, pp. 1141–1161.

Scholtès, L. and F-V. Donzé (2012). "Modelling progressive failure in fractured rock masses using a 3D discrete element method". In: *International Journal of Rock Mechanics and Mining Sciences* 52, pp. 18–30.

Schreyer, H. L., D. L. Sulsky, and S.-J. Zhou (2002). "Modeling delamination as a strong discontinuity with the material point method". In: *Computer Methods in Applied Mechanics and Engineering* 191.23-24, pp. 2483–2507.

Sekerka, R. (2005). "Analytical criteria for missing orientations on three-dimensional equilibrium shapes". In: *Journal of Crystal Growth* 275, pp. 77–82.

Shepard, D. (1968). "A two-dimensional function for irregularly spaced points". In: *Proceedings of the 23rd ACM National Conference*, pp. 517–524.

Sherburn, J. A. et al. (2015). "Meshfree modeling of concrete slab perforation using a reproducing kernel particle impact and penetration formulation". In: *International Journal of Impact Engineering* 86, pp. 96–110.

Sih, G. (1974). "Strain-energy-density factor applied to mixed mode crack problems". In: *International Journal of Fracture* 10, pp. 305–321.

Sih, G. C (1991). *Mechanics of Fracture Initiation and Propagation: Surface and Volume Energy Density Applied as Failure Criterion*. Dordecht, the Netherlands: Kluwer Academic.

Silling, S. A. (2000). "Reformulation of elasticity theory for discontinuities and long-range forces". In: *Mechanics and Physics of Solids* 48, pp. 175–209.

Simo, J. C. and J. W. Ju (1987). "Strain and stress-based continuum damage models-I. Formulation". In: *International Journal of Solids and Structures* 23.7, pp. 821–840.

Simo, J. C. and C. Miehe (1992). "Associative coupled thermoplasticity at finite strains: Formulation, numerical analysis and implementation". In: *Computer Methods in Applied Mechanics and Engineering* 98.1, pp. 41–104.

Simpson, R. and J. Travelyan (2011). "A partition of unity enriched dual boundary method for accurate computations in fracture mechanics". In: *Computer Methods in Applied Mechanics and Engineering* 200, pp. 1–10.

Snozzi, L. and J.-F. Molinari (2013). "A cohesive element model for mixed mode loading with frictional contact capability". In: *International Journal for Numerical Methods in Engineering* 93.5, pp. 510–526.

Sofianos, C. D. and V. K. Koumousis (2018). "Hysteretic behavior using the explicit material point method". In: *Computational Particle Mechanics* 1, pp. 1–18.

Song, Jeong-Hoon, Hongwu Wang, and Ted Belytschko (2008). "A comparative study on finite element methods for dynamic fracture". In: *Computational Mechanics* 42.2, pp. 239–250.

Soparat, P. and P. Nanakorn (2008). "Analysis of Cohesive Crack Growth by the Element-Free Galerkin Method". In: *Journal of Mechanics* 24, pp. 45–54.

Souza Neto, E. A. de, D. Peric, and D. Owen (2008). *Computational Methods for Plasticity: Theory and Applications*. Wiley, 1 edition.

Steffen, M., R. M. Kirby, and M. Berzins (2008). "Analysis and reduction of quadrature errors in the material point method (MPM)". In: *International Journal for Numerical Methods in Engineering* 76.6, pp. 922–948.

Stolarska, M. et al. (2001). "Modelling crack growth by level sets in the extended finite element method". In: *International Journal for Numerical Methods in Engineering* 51, pp. 943–960.

Sukumar, N., J. E. Dolbow, and N. Moës (2015). "Extended finite element method in computational fracture mechanics: a retrospective examination". In: *International Journal of Fracture* 196.1, pp. 189–206.

Sulsky, D. and J. U. Brackbill (1991). "A numerical method for suspension flow". In: *Journal of Computational Physics* 96.2, pp. 339–368.

Sulsky, D. and A. Kaul (2004). "Implicit dynamics in the material-point method". In: *Computer Methods in Applied Mechanics and Engineering* 193.12-14, pp. 1137–1170.

Sulsky, D., Z. Chen, and H. L. Schreyer (1994). "A particle method for history-dependent materials". In: *Computer Methods in Applied Mechanics and Engineering* 118.1-2, pp. 179–196.

Sulsky, D., S.-J. Zhou, and H. L. Schreyer (1995). "Application of a particle-in-cell method to solid mechanics". In: *Computer Physics Communications* 87.1, pp. 236–252.

Sun, C. T. and Z.-H. Jin (2012). *Fracture Mechanics*. Academic Press.

Sung, P-H. and T-C. Chen (2015). "Studies of crack growth and propagation of single-crystal nickel by molecular dynamics". In: *Computational Materials Science* 102, pp. 151–158.

Takei, A. et al. (2013). "Forbidden Directions for the Fracture of Thin Anisotropic Sheets: An Analogy with the Wulff Plot". In: *Physical Review Letters* 110.144301, pp. 1–5.

Tan, Y., D. Yang, and Y. Sheng (2009). "Discrete element method (DEM) modeling of fracture and damage in the machining process of polycrystalline SiC". In: *Journal of the European Ceramic Society* 29, pp. 1029–1037.

Teichtmeister, S. et al. (2017). "Phase field modeling of fracture in anisotropic brittle solids". In: *International Journal of Non-Linear Mechanics* 97, pp. 1–21.

Ting, T. (1996). *Anisotropic Elasticity: Theory and Applications*. Oxford University Press, New York.

Trädegard, A., F. Nilsson, and S. Östlund (1998). "FEM-remeshing technique applied to crack growth problems". In: *Computer Methods in Applied Mechanics and Engineering* 160.1-2, pp. 115–131.

Tromans, D. and J. Meech (2002). "Fracture toughness and surface energies of minerals: theoretical estimates for oxides, sulphides, silicates and halides". In: *Minerals Engineering* 15, pp. 1027–1041.

Turner, P. et al. (2018). "Three-dimensional woven carbon fibre polymer composite beams and plates under ballistic impact". In: *Composite Structures* 185, pp. 483–495.

Ullah, Z., W. M. Coombs, and C. E. Augarde (2013). "An adaptive finite element/meshless coupled method based on local maximum entropy shape functions for linear and nonlinear problems". In: *Computer Methods in Applied Mechanics and Engineering* 267, pp. 111–132.

Ventura, G., J. X. Xu, and T. Belytschko (2002). "A vector level set method and new discontinuity approximations for crack growth by EFG". In: *International Journal for Numerical Methods in Engineering* 54.6, pp. 923–944.

Verhoosel, C. V. and R. de Borst (2013). "A phase-field model for cohesive fracture". In: *International Journal for Numerical Methods in Engineering* 96.1, pp. 43–62.

Vree, J. H. de, Brekelmans W. A., and M. A. van Gils (1995). "Comparison of nonlocal approaches in continuum damage mechanics". In: *Computers and Structures* 55, pp. 581–588.

Winkler, B. (2001). *Traglastuntersuchungen von unbewehrten und bewehrten Betonstrukturen auf der Grundlage eines objektiven Werkstoffgesetzes für Beton*. Dissertation. University of Innsbruck, Austria.

Wolf, J. (1994). *Foundation Vibration Analysis Using Simple Physical Models*. Prentice Hall, Upper Saddle River, NJ.

Wu, J. et al. (2016). "Stochastic analysis of polymer composites rupture at large deformations modeled by a phase field method". In: *Computer Methods in Applied Mechanics and Engineering* 312.1, pp. 596–634.

Xu, S., H. Reinhardt, and M. Gappoev (1996). "Mode II fracture testing method for highly orthotropic materials like wood". In: *International Journal of Fracture* 75, pp. 185–214.

Xu, X.-P. and A. Needleman (1994). "Numerical simulations of fast crack growth in brittle solids". In: *Journal of the Mechanics and Physics of Solids* 42.9, pp. 1397–1434.

Yang, P. et al. (2014). "Improved decohesion modeling with the material point method for simulating crack evolution". In: *International Journal of Fracture* 186.1, pp. 177–184.

Yastrebov, V. A. (2013). *Numerical Methods in Contact Mechanics*. Numerical methods in engineering series. ISTE/Wiley, London/Hoboken.

Yolum, U., A. Tastan, and A. Guler (2016). "A Peridynamic Model for Ductile Fracture of Moderately Thick Plates". In: *Procedia Structural Integrity* 2, pp. 3713–3720.

Yoon, Y-C, S-H. Lee, and T. Belytschko (2006). "Enriched meshfree collocation method with diffuse derivatives for elastic fracture". In: *Computers and Mathematics with Applications* 51.8, pp. 1349–1366.

Zhang, H. (2010). "Simulation of crack growth using cohesive crack method". In: *Applied Mathematical Modelling* 34.9, pp. 2508–2519.

Zhang, J. and N. Makris (2001). "Rocking Response of Free-Standing Blocks under Cycloidal Pulses". In: *Journal of Engineering Mechanics* 127.5, pp. 473–483.

Zhang, X., Z. Chen, and Y. Liu (2016). *The Material Point Method: A Continuum-Based Particle Method for Extreme Loading Cases*. Academic Press.

Zhuang, X., C. Augarde, and S. Bordas (2011). "Accurate fracture modelling using meshless methods, the visibility criterion and level sets: Formulation

and 2D modelling". In: *International Journal for Numerical Methods in Engineering* 86, pp. 249–268.

Zhuang, X., C. E. Augarde, and K. M. Mathisen (2012). "Fracture modeling using meshless methods and level sets in 3D: Framework and modeling". In: *International Journal for Numerical Methods in Engineering* 92.11, pp. 969–998.